TU Delft

Delft University of Technology

Sea-level changes on multiple spatial scales: estimates and contributing processes

Frederikse, Thomas

DOI
10.4233/uuid:0912fa9b-4442-4a6b-8831-db5ec2603cb8

Publication date
2018

Document Version
Final published version

Citation (APA)
Frederikse, T. (2018). *Sea-level changes on multiple spatial scales: estimates and contributing processes*. [Dissertation (TU Delft), Delft University of Technology]. https://doi.org/10.4233/uuid:0912fa9b-4442-4a6b-8831-db5ec2603cb8

Important note
To cite this publication, please use the final published version (if applicable).
Please check the document version above.

Copyright
Other than for strictly personal use, it is not permitted to download, forward or distribute the text or part of it, without the consent of the author(s) and/or copyright holder(s), unless the work is under an open content license such as Creative Commons.

Takedown policy
Please contact us and provide details if you believe this document breaches copyrights.
We will remove access to the work immediately and investigate your claim.

This work is downloaded from Delft University of Technology.
For technical reasons the number of authors shown on this cover page is limited to a maximum of 10.

Sea-level changes on multiple spatial scales: estimates and contributing processes

Thomas Frederikse

Cover:
Boris Tellegen

Sea-level changes on multiple spatial scales: estimates and contributing processes

PROEFSCHRIFT

ter verkrijging van de graad van doctor
aan de Technische Universiteit Delft,
op gezag van de Rector Magnificus prof. dr. ir. T.H.J.J. van der Hagen
voorzitter van het College voor Promoties,
in het openbaar te verdedigen op maandag 19 maart 2018 om 12:30 uur.

door

Thomas FREDERIKSE

Natuurkundig Ingenieur,
Technische Universiteit Delft, Nederland
geboren te Amsterdam.

Dit proefschrift is goedgekeurd door de promotor en de copromotor.

Samenstelling promotiecommissie:

Rector Magnificus,	voorzitter
Prof. dr.-Ing. habil. R. Klees	Technische Universiteit Delft, promotor
Dr. R.E.M. Riva	Technische Universiteit Delft, copromotor

Onafhankelijke leden:

Prof. dr. J.D. Pietrzak	Technische Universiteit Delft
Prof. dr. C.W. Hughes	University of Liverpool
Prof. dr. J.L. Bamber	University of Bristol
Prof. dr. G. Wöppelmann	Université de La Rochelle
Dr. A.B.A. Slangen	Koninklijk Nederlands Instituut voor Onderzoek der Zee
Prof. dr. L.L.A. Vermeersen	Technische Universiteit Delft, reservelid

Dit onderzoek is financieel mogelijk gemaakt door de Nederlandse Organisatie voor Wetenschappelijk Onderzoek (NWO).

Keywords: sea-level rise, sea-level budget, physical oceanography, water mass redistribution

ISBN 978-94-6186-903-6

Copyright ©2018 by Thomas Frederikse

All rights reserved. No part of the material protected by this copyright notice may be reproduced or utilized in any form or by any means, electronic or mechanical, including photocopying, recording or by any information storage and retrieval system, without the prior permission of the author.

Typeset by the author with the LaTeX Documentation System.

The Rodney & Otamatea Times
WAITEMATA & KAIPARA GAZETTE.
PRICE—10s per annum in advance
WARKWORTH, WEDNESDAY, AUGUST 14, 1912.
3d. per Copy.

Science Notes and News.

COAL CONSUMPTION AFFECTING CLIMATE.

The furnaces of the world are now burning about 2,000,000,000 tons of coal a year. When this is burned, uniting with oxygen, it adds about 7,000,000,000 tons of carbon dioxide to the atmosphere yearly. This tends to make the air a more effective blanket for the earth and to raise its temperature. The effect may be considerable in a few centuries.

Preface

A long time ago, when I was a freshman studying applied physics, I went to a lunch lecture from a PhD candidate. The sole reason to join this lecture was that a free lunch was provided[1]. The guy giving the lecture was far from inspiring and his main conclusion was that even if it takes you 8 years to obtain a physics degree, you could still pursue a PhD afterwards.

My expectation about an average PhD trajectory a that time, which was roughly aligned to the average expectation from my fellow students, could be described as follows: 'You start your research full of enthousiasm, and keep up the good work for half a year, then you get stuck for three years, and finally, you try to put some uninteresting, disappointing, and unconvincing results into a booklet that ends up collecting dust at the back row of a bookshelf."

It was only six years later, during an internship in Germany, that Thijs Heus, an atmospheric scientist, who obtained a PhD in the same group at which I wrote my master thesis, said to me during a chat in the corridor: "You may not realise yet, but we both know that you are going to pursue for a PhD". I denied, but he turned out to be right. And although my thoughts as a freshman about life as a PhD candidate were not that far from the truth, I'd like to thank Thijs Heus for his wise words, since I now do believe that pursuing for a PhD has been a good decision.

The basis for this decision, however has probably been laid down by Stephan de Roode, my master thesis supervisor. His unconditional enthousiasm for all results I obtained, regardless whether they were useful or junk, interesting or not, as well as the hours we spent in front of the whiteboard full of equations, made me realise that puzzling to solve difficult problems may be fun after all.

It was thanks to Stephan that I came into contact with Riccardo during my search for a PhD position. Riccardo, thank you for your endless optimism and confidence in my work, even when I lost it! You always saw the strengths and possibilities while I was still worrying about weaknesses and pitfalls. Not only your endless ideas and corrections to all my papers, picture, manuscripts, abstracts, theses, posters, and presentations shaped this thesis, but also due to your seemingly endless network of fellow researchers, I became quickly part of many ongoing projects and got access to all the data hiding at other people's desks. Maybe related to your network, but nevertheless, I still admire your skill to figure out the names behind all those anonymous reviewers, in which you always seem to succeed. Thanks for all the help, without you, this thesis wouldn't have existed, and without your endless commitment, it wouldn't have been a succes!

[1] Again some evidence that there ain't no such thing as a free lunch.

The idea came from Riccardo, and has become an instant classic: the sea-level coffee! Every week, I learned from the latest sea-level gossip, and all the new projects going on in our group. Riccardo, Marcel, Jade, Karen, Francesca, thanks! It was always fun and insightful!

Svetlana, many thanks for making my visit to NOC Liverpool possible! Chapter 4 would not be possible without this visit, and next to that, it brought a lot of new ideas and contacts to me! I really enjoyed my stay in Liverpool!

Marcel, Julien and I started our PhD around the same time, so we were always able to understand each others frustration, and together we found the energy to survive the university graduate school, an institute that did not in any way contribute positively to this thesis. Julien, your contribution to this work is manifold, as both my mental mentor and pupil, you've shown me how to be lazy, and how to be an excellent scientist who knows how to publish rapidly (Chimot et al., 2016) and thoroughly (Chimot et al., 2017). Our daily struggles were invaluable! Marcel, we were both trying to understand sea level, but with our persistent mutual distrust in each others observation techniques, methods, and analyses, but with our common skepticism about everyone else's work, especially about the work of Julien, it was always fun around our office block. Of course, all other department members are to be acknowledged for the daily coffee machine gossip and much more, of course!

I'd like to thank Roland Klees for being my promotor and giving me the opportunity to carry out my PhD thesis in the Physical and Space Geodesy group. The discussions with all group members during our monthly meetings were always interesting. Cornelis, Taco, Miren, Sarah, Raymond, Laura, Pedro, Olga, Pavel, Roland, Riccardo, Marcel, Karen, Francesca, Jade, and all others, thanks!

Nowadays, the lonely scientist is a dying breed, which implies that the work in this thesis could not have been done without the support of many colleagues from outside our department. Martin, Yoshihide, Michiel, Ben, Caroline, Svetlana, Sönke, Matt, without their ideas, data, comments, and encouraging words, this thesis would have been an empty booklet.

All friends and family, always interested in whether their house was about to flood and rebuffed with advice about investing in floating real estate, you were always there to break out from the daily #PhDlife. It's no good to be always surrounded with other scientists.

Mieke and Toon, my parents, although you probably never fully understood what I was actually doing at the university all day. I really hope you give my thesis a read. Nevertheless, thanks for the endless belief and pride you had in me!

Last, but far, far, from least, Carine, 'Het meisje', 'Prinses Koudneus', 'Mevrouw-ik-ben-zielig-dus-jij-moet-ontbijt-maken', zonder jou was het allemaal een verdomd stuk saaier geweest! Talloos is het aantal keren dat ik bij jou over 'kantoor' aan het zeuren was, en minstens even talloos was het aantal keer dat jij zei dat ik moest kappen met dat gezeur, iets dat fors aan mijn voortgang heeft bijgedragen. Nu jij de graduate-school-misere nu ook zelf aan den levende lijve ondervindt en het gezeur nu wederzijds is, zal ik proberen altijd begripvol te blijven!

Finally, since a thesis is generally rather difficult to read for the broad audience,

the stakes are high that the booklet you're reading right now will end up in a bookshelf as a shelter for roaming dust particles looking for a long-term stay. Nevertheless, I sincerely hope that you'll continue to read. The introduction, which starts in a few pages, should be understandable to a broader audience, and gives some insight in what has kept me busy for the last four years. If that is too difficult, you could also try the Daily Mail or Breitbart, although using these sources to understand my work could result in a misinterpretation of the findings in this thesis. Nevertheless, enjoy the ride!

February 18, 2018

Contents

Preface **v**

Summary **xi**

Samenvatting **xv**

1 Introduction **1**
1.1 Sea-level rise in a warming world 1
1.2 Global sea-level rise over the geological and recent past 2
1.3 The open questions about global sea-level changes during the 20th century 5
1.4 Global and regional mean sea level 8
1.5 Regional differences in sea-level changes 9
1.6 Sea-level changes due to mass redistribution and the entanglement with vertical land motion 11
1.7 Sea-level changes, steric expansion, and ocean dynamics 14
1.8 Research objectives 17
1.9 Outline 19

2 Closing the sea-level budget on a regional scale: Trends and variability on the Northwestern European continental shelf **21**
2.1 Introduction 22
2.2 Data and models 22
2.3 Results 31
2.4 Discussion 33
2.5 Conclusions 36

3 The sea-level budget along the Northwest Atlantic coast: GIA, mass changes and large-scale ocean dynamics **39**
3.1 Introduction 40
3.2 Sea-level and GPS observations 42
3.3 Glacial Isostatic Adjustment 46
3.4 Present-day mass redistribution 48
3.5 Ocean dynamics 51
3.6 Regional vertical land motion and sea-level budgets 55
3.7 Discussion and conclusions 59

4 A consistent sea-level reconstruction and its budget on basin and global scales over 1958-2014 **63**
4.1 Summary . . . 63
4.2 Introduction . . . 64
4.3 Tide-gauge data and vertical land motion estimates . . . 65
4.4 Contributors to sea-level and land-level changes . . . 68
4.5 A local sea-level budget . . . 74
4.6 A basin-mean and global sea-level reconstruction . . . 79
4.7 Discussion . . . 82
4.8 Conclusions . . . 87

5 Ocean-bottom deformation due to present-day mass transport and its impact on sea-level observations **89**
5.1 Summary . . . 89
5.2 Introduction . . . 90
5.3 Methods and data . . . 91
5.4 The spatial pattern of the relative and geocentric sea-level response . . . 93
5.5 The effect on tide-gauge reconstructions . . . 95
5.6 Discussion and conclusions . . . 98

6 Estimating decadal variability in sea level from tide gauge records: An application to the North Sea **101**
6.1 Introduction . . . 102
6.2 The state-space formulation . . . 103
6.3 Three state-space models to parameterise regional sea-level changes . . . 108
6.4 Results and discussion for the North Sea . . . 112
6.5 Conclusions . . . 122

7 Conclusions and recommendations **125**
7.1 Conclusions . . . 125
7.2 Recommendations . . . 129

Bibliography **133**

Acknowledgements **147**

List of Publications **151**

Curriculum Vitae **153**

Summary

Being one of the major consequences of anthropogenic climate change, sea-level rise forms a threat for many coastal areas and their inhabitants. Because all processes that cause sea-level changes have a spatially-varying fingerprint, local sea-level changes deviate substantially from the global mean. As a consequence, there is no single location on the earth that is subject to the global-mean sea-level change. To understand and forecast future changes in both global and regional sea level, a thorough understanding of its major underlying processes and their regional fingerprints is necessary.

Nowadays, remote sensing from satellite altimetry provides an accurate estimate of changes in sea level on global and regional scales (Leuliette et al., 2004; Nerem et al., 2010; Ablain et al., 2017). The emergence of satellite gravimetry, in the form of the GRACE mission (Tapley et al., 2004), and the global coverage of in-situ subsurface temperature and salinity observations by the Argo programme (Roemmich et al., 2009; Roemmich and Gilson, 2009) has resulted in an extensive increase of our understanding of sea-level changes over the past decade, and the reliability of the estimates of the individual processes behind sea-level changes has reached the level where we can almost fully explain the observed sea-level changes from these contributors (Rietbroek et al., 2016; Leuliette and Miller, 2009; Dieng et al., 2015; Leuliette, 2015; Kleinherenbrink et al., 2016).

However, before this period the spatially-varying signals have been sampled only sparsely by in-situ observations, mainly by means of tide gauges, which limits our current understanding of sea-level changes on global and regional scales. This thesis aims to find an answer to the question whether the sum of the underlying processes that cause sea-level changes can explain the observations, not only on a global scale, which has been assessed a multitude of times (Moore et al., 2011; Church et al., 2011; Gregory et al., 2013; Jevrejeva et al., 2016b), but also on scales of individual ocean basins and coastal regions. The assessment of this so-called sea-level budget has been done for two regional cases, and for the global ocean and individual basins. Furthermore, the effect of ocean bottom deformation on the difference between relative and geocentric observations has been quantified. Finally, we have applied an alternative approach to time-series analysis, in which the various contributors of sea-level variability are co-estimated with a time-varying trend using a Kalman filter and smoother approach, on tide gauge observations.

Sea-level changes on the Northwestern European Shelf

To determine whether observed sea-level changes from tide-gauge records can be explained by the sum of contributors, a self-consistent framework has been developed, which combines observations of land motion and sea-level changes with independent estimates of ocean mass and volume changes. This framework takes the impact of non-linear vertical solid-earth deformation, resulting from present-day mass redistribution, into account. We apply this framework to the Northwestern European Shelf, for which many high-quality tide gauge records and GPS observations are available. The shelf is separated into two separate regions: the North Sea and the Norwegian Atlantic coast.

The contributing processes consist of the effects from glacier and ice sheet mass loss, groundwater depletion, dam retention, glacial isostatic adjustment (GIA), sea water volume changes, and the impact of wind and air pressure. Estimates of these processes have been obtained from multiple independent observations and models. On the Northwestern European Shelf, it is known that the decadal sea-level variability is caused by coastally-trapped waves that are driven by wind stress along the shelf boundary (Calafat et al., 2012, 2013; Marcos et al., 2013; Dangendorf et al., 2014a), for which subsurface density changes in the Bay of Biscay can be used as a proxy.

The sum of all processes explains the vast majority of the observed decadal variability, as well as the linear trend over the study period (1958-2014) for both the North Sea and the Norwegian coast. The decadal variability is dominated by the effects of the coastally-trapped waves, while the linear trend is mostly caused by ocean dynamic effects, glacial isostatic adjustment, present-day mass redistribution, and unexplained vertical land motion at tide gauge locations.

Sea-level changes along the Northwestern Atlantic ocean boundary

To assess the strong acceleration in observed sea level along the Northwestern Atlantic ocean boundary (Sallenger et al., 2012; Vinogradova and Ponte, 2017), the aforementioned framework has also been applied to this region. For this region, ocean models predict the southward propagation of sea-level anomalies in the Northern Seas along the western boundary of the Atlantic Ocean (Hsieh and Bryan, 1996; Johnson and Marshall, 2002; Roussenov et al., 2008; Minobe et al., 2017). We find a correlation pattern between coastal sea level and steric height anomalies in the southern part of the North Atlantic Subpolar Gyre area, which confirms that high-latitude density fluctuations are propagated southward along the ocean boundary. These density anomalies explain a large part of the observed decadal variability. Furthermore, this steric sea-level signal contains a strong acceleration, which explains the observed sea-level acceleration along the Northwestern Atlantic coast. Together with an updated GIA model (Simon et al., 2017), the sum of contributors explains the observed sea-level trends, accelerations and decadal variability in this region.

The sea-level budget on a basin-mean and global scale

The framework of combining observations of vertical land motion with modeled estimates of mass-related sea-level changes has been extended to study global and basin-mean sea-level changes. With this approach, a possible bias in sea-level reconstructions resulting from the uneven distribution of tide gauges (Thompson et al., 2016) is avoided.

We apply the virtual-station method, developed by Jevrejeva et al. (2006) and improved by Dangendorf et al. (2017) to reconstruct global-mean and basin-mean sea-level changes. Over the period between 1958 and 2014, we find a global-mean sea-level trend of 1.5 ± 0.2 mm/yr, which is lower than most previous estimates, but is consistent with the sum of contributors to global sea level, which we estimate to be 1.3 ± 0.1 mm/yr. Also, the observed sea-level acceleration of 0.07 ± 0.02 mm/yr^2 is in agreement with the contributors, in which we find an acceleration of 0.07 ± 0.01 mm/yr^2.

We find that in the Pacific and Indian Oceans, the observed decadal sea-level variability can be explained by the sum of contributors, with the steric signals explaining the vast majority of the observed variability. In the Atlantic ocean, the observed variability is not well reproduced by the contributors. This discrepancy may be caused by a combination of sparse observations, local non-linear subsidence, and the uneven sampling of tide gauges along the ocean boundaries. Due to this sampling, the tide gauges mostly give information about sea-level changes along the ocean boundary, which may not be representative for the full basin (Hughes and Meredith, 2006).

Ocean-bottom deformation resulting from ocean loading

The increase of total ocean mass due to present-day ice mass loss and a net flux of liquid water from land to oceans results in a higher load of the ocean bottom, which will deform under this increasing load. The resulting ocean-bottom deformation has not yet been quantified. Since the ocean bottom will subside under the increasing ocean mass, geocentric sea-level observations will underestimate barystatic sea-level rise, as well as the total ocean volume changes. We find that the global-mean geocentric sea-level change is about 8 percent smaller compared to the barystatic change resulting from mass changes associated with ice and terrestrial water storage. Over 1993-2014, altimetry observations underestimated the global-mean sea-level change by about 0.1 mm/yr due to this effect. On the scale of individual basins, larger deviations occurred, with a difference of 0.4 mm/yr in the South Pacific ocean. In the Arctic Ocean, the deviation is even larger due to mass loss from nearby ice sheets.

A state-space approach to analyse sea-level variability from tide gauge observations

One of the limitations when estimating a linear or quadratic trend from sea-level records is that the long-term behaviour of tide-gauge time series shows substantial decadal and multi-decadal variability, which cannot be properly described by a lin-

ear or quadratic trend. An alternative approach is to use a state-space model, in which seasonal cycles, the impact of climate indices, wind, and pressure can be co-estimated with the trend. In this model, the regression coefficients and trend do not have to be constant in time. This state-space-model is subsequently solved by means of a Kalman filter and smoother. We apply various state-space models to tide gauges around the North Sea. With this approach, we can separate the effects of local variability caused by wind and pressure from a basin-mean variability signal. Two different approaches to assess the local barotropic effects are compared. One in which local wind and pressure from an atmospheric reanalysis are used, and one in which the output of a barotropic storm-surge model are used to explain the variability. The barotropic model shows the best results and explains the largest fraction of the observed variability. The unexplained decadal variability signal, estimated by the state-space model can be linked to a large-scale signal present in the North-eastern Atlantic ocean.

Samenvatting

Zeespiegelstijging is een van de belangrijkste gevolgen van de door de mens veroorzaakte klimaatverandering, en vormt een bedreiging voor veel kustgebieden en hun bewoners. Alle processen die zeespiegelveranderingen veroorzaken zorgen voor een specifiek regionaal zeespiegelpatroon. Door al deze patronen wijken lokale veranderingen van de zeespiegel af van het wereldwijd gemiddelde. Als gevolg daarvan is er geen enkele plek op aarde waar de zeespiegel het globaal gemiddelde volgt. Om deze regionale patronen te begrijpen en regionale toekomstscenario's te ontwikkelen is een goed begrip van de relevante onderliggende processen en bijbehorende regionale patronen nodig.

Tegenwoordig kunnen lokale en globale zeespiegelveranderingen nauwkeurig worden geschat met behulp van satellietaltimetrie (Leuliette et al., 2004; Nerem et al., 2010; Ablain et al., 2017). Daarnaast zijn dankzij de GRACE-missie de massaveranderingen van de oceanen nauwkeurig in kaart gebracht (Tapley et al., 2004) en wordt dankzij het Argo-programma de temperatuur en het zoutgehalte van het oceaanwater continu gemeten (Roemmich et al., 2009; Roemmich and Gilson, 2009). De combinatie van GRACE en Argo geeft een vrijwel compleet beeld van de oorzaken van wereldwijde en regionale zeespiegelveranderingen gedurende het laatste decennium (Rietbroek et al., 2016; Leuliette and Miller, 2009; Dieng et al., 2015; Leuliette, 2015; Kleinherenbrink et al., 2016).

In de periode vóór het altimetrietijdperk hadden we slechts de beschikking over lokale zeespiegelmetingen op een beperkt aantal plaatsen. Deze metingen zijn grotendeels met behulp van peilmeetstations gedaan. Omdat het aantal metingen beperkt was, is er nog veel onduidelijk over de oorzaken van globale en regionale zeespiegelveranderingen in deze periode.

In dit proefschrift probeer ik een antwoord te vinden op de vraag of de gemeten zeespiegelstijgingen gedurende de decennia voor het altimetrietijdperk verklaard kunnen worden door de som van alle relevante fysische processen. Dit onderzoek naar het zogenaamde zeespiegelbudget is al meermaals gedaan op wereldwijde schaal (Moore et al., 2011; Church et al., 2011; Gregory et al., 2013; Jevrejeva et al., 2016b). In dit proefschrift wordt deze vergelijking tussen observaties en de som van processen onderzocht op een regionale schaal. Het zeespiegelbudget is onderzocht voor twee kustregio's, in iedere individuele oceaan, en op wereldwijde schaal. Daarnaast is een schatting gemaakt van de vervorming van de oceaanbodem, veroorzaakt door de toename van de totale massa van de oceaan en hoe deze vervorming het verschil tussen zeespiegelmetingen in een lokaal en geocentrisch referentiestelsel beïnvloedt. Als laatste hebben we een alternatieve benadering voor tijdreeksanalyse toegepast op zeespiegelmetingen, waarbij de verschillende processen die aan

zeespiegelvariabiliteit bijdragen tegelijkertijd worden geschat met een tijdsvariabele trend door middel van een Kalmanfilter.

Zeespiegelveranderingen op het continentale plat van Noordwest-Europa

Om te kunnen bepalen of de met behulp van peilmeetstations gemeten zeespiegelstijging kan worden verklaard door de som van fysische processen is een consistent raamwerk ontwikkeld, waarin metingen van zeespiegelveranderingen en bewegingen van de bodem gecombineerd worden met onafhankelijke schattingen van massaveranderingen en zeewatervolumeveranderingen van de oceaan. Dit raamwerk houdt rekening met de invloed van niet-lineaire bodembewegingen, veroorzaakt door hedendaags massatransport over het aardoppervlak. Dit raamwerk is toegepast op het continentale plat van Noordwest-Europa, waar een dicht netwerk van hoogwaardige peilmeetstations en GPS-observaties voorhanden is. Het continentaal plat is onderverdeeld in twee regio's: de Noordzee en de Noorse Atlantische kust.

Als fysische processen nemen we het massaverlies van gletschers en ijskappen, het uitputten van grondwaterreservoirs, het vasthouden van water achter stuwdammen, postglaciale isostatische vereffening, veranderingen van het specifieke volume van zeewater, lokale windeffecten en luchtdrukveranderingen in beschouwing. De grootte van deze processen is geschat met behulp van onafhankelijke waarnemingen en modellen.

Het is bekend dat de meerjarige zeespiegelvariabiliteit op het continentale plat van Noordwest-Europa veroorzaakt wordt door oceaangolven die door de kust zijn ingeklemd. Deze golven worden aangedreven door de wind die parallel aan de rand van het continentale plat waait (Calafat et al., 2012, 2013; Marcos et al., 2013; Dangendorf et al., 2014a). Om het effect van deze windgedreven golven op de zeespiegel te bepalen worden zeewaterdichtheidsvariaries in de Golf van Biskaje gebruikt.

De som van bovengenoemde processen verklaart vrijwel alle gemeten variabiliteit en de lineaire trend van de zeespiegel voor zowel de Noordzee als de Noorse kust gedurende het bestudeerde tijdsbestek (1958-2014). De meerjaarlijkse variabiliteit wordt gedomineerd door de bovengenoemde golven, terwijl de lineaire trend is toe te schrijven aan de oceaandynamica, postglaciale isostatische vereffening, hedendaags massatransport en onverklaarde bodembewegingen ter plaatse van de peilmeetstations.

Zeespiegelveranderingen langs de noordwestelijke rand van de Noord-Atlantische Oceaan

Om inzicht te verkrijgen in de oorzaken van de sterke gemeten versnelling van de zeespiegel langs de noordwestelijke rand van de Noord-Atlantische Oceaan (Sallenger et al., 2012; Vinogradova and Ponte, 2017) is het raamwerk ook toegepast op dit gebied. Oceaanmodellen laten zien dat verstoringen van de zeespiegel in de zeeën ten noorden van deze regio zich zuidwaarts voortplanten langs de westelijke rand van de Noord-Atlantische Oceaan (Hsieh and Bryan, 1996; Johnson and Marshall,

2002; Roussenov et al., 2008; Minobe et al., 2017). Er is een positieve correlatie tussen zeespiegelveranderingen in het zuidelijke deel van de Noord-Atlantische Subpolaire circulaire stroming en zeespiegelveranderingen langs de kust. Deze correlatie bevestigt dat dichtheidsfluctuaties zuidwaarts gepropageerd worden langs de rand van de oceaan. Deze fluctuaties verklaren een groot deel van de gemeten meerjaarlijkse zeespiegelvariabiliteit. Bovendien bevat het dichtheidssignaal in het zuidelijke deel van de Noord-Atlantische subpolaire circulaire stroming een sterke versnelling, hetgeen de sterke zeespiegelversnelling langs de kust verklaart. In combinatie met een verbeterd model van de postglaciale isostatische vereffening (Simon et al., 2017) kan de gemeten trend, versnelling en variabiliteit in de zeespiegel worden verklaard in dit gebied.

Het zeespiegelbudget per oceaan en voor de hele wereld

Om het zeespiegelbudget per oceaan en wereldwijd te kunnen bestuderen is het eerder genoemde raamwerk uitgebreid. Met deze uitbreiding wordt de mogelijke afwijking in zeespiegelreconstructies, die veroorzaakt wordt door de onevenwichtige verdeling van peilmeetstations (Thompson et al., 2016), voorkomen.

Om de individuele meetreeksen samen te voegen tot schattingen van oceaangemiddelde zeespiegelveranderingen wordt de virtuele-station-methode, ontwikkeld door Jevrejeva et al. (2006), en verbeterd door Dangendorf et al. (2017) gebruikt. Tussen 1958 en 2014 bedraagt de gereconstrueerde wereldwijd-gemiddelde zeespiegeltrend van 1.5 ± 0.2 mm/jr, wat een iets lager is dan de meeste eerdere schattingen, maar wel overeenkomt met de som van fysische processen, die geschat is op 1.3 ± 0.1 mm/jr. Ook de gereconstrueerde globale versnelling van de zeespiegel van 0.07 ± 0.02 mm/jr^2 kan worden verklaard aan de hand van de som van de individuele processen, die 0.07 ± 0.01 mm/jr^2 bedraagt. In de Stille Oceaan en in de Indische Oceaan kan de gereconstrueerde zeespiegelvariabiliteit goed worden verklaard door de individuele processen. In de Atlantische Oceaan is dat niet het geval. Mogelijke oorzaken voor deze discrepantie zijn een gebrek van peilschaalstations, lokale niet-lineaire bodembewegingen, en een onevenwichtige ruimtelijke verdeling van deze stations. De huidig verdeling zorgt ervoor dat de peilmeetstations voornamelijk variabiliteit langs de randen van de oceaan meten. Deze variabiliteit is vaak niet representatief voor de hele oceaan (Hughes and Meredith, 2006).

Vervorming van de oceaanbodem veroorzaakt door toename in het gewicht van de oceaan

De toename van de totale massa van oceaanwater door de afname van de hoeveelheid landijs en een nettotransport van vloeibaar water van land naar oceaan, leidt tot een hogere druk op de oceaanbodem. De oceaanbodem zal door deze extra druk elastisch vervormen. De grootte van deze vervorming is nog niet gekwantificeerd. Omdat de oceaanbodem door de toenemende belasting verzakt, zal de wereldwijd-gemiddelde geocentrische zeespiegelstijging kleiner zijn dan de toename van het oceaanvolume en bijbehorende barystatische zeespiegelstijging. De wereldwijd-gemiddelde geocen-

trische zeespiegelstijging is naar schatting circa 8 procent kleiner dan de barystatische stijging veroorzaakt door ijs en landhydrologie. Door dit effect wordt gedurende de periode 1993-2014 de totale zeespiegelstijging door satelliet-altimetrie onderschat met circa 0.1 mm/jr. Op de schaal van individuele oceanen komen grotere verschillen tussen relatieve en geocentrische zeespiegelstijgingen voor, met bijvoorbeeld een verschil van 0.4 mm/jr in de Zuidelijke Stille Oceaan. In de Noordelijke IJszee is door het massaverlies van de nabijgelegen gletschers en de Groenlandse ijskap het verschil nog groter.

Het analyseren van door peilmeetstations gemeten zeespiegelvariabiliteit met een staatruimtebenadering

Een van de beperkingen van het schatten van een lineaire of kwadratische trend uit tijdreeksen van zeespiegelmetingen is dat de aanwezigheid van variabiliteit op schalen van decennia niet afdoende kan worden beschreven door de geschatte functie. Een alternatief is het gebruik van een staatruimtemodel, waarmee de seizoenscyclus en de invloed van teleconnectiepatronen, wind en luchtdruk tegelijk kunnen worden geschat met de trend. In een dergelijk staatruimtemodel hoeven, in tegenstelling tot de klassieke kleinstekwadratenschatter, de regressiecoëfficiënten en de trend niet constant in de tijd te zijn. Dit staatruimtemodel kan vervolgens worden opgelost met behulp van een Kalmanfilter. Meerdere staatruimtemodellen worden toegepast op metingen van peilmeetstations langs de Noordzee. Dankzij deze aanpak kan de lokale variabiliteit veroorzaakt door wind en luchtdrukverschillen gescheiden worden van een Noordzee-gemiddeld variabiliteitssignaal. Twee verschillende methodes om de lokale barotrope effecten te schatten worden vergeleken: bij de eerste methode worden de windforcering en luchtdruk uit een atmosferisch data-assimilatie-model gebruikt, en bij de tweede methode wordt gebruik gemaakt van een barotroop getij- en windopzetmodel. Van de twee methodes verklaart de methode met het barotrope model de meeste lokale variabiliteit. Het door het staatruimtemodel geschatte onverklaarde variabiliteitssignaal kan worden gekoppeld aan een grootschalig dichtheidssignaal in de Noordoost-Atlantische Oceaan.

Chapter 1

Introduction

"U spreekt erg mooi en waardig, Mijnheer,
moet ik zeggen. Zoals in een boek klinkt het,
als U het mij niet kwalijk neemt."
"Allerminst Mevrouw."
"Ik heb U laten ontbieden, omdat ik U iets
wilde vragen: ik heb de grootste bewondering
voor Uw werk..."
"Ik leef en schrijf voor mijn volk, Majesteit."

Gerard Reve

1.1 Sea-level rise in a warming world

Although being only one of the many consequences of current anthropogenic climate change, sea-level rise in a future warming climate threatens large amounts of low-lying land, which hosts a substantial fraction of the global population (McGranahan et al., 2007; Kopp et al., 2014). Furthermore, rising seas result in increased salt-water intrusion of farmlands, and coastal erosion. It is widely accepted that the socio-economic impact will be very negative (Nicholls and Cazenave, 2010; Hinkel et al., 2014). Reliable forecasts of future regional sea-level changes form the basis for effective adaptation and mitigation measures. A thorough understanding of the underlying processes is indispensable to make these reliable forecasts. According to the fifth IPCC assessment report (Church et al., 2013), depending on the emission scenario, global-mean sea level will rise by 0.26 to 0.98 meter by the year 2100, compared to present-day levels.

At regional scales, sea-level changes in a future warming climate will differ from the global mean (Landerer et al., 2007b; Slangen et al., 2014a), which adds an extra uncertainty when determining design heights for coastal defense structures (Slangen et al., 2017b; Wahl et al., 2017). As an example of forecast requirements, the Dutch Delta Committee has developed guidelines for design heights based on a wide range of climate scenarios, with an upper-end forecast of 1.15 m above present-day values for the Dutch coast in 2100 (Katsman et al., 2011).

Although the scientific understanding of the processes behind sea-level changes have vastly increased over recent years, many aspects are still debated. For example, recent work on the instability of the Antarctic Ice Sheet (DeConto and Pollard, 2016) and advances in sea-level projections (Kopp et al., 2014; Jevrejeva et al., 2016a; Le Bars et al., 2017), point out that the upper-end projections of the IPCC and KNMI may underestimate the worst-case scenarios, and that a global-mean sea-level rise above 2 meters by the year 2100 cannot be ruled out. The large uncertainty in the projections is not only caused by the uncertainty in future greenhouse gas emissions, but also to a large extent due to uncertainties in the feedback of the oceans and ice sheets to an increase in global and regional temperatures.

Next to uncertainties in the processes driving global-mean sea-level changes, local deviations from the global mean are large. This local deviation, which has its origin in gravitational, earth rotation, and solid-earth deformation effects, as well as in local subsidence and ocean dynamics, forms an additional source of uncertainty (Slangen et al., 2014a). This stacking of uncertainties feeds the requirements for future sea-level allowances and design water levels (Wahl et al., 2017; Slangen et al., 2017b), which become high and cause the required measures to become very costly. In order to reduce these uncertainties, we need to improve our current knowledge of sea level in the recent past, as well as of the individual processes that contribute to these changes on local, regional, and global scales. The understanding of sea-level changes in the recent past, and their regional deviations from the global mean form the subject of this thesis.

1.2 Global sea-level rise over the geological and recent past

Our overview of changes in sea level in the past starts with sea-level changes at scales of millions of years. Using models and a wide range of proxies, reconstructions of long-term sea-level changes are possible. A compilation of various reconstructions of sea level over the past five million years is depicted in Figure 1.1a. The vertical axis in this picture is in meters, which shows that over these time-scales, sea-level changes in the order of hundred meters have occurred. These changes are closely tied to changes in the Earth's energy budget, and hence to global temperature. The distinct sea-level minima are linked to ice ages, during which large amounts of sea water was stored on land in the form of ice. Although the spread between the individual reconstructions is an indicator of their large uncertainties, they all show that sea levels of tens of metres above present-day levels have occurred in the past.

Even though the current greenhouse gas emission rate is unprecedented over the past 66 million years (Zeebe et al., 2016), such large fluctuations are not expected to happen during the coming century, since sea level shows a delayed response to changes in the climate system. Due to this delayed response, the time required for the oceans and ice sheets to reach an equilibrium with the surface temperature is much longer than a century. The so-called sea-level commitment (i.e. how much does the sea-level change after the climate system has reached an equilibrium state after

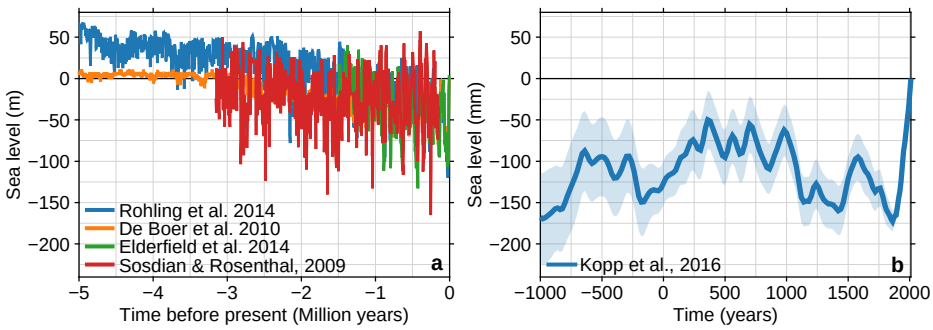

Figure 1.1: Sea-level changes on millennial and multi-millennial time scales. a. Various sea-level reconstructions on geological time scales (Sosdian and Rosenthal, 2009; de Boer et al., 2010; Elderfield et al., 2012; Rohling et al., 2014). The data has been obtained from Rohling et al. (2014). b. Reconstructed global-mean sea level from 1000 BC until present by Kopp et al. (2016). The shading denotes the uncertainty at 1σ. Note the change from units from meters to millimeters on the y-axis between both panels.

a global-mean temperature rise) is an ongoing research subject. In the latest IPCC assessment report (AR5, Church et al., 2013), a sea-level commitment value of about $2\text{m}/^{o}\text{C}$ has been estimated. This delayed response also implies that sea level will keep rising over the 21st century, even when the emission of greenhouse gases will be halted. One of the causes of this continuing sea-level response to emissions in the past is the presence of tipping points. Once the climate system has been perturbed beyond these points, the processes that have been set into motion are very unlikely to be reverted, and may cause large sea-level changes. One of these delayed mechanisms is known as the Marine Ice Sheet Instability (MISI) hypothesis. This instability may threaten the West Antarctic Ice Sheet (DeConto and Pollard, 2016), and could result in multi-meter global-mean sea-level rise in the year 2100.

Sea-level changes on the order of several meters are not new to our planet, but they are new for our human civilization. If we look over the past few millennia, global-mean sea-level changes have been much smaller. A sea-level reconstruction over this period is shown in Figure 1.1b. Note that in this figure, the y-axis has changed from meters to millimeters, and hence, the sea-level changes over the past millennia are very small in a geological perspective. However, our human civilization has adapted to changes over this range, rather than the geological range, which has resulted in a dense population of low-lying areas. This reconstruction also depicts that over the past few millennia, sea level has always been lower than the present-day value. Furthermore, the steep rise of sea level that has been observed over the past century is unprecedented over the past millennia, which suggests that over the last century, the oceans have changed at an unusual pace.

The aforementioned reconstructions are all based on proxy observations, such as ice cores, salt marshes, and coral atolls. Hence, the derived values of sea-level changes are subject to substantial uncertainties. To circumvent the uncertainty associated with these proxies, direct sea-level observations are used. Since 1993, sea-

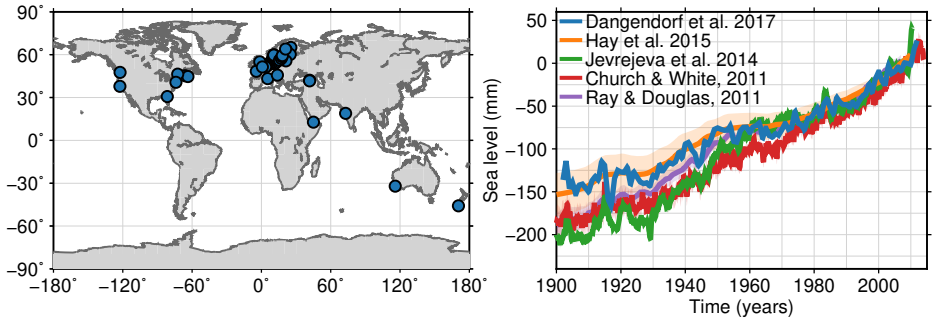

Figure 1.2: Tide-gauge reconstructions over the 20th century. Left: Location of tide-gauge stations with data before 1901 and after 2010. Right: some twentieth-century sea-level reconstructions based on tide gauge records using various averaging techniques.

level changes are continuously observed from space by satellite altimeters. This observation method provides an almost complete picture of global and regional sea-level changes over the last 25 years. These observations tell us that over the past two decades, sea level has risen at a rate of about 3.2±0.6 mm/yr (Chambers et al., 2016). This rate is faster than the sea-level rise at any point in Figure 1.1b. However, it is well-known that next to long-term changes related to anthropogenic climate change, variability on decadal and multi-decadal time scales exists (Haigh et al., 2014; Dangendorf et al., 2014b), which hampers our ability to separate the anthropogenic contribution from internal variability over the era of satellite altimetry. Furthermore, this decadal and multi-decadal variability cannot be captured by the paleo-sea-level proxies and hence, the reconstructions in Figure 1.1 will not show this variability. To reconstruct sea-level changes with a higher accuracy and temporal resolution than from the aforementioned proxies, but over a longer time span than the era of altimetry, we have to rely on tide gauges. Tide gauges are devices that measure local water level, often using a simple floating device whose height is recorded. Until a few decades ago, the floating device was connected to a pencil which recorded sea level on a slowly rotating piece of paper. This data was mostly used to make tidal predictions, but in some locations, this data has been registered with a high accuracy, and can be used to estimate the longer-term sea-level behaviour. However, tide gauge observations only tell us sea-level changes at the location of the station itself. Most stations, especially stations with a long record are located along the North Atlantic coasts, as shown in the left panel of Figure 1.2.

Because sea-level changes differ substantially from place to place, reconstructing changes in global-mean sea-level from a limited number of observations that are unevenly spread across the oceans is a challenging task. Multiple reconstruction methods have been proposed to estimate global sea-level changes over the twentieth century using the sparse data from tide-gauge records. Some of the most widely cited reconstructions are shown in the right panel of Figure 1.2. The reconstructions in Figure 1.2 all show a steady sea-level rise over the twentieth century, although a substantial spread between the reconstructions is visible, especially over the first half of the century. Despite these differences, the reconstructions consistently show that

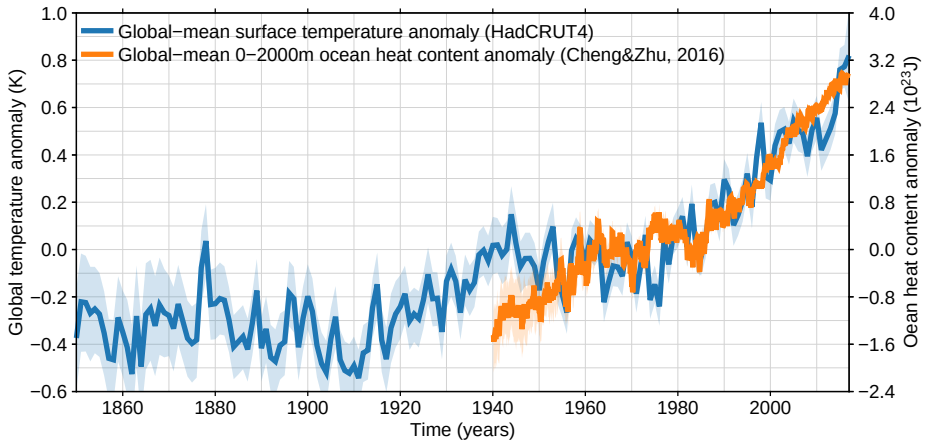

Figure 1.3: Development of global-mean surface temperature anomalies since 1850 (orange) and total ocean heat content anomalies in the upper 2000m since 1940 (blue). Surface temperature data based on HadCRUT4 (Morice et al., 2012) and OHC data from (Cheng and Zhu, 2016).

global-mean sea-level changes over the 20th century are unprecedented over the last few millennia, as depicted in Figure 1.1b.

1.3 The open questions about global sea-level changes during the 20th century

The results of the global reconstructions in Figure 1.2 and the differences between them lead to multiple questions, to which the sea-level research community does not yet have fully satisfying answers. Here, some of the most pressing open questions are discussed:

- Why do we see a high sea-level rise at the beginning of the twentieth century and why does the 20th century sea-level curve only show a small acceleration?

On many time scales, global temperature and sea level are strongly correlated (Vermeer and Rahmstorf, 2009). However, we know that the global surface temperatures, as well as the total ocean heat content, have accelerated substantially over the past century (Hartmann et al., 2013; Rahmstorf et al., 2017). This acceleration is clearly visible in Figure 1.3, which shows recent estimates of global-mean surface temperature and ocean heat content anomalies. The surface temperature shows a clear acceleration over the last 150 years, and also changes in the global ocean heat content are accelerating. However, such an acceleration is not visible in Figure 1.2, as sea level was already rising at the beginning of the 20th century. This problem has been stated by the famous oceanographer Walter Munk, and is known under the term 'Munk's Enigma'(Munk, 2002). The enigma states:

"*The historic rise started too early, has too linear a trend, and is too large.*"

The cause of this discrepancy is still unknown. Some solutions have been proposed, mostly focussing on lower estimates of sea-level changes at the beginning of the century (Hay et al., 2015; Mitrovica et al., 2015; Dangendorf et al., 2017), although this topic is still under debate.

- What causes the differences between the reconstructions, and which one is the most reliable?

The reconstructions in Figure 1.2 show substantial mutual differences, and estimates of total sea-level changes over the 20th century range between 150 and 200 mm. These differences are often larger than the estimates of the reconstruction uncertainties and are therefore statistically significant. Each reconstruction uses its own subset of tide-gauge records, as well as different choices on how GMSL is estimated from the tide-gauge record, and all these choices affect the final reconstruction (Calafat et al., 2014; Hamlington and Thompson, 2015).

In recent reconstructions, prior information about the expected spatial pattern of sea-level rise has been used to improve the estimates (Hay et al., 2015; Dangendorf et al., 2017), although these techniques are still new, and are subject of an ongoing debate on the added value of these extra sources of information and the procedures to implement them (Thompson et al., 2016; Hay et al., 2017; Santamaría-Gómez et al., 2017).

- What is the meaning of the decadal oscillations in sea-level reconstructions?

Global sea level can not be described by a linear or quadratic trend with white noise residuals. One of the reasons why simple functional models are not well-suited to describe the global sea-level curves is the presence of temporal autocorrelation, which manifests itself as large decadal and multi-decadal oscillations in the curve. This property of auto-correlated residuals is well-known, and results in substantial uncertainties when estimating long-term trends and accelerations from tide-gauge records and reconstructions (Dangendorf et al., 2014b; Haigh et al., 2014). All global reconstructions in Figure 1.2 show decadal variability, although the variability is far from consistent between the methods. Hence, it is difficult to assess whether this variability is a real phenomenon in global-mean sea level or an artefact of the sparse observations. Some work suggests the presence of long-term oscillations with a fixed period in global sea level (Chambers et al., 2012). The attribution of this variability on a wide range of scales to individual processes still forms a challenge.

- Which fraction of the observed sea-level rise has an anthropogenic cause?

Since sea-level change is not a recent phenomenon, as visible in Figure 1.1a, one key question is which part of the observed rise can be attributed to human causes, and which part is due to natural fluctuations. Using statistical values or earth system models, various studies find widely-varying fractions of observed 20th-century sea-level changes that can be attributed to anthropogenic activities (Slangen et al., 2016;

Dangendorf et al., 2015; Marcos et al., 2017; Kopp et al., 2016), although most are in the order of 30 to 60 percent. One of the problems for estimating this fraction is the inability of earth system models to reproduce the observed sea-level changes over the 20th century: the observed sea-level rise substantially outpaces the rate predicted by the earth system models (Slangen et al., 2016, 2017a), and hence, attributing the changes to specific changes in the forcing of the earth system remains challenging.

- We have estimates of many individual processes that cause sea-level changes. Does the sum of these processes explain the curves shown here?

One of the main arguments that led to Munk's enigma is the inability of the ocean volume and mass changes to explain the reconstructed sea-level rise. When ice sheets and glaciers lose mass, a net shift of water from high latitudes towards the equator affects the earth's dynamic oblateness, and hence, its rate of rotation. The increase of the earths moment of inertia around its axis of rotation increases when ice sheets and glaciers lose mass, resulting in an increase of the earth's length-of-day. Specific phenomena, such as solar eclipses, critically depend on the length-of-day, which allows for an accurate reconstruction of its changes back in time. The observed increase in the length-of-day over the 20th century cannot be reconciled with the amount of ice mass loss required to explain the reconstructed sea-level rise (Munk, 2002; Mitrovica et al., 2015). However, as already noted above, recent reconstructions suggest a substantially lower sea-level change over the twentieth century (Hay et al., 2015; Dangendorf et al., 2017). Furthermore, over the last decade, tremendous progress has been achieved in quantifying changes of multiple components in the earth system over the last decades. This progress has led to reliable estimates of, amongst other things, changes of ice sheets (Kjeldsen et al., 2015), glaciers (Marzeion et al., 2015), and ocean volume (Levitus et al., 2012). However, we are still unable to fully separate the observed 20th-century sea-level rise into its individual contributors (Jevrejeva et al., 2016b). This inability affects both the explanation of the observed sea-level change by observational estimates of the individual contributors (Moore et al., 2011; Gregory et al., 2013; Slangen et al., 2014b), as well as estimates of the contributors based on output from earth system models (Slangen et al., 2016, 2017a).

A possible solution to this problem is to explain the observed sea-level changes on a regional or basin-mean rather than global scale and to separate regional sea-level changes into the contributing processes. This separation may give insight into whether the inability to explain the observations is a omnipresent phenomenon, or only affects a limited number of locations. This approach is one of the subjects of this thesis. To explain the observations on a regional scale, we need knowledge about the processes that affect sea level and its changes. The differences between global and regional time-mean sea level and sea-level changes will be discussed in the next section.

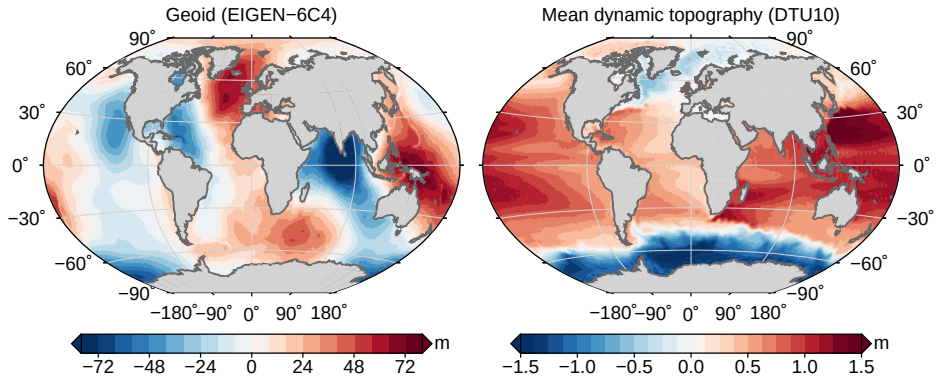

Figure 1.4: Spatial variability in time-average sea level. Left: the global geoid relative to the EGM2008 reference ellipsoid, based on the EIGEN-6C4 model (Förste et al., 2014). Right: the global mean dynamic topography relative to the geoid, based on the DTU10 model (Andersen and Knudsen, 2009)

1.4 Global and regional mean sea level

In the previous section, we only discussed changes in global-mean sea level. However, it is of vital importance to understand that both time-averaged and time-varying global mean sea level are an abstraction, as mean sea level varies considerably around the planet. Let's define Earth as an ellipsoid. Due to large deviations in the density of the underlying earth mass, the gravity potential at this ellipsoid is far from constant, which leads to an equipotential surface, the so-called geoid, that has large hills and trenches around the ellipsoid. An accurate model of the geoid, relative to the earth's ellipsoid is depicted in the left panel of Figure 1.4. Mean sea level is heavily affected by the height of the geoid, and in the hypothetical situation that the ocean is not in motion, the sea surface would be equal to the geoid. Although the ocean is never at rest, sea level will approximate the heights shown in the left panel of Figure 1.4 within a few meters. The figure clearly shows that the Earth's gravity field does not result in a nice elliptic ocean surface: the geoid shows hills and valleys with amplitudes in the order of tens of meters.

Due to the combined effects of winds, earth rotation, and ocean currents, the ocean is never at rest, and the actual time-mean sea level does deviate from the geoid. This time-averaged anomaly, known as the mean dynamic topography, adds another spatially-varying term to the problem, with amplitudes up to about two meters, as shown in the right panel of Figure 1.4. Relative to these large global variations in time-mean sea level, the century-scale and millennium-scale global sea-level changes are orders of magnitudes smaller. Hence, estimating global-mean sea-level changes means looking for very small variations in time in a spatially-varying sea-level field. Moreover, the spatial patterns in the geoid and the mean dynamic topography, as depicted in Figure 1.4 are actually not constant in time, and therefore, the sea-level changes themselves also have distinct regional patterns, which will be discussed in the next section.

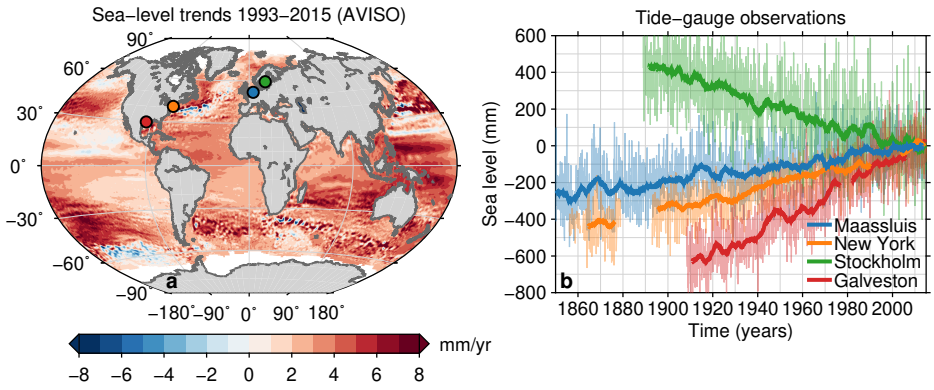

Figure 1.5: Geographic variability of trends in sea level. a. Geocentric sea-level trends over the oceans, derived from satellite altimetry between 1993 and 2015. Altimetry data has been obtained from AVISO (`aviso.altimetry.org`). The dots denote the locations of the tide gauge stations from the right panel. b. Tide-gauge records from four North Atlantic stations. Shown are monthly-mean values (light colors) and the 60-month running mean (dark colors). From each time series, the mean over 2006-2015 has been removed. The data have been obtained from the Permanent Service for Mean Sea Level (PSMSL, Holgate et al., 2013)

1.5 Regional differences in sea-level changes

In a changing climate, not only global-mean sea level will change, but due to the exchange of mass between land and ocean, and changes in ocean dynamics, both the geoid and the dynamic topography will be affected by long-term and short-term variations. Hence, past and future sea-level changes vary from location to location. Since the year 1993, satellite altimetry provides a near-global overview of sea-level changes and gives detailed information about regional variations in sea-level changes over the past two decades. In Figure 1.5a, the regionally-varying linear sea-level trends, as observed by altimetry, are depicted. These observations demonstrate that sea-level trends over the past decades show large spatial variations. Especially the Pacific Ocean stands out with large trends along its west coast and barely any trend along the east coast. In the North Atlantic Ocean, high rates are visible in the Western Subpolar regions close to Canada, as well as a strong gradient perpendicular to the path of the Gulf Stream. Some regions feature variability at high spatial frequencies, especially around the Gulf Stream path and around Antarctica. This variability is generally caused by ocean eddies and variable currents (Piecuch and Ponte, 2011; Forget and Ponte, 2015). Close to the North and South Pole, satellite observations are missing, since the satellite orbits do not cover the polar regions, and the presence of sea ice forms a challenge to convert the radar signal into a sea-level estimate.

From the data shown in Figure 1.5a, it's a straightforward task to determine global-mean changes. However, to reconstruct sea-level changes further back in time, we have to rely on observations at a limited number of locations, and deriving an ocean-mean value becomes more challenging. The dominant strategy that has been applied to this problem in the past is to assume that, given a substantial amount of ob-

servations at different locations, these anomalies cancel out. Unfortunately, the large differences observed over the altimetry area are not only caused by decadal variability that will cancel out over longer time scales, but the observed differences in trends are often persistent over time. These persistent differences are for example observed from tide-gauge records in the North Atlantic Ocean. Along its coasts, observations date back into the 19th century. It's worthwhile to note that the Dutch tide gauge network, maintained by Rijkswaterstaat, contains many of the worlds longest and most complete records. The records in Amsterdam lasted from 1700 to 1924, which makes it the oldest known written sea-level record. The observed sea-level changes from four tide gauges along the North Atlantic Ocean are depicted in Figure 1.5b. Let's compare for example the start and end point of the former 'Holland Amerika Lijn' shipping line from Rotterdam to New York. At both ends of the line, long-term tide gauge records are available: we compare the Maassluis tide gauge record to the record from the Battery Park in New York, which are both shown in Figure 1.5b. Since 1850, sea level in New York has risen about twice as fast as in Maassluis. Next to the difference in the long-term trend, the amplitude of the monthly variability in Maassluis is larger than in New York. This difference is to a large extent caused by the differences in the water depth around the tide gauge: the North Sea is located on a continental shelf and therefore shallow. Due to this large shallow sea, storms cause relatively high surges, which results in a large monthly sea-level variability signal. The shelf around New York is considerably less wide.

It's however not only the storminess that's different. The variability on decadal time scales, which is not related to storminess, is also different on both sides of the Atlantic. At other locations along the North Atlantic, even larger deviations in the long-term trend can be seen. For example, Stockholm experiences a substantial sea-level drop, while Galveston (which is a harbor city close to Houston) is affected by a rapid rise of more than 50 centimeters over the 20th century.

With these four records, it becomes difficult to estimate average sea-level changes over the whole North Atlantic basin. Hence, to reconstruct sea level over a specific region, we need information on the underlying causes of the observed differences and the spatial extent of these processes. Even when we increase the number of tide-gauge records in the reconstruction, the spread in observed sea-level changes will result in a high uncertainty of the basin-mean signal if the underlying causes of the regional deviations are unknown.

The differences in sea-level changes between tide-gauge records must be caused by changes in the geoid, or by changes in the mean dynamic topography, or it may also be caused by a third process that is relevant for tide-gauge observations. This third process is related to the fact that tide gauges observe sea-level changes relative to the instrument, and hence, relative to the land: vertical movement of the land without changes in 'real' sea level results in observations of a changing sea level. Hence, it may be very well the case that the difference between New York and Maassluis is fully or partially a result of subsidence in New York, and/or uplift in Maassluis.

How do we actually distinguish between sea-level and land-level changes? To separate both, we define two measures of sea-level changes: relative and geocentric

sea-level changes. Relative sea-level changes are defined as sea-level changes relative to the land where it is observed from, as shown in Figure 1.5b. Geocentric sea-level changes are changes relative to the centre-of-mass of the earth. The satellite observations in Figure 1.5a are expressed in a geocentric reference frame. With these definitions, the difference between relative and geocentric sea level is the vertical motion of the tide-gauge station, relative the the earth's centre of mass. Nowadays, we can observe this vertical land motion directly using permanent GPS receivers and satellite altimetry, but before the 1990s, direct estimates of vertical land motion are non-existent, and we have to rely on models or geological evidence of land motion.

1.6 Sea-level changes due to mass redistribution and the entanglement with vertical land motion

Luckily, for some processes that cause global and regional sea-level changes in the past we have reliable estimates, and they allow to separate local sea-level changes from changes that occur over large distances.

Let's first discuss the effects of mass transport in the earth system on sea-level observations. Multiple processes that affect sea level involve transport of mass between land and ocean. For example, when a glacier shrinks, ice melts and the water eventually reaches the ocean. Such transport of surface water mass results in four effects that together affect the height of the sea level as well as the height of the land:

- **Barystatic changes**: when water flows from land to ocean, the ocean gains mass. This mass gain causes a rise of global-mean sea level.

- **Solid-earth changes**: the solid earth is not rigid: when we add a large mass to a specific region, it will subside under its load. Since the total volume of the earth remains almost constant, far away from the extra load, the solid earth will lift up slightly.

- **Geoid changes**: the redistribution of mass changes the shape of the geoid, hence also the shape of the ocean surface: when mass accumulates at a specific location, ocean water is attracted to this mass, and sea level close to the extra mass will rise, while far away it will drop.

- **Earth-rotation changes**: the earth is a rotating body, with its rotational axis running from pole to pole. When mass is redistributed over the surface of this body, the earth rotation axis and its rotational speed will change, comparable to gymnasts who stretch and fold their arms to change their rotational speed and axis. Changes in the earth rotation parameters affect both the shape of the solid earth and the geoid.

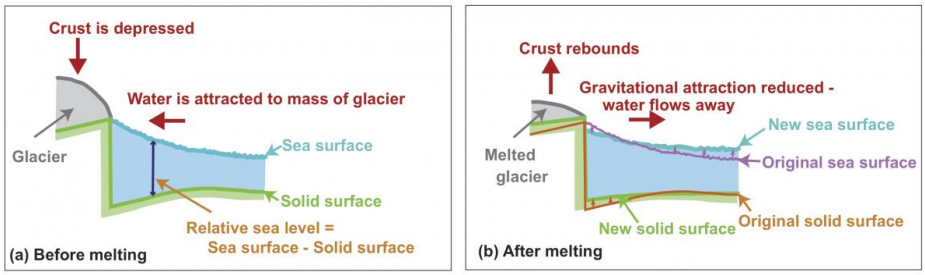

Figure 1.6: Effects of self-attraction and loading resulting from a melting glacier. Source: Emma Hill, Earth Observatory of Singapore, NTU

Let's see what happens when a glacier loses mass. A graphical demonstration is shown in Figure 1.6. Before the ice melts (Figure 1.6a), the heavy glacier depresses the earth crust below it, and attracts the ocean water towards it. Hence, the land is lying low, and the geocentric sea level is high around the glacier. Now, if the glacier has melted, and lost mass (Figure 1.6b), the crust underneath it rebounds, and rises, while the attraction of ocean water decreases, resulting in a drop of geocentric sea level. Since relative sea level is the sea-level change relative to the solid earth below, both the solid earth rebound and the reduced attraction of sea water result in a drop of relative sea-level close to the glacier, and a rise far away from the glacier. If we know the location and rate of mass loss, we can compute the resulting effects on the solid earth, gravity field, and sea level, by solving the so-called 'sea-level equation' (Farrell and Clark, 1976; Clark and Lingle, 1977). The resulting patterns of regional sea-level changes are known as 'sea-level fingerprints' (Mitrovica et al., 2001). An example of how regional sea-level changes due to mass loss of the Greenland Ice Sheet is shown in Figure 1.7a. In this figure, the static response of the geoid, solid earth, and relative sea level to a mass loss of 362 gigaton in Greenland is depicted. 362 gigaton of ice equals a volume of 362 cubic kilometer liquid water. When this amount of ice melts and enters the ocean, global-mean sea-level rises by about 1 mm. Figure 1.7a qualitatively shows what we discussed above: uplift around the melt source, and subsidence far away, less attraction of sea water, and a sea-level drop around the ice sheet, and an above-average sea-level rise far away from the ice sheet. It is interesting to note that for the North Sea, the impact of Greenland mass loss is about zero. Hence, when Greenland loses mass, sea level in the North Sea will hardly change. This is not the case for the Antarctic Ice Sheet. Both the Greenland and Antarctic Ice Sheet and most glaciers are currently losing mass (Talpe et al., 2017; Marzeion et al., 2017). Next to the contribution from ice mass loss, a substantial amount of water is depleted from underground aquifers for human use, and since these aquifers do not recharge at the same pace, a large part of this depleted water enters the ocean (Konikow, 2011; Wada et al., 2010, 2016). On the other hand, dams retain water in their reservoirs. Hence, the construction of new dams reduces the total amount of water that rivers discharge into the ocean (Chao et al., 2008). Next to these man-made changes, substantial decadal variability in the amount of water on land occurs due to natural phenomena, including El Niño and

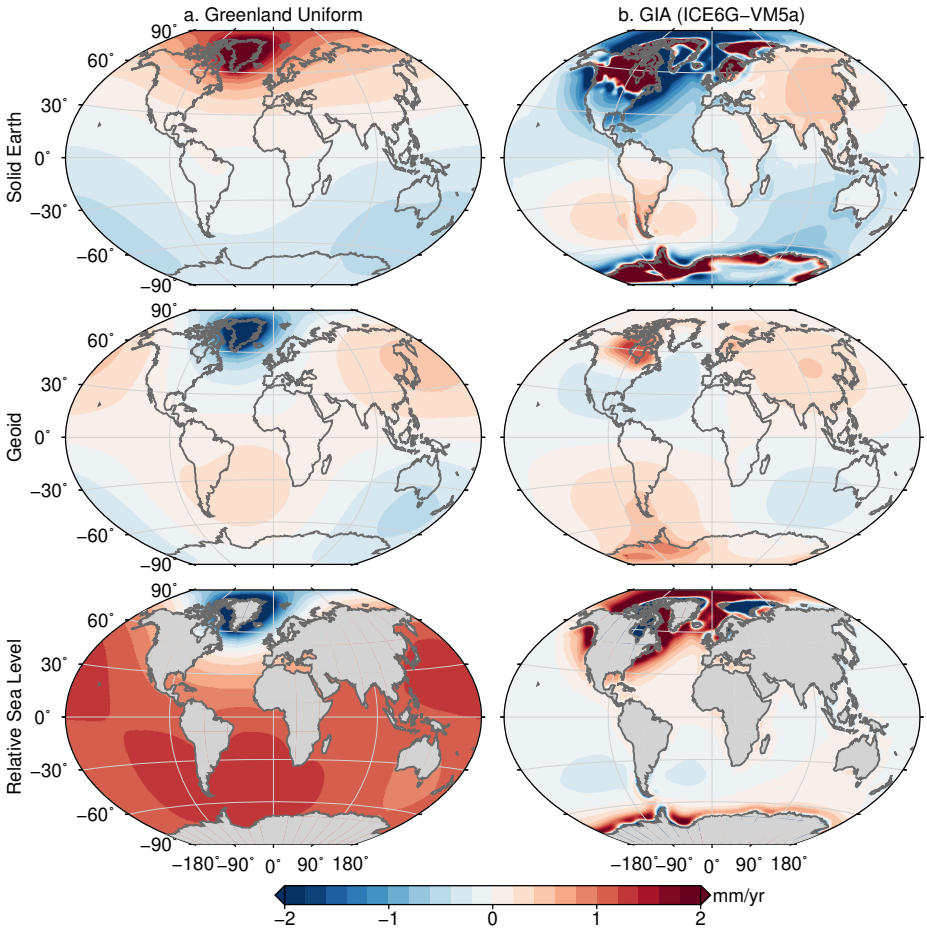

Figure 1.7: Spatial patterns associated with Greenland mass loss and GIA. a: Resulting changes in the solid earth height, geoid, and relative sea level to a uniform melt of Greenland of 362 Gigaton of ice. The spatial patterns have been computed using the method described in Section 2.2.1 . b. the effects of Glacial Isostatic Adjustment estimated by the global ICE6G-VM5a model (Peltier et al., 2015)

the Pacific Decadal Oscillation (Boening et al., 2012; Reager et al., 2016; Hamlington et al., 2017).

The fingerprints shown in Figure 1.7a assume that the gravity field and the solid earth react immediately to changes in mass. This approximation, known as the 'elastic response' holds well for the mass loss that is currently observed. However, on the time scales of glaciation-deglaciation cycles corresponding to ice ages, the elastic approximation does not hold anymore, since stress gradients induced by surface loads induce a flow in the earth mantle. As a result, the solid earth is still adjusting to mass changes from the past. This visco-elastic response to ice mass changes over past glacial cycles is known as 'Glacial Isostatic Adjustment' (GIA), and causes a substantial VLM signal along many ocean boundaries. Models of the impact of GIA on solid-earth deformation and sea-level change require estimates of the evolution of the former ice sheets and information about the viscous structure of the earth, and both are difficult to constrain. Hence, GIA models have a considerable margin of uncertainty, although broad agreement on major features exists. One of the most widely used models is the global ICE6G-VM5a model (Peltier et al., 2015), whose resulting sea-level fingerprints are shown in Figure 1.7b. The former ice sheets over Fennoscandia and North America, as well as the Antarctic Ice Sheet are visible as locations that exhibit strong uplift as the solid earth is still reaching equilibrium to mass loss in the past. The resulting relative sea-level changes, which are felt by tide gauge observations, are affected by this land movement. A closer look reveals that due to GIA, sea level along the east coast of the United States rises more rapidly than along the mid-European coast. This difference partially explains the observed differences in Figure 1.5b.

1.7 Sea-level changes, steric expansion, and ocean dynamics

Global sea-level changes are not only caused by past and present mass redistribution, but also by changes in the specific volume of seawater. As shown in Figure 1.3, the oceans are absorbing large amounts of heat that is added to the earth system due to anthropogenic climate change (Levitus et al., 2012; Slangen et al., 2016). Since sea water expands when it becomes warmer, the total volume of ocean water is increasing. Furthermore, the density of seawater is dependent on its salinity. Sea-level changes related to changes of the specific volume of seawater are called steric changes. We distinguish between thermosteric changes, which are temperature-related volume changes, and halosteric changes, which are salinity-related volume changes. While mass redistribution results in global ocean mass changes, steric expansion only leads to a volume change, and hence does not result in an increase of the total ocean mass.

Next to global changes due to thermosteric expansion, changes in ocean dynamics result in regionally-varying thermo- and halosteric sea-level changes. Driven by winds and density differences, the ocean is continuously in motion. Due to the rotation of the earth and the resulting Coriolis force, the leading terms in the momentum

balance of the equations are generally the pressure gradient and the Coriolis force. As a result, surface ocean currents and the horizontal gradient in sea level are perpendicular. Hence, many large-scale ocean dynamic features can be seen in Figure 1.4b, including the North Atlantic Gulf Stream, which follows the US coast before separating from the coast at about 35 ^{o} latitude. Around Antarctica, the strong Antarctic Circumpolar Current can be distinguished. The relation between sea level and surface currents implies that changes in currents result in changes in regional sea level and vice versa. For example, one of the features visible in Figure 1.5a is the rapid sea-level rise in the Subpolar Gyre between Canada and Greenland. This sea-level increase can be linked to a decrease in the velocity of the counterclockwise-rotating Subpolar Gyre (Zhang, 2008).

In a changing climate, the ocean currents may show substantial changes, which result in distinct regional sea-level change patterns. For example, the Atlantic Meridional Overturning Circulation (AMOC), a large-scale transport mechanism in the Atlantic Ocean, will probably slow down due to the freshwater influx caused by Greenland mass loss and enhanced surface warming (Stouffer et al., 2006; Rahmstorf et al., 2015), which has profound effects on future regional sea level (Bingham and Hughes, 2009; Yin et al., 2010; Little et al., 2017).

On interannual and longer time scales, the sea-level response to changes in ocean currents is to a large extent baroclinic in nature, which means that dynamic sea-level variability is primarily caused by local density variations, and only to a small extent caused by changes in the bottom pressure (Bingham and Hughes, 2008; Piecuch et al., 2013; Forget and Ponte, 2015). Subsurface profiles of temperature and salinity have been obtained by hydrographic surveys, and more recently, by autonomous Argo floats (Roemmich et al., 2009). Although the spatial coverage before the introduction of the Argo floats was sparse in many regions, especially in the Southern Oceans, the observations allow to make estimates of subsurface salinity and temperature changes that cover all oceans, although, due to the sparse observations before the Argo era, the uncertainties are substantial. From the reconstructed temperature and salinity evolution of the oceans, density changes can be computed, from which we can infer regional sea-level change patterns associated with ocean dynamics. A reconstruction of density-induced sea-level changes over the past five decades, based on the EN4 temperature and salinity reconstruction (Good et al., 2013) is shown in Figure 1.8a. The figure reveals the presence of large spatial variations in steric sea-level trends. This spatial variability associated with density effects outpaces the variability associated with present-day mass redistribution, of which an estimate is shown in Figure 1.8b. The density-induced trend in sea level along the US coast is much larger than along the European coast, which may be another explanation for the differences between New York and Maassluis.

Unfortunately, the effects of ocean dynamics on sea level become complicated along shallow continental shelves and ocean boundaries. In shallow coastal seas and continental shelves, the local effect of salinity and temperature on sea level becomes smaller, as its changes only affect a shallow water column. However, suppose that over a deep column, next to a shallow shelf, sea level rises due to a change of the water density. Then, shelf sea level will adjust to this rise as a response to the emerging

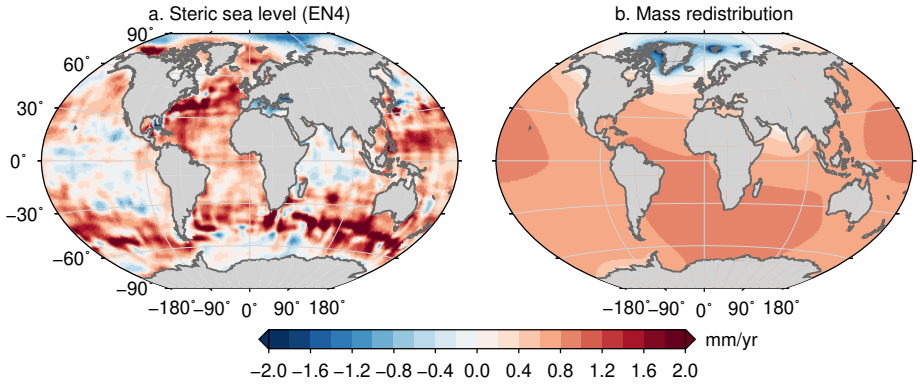

Figure 1.8: Sea-level trends over 1958-2014 associated with local density changes and mass redistribution. a: Density-related sea-level trends. Steric height anomalies have been computed using TEOS-10 (Roquet et al., 2015) from gridded in-situ observations from the EN4.1.1 database from the surface to 2000m (Good et al., 2013). b. Trends caused by present-day mass redistribution. Mass redistribution is estimated from the modelled contributions from glaciers, ice sheets, and terrestrial water storage. See Chapter 2 and 3 for the underlying models.

horizontal pressure gradient. This sea-level rise is accompanied by an increase of the bottom pressure on the shelf, and thus, by an increase of mass on the shelf (Landerer et al., 2007a). Hence, the density effects in Figure 1.8a will not only affect local sea level, especially around areas with shallow seas. However, even on decadal time scales, coastal and shelf sea-level changes differ from those in the nearby open ocean (Bingham and Hughes, 2012). One of the reasons for this difference is the presence of coastally-trapped waves (Huthnance, 1978). These waves, which propagate counterclockwise along the ocean boundaries in the Northern Hemisphere, result in the propagation of anomalies in coastal sea level along the shore, sometimes over thousands of kilometers (Hughes and Meredith, 2006). Since these waves are constrained by the shallow shelf, which is often only a few kilometers wide, the resulting effects on temperature and salinity are often not observed by the sparse measurements of temperature and salinity, and therefore, not well represented in Figure 1.8 (Calafat et al., 2013). To understand the impact of ocean dynamics on an individual tide gauge record or a specific region, in-depth knowledge of the relevant processes is required, and one can not simply sample the field in Figure 1.8a at the location of the tide gauge. Also most ocean models have difficulties resolving the relevant coastal processes (e.g. Piecuch et al., 2016), which hampers attempts to separate larger-scale trends from regional variability.

Summarizing, sea level is a quantity that can be characterised at a wide range of spatial and temporal scales. This characterisation imposes a major challenge for understanding and reconstructing sea-level changes over the wide range of spatial scales. This thesis aims to understand how sea-level observations from tide gauge records are affected by these processes and whether the sum of these processes explains observed local, regional, and global sea-level changes.

1.8 Research objectives

As outlined in the above sections, many questions regarding the spatial and temporal variability of sea level are still open. The aim of this thesis is to understand how the individual processes affect sea level on local, regional, and global scales. A key ingredient to answer this question is whether and on which temporal and spatial scales the sea-level budget can be closed. 'Closing the sea-level budget' means that the observed trends and variability of sea level can be explained by the sum of the contributors.

To obtain estimates of the sea-level budget, insight has to be gained into the quality and representativeness of tide-gauge observations, as well as understanding of all relevant contributing processes over a wide range of spatial and temporal scales. In this thesis, the sea-level budget is studied at regional, basin-mean and global scales. The following open questions will be addressed:

1. **Can the sea-level budget be closed on a regional scale?**
   Over the era before satellite observations, sea-level budget studies mostly focused on global scales. Many of these studies show that not all sea-level changes can be explained. For instance, the studies of Gregory et al. (2013) and Moore et al. (2011) show that the sum of known processes is lower than the observed sea-level rise over the past decennia, which is also one of the core elements of Munk's Enigma. Due to the sparse nature of most sea-level observations, constraining global sea-level changes and its contributors is a challenging task. A different approach, which we propose in this thesis, is to focus on regions in which observations are dense. Using these densely-observed regions allow us to make accurate estimates of sea-level and land-level observations. These processes can be combined with information of the impact of ocean dynamics on regional sea level to determine whether the gap between observations and sum of processes is also present in regional sea level.

2. **How can local sea-level and vertical land-motion observations be combined into reconstructions of regional sea level in a self-consistent manner?**
   The employment of permanent GPS stations close to tide gauges and altimetry over the past two decades have resulted in reliable estimates of local vertical land motion at many tide gauge locations (Wöppelmann et al., 2009; Santamaría-Gómez et al., 2012; Santamaría-Gómez and Mémin, 2015; Wöppelmann and Marcos, 2016). This development allows sea level observations from tide gauges to be transformed into geocentric observations. One problem that arises from these estimates is that tide gauge observations and vertical land motion estimates span different epochs. Therefore, the common approach to remove the linear trend in vertical land motion from the tide gauge record may results in an under- or overestimation of vertical land motion over the epoch of the tide gauge observations. The solid-earth deformation resulting from present-day mass transport, which is non-linear over typical epoch lengths of tide gauges is one of the processes that affect vertical land motion.

A self-consistent framework is proposed that allows the combination of tide gauge and land motion estimates, together with prior estimates of large-scale mass transport processes to estimate regional relative and absolute sea-level changes.

3. **Can we improve estimates of global and basin-mean sea-level changes by using prior information of regional variations?**
   As discussed in the previous sections, the sparse sampling of the spatially-varying sea-level field forms a major challenge in reconstructing global and basin-mean sea level changes. Prior information about this redistribution can give insight in how sea level at a specific location is related to global or basin-mean sea level. Adding this information to sea-level reconstructions removes a potential bias source. The prior knowledge about regional sea-level variations will be combined with local VLM observations to reconstruct sea-level changes over the past five decades in each ocean basin and for the global ocean. The impact of the extra prior information in the reconstruction will be determined. The basin-mean estimates could add extra information about the understanding of the sea-level budget, as it will give insight in the regions for which the budget can be closed, and for which it cannot.

4. **How does deformation of the solid earth affect sea-level observations by tide gauges, GPS, and altimetry?**
   As described above, sea level can be expressed in a relative and geocentric reference frame, which differ by the vertical motion of the solid earth. Since the combination of present-day ice mass loss and terrestrial water storage changes result in an increase of total ocean mass, it is expected that the ocean bottom will deform under the increasing load. Hence, the total change of ocean volume, or barystatic sea level will deviate from the global-mean absolute sea level. This effect has never been quantified. Based on modelled contributions from ice mass loss and terrestrial water storage changes, this effect will be quantified over the altimetry period.

5. **How can a state-space model be used to avoid the assumption of a prescribed shape of the long-term trend in tide gauge records?**
   To quantify longer-term changes in tide-gauge observed sea level, a linear or quadratic trend is often fitted to the data. However, the assumption that sea level can be parametrised as a polynomial with a serially correlated residual signal may not be the most suitable form. An alternative model to describe the time series of sea-level observations is a state space model. Combined with atmospheric reanalysis and storm-surge model output, the state-space model can separate long-term variability from high-frequency variability related to wind and air pressure changes. We will study the possibilities to use such a state space model to find and quantify low-frequency variability in tide-gauge records and to determine whether coherent long-term variability signals in multiple tide-gauge records exist.

1.9 Outline

The aim of this thesis is to improve the understanding and attribution of sea-level rise from local to global scales. The thesis has been organised in seven chapters.

Research objectives 1 and 2 are investigated using two case studies. In Chapter 2 and Chapter 3, we develop a self-consistent framework, in which sea-level and VLM observations are combined, and compared with the spatial fingerprints that result from GIA and present-day mass transport. In Chapter 2 we compare the observations of sea level in the North Sea over the past decades to the contributors. We find that in the North Sea and along the Norwegian coast the sea-level budget can be closed well within confidence intervals. Furthermore, we discuss a new proxy for the remotely-forced variability in ocean dynamics. We also show that the 18.6-year nodal cycle in the North Sea behaves according to tidal equilibrium.

In Chapter 3, we use the framework of Chapter 2 to study variability and trends in sea level along the Northwestern Atlantic Coast. In this region, a large sea-level acceleration can be observed over the past 50 years (Sallenger et al., 2012). We show that this acceleration does not have its main cause in ice melt, but can be linked to the propagation of high-latitude forcing along the shelf. This propagation has close ties to changes in the Atlantic Meridional Overturning Circulation.

Chapter 4 extends the previous work towards global scales to study research objective 3. We show that the combination of vertical land motion, knowledge about the spatial variability resulting from mass transport, and steric sea-level changes can be combined to update estimates of global and basin-mean sea-level changes. These updated sea-level curves are lower than most other sea-level estimates, which results in consistency with the sum of the contributors.

In Chapter 5, we discuss the impact of solid earth deformation on global and regional sea-level observations. We show that, because the oceans are becoming heavier, the ocean bottom subsides, which results in a lower global-mean geocentric sea-level change, compared to the total ocean volume change. Hence, altimetry observations, as well as VLM-corrected tide gauge observations, may underestimate global-mean sea-level change. This difference does not only affect the global mean, as large regional variations occur.

In Chapter 6, we discuss an alternative approach to estimate sea-level changes. Using a state space approach, we estimate trends, decadal variability, and the effects of wind and air pressure simultaneously. With this approach, we can omit the requirements of a linear or quadratic trend. We show that this method can be used to find regionally coherent sea-level patterns, and how they can be linked to large scale ocean dynamics.

The concluding remarks, as well as some suggestions to extend and improve this work are the subject of Chapter 7.

Chapter 2

Closing the sea-level budget on a regional scale: Trends and variability on the Northwestern European continental shelf

> Een boodschap aan het Nederlandse Volk, ja,
> die heb ik wel, maar ik denk dat genoemd
> volk daar geen boodschap aan heeft.
>
> Gerard Reve

Summary

Long-term trends and decadal variability of sea level in the North Sea and along the Norwegian coast have been studied over the period 1958-2014. We modeled the spatially non-uniform sea-level and solid earth response to large-scale ice melt and terrestrial water storage changes. GPS observations, corrected for the solid earth deformation, are used to estimate vertical land motion. We found a clear correlation between sea level in the North Sea and along the Norwegian coast and open-ocean steric variability in the Bay of Biscay and west of Portugal, which is consistent with the presence of wind-driven coastally-trapped waves. The observed nodal cycle was found to be consistent with tidal equilibrium. We were able to explain the observed sea-level trend over the period 1958-2014 well within the standard error of the sum of all contributing processes, as well as the large majority of the observed decadal sea-level variability.

Parts of this chapter have been published as: Frederikse, T., Riva, R.E.M., Kleinherenbrink, M., Wada, Y., van den Broeke, M.R, & Marzeion, B.: Closing the sea level budget on a regional scale: Trends and variability on the Northwestern European continental shelf. Geophysical Research Letters, doi:10.1002/2016GL070750, 2017.

2.1 Introduction

Sea-level rise is one of the most important consequences of climate change. On regional scales, large deviations from the global mean trend are observed, as well as significant variability on interannual and decadal scales (Stammer et al., 2013; Hughes and Williams, 2010). The emergence of remote sensing techniques and the global Argo program has allowed closure of the sea-level budget over the last decade by direct observations of mass and steric components, both on global (Leuliette and Willis, 2011) and regional scales (Rietbroek et al., 2016). However, the presence of multidecadal variability hampers the estimation of long-term trends from short records. Multiple studies have been undertaken to explain the observed global trends over the past few decades by looking into the sources of sea-level change (Church et al., 2011; Gregory et al., 2013; Hay et al., 2015). On time scales longer than the satellite era, closing the sea-level budget on regional scales still forms an open challenge. Knowledge about the origin of trends and variability of regional mean sea level on these longer time scales is of key importance for determining future regional sea-level rise, which is needed to ensure coastal safety (Nicholls and Cazenave, 2010). One of the first attempts to close the regional sea-level budget on multi-decadal time scales has been made by Slangen et al. (2014b), who studied regional trends, and found an acceptable agreement for most basins, but for individual tide gauge stations, large deviations occur.

In this chapter we present a study into the sea-level budget at the North-western European continental shelf over the period 1958-2014. This region has a dense network of tide gauges and frequent hydrographic measurements are conducted in the surrounding North-east Atlantic ocean. Sea-level rise in this region is widely recognized (Wahl et al., 2013). The decadal variability has also been extensively studied and has been linked to wind-driven coastally-trapped waves, which can travel large distances along the shelf edges (Richter et al., 2012; Calafat et al., 2013; Dangendorf et al., 2014a). To date, no studies exist that explain the observed sea-level trends in this region. We use a combination of models and observations to determine the influence of mass and steric effects on sea-level trends and interannual to decadal variability. GPS observations are used to account for vertical land motion (VLM) that cannot be explained by GIA and present-day mass redistribution effects. The modelled sea level is compared to tide gauge observations in the North Sea and along the Norwegian coast.

2.2 Data and models

We have obtained monthly tide gauge (TG) records from the Permanent Service for Mean Sea Level (PSMSL) (Holgate et al., 2013). The tide gauge stations have been divided into two regions, based on their location, as shown in Figure 2.1. All stations have a long (50+ years) record, are not subject to known datum instability, and are in proximity of a permanent GPS station. The stations are listed in Table 2.2 and depicted in Figure 2.1. For each station, to reduce the inter-station variability, the

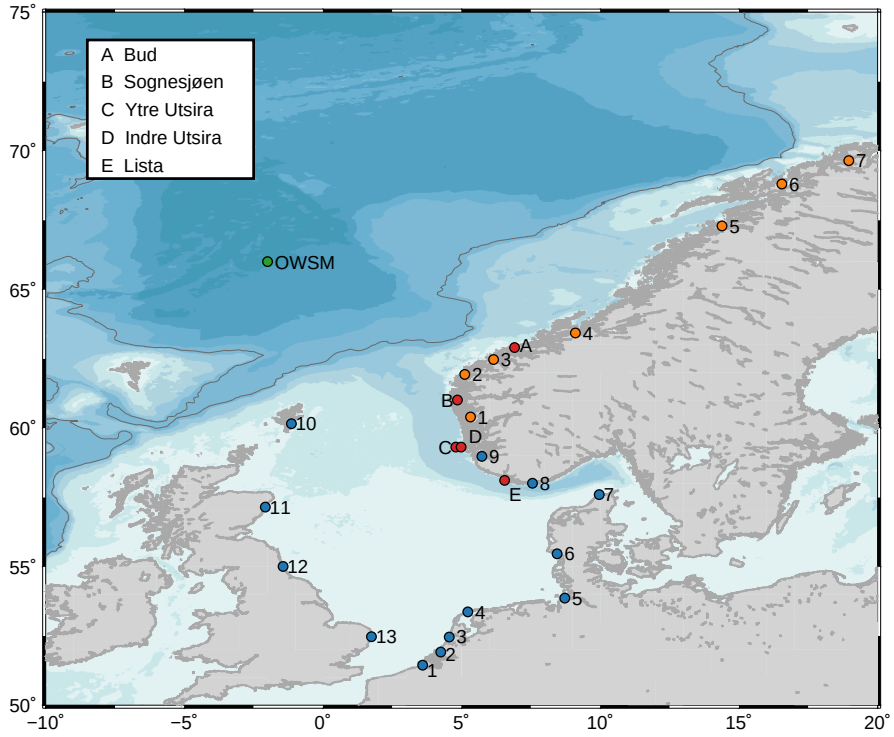

Figure 2.1: Location of the tide-gauge stations (blue for North Sea stations, orange for Norwegian stations), Ocean Weather Ship Mike (OWSM), and fixed hydrographic stations (red). The tide-gauge labels correspond to Table 2.2.

local effects of wind stress and atmospheric pressure on sea level are removed using simple multiple linear regression with time series from the 20th Century Reanalysis project (Compo et al., 2011), similar to the method of Dangendorf et al. (2014a). For each component (sea-level pressure anomalies and wind stress in the zonal and meridional direction), the grid point within 250 km around the station not located on land that shows the highest correlation is used as regressor. For both regions, an index time series is constructed from the arithmetic mean of all stations that have data at the specific month. Satellite altimetry observations are based on AVISO's multimission gridded SLA product (aviso.altimetry.fr) over 1993-2014. A Gaussian filter with a 1σ radius of 150 km has been applied to remove ahort-wavelength signals.

2.2.1 Mass signals and fingerprints

Mass exchange between land and ocean causes a spatial non-uniform relative sea-level (RSL) response, due to changes in the geoid and eustatic sea level, and deformation of the solid earth. This effect is taken into account by solving the elastic sea-level equation (Clark and Lingle, 1977; Tamisiea et al., 2010) including the earth-rotational feedback (Milne and Mitrovica, 1998). We consider the mass contribution

of glaciers, Greenland and Antarctic ice sheets and terrestrial water storage (TWS).

2.2.2 Sea-level response to mass transport

To determine the effect of large-scale sea-level changes due to mass transport in the earth system, we compute fingerprints that use mass gain or mass loss on a specific location to calculate the response of the geoid, solid earth and relative sea level on a 0.5° grid. Since the time scales of the mass transport terms in this study are decadal in origin, we only regard the elastic response. A local change of load $\Delta L(\theta, \phi)$ results in three distinct effects:

1. A change in the geoid height: $\Delta G(\theta, \phi)$.

2. A change in the solid earth height : $\Delta C(\theta, \phi)$.

3. A change in relative sea level: $\Delta R(\theta, \phi) = \Delta G(\theta, \phi) - \Delta C(\theta, \phi) + \mathscr{L}$.

$\mathscr{L}$ is the global-mean sea-level change due to the requirement of mass conservation. To obtain the resulting changes in geoid, solid earth and RSL, we solve the sea-level equation (Clark and Lingle, 1977) by means of the pseudo-spectral method, as described by Tamisiea et al. (2010), together with the earth rotational feedback (Milne and Mitrovica, 1998). To determine the geoid and solid-earth response, the elastic load Love numbers are computed from the Preliminary Referenced Earth Model (PREM, Dziewonski and Anderson, 1981). We use a center-of-mass reference frame, and compute our solution up to spherical harmonic degree 360. To prevent aliasing effects in the resulting geoid and deformation fields, a Gaussian filter is applied to all input loads with a 1σ radius of 42 km, which is a trade-off between suppressing aliasing effects and retaining input load information at high-degree harmonics.

2.2.3 Glaciers

Mass changes due to glacier melting are based on Marzeion et al. (2015). The regional glacier mass balances of all individual regions are used, except for Greenland and Antarctica, since they are included in the mass change signal of the ice sheets. The glacier mass balance for 2014 is estimated using simple linear extrapolation. Each regional mass balance estimate is mapped onto the corresponding glacier region mask from Randolph Glacier Inventory 5.0 (Pfeffer et al., 2014). For each region, the sea-level equation is solved, and all individual regions are added for the total sea-level response. From the regional mass balance error estimates, the upper and lower bound for each region is calculated. The sea-level equation is also solved for the upper and lower bound mass estimates, and the absolute values of the fingerprint difference with the mean for each region are added in quadrature to obtain the mean glacier error estimate. To obtain estimates of uncertainties in the trend, a linear trend is also estimated from the fingerprints resulting from the upper bound of the mass estimate. The difference between the two trends is used as an estimate of the trend uncertainty.

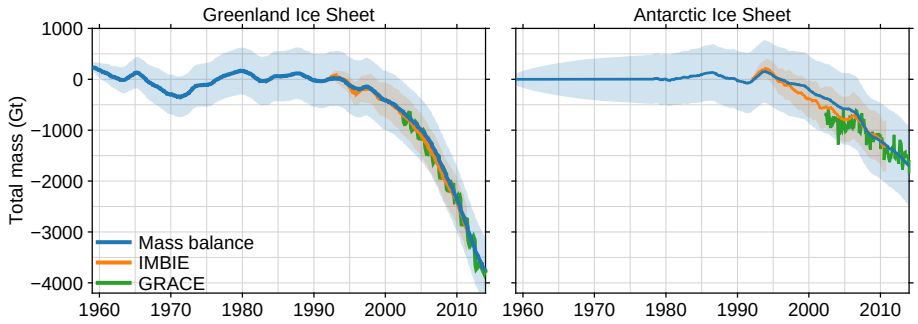

Figure 2.2: Estimate of Greenland and Antarctic mass balance, compared with IMBIE and GRACE estimates

2.2.4 Ice sheets

The contribution of ice sheets is estimated using an input-output method (IOM). The results have been calibrated by the estimates from the IMBIE intercomparison project (Shepherd et al., 2012) and GRACE data. For GRACE, the JPL 3° by 3° mascon solution is used, together with a Coastline Resolution Improvement scheme (Watkins et al., 2015). For Greenland, the GIA correction of A et al. (2013), and for Antarctica, the V2a model from Whitehouse et al. (2012) is applied.

The input comes from RACMO2.3 (Noël et al., 2015; van Wessem et al., 2014) surface mass balance (SMB), for the period 1958-2014 for Greenland and 1979-2014 for Antarctica. For Greenland, the output estimate for 1991-2014 is based on results listed in van den Broeke et al. (2016), which estimates an acceleration of 6.6 Gt/yr^2 over this period. Before 1991, we assume that the ice sheet is in long-term balance: we estimate a linear trend through the total SMB between 1958 and 1991, and use this trend as an estimate for the ice discharge before 1991.

For Antarctica, Rignot et al. (2011) estimates an ice discharge acceleration of 9.0 Gt/yr^2 since 1992. When this estimate is used for Antarctica, the resulting mass imbalance is larger than IMBIE and GRACE estimates. Therefore, we use a heuristic value of 2.0 Gt/yr^2 for the acceleration of the discharge, which gives a good fit to both IMBIE and GRACE. For the period 1979-1992, we assume long-term balance, similar to Greenland. Before 1979, we assume that the ice sheet is in balance (SMB-discharge $= 0$).

The load is not uniformly applied to the whole ice sheet, but partitioned following the GRACE mascon estimates, for which a linear trend in each 3° by 3° mascon block is calculated.

Since RACMO2.3 does not provide uncertainty estimates, we assume that the error grows with the average error accumulation of IMBIE. The resulting total mass balance, together with the validation time series is depicted in Figure 2.2. Similar to the glacier mass balance, the uncertainty in the resulting regional sea-level trends and variability is estimated from fingerprints of the upper bound of the mass balance.

2.2.5 Terrestrial water storage

In the model, three TWS effects are included: dam retention, groundwater depletion and natural variability. For dam retention, we use the method of Chao et al. (2008) to determine the filling and seepage rate. The dam data has been obtained from the GRanD Global Reservoir and Dam database (Lehner et al., 2011), and the load is attributed to the nearest grid cell. The list contains 6862 dams. Dams from the Netherlands all enclose former seas, which only causes mass effects if the lake water level deviates from mean sea level. We assume that this deviation is small and therefore, these dams have been removed from the list.
The effects of natural hydrology are estimated using PCR-GLOBWB version 2.0 (Wada et al., 2014), run on a 0.5° horizontal resolution. For groundwater depletion, the estimates of Wada et al. (2010) have been used. For all processes, we assume a rate uncertainty of 15 %.

2.2.6 Nodal cycle

For the nodal cycle, we use the principle of Proudman (1960), which states that the nodal tide should almost certainly follow the equilibrium law, which reads:

$$\Omega = \alpha \cdot (1 + k_2 - h_2) \cdot (3 \sin^2 \theta - 1), \tag{2.1}$$

with tidal Love numbers are $k_2 = 0.36$ and $h_2 = 0.60$, tidal equilibrium magnitude $\alpha = 8.8$ mm and latitude θ. Following Woodworth (2012), we calculate the self-attraction and loading response of this tidal load and add the resulting changes in geoid, crust and RSL to the equilibrium sea-level response.

2.2.7 Vertical land motion, GIA, and the nodal cycle

Tide gauges measure sea level relative to land, and therefore, VLM will affect the observations (Wöppelmann and Marcos, 2016). Both GIA and present-day mass effects cause solid earth deformation, which results in VLM. To separate these known effects from unknown VLM, we use GPS observations to estimate VLM not explained by GIA and present-day mass effects:

$$h_{\text{VLM-r}}(t) = h_{\text{GPS}}(t) - h_{\text{mass}}(t) - h_{\text{GIA}}(t), \tag{2.2}$$

with h_{mass} the solid earth deformation due to large-scale mass effects and h_{GIA} solid earth deformation due to GIA. The residual VLM term $h_{\text{VLM-r}}$ hence accounts both for unmodelled VLM and errors in GIA and mass loading models. For each tide gauge station, we determine a linear rate of residual VLM from a nearby permanent GPS site. Processed GPS time series were obtained from Nevada Geodetic Laboratory (`geodesy.unr.edu`). For the stations along the Norwegian coast, linear trends from Kierulf et al. (2014) have been used. Estimates of the GIA impact on VLM and sea level come from the global ICE6G-VM5a model(Peltier et al., 2015). Figure 2.3 shows the modelled GIA signal for crustal motion and relative sea level in our region

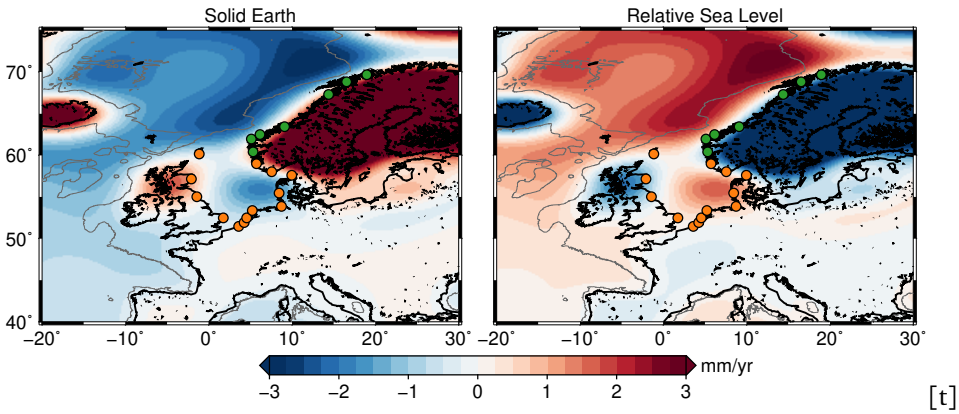

[t]

Figure 2.3: Present-day vertical crustal motion (left) and relative sea level (right) due to GIA from a global model (ICE-6G VM5a, Peltier et al., 2015).

of interest.
The 18.6 year nodal cycle also causes variability on decadal scales. According to a long-standing belief, the phase and amplitude of the nodal cycle follow the equilibrium law (Proudman, 1960; Woodworth, 2012). We account for the nodal cycle by assuming that the amplitude follows the self-consistent equilibrium law and no phase shift occurs (Woodworth, 2012).

2.2.8 Estimating trends from GPS records

For vertical land motion at tide gauges, horizontal and vertical positions in the IGS08 reference frame have been obtained from the Nevada Geodetic Laboratory, together with epochs of known equipment changes. Vertical trends are obtained following a step-wise procedure:

1. For the time series of north, east, and vertical positions, estimate a provisional trend by fitting a linear trend, offsets at times with known equipment changes or data gaps, an annual cycle and a semi-annual cycle.

2. Subtract the estimated model from the time series and remove outliers (larger than 3σ) in the residual.

3. Following the JPL strategy, detect possible offsets in the residual computed at 1 and 2 in all directions by determining the χ^2-statistic for each point with and without break:

$$F(t) = \frac{\chi^2_{\text{no break}} - \chi^2_{\text{break}}}{\chi^2_{\text{break}}} \cdot \frac{n-4}{2}. \tag{2.3}$$

   χ^2 is estimated from the sum of squared residuals. n is the number of data points. A point with $F > 25$ is a possible offset candidate. The possible offset is subsequently removed from the provisional time series. This procedure is iterated until no new possible offset candidates are found.

4. Estimate the size of the vertical offset for all offset candidates (equipment changes, data gaps and detected offset candidates). For jumps not related to equipment changes, only take offsets with a minimum of 4 mm into account.

5. The solid earth deformation from all mass-transport effects is estimated using the sea-level equation, and subtracted from the GPS time series. The solid earth deformation due to GIA is also removed. A linear trend and confidence interval is estimated from the corrected time series using Hector software (Bos et al., 2013). The time series is assumed to consist of a linear trend, an annual and semi-annual cycle. The noise is assumed to follow a combined white and power law distribution.

For Norwegian tide gauges, no GPS data is included in the Nevada Geodetic Lab database. Therefore, we make use of the estimates of Kierulf et al. (2014). Solid earth deformation effects are removed from the trend. The GPS uncertainty is assumed to stay constant over the whole time span of the tide-gauge observation:

$$\sigma_t = \sigma_{\text{trend}} |t - t_0| . \tag{2.4}$$

t_0 is the mean time of the GPS time series. For the Norwegian GPS stations we use the provided uncertainties from Kierulf et al. (2014), which are based on a Flicker noise model. All GPS trends are assumed to be independent, so the regional VLM uncertainty is the square root of the quadrature sum of the individual errors.

2.2.9 Steric height

The continental shelf is generally shallow, and therefore, the local contribution of steric expansion will be small on interannual time scales. However, steric effects in nearby open ocean will influence sea level on the shelf (Landerer et al., 2007a), although serious decoupling between coastal sea-level and open-ocean steric variability could occur (Bingham and Hughes, 2012). Wind-driven coastally-trapped waves are known to decouple coastal from open-ocean sea level and dominate the decadal sea-level variability in our region of interest (Calafat et al., 2012, 2013; Dangendorf et al., 2014a).
To determine the relationship between open-ocean steric signals and shelf sea level, we remove the sea-level response to all large-scale mass contributors and the equilibrium nodal cycle from observed RSL, and compute the correlation between the resulting de-trended and 25-month low-pass filtered residual RSL and steric sea level over the North Atlantic. Steric changes have been computed from 3D temperature and salinity grids from EN4 version 4.1.1 (Good et al., 2013) from a depth of 1000 m to the surface over the period 1958-2014. The resulting correlation pattern (Figure 2.4a) shows that the open-ocean steric height in the Bay of Biscay and west of Portugal correlates strongly with sea-level variability in the North Sea. Satellite altimetry observations show a very similar correlation pattern and they also point at the coherence between the North Sea and the Norwegian coast (Figure 2.4b). Therefore, we use the average steric signal over the Bay of Biscay and the Atlantic Ocean west of Portugal, as depicted in Figure 2.5 as a proxy for the impact of ocean dynamics on

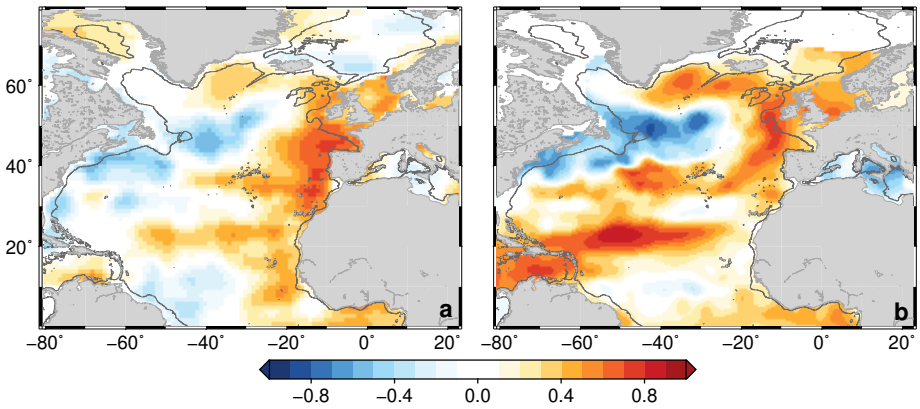

Figure 2.4: a: correlation between TG sea level in the North Sea after removing all mass contributors and steric height computed at each grid point from the surface to the sea floor or 1000m, depending on which is reached first. b: correlation between TG sea level in the North Sea and sea level observed by satellite altimetry between 1993-2014. The grey line depicts the 1000 m isobath. All time series have been detrended and low-pass filtered using a 25-month running mean, and all mass contributors have been removed before computing the correlation.

the shelf. Since open-ocean steric anomalies below the shelf bottom affects on-shelf bottom pressure, self-attraction and loading effects will amplify the signal. This effect, however is relatively small (Richter et al., 2013), and therefore not taken into account.

2.2.10 Computing steric height anomalies

The EN4 objectively analyzed gridded product has been used (Good et al., 2013), with the XBT and MBT bias corrections of Gouretski and Reseghetti (2010) applied. From the T and S fields, a steric height is calculated from a depth of 1000 m to the surface using the TEOS-10 software package (Pawlowicz et al., 2012). To determine the relationship between the tide gauge sea level and the steric effect, two products are computed:

1. A spatial grid with the correlation between de-trended sea level, corrected for all but the steric term and the gridded detrended steric sea level. Both time series are low-pass filtered using a 25-month running mean.

2. The same grid as above, but the R^2-value instead of the correlation. The R^2-value depicts the fraction of sea-level variance that is explained by the steric sea level without any scale factor.

The points with a correlation above 0.5 and a positive value for R^2 are selected and used. Figure 2.5 shows the grid points, over which the average steric component has been calculated.
For each grid point, EN4 provides a standard error for the salinity and temperature.

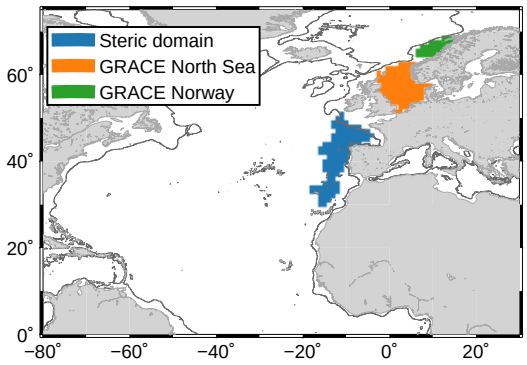

Figure 2.5: Masks used to determine steric signal and GRACE mass signals. Grid points for which the EN4 steric height has a coefficient of determination $R^2 > 0.0$ and a correlation > 0.5, with North Sea sea level after removal of known mass effects. These points are averaged to form the deep sea steric signal.

We use a Monte-Carlo simulation by, for each month, perturbing the mean fields with a normally distributed error with the provided standard deviation. We simulate 100 realizations per grid cell. The perturbation is equal for all depth levels as it is reasonable to assume that the errors are highly correlated in the vertical direction. The standard deviation in the produced steric height is then used as a standard error of the steric height at each grid cell. We then calculate the mean and standard error for the whole region by using the following spatial covariance function, based on Roemmich and Gilson (2009):

$$\sigma_{ij} = \sigma_i \sigma_j \left[0.77 \mathrm{e}^{-\left(\frac{l}{140}\right)^2} + 0.23 \mathrm{e}^{-\frac{l}{1111}} \right]. \tag{2.5}$$

l is the distance between point i and j in kilometers. The term a that is present in Roemmich and Gilson (2009) evaluates to one in our case, since all grid points over which the steric signal is averaged are located north of 20°. When calculating the running mean, the monthly steric errors are assumed to be independent. Variability in the tide gauge records mostly shows generalized Gauss-Markov (GGM) distribution of serially correlated noise (Bos et al., 2014). Since the tide gauge variability mainly originates from steric variability, we also use GGM as model for the temporal correlation of the noise in the steric component. The linear trends are computed using Hector software.

2.2.11 GRACE processing

The monthly GRACE OBP time series are estimated using post-processed ITSG - Grace2016 time-varing gravity fields (Klinger et al., 2016), averaged over the polygons shown in Figure 2.5. These gravity fields are provided with full covariance matrices, which allows the use of an anisotropic Wiener filter (Klees et al., 2008) to reduce the noise and striping effects. ITSG monthly gravity solutions are computed with respect to a static gravity field including a secular trend and an annual cycle

and the Atmosphere and Ocean Dealiasing (AOD1b) product (Dobslaw et al., 2013). The anisotropic Wiener filter is applied to the solutions after which the annual and secular signal are restored. Geocenter motion (degree 1) is estimated for the ITSG gravity fields based on the method of Swenson et al. (2008). The C_{20} component is replaced by satellite laser ranging estimates from Cheng et al. (2013). Eventually, the monthly averages of the OBP component of the AOD1b product are restored.

2.2.12 Reconstructed RSL

We define our reconstructed RSL as the sum of all contributing processes, which reads:

$$\zeta(t) = \zeta_{\text{dyn}}(t) + \zeta_{\text{mass}}(t) + \zeta_{\text{GIA}}(t) + \zeta_{\text{nodal}}(t) - h_{\text{VLM-r}}(t). \tag{2.6}$$

$\zeta(t)$ represents reconstructed RSL at time t. ζ_{dyn} is the dynamic contribution, for which the steric height over the aforementioned area is used, ζ_{mass} the local RSL response to the sum of mass effects, ζ_{GIA} the RSL response to GIA. The RSL response to GIA and mass effects consists of geoid and eustatic changes, and solid earth deformation. ζ_{nodal} the contribution of the nodal cycle, and $h_{\text{VLM-r}}(t)$ the residual vertical land motion as defined in equation 2.2. The mean has been removed from all time series. Note that the reconstructed RSL is simply the sum of all components and no parameters are estimated in equation 2.6.

2.3 Results

The observed and reconstructed relative sea level for both regions of interest are displayed in Figure 2.6. The dynamic signal shows large variability on decadal scales, while large-scale mass effects are varying more slowly, but show a clear acceleration. The amplitude of the equilibrium nodal cycle is on the order of 10 mm.
The bottom part of Figure 2.6 shows that the sum of all contributors explains the large majority of the observed variability on interannual and decadal scales. Along the Norwegian coast, the same dynamic signal is still clearly visible, although the residual shows larger peaks than in the North Sea. After removing the linear trend and applying a 25-month running mean, the fraction of explained variance (R^2) is 0.79 between the detrended contributors and sea level in the North Sea. The corresponding correlation coefficient is 0.89. For Norway, the numbers are 0.63 and 0.79 respectively.
When we compare the linear trends of the reconstructed and observed sea level (Table 2.1) we see that the model explains the observed trend well within confidence intervals for both regions. Note that the listed uncertainties are on the 1σ level. Significant uplift takes place along the coast, for which a large part is explained by GIA and solid earth deformation due to mass exchange. It must be noted that GIA models predict a steep gradient in vertical land motion and relative sea level along the coastline, which makes the model locally prone to model errors. The residual VLM term can compensate for these errors under the condition that the errors in geoid changes stay small. Without correcting GPS observations for solid earth deformation

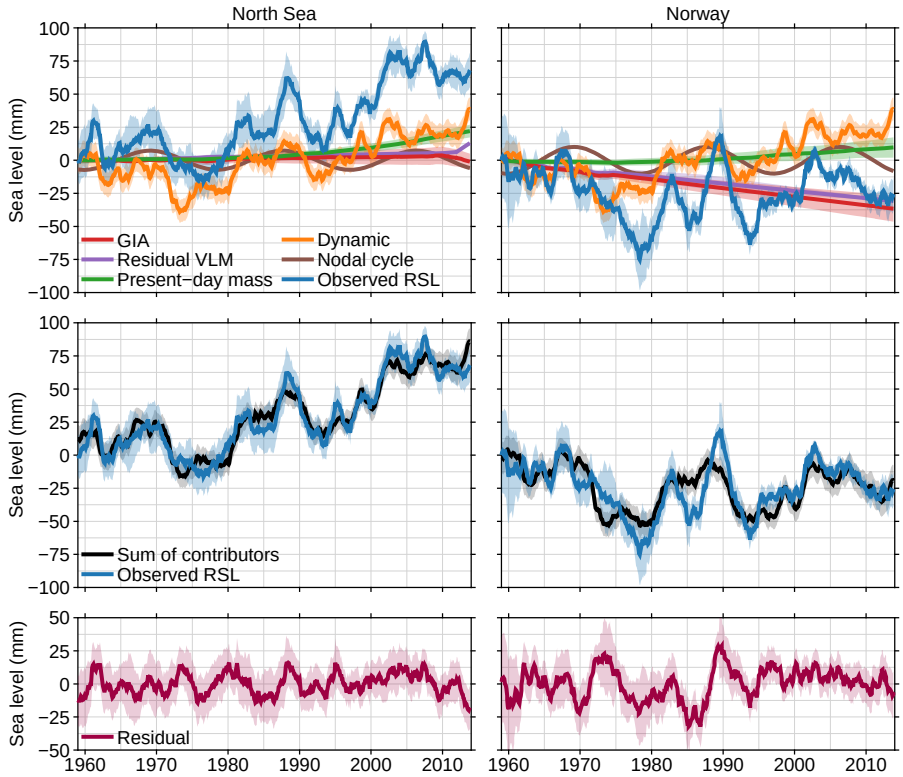

Figure 2.6: Measured relative sea level, together with the contributing processes (top), the sum of the contributing processes (middle), and the residual RSL (bottom). The shaded areas denote one standard error (sum of contributors) and the spread between the different tide gauge stations (measured RSL). Left: North Sea stations, right: Norway stations. All time series have been low-pass filtered with a 25-month running mean.

due to present-day mass transport, the observed VLM trend over the GPS era would be regarded as a long-term trend. However, the modelled solid earth response shows an upward acceleration over the period of interest, which causes GPS observations to overestimate the long-term linear trend in vertical land motion. For the North Sea, removal of solid earth deformation caused by present-day mass changes results in a decrease of 0.5 mm/yr of the estimated long term VLM trend. For Norway, this effect is even larger, due to the proximity of the Greenland ice sheet.

Because of the proximity of many glaciated regions and the Greenland Ice Sheet, their contribution is well below the global average, while the dynamic contribution is close to the global mean. Due to the contributions of GIA, vertical land motion and the nodal cycle, the sum of all contributors to the North Sea is close to the global mean sum of processes. For Norway, no significant upward trend can be found: GIA and residual VLM compensate for all mass and steric effects.

Table 2.1: Linear trends (mm/yr) in the individual processes, reconstructed and observed relative sea level for both regions and the global mean over 1958-2014. Global mean dynamic sea level based on steric estimates from Levitus et al. (2012) and Purkey and Johnson (2010). All errors represent 1σ.

	North Sea	Norway	Global
Glaciers	0.25 ± 0.02	0.07 ± 0.06	0.47 ± 0.05
Greenland	0.00 ± 0.01	-0.04 ± 0.01	0.12 ± 0.02
Antarctica	0.06 ± 0.03	0.07 ± 0.03	0.07 ± 0.03
Dam retention	-0.19 ± 0.03	-0.17 ± 0.03	-0.28 ± 0.04
Groundwater / natural	0.26 ± 0.04	0.27 ± 0.04	0.30 ± 0.05
Dynamic	0.73 ± 0.19	0.73 ± 0.19	0.73 ± 0.11
GIA	0.06 ± 0.02	-0.65 ± 0.16	-
-GPS[a]	*-0.44 ± 0.10*	*-2.34 ± 0.18*	-
-VLM-r	0.14 ± 0.10	-0.55 ± 0.18	-
Nodal cycle	0.03 ± 0.00	0.05 ± 0.00	-
Reconstructed RSL	1.33 ± 0.22	-0.22 ± 0.32	1.42 ± 0.14
Observed RSL	1.35 ± 0.28	-0.16 ± 0.30	

[a] Not part of the sum of contributors

2.4 Discussion

To evaluate the properties of the correlation pattern between the open-ocean steric and along-shelf sea-level signal, we use the historical run from CMIP5 earth system model NorESM1-M (Bentsen et al., 2013). The ocean component has a horizontal resolution of 1° and the isopycnal-coordinate model is mass-conserving, which makes the model suitable to study sea-level variability driven by changes in steric height and ocean bottom pressure (Richter et al., 2013). The model is able to reproduce the observed longshore coherence, as depicted in Figure 2.7a. Figure 2.7b shows that the open-ocean steric signal correlates with the mass signal in the North Sea and at the Norwegian shelf. Along the Norwegian coast, local steric effects still explain the majority of sea-level variability (Figure 2.7c). Consequently, to maintain longshore coherence, the steric component along the shelf should mimic the steric effect in the Bay of Biscay. Steric heights computed from T/S profiles from fixed hydrographic stations along the Norwegian coast (Bud, Sognesjøen, Ytre Utsira, Indre Utsira and Lista, data from imr.no/forskning/forskningsdata/stasjoner, a map with all stations is shown in Figure 2.1.) confirm the coherence between open-ocean and on-shelf steric variability on the lowest frequencies (Figure 2.8a), though on sub-decadal scales, differences can be noticed. GRACE-derived on-shelf OBP signals are consistent with sea level on both shelves, which indicates that the remote steric signal also appears as an on-shelf mass signal. The observed along-shelf coherence corresponds well with the presence of coastally-trapped waves, which travel counterclockwise on the northern hemisphere (Huthnance, 1978). These waves have the ability to create a spatially coherent monthly to decadal sea-level signal over along-shelf distances exceeding thousand kilometer (Hughes and Meredith, 2006; Sturges and Douglas, 2011). Along the eastern Atlantic boundary, longshore winds drive coastally-trapped waves over long distances, leading to a coherent decadal sea-level

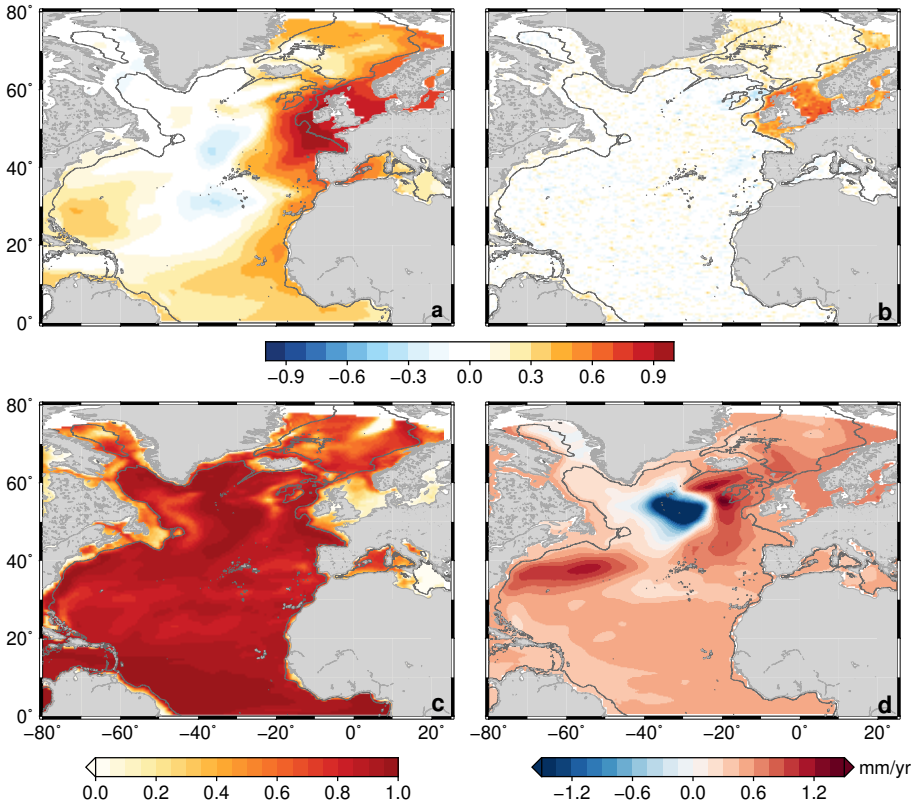

Figure 2.7: NorESM1-M (1900-2005) output. a. correlation of steric height in the Bay of Biscay with local dynamic sea level. b: correlation of steric sea level in Bay of Biscay with local OBP. c. fraction of dynamic sea-level variability explained by local steric sea-level variability. All time series have been detrended and low-pass filtered using a 25-month running mean. Steric sea levels have been computed from T/S fields up to a depth of 1000m. The effects of local winds on dynamic sea level have been removed using the same regression model as for the observations. d. Linear trend in dynamic sea level.

signal (Calafat et al., 2012, 2013). These waves trigger westward-travelling Rossby waves, causing open-ocean adjustment to coastal sea level (Marcos et al., 2013). Hence, the open ocean and shelf sea are both affected by decadal variability in the longshore winds, which explains the observed correlation pattern. The propagation of the coastal signals into the open ocean is hampered by decreasing Rossby wave speeds at high latitudes and hence, the correlation between shelf sea level and the nearby open ocean steric height vanishes at high latitudes. The coastally-trapped waves will be continuously affected by regional longshore winds when propagating northward, thereby gradually altering the wave properties, which may be one of the causes of the residual signal for the Norwegian stations in Figure 2.6 and corresponds well to the findings of Calafat et al. (2013), who show that Norwegian coastal sea level is affected by regional and remote longshore winds.

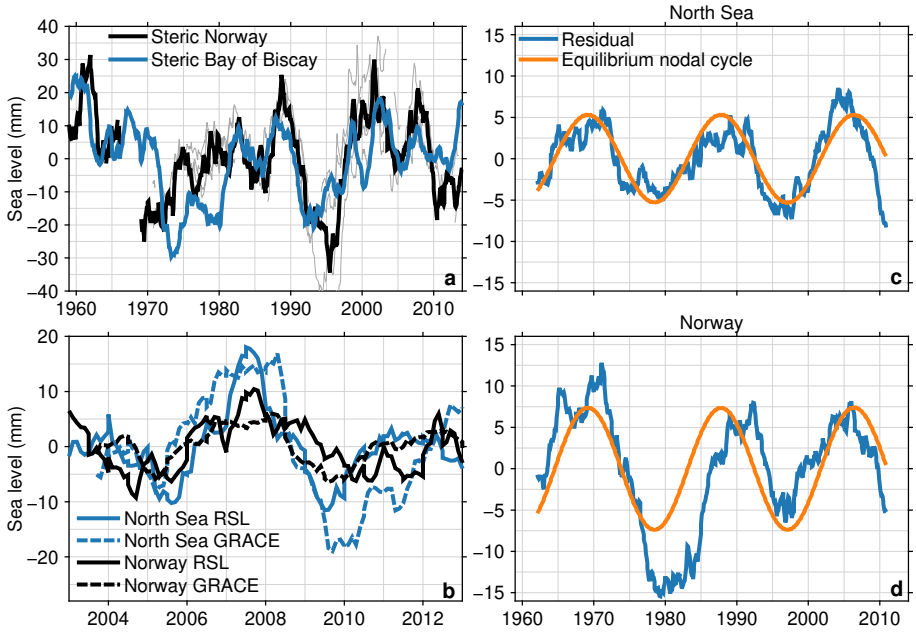

Figure 2.8: a: comparison between observed steric signal in the Bay of Biscay and the steric signal on the Norwegian shelf from hydrographic station measurements. Individual stations in grey. b: GRACE on-shelf mass signals and RSL for both regions. All time series in Figure a and b have been detrended and low-pass filtered using a 25-month running mean. c and d: comparison of measured RSL after subtraction of all terms in equation 2.6, except for the nodal term versus the equilibrium nodal cycle. The residual time series and the equilibrium cycle have been detrended and low-pass filtered using a 97-month running mean.

The steric signal in the Bay of Biscay is also used as a proxy for the long-term trend in dynamic shelf sea level, with the underlying assumption that the trend does not show large variations over our region of interest. Since the long-term trend is likely to be driven by other processes than longshore wind variability, this assumption must be verified. The averaged steric height time series from the permanent hydrographic stations along the Norwegian coast has a linear trend of 0.68 ± 0.26 mm/yr. Ocean Weather Station Mike, located in the interior of the Norwegian Sea (see Figure 2.1), shows a steric height trend of 0.72 ± 0.19 mm/yr over the upper 1000 m between 1958 and 2009. Both the shelf and open-ocean trends are close to the observed 0.73 ± 0.15 mm/yr in the Bay of Biscay. The dynamic sea-level trends in NorESM (Figure 2.7d) also depict the low spatial variability of dynamic sea-level trends in the region.

Some studies suggest that the observed nodal cycle departs from astronomical equilibrium (Houston and Dean, 2011; Baart et al., 2011), and explains a large fraction of the observed decadal variability. We have re-done our analysis, but without the nodal term in equation 2.6. The resulting residual (Figure 2.8c and 2.8d) shows a phase and amplitude which are in agreement with equilibrium tide. This observation corresponds well to the conclusion of Proudman (1960) that the sea-level response

Table 2.2: Tide gauge stations and accompanying GPS stations for the North Sea (NS) and the Norwegian coast (NO). Numbers correspond to Figure 2.1. Linear GPS rates (h_{GPS}), GPS corrected for crustal deviation from load effects and GIA($h_{\mathrm{VLM\text{-}r}}$). All rates in mm/yr. All errors are on the 1σ level.

		Tide gauge	GPS	h_{GPS}	$h_{\mathrm{VLM\text{-}r}}$
1	NS	Vlissingen	VLIS	-0.27 ± 0.38	-0.80 ± 0.38
2	NS	Maassluis	DELF	-0.73 ± 0.26	-1.01 ± 0.26
3	NS	IJmuiden	WIJK	-0.51 ± 0.33	-0.88 ± 0.33
4	NS	W-Terschelling	TERS	-0.64 ± 0.29	-0.43 ± 0.29
5	NS	Cuxhaven	TGCU	0.11 ± 0.52	0.13 ± 0.52
6	NS	Esbjerg	ESBC	0.43 ± 0.31	1.10 ± 0.31
7	NS	Hirtshals	HIRS	2.40 ± 0.31	1.11 ± 0.31
8	NS	Tregde	TGDE	1.99 ± 0.15	0.89 ± 0.15
9	NS	Stavanger	STAS	1.37 ± 0.57	-0.20 ± 0.57
10	NS	Lerwick	LWTG	0.71 ± 0.57	-0.06 ± 0.57
11	NS	Aberdeen	ABER	0.89 ± 0.12	-0.83 ± 0.12
12	NS	North Shields	NSTG	0.96 ± 0.21	-0.03 ± 0.21
13	NS	Lowestoft	LOWE	-0.44 ± 0.15	-0.49 ± 0.15
1	NO	Bergen	BRGS	1.50 ± 0.32	-0.54 ± 0.32
2	NO	Maløy	FLOC	1.40 ± 0.55	0.32 ± 0.55
3	NO	Alesund	ALES	1.70 ± 0.19	0.59 ± 0.19
4	NO	Heimsjø	HEMC	3.30 ± 0.91	0.56 ± 0.91
5	NO	Bodo	BODS	4.20 ± 0.31	1.41 ± 0.31
6	NO	Harstad	BJAC	2.30 ± 0.45	0.89 ± 0.45
7	NO	Tromsø	TROM	2.70 ± 0.29	0.64 ± 0.29

to the nodal tide should follow the equilibrium law.

2.5 Conclusions

Sea-level trends and decadal variability over the North European continental shelf over the second half of the 20th century until 2014 have been studied. The combination of mass, steric, and solid earth deformation effects explains the large majority of interannual and decadal variability in the region as well as the observed trends. The trend varies throughout the region due to GIA and unmodelled VLM. GPS measurements can partially compensate uncertainties in modelled GIA. A strong correlation is found between steric variability in the open ocean in the Bay of Biscay and west of Portugal and sea level on the shelf. This correlation is not only visible in hydrographic observations, but also in satellite altimetry and the NorESM1-M earth system model and is consistent with the existence of wind-driven coastally-trapped waves that radiate westward-travelling Rossby waves into the open ocean. The linear trend in dynamic sea level is consistent over the region, and the observed steric height in the Bay of Biscay and west of Portugal is used as a proxy for the trend and decadal variability in dynamic shelf sea level. This proxy explains the vast majority of the observed decadal sea-level variability, while the mass contributors mostly explain longer-term changes. The observed nodal cycle, for which equilibrium tidal theory predicts a relatively large amplitude in the region of interest, follows the equilibrium law. The steric signal shows large variability at decadal time scales, which contaminate nodal cycle estimates from classical least squares. Estimating the nodal cycle

from tidal equilibrium, as proposed by Woodworth (2012), is therefore the preferred method.

The North Sea shows a positive trend in sea level, while along the Norwegian coast, GIA and VLM offset the mass and dynamic effects, which leads to a negligible trend over the study period. The method used in this study is easily applicable to other regions as long as high quality regional measurements of RSL, VLM and T/S profiles are available. Applying this method to more regions could provide more insight in the link between coastal and open ocean sea-level changes and help improving future coastal sea-level forecasts.

Chapter 3

The sea-level budget along the Northwest Atlantic coast: GIA, mass changes and large-scale ocean dynamics

> Sobald sich Politikerentscheidungen nach diesem, wie ich es nenne "gesunden Volksempfinden" zu richten beginnen, sobald man sich also von diesen Agenturen dieses Volksempfindens vor sich hertreiben läßt und Entscheidungen schon im Hinblick darauf trifft, empfinde ich das als Gefahr für die Demokratie.
>
> Elfriede Jelinek

Summary

Sea-level rise and decadal variability along the northwestern coast of the North Atlantic Ocean are studied in a self-consistent framework that takes into account the effects of solid-earth deformation and geoid changes due to large-scale mass redistribution processes. Observations of sea and land level changes from tide gauges and GPS respectively, are compared to the cumulative effect of GIA, present-day mass redistribution, and ocean dynamics over a 50-year period (1965-2014). GIA explains the majority of the observed sea-level and land motion trends, as well as almost all inter-station variability. Present-day mass redistribution resulting from ice melt and land hydrology causes both land uplift and sea-level rise in the region.

We find a strong correlation between decadal steric variability in the Subpolar Gyre and coastal sea level, which is likely caused by variability in the Labrador Sea that propagates southward. The steric signal explains the majority of the observed decadal sea-level variability and shows a positive trend and a significant acceleration, which are also found along the coast.

Parts of this chapter have been published as: Frederikse, T., Simon, K.M., Katsman, C. A., and Riva, R.E.M.: The sea-level budget along the Northwest Atlantic coast: GIA, mass changes and large-scale ocean dynamics, Journal of Geophysical Research: Oceans, doi:10.1002/2017JC012699, 2017.

The sum of all contributors explains the observed trends in both sea level rise and vertical land motion in the region, as well as the decadal variability. The sum of contributors also explains the observed acceleration within the 66% confidence level. The sea-level acceleration coincides with an accelerating density decrease at high latitudes.

3.1 Introduction

Observations show that sea level along the northwestern coast of the Atlantic Ocean north of Cape Hatteras (35°N, Figure 3.1) rises faster than the global average (Boon, 2012) and shows an acceleration over the last decades (Ezer and Corlett, 2012; Sallenger et al., 2012). However, the multitude of processes that affect regional sea level show variability on a wide range of temporal scales, which hinders the separation between climate-driven trends and accelerations, and internal variability (Haigh et al., 2014). Kopp (2013) argues that in this region, the observed sea-level acceleration does not yet exceed the likely range of natural variability. Further insight can be obtained by considering the contribution of each individual process on regional sea level.

It is well-known that in general, regional sea level is influenced by multiple processes (Stammer et al., 2013). Along our region of interest, which covers the Atlantic coast between $35°N$ and $45°N$, many studies discuss the individual contributors to sea-level trends, accelerations, and variability (e.g. Bingham and Hughes, 2009; Engelhart et al., 2009; Ezer, 2013; Woodworth et al., 2014; Karegar et al., 2016), although to date, no study has yet combined these processes to close the regional sea-level budget.

Tide gauges are the main source of sea-level data over the last century, and the northwestern Atlantic coast is covered by a dense network of high-quality tide gauges with long records (Woodworth et al., 2014). Since tide gauges observe sea level relative to the land, tide gauges register vertical land motion (VLM) as a change in sea level. Permanent GPS receivers co-located with tide gauges can provide VLM rates, which allows separating vertical land motion from geocentric sea-level change (Santamaría-Gómez et al., 2012; Wöppelmann and Marcos, 2016). At many locations along the northwestern Atlantic coast, vertical land motion (VLM) forms a large contribution to sea-level changes (Han et al., 2014). The region is closely located to both the former Laurentide Ice Sheet and its forebulge, and therefore, large trends and regional differences in VLM, and thus in sea level, can be expected (Engelhart et al., 2009; Peltier et al., 2015). Some stations in the region also suffer from local subsidence due to present-day groundwater depletion (Karegar et al., 2016), while larger areas are affected by elastic uplift as a response to the decrease of surface load due to groundwater pumping (Veit and Conrad, 2016).

Next to GIA, present-day mass redistribution due to ice melt, land hydrology, and dam retention causes changes in global mean sea level (barystatic changes), as well as in regional relative sea level and vertical land motion (Bamber and Riva, 2010; Santamaría-Gómez and Mémin, 2015).

Multiple studies investigate the impact of processes related to atmosphere and ocean dynamics on sea level in this region. On decadal and multi-decadal time scales, weakening of the Atlantic Meridional Overturning Circulation (AMOC) will cause a rise of the dynamic sea level along the coast (Landerer et al., 2007b; Bingham and Hughes, 2009; Ezer, 2013). Since the AMOC has only been observed directly since 2004, no information about its behaviour is available on multi-decadal time scales. Furthermore, Thompson and Mitchum (2014) argue that sea-level variability along the east coast of the North American continent has a common mode, caused by zonal transport between the ocean interior and the western ocean boundary. Next to large-scale oceanic forcing, the sea-level response to local winds and sea-level pressure cause interannual variability of coastal sea level which may hide the effects of large-scale ocean dynamics on coastal sea level (Woodworth et al., 2014; Li et al., 2014; Piecuch and Ponte, 2015; Piecuch et al., 2016). Hence, the effect of ocean dynamics consists of processes related to regional atmospheric forcing, and processes acting on larger spatial scales.

In this chapter we investigate the influence of various large-scale processes on sea-level rise and variability along the American Atlantic coastline north of Cape Hatteras over the period 1965-2014. Over this period, high quality tide gauge observations are available, as well as in-situ subsurface temperature and salinity profiles in the northwestern Atlantic ocean, which are used to study the effects of ocean dynamics and changes in sea water density on coastal sea level. We use a self-consistent framework, identical to the framework descried in Chapter 2, which explicitly incorporates the effects of GIA and present-day mass redistribution on both sea-level changes and vertical land motion. Using this framework, we compare the observed changes in sea level and land level with the sum of the individual processes. We show that the sum of the processes explains the observed decadal variability, trend, and acceleration in sea level along the northwestern Atlantic coast.

This chapter is structured as follows: in Section 3.2, we introduce the observed sea-level trends and variability from tide gauges and the linear rates of vertical land motion from GPS observations. In Section 3.3 we discuss the role of GIA and introduce an updated data-driven model, which explains a large fraction of the observed VLM trends and most of the inter-station variability. In Section 3.4 the role of present-day mass transport due to ice melt and land hydrology is discussed. We show that present-day mass redistribution affects both sea-level and land-level observations and that the resulting VLM trends over the GPS era are not fully representative for the full 50-year study period. In Section 3.5, we discuss the role of ocean dynamics on sea level in the region and show that steric changes in the Subpolar Gyre are highly correlated with sea-level changes along the coast. In section 3.6, we combine the estimates of all terms and present the estimate of the sea-level and VLM budget in the region and we show that the vast majority of the observed decadal variability, trend and acceleration of sea level in the region can be explained by the individual processes. Finally, the discussion of the results and the conclusions are presented in Section 3.7.

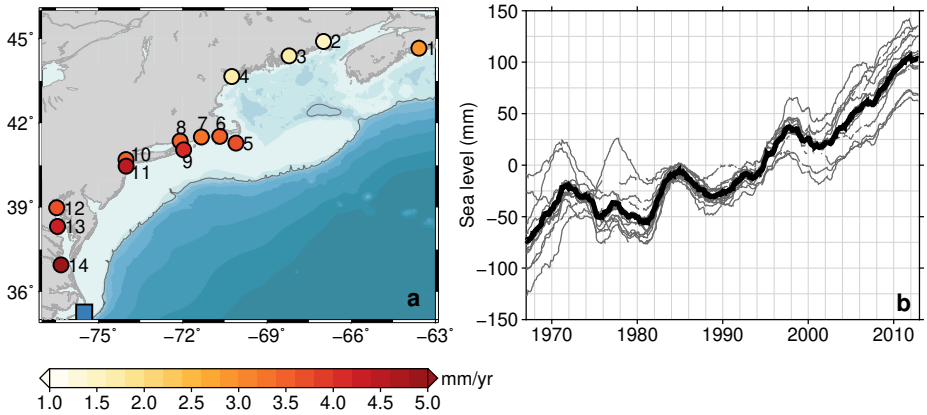

Figure 3.1: a: Location of each tide gauge listed in Table 3.1. The color denotes the observed linear sea-level trend over 1965-2014 at the tide gauge,the grey line denotes the 250 meter isobath, and the blue square denotes Cape Hatteras. b: Residual time series of station-averaged sea level (thick, black) and each individual station (grey) after applying the regression model. The time series have been low-pass filtered using a 49-month running mean.

3.2 Sea-level and GPS observations

For the observations of trends and variability in mean sea level, we have selected 14 tide gauges from the Permanent Service for Mean Sea Level (PSMSL) database (Holgate et al., 2013). We have selected stations that are within 25 km of one or more permanent GPS stations and are not known for datum instability. All tide gauge stations with their location and GPS stations are listed in Table 3.1. Local barotropic effects may play a large role in the variability at individual tide gauge locations. Since we are interested in a region-mean signal, we remove the local effects of the seasonal cycle, wind stress, and sea-level pressure from monthly mean sea level by applying a simple linear regression model, similar to the procedure followed in Dangendorf et al. (2014a). Indices of wind and sea-level pressure have been obtained from the 20th Century Reanalysis project version V2C (Compo et al., 2011). For each index we select the grid cell within a 250-km radius of the tide gauge with the highest correlation with monthly mean sea level. We subsequently compute the coefficients and the accompanying confidence intervals using linear least squares:

$$\begin{aligned}\zeta(t) = \quad & \zeta_0 + \alpha_1 t + \frac{1}{2}\alpha_2 t^2 + \alpha_3 (p(t) - \overline{p}(t)) + \alpha_4 \tau_u(t) + \alpha_5 \tau_v(t) \\ + \quad & \beta_1 \sin(\frac{2\pi t}{365.25}) + \beta_2 \cos(\frac{2\pi t}{365.25}) + \beta_3 \sin(\frac{2\pi t}{182.63}) + \beta_4 \cos(\frac{2\pi t}{182.63})\end{aligned} \tag{3.1}$$

with $\zeta(t)$ monthly mean sea level, ζ_0 mean sea level, t the time epoch, $p(t)$ sea-level pressure, $\overline{p}(t)$ sea-level pressure averaged over all oceans, and τ_u and τ_v the zonal and meridional wind stress. When the estimated values of α_3, α_4, and α_5 are significant at the 95% confidence level, their accompanying regressor is removed from the

Table 3.1: List of tide gauge stations used in this study, the location, and the accompanying GPS station

Index	Name	Longitude	Latitude	GPS station
1	Halifax	-63.58	44.67	HLFX
2	Eastport	-66.98	44.90	EPRT
3	Bar Harbor	-68.21	44.39	BARH
4	Portland	-70.25	43.66	YMTS
5	Nantucket Island	-70.10	41.29	IMTS
6	Woods Hole (Ocean. inst.)	-70.68	41.52	AMTS
7	Newport	-71.33	41.51	NPRI
8	New London	-72.09	41.36	CTGR
9	Montauk	-71.96	41.05	MNP1
10	New York (The Battery)	-74.01	40.70	NYBP
11	Sandy Hook	-74.00	40.46	SHK1, SHK2, SHK5, SHK6
12	Annapolis (Naval Academy)	-76.48	38.98	USNA
13	Solomon's Island (Biol. lab.)	-76.45	38.32	SOL1, MDSI
14	Sewells Point, Hampton Roads	-76.33	36.95	DRV1

mean sea-level time series, as well as the mean ζ_0 and the annual and semi-annual cycle $(\beta_1, \beta_2, \beta_3, \beta_4)$. The linear trend and acceleration term are co-estimated, but not removed from the signal. Note that leaving out the trend or acceleration estimate in equation 3.1 has a negligible effect on the resulting regression coefficients. Figure 3.2 shows the signal that is removed for each individual station, as well as the station-mean removed and retained signals. Consistent with findings of Piecuch and Ponte (2015) and Woodworth et al. (2014), the removed signal also contains a station-mean signal, although this signal is smaller than the residual station-mean signal and does not show a significant trend or acceleration. Also for the individual stations, the removed signal does not contain significant trends or accelerations.

To test the sensitivity of the regression model against the choice of the reanalysis product, we have tested our regression model using data from the JRA55 reanalysis (Kobayashi et al., 2015) and the ICOADS 3.0 gridded observations database (Freeman et al., 2016). Both data sets cover the full 1965-2014 period. The removed and retained signals for these data sets are also shown in Figure 3.2. Choosing a different model does not have a large effect on the resulting station-mean variability signal: the mutual correlation coefficients between the retained signals using different model data stays above 0.96, even when no atmospheric variability signal is removed. However, the removed signal using JRA55 and ICOADS does have a significant linear trend, while the 20th Century Reanalysis does not. To account for this uncertainty, we use the standard deviation of the different trends as a source of uncertainty. The removed signal does not contain a significant acceleration, regardless of the dataset used.

After the removal of the local effects of wind and air pressure, the linear trends and accelerations, together with their uncertainties are estimated for each time series by assuming a generalized Gauss-Markov (GGM) noise structure. This noise model adequately describes the serially correlated noise structure in most tide gauge time series (Bos et al., 2014). The Hector software (Bos et al., 2013) is used to compute the trends, accelerations and their uncertainties. The uncertainty related to the use of different models for the regression analysis is added in quadrature to the error

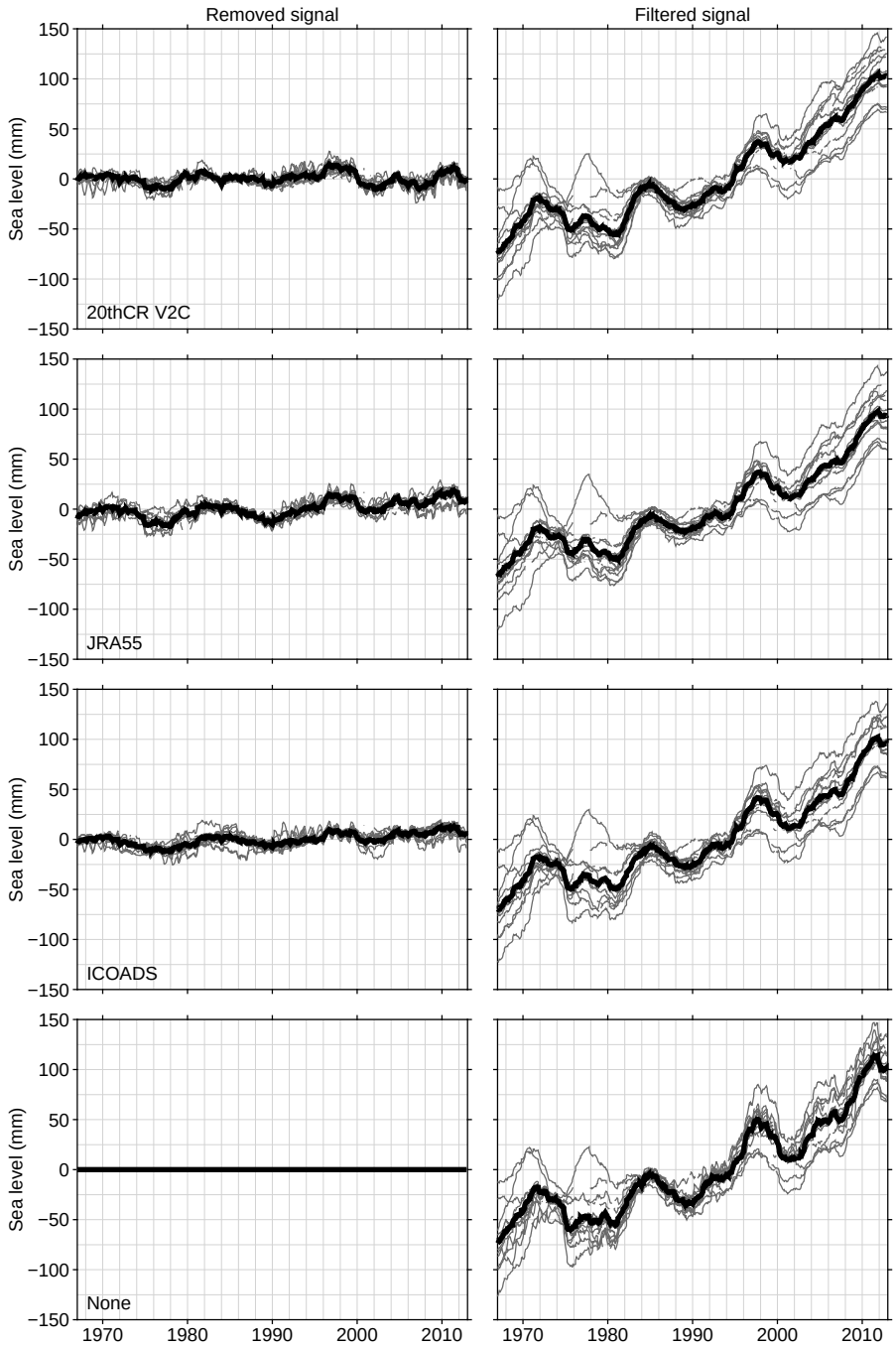

Figure 3.2: Comparison of different reanalysis and observation products used by the regression model. Top: 20th Century Reanalysis Project V2C. Middle: JRA-55, Bottom: ICOADS. Left: signal removed by the regression model. Right: signal left after applying the regression model. Thin lines represent individual stations. Thick lines represent the station-mean signal. All time series have been low-pass filtered using a 49-month running mean.

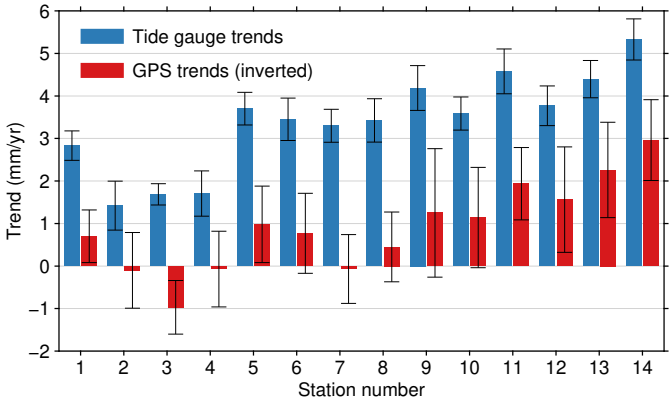

Figure 3.3: Linear trends and confidence intervals in observed vertical land motion (red) and relative sea level (blue) at each tide gauge site. Note that the trends in vertical land motion have been inverted, so a positive GPS trend corresponds to subsidence.

estimates. All confidence intervals presented in this study are at the one sigma level.

To separate decadal variability from high-frequency signals, the time series, after correcting for wind and pressure, are low-pass filtered using a 49-month running mean. Note that trends and accelerations are estimated from the signal before the running mean filter is applied.

The station locations and the observed linear trends are depicted in Figure 3.1a. The linear trends show large inter-station differences, with lower trends mostly located in the northeast and higher trends in the southwest. On the other hand, the pattern of decadal variability after applying the regression model, shown in Figure 3.1b, is very similar between stations. This coherent pattern of decadal variability has already been observed in many studies (e.g. Thompson (1986); Thompson and Mitchum (2014); Woodworth et al. (2014) and others).

For each GPS receiver, linear vertical land motion trends have been obtained from the Nevada Geodetic Laboratory (geodesy.unr.edu). For some tide gauge stations, multiple GPS receivers are nearby. In that case, the rates of all nearby GPS stations have been averaged. The provided trends have been computed using the MIDAS robust trend estimator (Blewitt et al., 2016), which provides trends and uncertainties that are not affected by unknown jumps in GPS time series, which could cause large biases if they remain uncorrected (Gazeaux et al., 2013). The vertical land motion rates as observed by GPS and their confidence intervals are depicted in Figure 3.3. The rates have been inverted and plotted next to the observed sea-level trends. A clear connection between the sea-level and inverted land-motion trend can be seen: stations with high sea-level trends generally show high subsidence and vice versa. The distinct northeast-southwest pattern of lower and higher rates in the tide gauge records can also be observed from GPS. The difference between the observed sea-level and inverted VLM trend does not show large variations over the region, which suggests that the large inter-station differences have their origin mostly in vertical land motion. In the next sections, we will examine the influence of glacial isostatic

adjustment (GIA) and present-day mass transport on the regional sea-level and VLM trends and whether these processes explain the differences between the individual stations.

3.3 Glacial Isostatic Adjustment

The primary candidate for explaining the differences between the individual stations in observed sea-level and land-level change is glacial isostatic adjustment (GIA). GIA affects both GPS and tide gauge observations: deformation of the solid earth is registered as vertical land motion by GPS observations, while tide gauges observe the resulting relative sea-level changes (Tamisiea, 2011).

The observed northeast-southwest gradient in relative sea level has already been linked to GIA in multiple studies (Engelhart et al., 2009; Kopp, 2013). Both uplift due to the proximity of the former Laurentide Ice Sheet, and subsidence caused by the collapse of the ice sheet forebulge occur in this region. Both effects result in a complex uplift-subsidence structure that poses a challenge for many GIA models (Davis and Mitrovica, 1996; Roy and Peltier, 2015). Here we revisit the influence of GIA in the region with the regional GIA model from Simon et al. (2017). This model is based on a joint inversion of VLM rates from GPS, gravity rates from GRACE, and a large suite of forward GIA models that comprises plausible ice sheet and earth viscosity model parameters. Compared to the global ICE6G-VM5a model (Peltier et al., 2015), the resulting GIA solution gives an overall lower misfit to observed gravity changes and vertical land motion over the North American continent (Simon et al., 2017). This model also provides estimates of the formal uncertainty of the predicted sea-level and land-level velocities.

The modelled present-day trends in sea level and land level caused by GIA, together with the observed trends in sea level and land level are shown in Figure 3.4a,b. The figure also shows a comparison of the model to the global ICE6G-VM5a model (Peltier et al., 2015). The location of the forebulge collapse is visible as a positive trend in relative sea level (Figure 3.4a) and strong land subsidence (Figure 3.4b). The predicted region of the forebulge collapse coincides well with the south-western stations that show high rates of subsidence and sea-level rise. The northeastern stations are located farther away from the middle of the forebulge collapse area, and relative to the more southerly stations, are characterized by less negative or slightly positive rates of VLM. Therefore, the horizontal gradient in observed vertical land motion and sea-level rise along the coastline, as shown in Figure 3.3a, is consistent with the complex structure seen in the predicted present-day effect resulting from GIA. When the relative sea-level estimates are removed from the tide gauge observations, the inter-station spread, visible in Figure 3.1b, is reduced, as depicted in Figure 3.5. The standard deviation of the observed relative sea-level trends is reduced from 1.12 mm/yr without GIA correction to 0.66 mm/yr after removing the local GIA signal. However, it must be noted that the exact location of the forebulge is uncertain and the presence of a strong gradient in modelled vertical land motion and sea-level trends perpendicular to the coastline makes sampling of the GIA signal

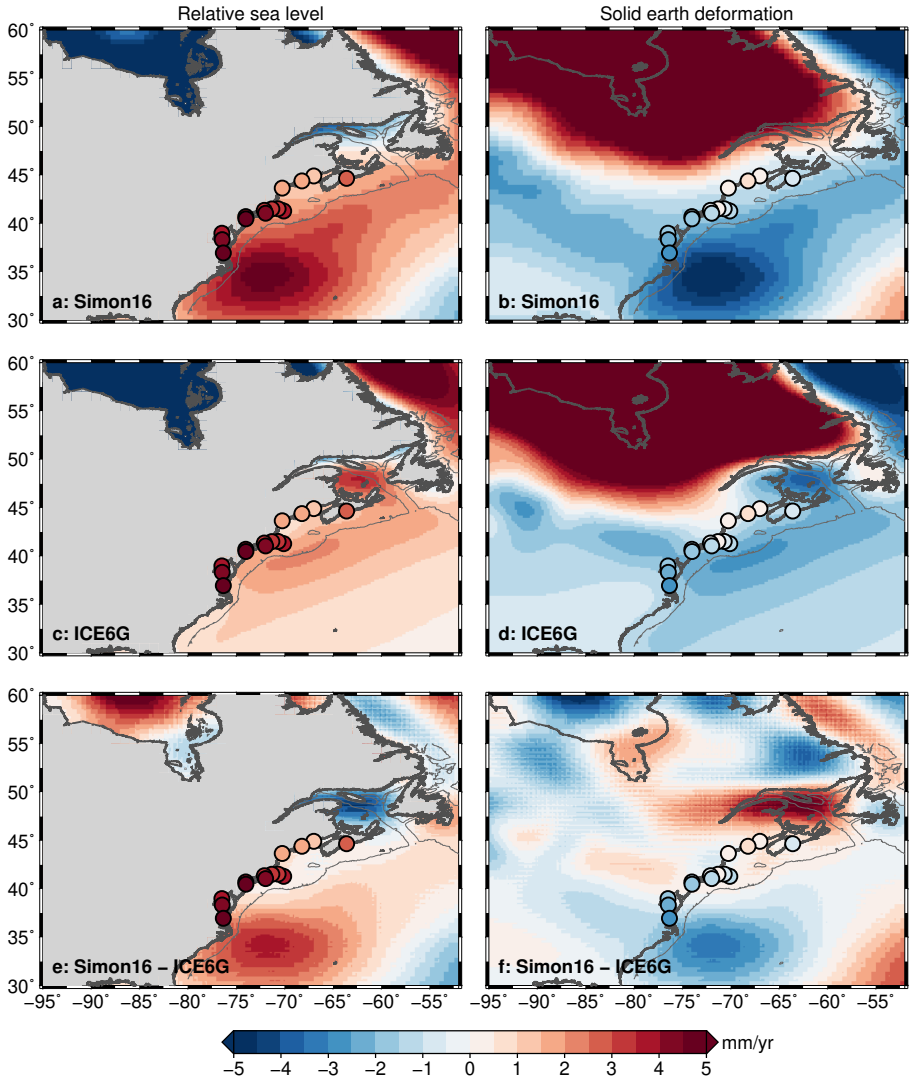

Figure 3.4: Modelled present-day trend in relative sea level and land level due to glacial isostatic adjustment. a,b: Modelled trends in the GIA model deployed in this study (Simon and Riva, 2016). b,c: Modelled trends from the global ICE6G-VM5a model. e,f: Difference between both models. a,c,e: Modelled relative sea level response. b,d,f: Modelled solid earth deformation. Tide gauge locations are marked by dots, with the color of the dot in a,c,e denotes the observed relative sea-level trend. In b,d,f the dot denotes the observed vertical land motion trend.

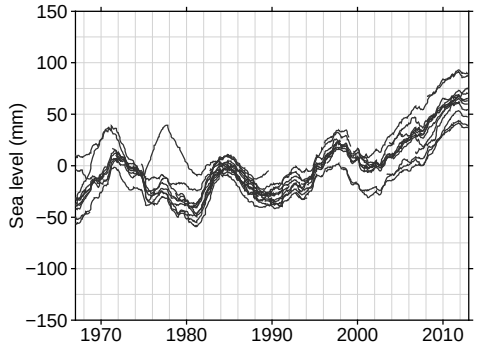

Figure 3.5: Time series of the individual tide gauge records after removing the modelled relative sea-level response to GIA. The time series have been low-pass filtered using a 49-month running mean.

at tide gauge stations prone to errors, which are not fully quantified in the formal uncertainty estimates.

3.4 Present-day mass redistribution

Redistribution of mass between land and ocean causes, in addition to changes in the global-mean barystatic sea level, regionally-varying sea-level changes. These regional variations are caused by changes in the earth gravity field (geoid changes), deformation of the solid earth, and earth rotation effects (Tamisiea and Mitrovica, 2011). Hence, similar to GIA, both tide gauge and GPS observations are affected by present-day mass redistribution. In this section, we quantify the influence of the major mass exchange processes on sea level and vertical land motion in our region of interest.

The effects of mass redistribution on sea level are computed by solving the elastic sea-level equation (Farrell and Clark, 1976). We apply the spherically-symmetric approximation and solve the equation in the center-of-mass (CM) frame using the pseudo-spectral method as described by Tamisiea et al. (2010). The earth rotation effect is modelled following the description in Sabadini et al. (2016). The resulting effects of mass transport on local observations of relative sea level can be split in different contributors:

$$\eta'(\theta,\phi,t) = \overline{\eta}'(t) + G'(\theta,\phi,t) - R'(\theta,\phi,t). \tag{3.2}$$

$\eta'(\theta,\phi,t)$ is the local relative sea-level anomaly at longitude ϕ and latitude θ and time t as a result of the mass redistribution, which is observed by tide gauges. $\overline{\eta}'(t)$ is the global-mean term that is required to ensure global mass conservation. $G'(\theta,\phi,t)$ denotes changes of the geoid and $R'(\theta,\phi,t)$ is the resulting deformation of the solid earth. Note that $\overline{\eta}'(t)$ is not the same as the global-mean barystatic contribution, since the geoid and solid earth deformation fields do not evaluate to zero over the

whole ocean. Mass redistribution affects GPS observations only by the resulting solid earth deformation, while tide gauge observations are affected by all processes on the right hand side of Equation 3.2.

Here, we consider the large scale mass redistribution due to glacier and ice sheet melt, natural hydrology, groundwater depletion, dam retention, and the 18.6-year nodal tide. Except for the Greenland ice sheet, we use the same estimates for the individual mass redistribution processes as in Chapter 2, which provides a detailed description of the used models and the derivation of formal uncertainties. Here we review the mass redistribution models briefly. For glacier melt, we use the modelled mass balance estimates of Marzeion et al. (2015), which provides estimates of the mass evolution of 18 glaciated regions.

For the Greenland Ice Sheet, the mass balance estimates and their uncertainties from Kjeldsen et al. (2015) are used before 1992. After 1992, the Greenland mass change is estimated from the Surface Mass Balance (SMB) and solid ice discharge. SMB is modelled using RACMO2.3 (Noël et al., 2015), while ice discharge is modelled using a constant acceleration of 6.6 Gigaton/yr^2, based on results from van den Broeke et al. (2016). For the Antarctic ice sheet, we assume no mass changes before 1979, a long-term balance between the Antarctic Ice Sheet SMB (van Wessem et al., 2014) and ice discharge between 1979 and 1992, and a 2.0 Gt/yr^2 acceleration of the ice discharge after 1993, which gives a reasonable fit to both the results of the IMBIE intercomparison case (Shepherd et al., 2012) and GRACE observations of ice mass loss over more recent years (e.g. Watkins et al., 2015). Note that the contribution of the Antarctic ice sheet before the nineties is very uncertain, although observations of earth rotation suggests that the total ice sheet contribution before the nineties is probably below 0.2 mm/yr (Mitrovica et al., 2015).

The resulting regional sea-level patterns are sensitive to the location of mass loss. Therefore, the mass loss of each ice sheet is partitioned by scaling the ice-sheet averaged trend by the individual trend in each grid cell, computed from GRACE mascon solutions (Watkins et al., 2015). Variability in natural hydrology and the depletion of groundwater are based on the outcomes of the PCR-GLOBWBv2 global land hydrology model (Wada et al., 2011, 2014). For dam retention, we have used the GRanD Global Reservoir and Dam database (Lehner et al., 2011) to estimate the location and capacity of all reservoirs. The filling and seepage rates of the reservoirs is estimated following the method of Chao et al. (2008). The astronomical nodal cycle causes a tidal signal with a period of 18.61 years. This tidal signal also acts as a mass redistribution process, and thus results in geoid changes and solid earth deformation. We model the effects of the nodal cycle under the assumption that the amplitude and phase of the nodal cycle do not depart from tidal equilibrium (Woodworth, 2012). Since our region is close to 35^o latitude, where the amplitude of the nodal cycle is zero, the impact of the nodal cycle is small, with an amplitude of about 1 to 4 mm in sea level and 0 to 0.2 mm in the solid earth height.

For each individual process, the sea-level equation is solved for the annual-mean mass redistribution. The time series of vertical land motion and sea-level change resulting from the individual mass transport processes and their confidence intervals, averaged over all 14 stations, are depicted in Figure 3.6. The resulting vertical land

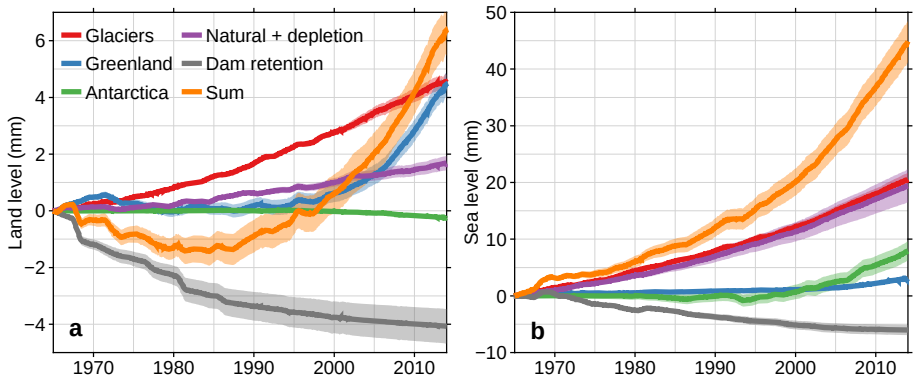

Figure 3.6: Station-mean effects of the individual mass transport terms and their sum: a: resulting vertical land motion and b: relative sea level. The shading denotes the uncertainty at 1 σ.

motion from the sum of processes shows a clear acceleration. Mostly due to the decrease in dam construction and the increase of Greenland melt, the solid earth response shows an upward acceleration since the nineties (Figure 3.6a). Note that due to its proximity, Greenland mass loss causes uplift in the region, while the distant Antarctic ice sheet causes subsidence. Due to the acceleration since the nineties, the region-mean VLM trend since 2000 is on the order of 0.5 mm/yr. This trend is larger than the trend over the full period, which is on the order of 0.1 mm/yr. Since GPS observations typically cover only the last 10-15 years, the observed trend over that period is not fully representative for the long-term VLM trend. This difference causes a bias if the GPS trend is assumed to be representative for the full tide gauge record.

The regional land uplift and geoid changes are not large enough to offset the barystatic sea-level changes, and hence the cumulative effect of all contributors still results in a positive regional relative sea-level trend and an acceleration over the period of interest.

Since the northernmost station Halifax and the southernmost station Sewells Point are about 1500 km apart and the region is in close proximity to some glaciated regions and the Greenland ice sheet, inter-station differences in the mass contribution to sea-level rise are present. In Figure 3.7 these differences are quantified by estimating the linear trend resulting from each contributor and their sum at each grid cell. A gradient along the coast can be seen in the contribution of glaciers and Greenland (Figure 3.7a,b), while the other processes (Figure 3.7c-e) vary less over the region. The sum of processes (Figure 3.7f) shows that in our region of interest the inter-station differences are on the order of 0.1 mm/yr, which is an order of magnitude smaller than the differences caused by GIA. Therefore, present-day mass transport will only explain a negligible fraction of the observed inter-station variability in sea-level trends.

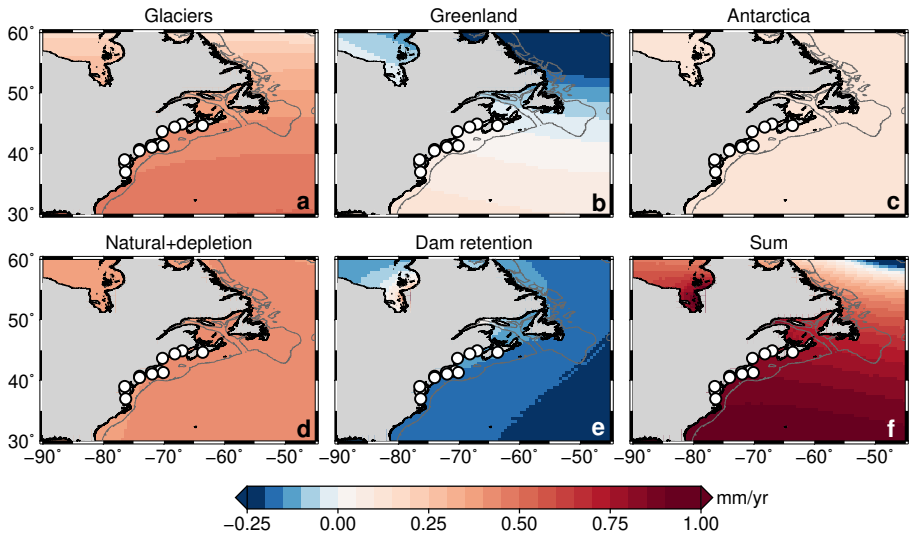

Figure 3.7: Linear trends in the resulting relative sea-level changes caused by (a-e): each individual present-day mass redistribution process and f: the sum of these processes.

3.5 Ocean dynamics

We have now quantified the major past- and present-day mass transport effects, and the next step is to determine the role of ocean dynamics on coastal sea level. Since we have applied a simple regression model (Equation 3.1) to remove the local impact of wind and pressure, we will look for remote drivers of variability. Due to the presence of, among other processes, boundary waves and currents, coastal sea-level trends and variability are often de-coupled from the nearby open ocean, even on decadal time scales (Bingham and Hughes, 2012). In contrast, coastal sea level often shows alongshore coherence over thousands of kilometers (Hughes and Meredith, 2006). Hence, we cannot directly use the steric height signal in the nearby open ocean as a proxy for dynamic sea-level changes along the coast. To determine whether a link exists between dynamic sea-level changes in the open ocean and along the coast, we determine the correlation between tide gauge and altimetry observations. We obtained a multimission gridded altimetry sea-level anomalies product from Archiving, Validation and Interpretation of Satellite Oceanographic data (AVISO). To remove high-frequency signals related to ocean eddies, but to retain the large-scale oceanographic signals, a Gaussian filter with a 1σ radius of 75 km has been applied to the fields. The correlation pattern between region-mean sea level from tide gauges and sea level in the Northwest Atlantic from altimetry is shown in Figure 3.8a. This figure clearly shows a high correlation over the shelf along the coast, which confirms that the coastal sea-level signal is reproduced by altimetry. Furthermore, a large area of high correlation is visible in the southern part of the North Atlantic Subpolar Gyre. Both findings correspond well to the results of Andres et al. (2013), who also found this correlation pattern. If we remove the signals related to present-day mass effects

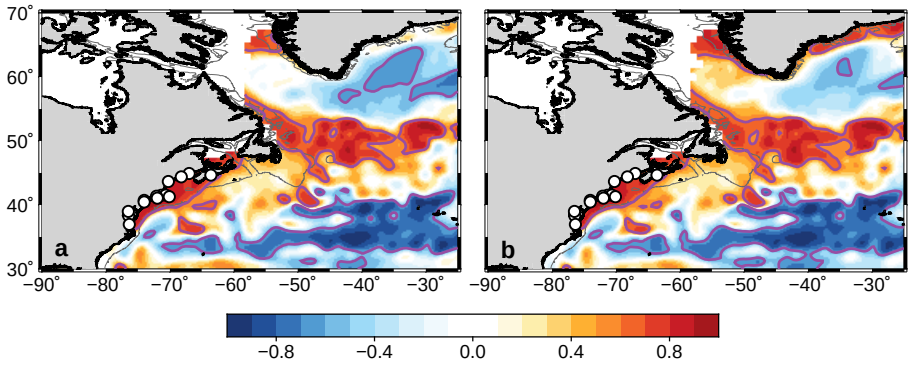

Figure 3.8: Correlation of region-mean sea level from tide gauges and altimetry sea level at each grid cell. a. Correlation between the original tide gauge and altimetry signals. b. Correlation after removing the effects of present-day mass transport from both tide gauge and altimetry data. All time series have been detrended and low-pass filtered using a 49-month running mean before computing the correlation. The grey line depicts the 250m isobath and the white circles show the tide gauge locations. The purple line encircles the areas for which the correlation is significant at the 95% level.

from the tide gauge and altimetry records, and we recompute the correlation (Figure 3.8b), coastal sea level is also highly correlated with the boundary of the North Atlantic Ocean along the coast of Greenland. One of the main reasons for the improvement in the correlation pattern after removing the mass contributors is the contribution of the 18.6-year nodal cycle. Its amplitude increases with higher latitudes and forms a substantial contribution to the decadal sea-level signal around Greenland. Removing the equilibrium nodal cycle from the altimetry record explains the majority of the observed increase in correlation along the Greenland coast. Because we have removed the modelled sea-level response to ice and land water storage, this correlation pattern likely has its origin in ocean dynamics. Hence, this correlation pattern suggests a link between sea-level variability in the boundary current of the Subpolar Gyre and dynamic sea level near the coast.

Since density effects are one of the factors that drive dynamic sea-level changes, the next step is to use in-situ temperature and salinity observations to compute steric height changes. Regular in-situ measurement campaigns have been conducted in the region (Kieke and Yashayaev, 2015), which allows us to estimate steric height changes over the last 50 years from in-situ data. However, in the northern part of the Subpolar Gyre, the amount of observations is lower, and due to sea ice and weather conditions, biased towards summer observations. We computed steric heights from the EN4 dataset (Good et al. (2013), version 4.1.1, with the Gouretski and Reseghetti (2010) XBT and MBT fall rate correction applied.) over the period 1965-2014. The EN4 database provides gridded temperature and salinity observations, from which steric height anomalies are derived using the TEOS-10 package (Roquet et al., 2015). Since the amount of observations below 2000 m in the Subpolar Gyre is limited, we only use observations in the upper 2000m. We computed the correlation between

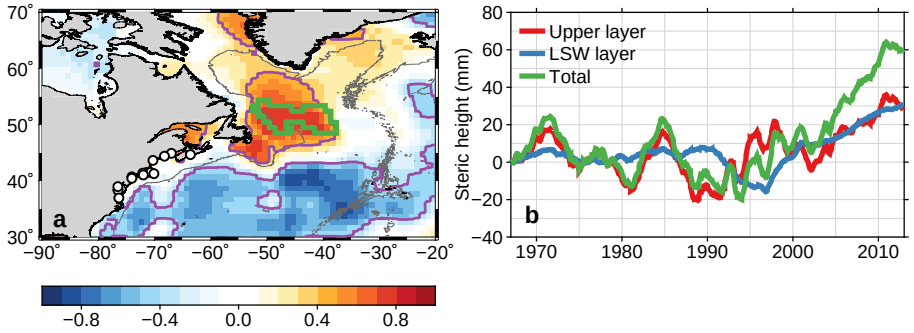

Figure 3.9: Observed steric height signal. a: Correlation between observed tide gauge sea level over 1965-2014 after present-day mass effects have been removed and steric height integrated from the surface to either the ocean floor or 2000m, depending on which is reached first. The grey line depicts the 2000m isobath. All time series have been de-trended and low-pass filtered using a 49-month running mean before computing the correlation. The purple line encircles the areas for which the correlation is significant at the 95% level. b: time series of steric height over the upper layer (0-650m), the LSW layer (650-2000m) and the full layer averaged over the area encircled by the green line in a.

the station-mean tide gauge signal, with the mass signal removed, and steric height anomalies, evaluated over the upper 2000m. The correlation pattern (figure 3.9a) shows that the high correlation between coastal sea-level changes and dynamic sea-level changes in the southern part of the Subpolar Gyre in Figure 3.8b is also visible in in-situ observations over a longer time span. Since steric height changes in shallow water are small, the correlation between on-shelf steric height and tide gauge observations decreases, which probably causes the low correlation on the shelf in Figure 3.9a.

The observed high correlation between dynamic sea level on the shelf and in the southern Subpolar Gyre is in line with multiple modelling studies. Häkkinen (2001) finds a coherent decadal sea-level signal in the Subpolar Gyre and along the US east coast using empirical orthogonal functions from model data. Using highly simplified models, Hsieh and Bryan (1996) and Johnson and Marshall (2002) argue that Kelvin waves along the western boundary of the North Atlantic result in a quick alongshore adjustment to sea-level perturbations at high latitudes. This quick response is followed by a slower response resulting from advective processes. However, the sidewalls of the western boundary are not vertical, and hence, the boundary wave propagation will take the form of a coastally-trapped wave instead of a pure Kelvin wave (Huthnance, 1978). Using an isopycnal ocean model with realistic topography, Roussenov et al. (2008) find that sea surface height anomalies in the Labrador Sea propagate along the southern Subpolar Gyre and the western boundary of the North Atlantic coast. Hodson and Sutton (2012) confirm this propagation mechanism, and argue that the propagated density anomalies at 800-1800m depth are related to changes in the AMOC strength. Roberts et al. (2013) compare multiple coupled climate models, and using a lead-lag correlation analysis, they show that

density anomalies in the Labrador Sea are propagated both along the Subpolar Gyre and the western boundary. Hence, these model results clearly suggest that the correlation pattern in figure 3.9 is a result of high-latitude anomalies that are propagated both into the Subpolar Gyre and along the western boundary. These adjustment processes not only result in a coherent sea-level variability signal, but on multi-decadal time scales, also in a coherent sea-level rise signal (Yin et al., 2009).

To obtain a proxy for the high-latitude sea-level anomalies that affect coastal sea level, we average the steric signal over the region of high correlation in the southern Subpolar Gyre. We define this region as all grid cells with a depth of at least 2000m, a non-negative correlation coefficient and coefficient of determination (R^2) with detrended coastal sea level. These points are encircled by the green line in Figure 3.9a. The resulting time series of steric height changes in the area encircled by the green line is shown in figure 3.9b. The steric signal is not correlated with the signal that has been removed by the regression analysis in equation 3.1 (correlation coefficient of 0.06 between both low-pass filtered and detrended signals).

Various processes may be responsible for the observed steric variations. In the upper ocean, the East- and West Greenland Current and the Labrador Current form a cyclonic boundary current system (Fischer et al., 2004). The variability in this upper layer is largely driven by atmospheric processes (Han et al., 2010). At intermediate depths, Labrador Sea Water (LSW) can be found, which is formed during deep convection events in the Labrador Sea. After formation, LSW is transported at depth along the western boundary of the Atlantic by the Deep Western Boundary Current (Rhein et al., 2011). This DWBC forms the lower limb of the Atlantic Meridional Overturning Circulation (AMOC), and changes in the density of LSW are believed to impact its strength (Robson et al., 2014). Model predictions show that changes in the AMOC strength have a large impact on sea level along the US coast, and its projected slowdown in a warmer climate leads to sea-level rise in the Subpolar Gyre and along the US coast (Yin et al., 2009; Bingham and Hughes, 2009). Below the LSW deep water masses are present that are formed from Denmark Strait Overflow Water (DSOW) and Iceland-Scotland Overflow Water (ISOW), which are also transported by the DWBC (Rhein et al., 2011).

To separate the signal of our proxy for the high-latitude steric variability into the individual contributions from the aforementioned water masses, we compute the steric height variability over the depth layers that contain these different water masses. These layers can be separated using a potential density anomaly criterion. Following Rhein et al. (2011), we define Labrador Sea Water as water with a potential density anomaly of $\sigma_\theta = [27.68, 27.80]$ kg/m^3. When we average the potential density anomalies over the area of high correlation (denoted by the green line in Figure 3.9a), we find LSW below 650m depth. The lower bound of the LSW layer is generally located around or below 2000m (see Figure 3.10). The resulting steric height anomalies in both layers and over the full column, averaged over the area of high correlation, are depicted in Figure 3.9b. The upper layer (red line) exhibits strong decadal variability, while variability in the deeper layer (blue line) acts mostly on multi-decadal scales with an acceleration starting halfway into the nineties. Due to the limited availability of observations below 2000m, we do not include the effects

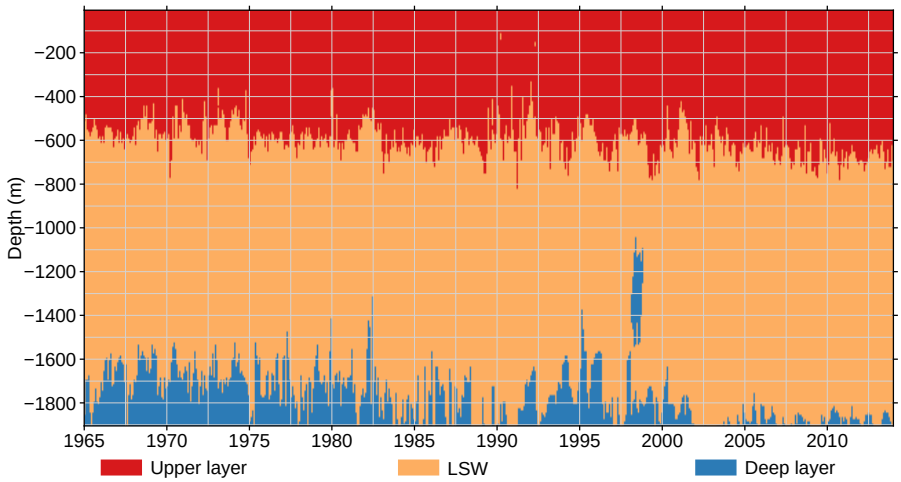

Figure 3.10: Vertical distribution of different water masses, as observed in the southern Subpolar Gyre. The observations have been averaged over the region bounded by the green line in Figure 8a. The individual water masses are classified following a potential density anomaly criterion: $\sigma_\theta < 27.68$ kg/m^3 for the upper layer, $\sigma_\theta = [27.68\ 27.80]$ kg/m^3 for LSW, and $\sigma_\theta > 27.80$kg/m^3 for deep water.

of changes in deep water density on coastal sea level. The steric signal integrated over both layers (green line) contains a strong increase in steric height since the nineties.

In this section, we have shown that a strong correlation exists between steric variability on decadal scales along the northwestern Atlantic coast and in the Subpolar Gyre. Multiple model studies pointed at a very similar correlation pattern, which is related to the southward propagation of density anomalies in the Labrador Sea. We use the density changes in the southern Subpolar Gyre as a proxy for the impact of this high-latitude variability on the trend and decadal variability of coastal dynamic sea level. Therefore, we use the steric signal in the upper 2000m in the southern Subpolar Gyre (denoted with the green line in Figure 3.9b) as a proxy for dynamic sea-level response along the northwestern Atlantic coast to this variability.

3.6 Regional vertical land motion and sea-level budgets

In the previous sections, we have obtained estimates of the impact of GIA, present-day mass transport and high-latitude steric variability on coastal sea-level changes. In this section, we compare the sum of all contributors with the observed sea level and vertical land motion, and verify whether the regional sea-level budget can be closed between 1965-2014. To avoid the bias due to non-linear solid earth deformation resulting from present-day mass redistribution, we split the observed VLM trend $\frac{d\bar{z}}{dt}$

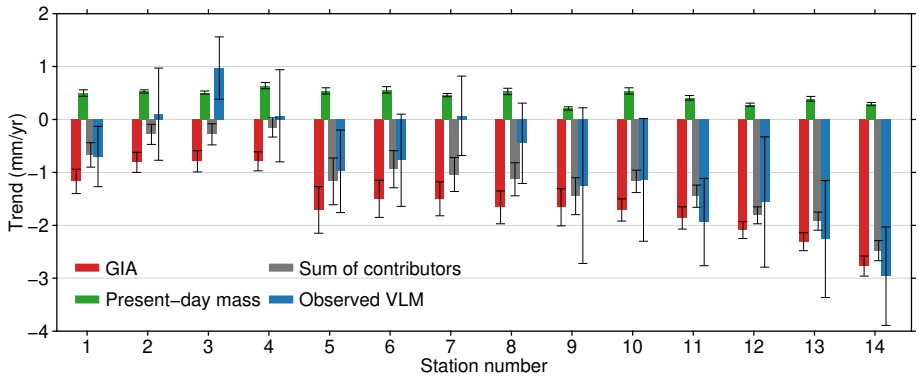

Figure 3.11: Modelled and observed vertical land motion at each tide gauge, together with the uncertainty estimate at the 1 σ level. The trends of solid-earth deformation resulting from present-day mass redistribution are computed over the time span of the individual GPS record. The sum of contributors consists of the effects of solid earth deformation due to GIA and present-day mass redistribution. The stations are numbered according to Table 3.1.

into two known contributors and a residual trend:

$$\frac{d\overline{z}}{dt} = \frac{d\overline{R}_{\mathrm{GIA}}}{dt} + \frac{d\overline{R}_{\mathrm{PD}}}{dt} + \frac{d\overline{z}_r}{dt}. \tag{3.3}$$

$\frac{d\overline{R}_{\mathrm{GIA}}}{dt}$ is the modelled linear VLM trend resulting from GIA; $\frac{d\overline{R}_{\mathrm{PD}}}{dt}$ is the linear trend in solid earth deformation resulting from present-day mass redistribution over the period covered by the GPS observation at each station; $\frac{d\overline{z}_r}{dt}$ is the residual vertical land motion that cannot be explained by the other terms. We make the assumption that the residual VLM term stays constant over the complete time span, and the residual VLM term appears as a linear trend in the relative sea-level budget. The VLM budget for each GPS station is shown in Figure 3.11. For most stations, the largest fraction of the observed VLM trend can be explained by GIA, which varies considerably over the region. Present-day mass effects cause an uplift rate at the order of 0.5 mm/yr. The inter-station differences in the contribution of present-day mass effects are largely caused by different lengths of the GPS records and only to a small extent by spatial variability of the solid earth deformation. For twelve out of fourteen stations, the combination of GIA and present-day mass effects explain the observed VLM trend within 1 σ confidence intervals. For two stations (3 and 7), a significant difference between the modelled and observed VLM remains.

Now we have removed the impact of GIA and present-day mass redistribution on vertical land motion, we can use the modelled relative sea-level change from Equation 3.2 in our budget. When we combine all terms, our sea-level budget equation reads:

$$\eta_{\mathrm{Sum}}(t) = \eta_{\mathrm{GIA}}(t) + \eta_{\mathrm{PD}}(t) + \eta_{\mathrm{Dyn}}(t) - \overline{z}_r(t). \tag{3.4}$$

Here, $\eta_{\mathrm{Sum}}(t)$ is the sum of the modelled contributors; $\eta_{\mathrm{GIA}}(t)$, $\eta_{\mathrm{PD}}(t)$, and $\eta_{\mathrm{Dyn}}(t)$ are the contributions of GIA, present-day mass transport and ocean dynamics. The

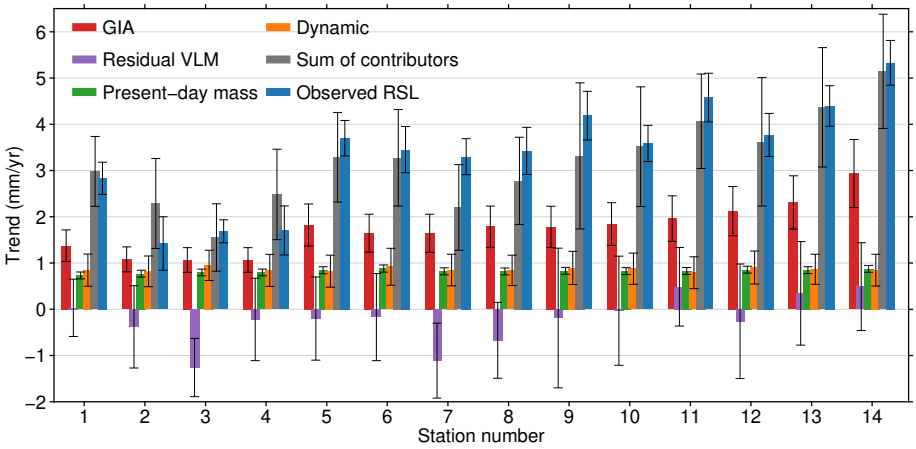

Figure 3.12: Observed and modelled trends (1965-2014) in sea level for all individual stations, together with the accompanying uncertainty estimates. The residual VLM term is inverted to show its contribution to the sea-level budget.

ocean dynamic contribution is approximated by the open-ocean steric signal from the Northwest Atlantic, as discussed in Section 3.5, and displayed in Figure 3.9b. For the ocean dynamics, similar to the observed sea level, we assume that the temporal autocorrelation of the noise follows a Generalized Gauss-Markov distribution. We use this budget equation to compute trends in all contributors and compare their sum with the observed trend in sea level. The budget for each individual station is depicted in Figure 3.12. It is shown that for each individual tide-gauge station, the observed sea-level trend can be explained by the sum of contributors within the overlapping 1 σ confidence intervals. Again, GIA is the dominant term, especially for the southwestern stations. The role of present-day mass and ocean dynamics are both similar in size. Note that for each stations, the same proxy for ocean dynamics is used. Also for present-day mass effects, the inter-station spread is small. The residual VLM term is generally smaller than the other terms, but for some stations, its size is considerable.

To obtain a region-mean budget, we average the observed and modelled time series of the individual stations. To obtain estimates for the station-mean uncertainties, we use the average uncertainty of all individual contributors, since these processes have a common origin. For the uncertainty in vertical land motion, we assume that the errors of the individual stations are independent, and the individual VLM uncertainty estimates are averaged in quadrature. The uncertainty of the observed station-mean sea level is computed under the assumption of a generalized Gauss-Markov (GGM) noise structure, with the uncertainty that originates from the regression model, as discussed in section 3.2, added in quadrature. The resulting region-mean trends and accelerations are listed in Table 3.2. As expected, GIA dominates the station-mean linear trend. The nodal cycle only plays a very small role, while the residual VLM term is not statistically not different from zero at the 1 σ

Table 3.2: Linear trends and accelerations for individual contributors, the sum of contributors and observed relative sea level over 1965-2014. The uncertainties are on the 1σ level. The bold contributors are summed to obtain the total contribution.

	Linear trend (mm/yr)	Acceleration (mm/yr^2)
Glaciers	0.41 ± 0.02	0.009 ± 0.001
Greenland	0.04 ± 0.01	0.003 ± 0.001
Antarctica	0.12 ± 0.03	0.015 ± 0.002
Dam retention	-0.14 ± 0.02	0.003 ± 0.001
Natural+depletion	0.40 ± 0.06	0.010 ± 0.003
Present-day mass	0.83 ± 0.07	0.040 ± 0.003
Ocean dynamics	0.88 ± 0.25	0.136 ± 0.038
GIA	1.75 ± 0.44	-
-Residual VLM	-0.22 ± 0.26	-
Nodal cycle	-0.02 ± 0.00	-
Sum of contributors	3.22 ± 0.57	0.176 ± 0.038
Observed RSL	3.35 ± 0.38	0.126 ± 0.046

level. As for each individual station, the sum of contributors explains the observed station-mean trend well within the confidence intervals.

Under the assumption that the noise in the observations follows a generalized Gauss-Markov (GGM) distribution, the observed sea level shows a significant upward acceleration of 0.126 ± 0.046 mm/yr^2 over our period of interest. The acceleration in present-day mass redistribution is positive, but too small to explain the acceleration in observed sea level. The acceleration of the ocean dynamics term is larger than the mass redistribution term, and when both terms are added, the acceleration in observed sea level can be explained within 1 σ confidence intervals. Hence, the observed large acceleration in regional sea level can be linked to the ocean dynamics signal.

To study the origin of the observed decadal sea-level variability, the observed station-mean sea-level time series and the individual contributors are shown in Figure 3.13a. The ocean dynamics term explains almost all observed decadal variability, while the contribution of present-day mass largely consists of an acceleration and does not show substantial decadal variability. GIA and residual VLM are assumed to be linear, and hence, only explain a part of the observed trend. When we compare the time series of observed sea level to the sum the individual contributors (Figure 3.13b), we see that both the long-term trend as well as the majority of observed decadal variability are explained by the sum of contributors: the correlation between the de-trended observation and sum of contributors is 0.86, with a coefficient of determination (R^2) of 0.68. The residual is depicted in Figure 3.13c. The bound of the confidence interval, which is computed by summing the confidence intervals of the individual terms in quadrature, does not significantly deviate from zero, except for one distinctive event around 1997, where the peak in coastal sea level is not captured by the steric height observations. We have verified the altimetry observations, which do show a similar peak around 1997 in the Subpolar Gyre. Furthermore, the profiles show an unstable stratification in 1997 (See figure 3.10), which suggests that the mismatch may be related to issues with the hydrographic profiles.

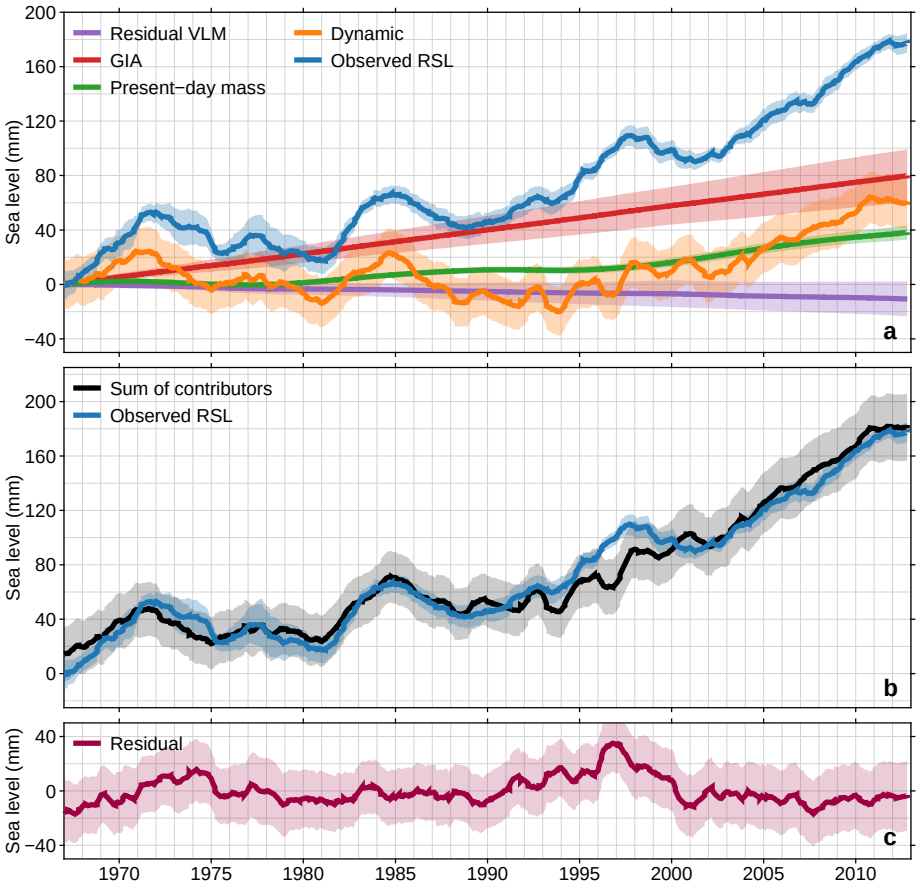

Figure 3.13: Region-mean sea-level budget. a: Individual contributing processes and observed sea level. b: Sum of all contributing processes. c: Observations minus sum of contributors. Shaded areas denote the confidence interval of all processes at the one sigma level. All time series have been low-pass filtered with a 49-month running mean.

These results show that a large fraction of the observed sea-level acceleration and decadal sea-level variability are also found in the proxy for high-latitude steric variability, while the trend is mainly determined by the combined effect of GIA, present-day mass redistribution and the contribution of high-latitude steric variability. The sum of contributors explains the observed trend and accelerations well within 1 σ confidence intervals, as well as a large fraction of the decadal sea-level variability.

3.7 Discussion and conclusions

We have studied the individual contributors to the observed sea-level trend and decadal sea-level variability along the Northwest Atlantic coast over 1965-2014. The effects of GIA, present-day mass redistribution, and the dynamic signal driven by

high-latitude steric variability have been compared to observations of sea level and vertical land motion. For this comparison, we have used a self-consistent framework that takes the difference in observation lengths of GPS and tide gauge records into account. This framework consists of two separate budgets: one for vertical land motion and one for sea level. The vertical land motion that results from present-day mass redistribution (i.e. ice melt, dam retention, and groundwater depletion) is not linear over the full time span of this study. Therefore, a linear trend, estimated over the lengths of the GPS observation is not fully representative for the local long term vertical land motion. To overcome this problem, we separate the observed VLM into a part explained by GIA and present-day mass redistribution, and an unexplained part. Only the GIA contribution and the unexplained part of the observed VLM are assumed to be linear over the studied period.

GIA causes a complex spatial pattern of land subsidence and sea-level rise in the region: the coast is affected by both uplift from the Laurentide Ice Sheet and by subsidence due to its forebulge collapse. An updated data-driven GIA model is used to explain the tide gauge and GPS observations. With this model, we can explain the observed trends in sea level and vertical land motion to a high extent, as well as the inter-station variability of sea-level and VLM trends.

To assess the impact of present-day mass redistribution on regional sea level and land level, we solve the elastic sea-level equation for each mass redistribution process. The effect of ice melt from glaciers and ice sheets, dam retention, and terrestrial water storage changes due to natural variability and groundwater depletion have been taken into account. The combined mass contribution causes a positive trend and acceleration in both sea level and land motion over our period of interest. The inter-station variability in the contribution of present-day mass transport is small.

Model results, altimetry and hydrographic observations show a strong correlation between steric height in the southern Subpolar Gyre and sea level on the Northwestern Atlantic coast north of Cape Hatteras. This signal is consistent with the southward propagation of density anomalies from the Subpolar Gyre along the Northwestern Atlantic coast. The resulting signal causes a positive sea-level trend, explains the large acceleration in observed sea level, and dominates the observed decadal variability along the coast.

Since the Gulf Stream affects coastal sea-level variability south of Cape Hatteras (McCarthy et al., 2015), this correlation cannot be observed further south. The observed acceleration in dynamic sea level agrees well with a strong decrease of the water density in the Labrador Sea (Robson et al., 2014).

The combination of all these effects allows us to explain the observed station-mean sea-level trend, acceleration, and decadal variability well within 1 σ confidence intervals. Observed linear trends at individual tide gauge stations can be explained by the sum of contributors at all stations within the confidence intervals. For 12 out of 14 GPS stations, we can also explain the observed vertical land motion. GIA explains the vast majority of the observed VLM behaviour, which causes large inter-station differences.

The acceleration in observed sea level in this region is strong, which has already been noted in other studies (e.g. Sallenger et al., 2012; Ezer and Corlett, 2012). This

strong acceleration is also found in the southern Subpolar Gyre steric observations. However, our 50-year record is too short to separate a secular acceleration from multi-decadal variability. It is known that multi-decadal variability has a large effect on acceleration estimates from tide gauge records (e.g. Dangendorf et al., 2014b; Haigh et al., 2014). In our region, Kopp (2013) argues that the observed acceleration does not yet exceed the likely range of multi-decadal variability. Hence, the acceleration that we observe in this study may not be representative for longer periods.

Some of the questions that are not yet fully answered in this study are the physical mechanisms behind the high-latitude steric variability and whether other dynamical processes affect decadal sea-level variability, trends and acceleration in the southern Subpolar Gyre and along the coast. Since changes in the density of the Labrador Sea are linked to both changes in the strength of the AMOC and the Deep Western Boundary Current (Hodson and Sutton, 2012; Roberts et al., 2013), understanding how these mechanisms are linked to coastal sea-level changes may help gaining insight into the impact of AMOC changes and other ocean dynamic processes on coastal sea level. Furthermore, separating the impact of the AMOC from other processes on sea level in this region may aid in improving coastal sea-level projections, which heavily depend on the coupling between expected decline of AMOC strength and higher sea level along the US Atlantic coast.

Chapter 4

A consistent sea-level reconstruction and its budget on basin and global scales over 1958-2014

> De Winter is typisch onderdeel van een generatie van die Trump-achtige oude mannen die vrolijk doortuffen in hun vieze autootjes. Ze hebben zichzelf ontslagen van elke verantwoordelijkheid voor een leefbare planeet voor de volgende generatie, want ze hebben op de achterkant van een envelopje uitgerekend dat de mens niets met klimaatverandering te maken heeft. Of ze hebben zichzelf wijsgemaakt dat verandering toch geen zin heeft zolang mensen kinderen krijgen. Nieuwe klootzakkerigheid. Een ravage aanrichten en het keihard ontkennen. Straks zijn ze dood en zitten wij met de ellende.
>
> Rosanne Hertzberger

4.1 Summary

Different sea-level reconstructions show a spread in sea-level rise over the last six decades and it is not yet known whether the sum of contributors explains the observed rise of the reconstructions. Possible causes for this spread are, amongst others, vertical land motion at tide-gauge locations and the sparse sampling of the spatially-variable ocean. To assess these open questions, reconstructed sea level and the contributors are investigated on a local, basin, and global scale. High-latitude seas are excluded. Tide-gauge records are combined with observations of vertical land motion, independent estimates of ice-mass loss, terrestrial water storage, and barotropic atmospheric forcing in a self-consistent framework to reconstruct sea-level changes on basin and global scales, which are compared to the estimated sum of contributing processes. For the first time, it is shown that for most basins, the reconstructed sea-level trend and acceleration can be explained by the sum of contributors, as

Parts of this chapter have been been published as: Frederikse, T., Jevrejeva, S., Riva, R. E. M., and Dangendorf, S.: A consistent sea-level reconstruction and its budget on basin and global scales over 1958-2014, Journal of Climate, doi:10.1175/JCLI-D-17-0502.1, 2017.

well as a large part of the decadal variability. The sparsely-sampled South Atlantic Ocean forms an exception. The global-mean sea-level reconstruction shows a trend of 1.5 ± 0.2 mm/yr over 1958-2014 (1σ), compared to 1.3 ± 0.1 mm/yr for the sum of contributors. Over the same period, the reconstruction shows a positive acceleration of 0.07 ± 0.02 mm/yr^2, which is also in agreement with the sum of contributors, which shows an acceleration of 0.07 ± 0.01 mm/yr^2. Since 1993, both reconstructed sea level and the sum of contributors show good agreement with altimetry estimates.

4.2 Introduction

Global sea-level reconstructions before the satellite altimetry era mostly depend on tide-gauge records, which are sparsely sampled over the globe, contain data gaps, and are affected by vertical land motion (VLM). These problems pose a challenge for reconstructions of global and regional sea-level rise. A wide variety of methods has been used to reconstruct global sea-level changes from individual tide-gauge records. These methodological differences, together with the in- or exclusion of specific tide-gauge stations, result in a large spread in published sea-level rise estimates. As an example, the mean estimates of sea-level rise from 1900 to 1990 vary between 1.1 and 2.0 mm/yr (Church and White, 2011; Jevrejeva et al., 2014; Hay et al., 2015; Dangendorf et al., 2017). This large spread in reconstructed sea-level trends hinders the attribution of observed sea-level changes to the individual processes. Over the twentieth century, Gregory et al. (2013) and Slangen et al. (2016) find that the sum of contributors, based on climate model results, is lower than the observed rise in global mean sea level. The latter study denotes that the largest difference occurs during 1940-1970. Consequently, most estimates (both modelled and observed) of the contributors over the second half of the twentieth century fail to explain the observational record (Moore et al., 2011). Only after 1971 and during the altimetry era, the sea-level budget can be reasonably closed (Church et al., 2011; Chambers et al., 2016). It is not yet known whether this budget gap before the seventies is present in all ocean regions, or that it is only present in some areas. To our knowledge, the only study before the satellite era that discusses this problem is Slangen et al. (2014b), who also find a budget gap on a global scale, but cannot find specific regions to which this gap can be linked.

Recently, two new global sea-level reconstructions point at substantially lower sea-level changes before 1990 (Hay et al., 2015; Dangendorf et al., 2017). In these reconstructions, known information about the spatial patterns of VLM and sea-level rise, and in the latter study, direct VLM observations have been explicitly taken into account. The tide-gauge selection criteria have a profound impact on the resulting sea-level curve (Hamlington and Thompson, 2015). However, the addition of prior knowledge of these spatial patterns result in a sea-level curve that is more robust to the tide-gauge selection criteria (Hay et al., 2017; Dangendorf et al., 2017).

Whether these new sea-level curves are in agreement with the observations of the contributors is an open question, and it is not yet clear whether this addition of knowledge about local VLM and spatial patterns affects the sea-level budget on a

regional scale.

To answer these questions, a new reconstruction technique is proposed that takes the spatial sea-level variability associated with glacial isostatic adjustment (GIA) and present-day mass redistribution into account, as well as local VLM at the tide-gauge location. Based on the results of Thompson and Merrifield (2014), we have divided the global ocean in six regions, which share a common signal of decadal sea-level variability. We reconstruct sea level in each basin, as well as for the global ocean, and compare the reconstructions to the sum of contributors. This comparison on a basin scale also enables us to directly identify particularly critical regions.

Nowadays, robust estimates of local VLM at tide gauges are available from continuous GPS receivers and from the difference between satellite altimetry and tide-gauge observations (Wöppelmann and Marcos, 2016). These estimates have generated a more homogeneous picture of regional sea-level estimates (Wöppelmann et al., 2009). While traditionally only the GIA component of VLM was removed in global sea-level reconstructions, recent studies point towards a bias in GMSL when the VLM signal is not taken into account (Hamlington et al., 2016; Dangendorf et al., 2017). However, estimates of VLM are usually based on GPS time series of much shorter duration than the tide-gauge records in use, leading to the formerly necessary assumption that they can be linearly extrapolated back in time. This assumption holds for long-term contributions, such as GIA, but certainly fails for most processes related to present-day mass transport. For instance, present-day ice-mass loss as well as terrestrial fresh water sources are highly nonlinear and partly contain accelerating components, which affect relative sea level, but also the height of the solid earth surface (Tamisiea, 2011; Riva et al., 2017). To circumvent this resulting bias, we use the modelling framework from Frederikse et al. (2016, 2017), in which the observed VLM is separated into a part explained by present-day mass redistribution and GIA, constrained by forward models, and an unexplained part, constrained by direct VLM observations.

This chapter is structured as follows: the tide-gauge selection and VLM observations are discussed in section 4.3. In section 4.4, we discuss the modelled and observed individual contributors to local, regional, and global sea-level changes. The local sea-level and VLM observations are compared to the sum of contributors in section 4.5. The reconstruction of basin-mean and global sea level and the comparison with the sum of contributors are discussed in section 4.6, followed by the discussion and conclusions.

4.3 Tide-gauge data and vertical land motion estimates

Monthly-mean tide-gauge observations have been obtained from the Permanent Service for Mean Sea Level (PSMSL, Holgate et al., 2013). VLM observations are either computed from nearby permanent GPS stations or from the difference between tide-gauge and altimetry observations. A list of collocated GPS and tide-gauge locations has been obtained from SONEL (`www.sonel.org`). GPS observations of VLM have been obtained from Nevada Geodetic Laboratory, for which trends and the accom-

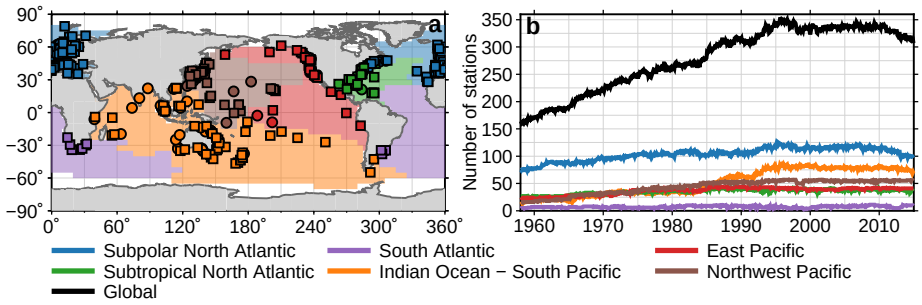

Figure 4.1: Stations and ocean basins used in this study. a. Location of each tide-gauge station and the definition of each ocean basin. The color of the dots depict the region to which each tide gauge is tied to. Square dots denote tide gauges for which VLM is determined from GPS observations, while circles denote stations for which altimetry minus tide-gauge data is used to determine VLM. b. Number of stations per basin that have data in each month.

panying uncertainties have been estimated using the MIDAS method (Blewitt et al., 2016). VLM estimates based on altimetry minus tide-gauge observations are the same as in Wöppelmann and Marcos (2016). We have selected stations for which at least 240 monthly-mean sea-level observations are available, for which the 1σ confidence interval of the VLM trend is smaller than 2 mm/yr and for which the difference between the observed trend and the sum of individual processes, defined in equation 4.3 is smaller than 3 mm/yr. Furthermore, we have excluded the station 'Ilha Fiscal' along the western boundary of the South Atlantic oceans, since this station shows a very strong multi-decadal variability pattern which is unlikely to be related to large-scale patterns. This station has also been ignored in the reconstructions of Church and White (2011) and Dangendorf et al. (2017). With these selection criteria, we obtain 396 tide-gauge stations. For station locations for which multiple GPS observations are available, the total trend is computed as the mean over all local GPS stations, weighted by the inverse of the variance of each individual trend.

For estimates of basin-mean sea level, we distinguish six ocean basins, based on the regions defined in Thompson and Merrifield (2014), who found a coherent decadal sea-level variability signal in each region. Each tide-gauge station is linked to a specific basin. Figure 4.1a shows the locations of the selected tide-gauge stations, the method to estimate VLM, as well as the ocean basins to which each station is linked. The figure shows that the ocean basins in northern hemisphere have a comparably high data coverage, while the South Atlantic basin is only sparsely covered: the African and South-American coast only have a few records, and no long-term records from open-ocean islands are available in this basin. The availability of station data per month is depicted in figure 4.1b. For all basins, except for the South Atlantic region, for which only a few tide-gauge observations are available, observations come from at least 10 stations during any time of the analysis. The ocean basins do not cover parts of the Arctic and Southern Ocean. These uncovered areas, which are shown in white in figure 4.1a, form 7 percent of the global oceans. In this study, we do not include these areas, and where we use the word 'Global', we mean the total

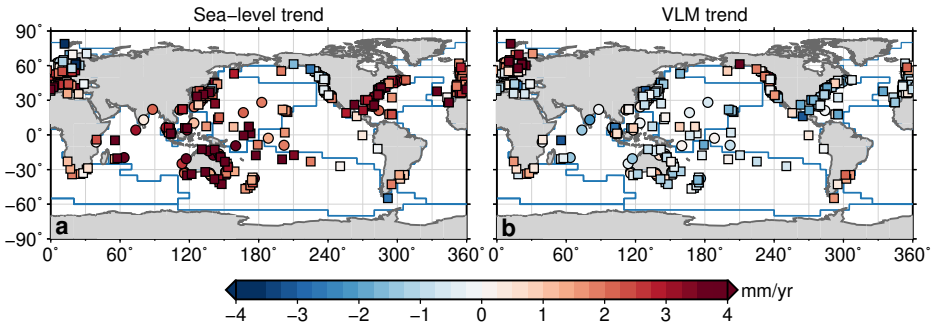

Figure 4.2: Linear trends at individual tide-gauge locations. a: trend in relative sea level over available data within 1958 - 2014. The local barotropic effects of wind and pressure were removed using the regression model before computing the trend. b: Linear trends in VLM. The blue line depict the boundaries of the ocean basins. Note that due to the availability of observations, the period over which the trends are computed differs between stations.

area covered by the six aforementioned ocean basins, excluding the white parts in figure 4.1a.

Local barotropic effects due to wind and sea-level pressure changes can have a profound impact on local sea-level variability, even on longer time scales (e.g. Dangendorf et al., 2013; Piecuch et al., 2016). Since these signals are generally not basin-wide in origin, we estimate and remove this signal by using a simple linear regression model, similar to Frederikse et al. (2016) and Frederikse et al. (2017). The regression model contains an annual cycle, semi-annual cycle, wind stress in the zonal and meridional direction, and the local deviation from the ocean-mean sea-level pressure. Pressure and wind fields are obtained from the 20th Century Reanalysis Project (Compo et al., 2011), and for each tide-gauge station, the model grid point with the highest correlation with local sea level within a radius of 250 kilometer is used. The signals related to wind and pressure are only removed if the regression coefficient is significantly different from zero at the 2σ level, which is tested using t-test statistics.

After removing local barotropic effects, we compute linear trends in sea level and VLM at each tide-gauge location. These trends are displayed in Figure 4.2. At most stations, the sea-level trend is positive, with some regions having a common signal: the trends along the US East Coast and around Australia appear to be high, while at the US west coast, the trends appear to be almost zero. The VLM trends are generally smaller, and have less profound regional signals, except for the positive VLM trends at the Western US coast, that may partially explain the low trends in that region, and the uplift around Northern Europe, which is to a large extent caused by GIA (Hill et al., 2010).

We use satellite altimetry to compare our tide-gauge reconstruction with independent observations. Gridded monthly-mean observations have been obtained from the ESA CCI sea-level product version 2.0 (Ablain et al., 2015). The gridded estimates are averaged over each ocean basin to obtain basin-mean estimates.

4.4 Contributors to sea-level and land-level changes

Sea-level and land-level changes are caused by a multitude of processes, which all have their own temporal and spatial characteristics. In this section, we discuss the used estimates of the various processes affecting sea-level changes.

Past and present-day mass exchange between land and ocean not only leads to changes in the global ocean volume: due to changes in the earth rotation, gravity field and deformation of the solid earth, local and regional sea-level change can differ from the global-mean barystatic response. The combination of gravitational and earth-deformation effects causes a distinct regional sea-level response pattern to mass exchange between land and ocean (Clark and Lingle, 1977; Mitrovica et al., 2001; Bamber and Riva, 2010). The local sea-level response to mass redistribution can be separated in three individual components:

$$\eta(\theta,\phi,t) = G(\theta,\phi,t) - R(\theta,\phi,t) + \mathscr{L}(t). \tag{4.1}$$

$\eta(\theta,\phi,t)$ is the resulting local relative sea-level anomaly from the mass change, $G(\theta,\phi,t)$ is the deformation of the geoid, $R(\theta,\phi,t)$ the solid earth deformation, and $\mathscr{L}(t)$ is a global-mean term, which is required to ensure global mass conservation. The term $\eta(\theta,\phi,t)$ expresses local sea-level changes relative to the solid earth, which implies that deformation of the solid earth will be part of local relative sea-level changes. We solve equation 4.1 for present-day mass exchange using the elastic sea-level equation (Tamisiea et al., 2010), with the method described by Sabadini et al. (2016) to compute the earth rotational feedback.

For GIA, we use output from the global ICE6G_VM5a model (Peltier et al., 2015), which provides estimates of both changes in the geoid, solid earth and relative sea level due to GIA.

For present-day mass redistribution, we include the effects of glacier and ice sheet mass loss, dam retention and groundwater depletion, for which the same estimates as in Frederikse et al. (2017) are used. We will discuss these estimates briefly. Glacier mass loss is based on data from Marzeion et al. (2015), which provides mass balance evolution estimates for the 18 major glacier-covered regions. For the Greenland Ice Sheet, we use the total mass balance estimates and the accompanying uncertainties of Kjeldsen et al. (2015) between 1958 and 1992. Between 1992 and 2014, the mass balance is based on RACMO2.3 for the surface mass balance (SMB), while ice discharge is modelled using a constant acceleration of 6.6 Gt/yr^2, following van den Broeke et al. (2016). The Antarctic contribution is less certain, especially before the nineties, due to the sparse observations during the pre-satellite era. However, from earth rotation observations it can be inferred that the Antarctic contribution before the nineties has been below 0.2 mm/yr (Mitrovica et al., 2015). Therefore, we assume no mass change before 1979. Between 1979 and 1993, we adopt a long-term balance between the Antarctic Ice Sheet SMB, based on RACMO2.3 (van Wessem et al., 2014) and ice discharge between 1979 and 1993. After 1993, we impose an 2.0 Gt/yr^2 acceleration of the ice discharge, which gives a reasonable fit to both the results of the IMBIE intercomparison case (Shepherd et al., 2012) and GRACE

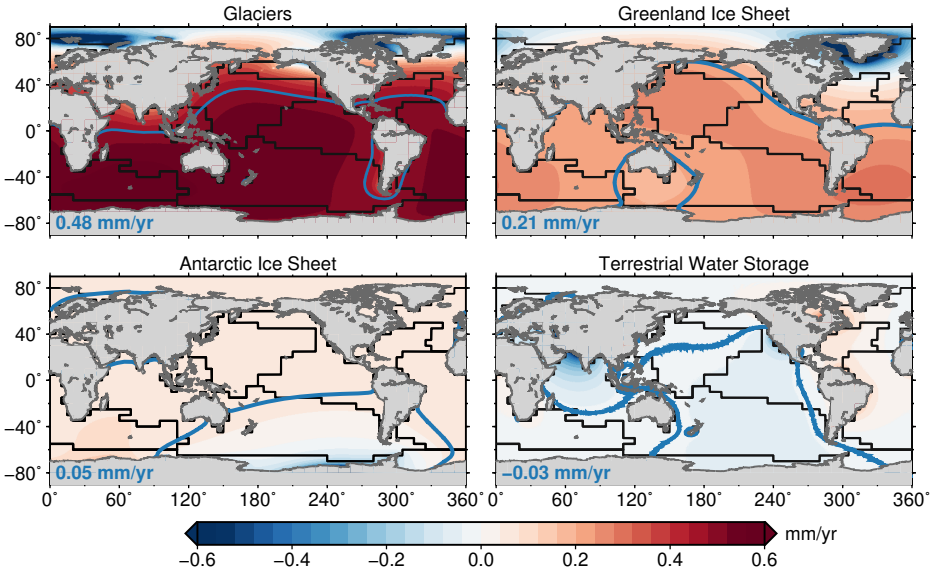

Figure 4.3: Trends in local relative sea level resulting from the individual present-day mass-redistribution processes over 1958-2014. The number in the lower left corner denotes the barystatic trend. The blue lines depict the contour where the local trend equals the barystatic trend. Orange lines depict the boundaries of the individual ocean basins.

observations of ice-mass loss over more recent years (e.g. Watkins et al., 2015). Terrestrial Water Storage (TWS) changes are based on the effects of groundwater depletion and dam retention. Groundwater depletion is based on PCR-GLOBWB model outcomes (Wada et al., 2014), multiplied by a correction factor of 0.8 to account for depleted groundwater that does not reach the ocean (Wada et al., 2016). Note that we only compute the large-scale solid-earth response to groundwater depletion, and local groundwater depletion results in uplift due to a decrease of the load. Local subsidence due to sediment compaction after groundwater withdrawal is thus not modelled by the TWS term. On local scales, this effect can be substantial (Chaussard et al., 2013; Minderhoud et al., 2017). Dam retention estimates are based on the GRanD Global Reservoir and Dam database (Lehner et al., 2011), which provides the location, storage capacity and year of construction. Filling and seepage rates are estimated following the method of Chao et al. (2008). See Chapter 2 for a full description of the derivation of the present-day mass effects and the accompanying uncertainties. Figure 4.3 shows the resulting linear relative sea-level trends of all aforementioned present-day mass processes. An overview of the time series from the individual contributors to the present-day mass redistribution term in each basin is shown in Figure 4.4.

Satellite altimetry does not detect solid earth deformation, since it observes sea level in a geocentric reference frame. Therefore, to compare altimetry to tide-gauge observations, we have to account for the deformation of the solid earth and put the observations in a relative reference frame. To do so, we subtract the modelled solid earth deformation due to GIA and present-day mass transport from the observed

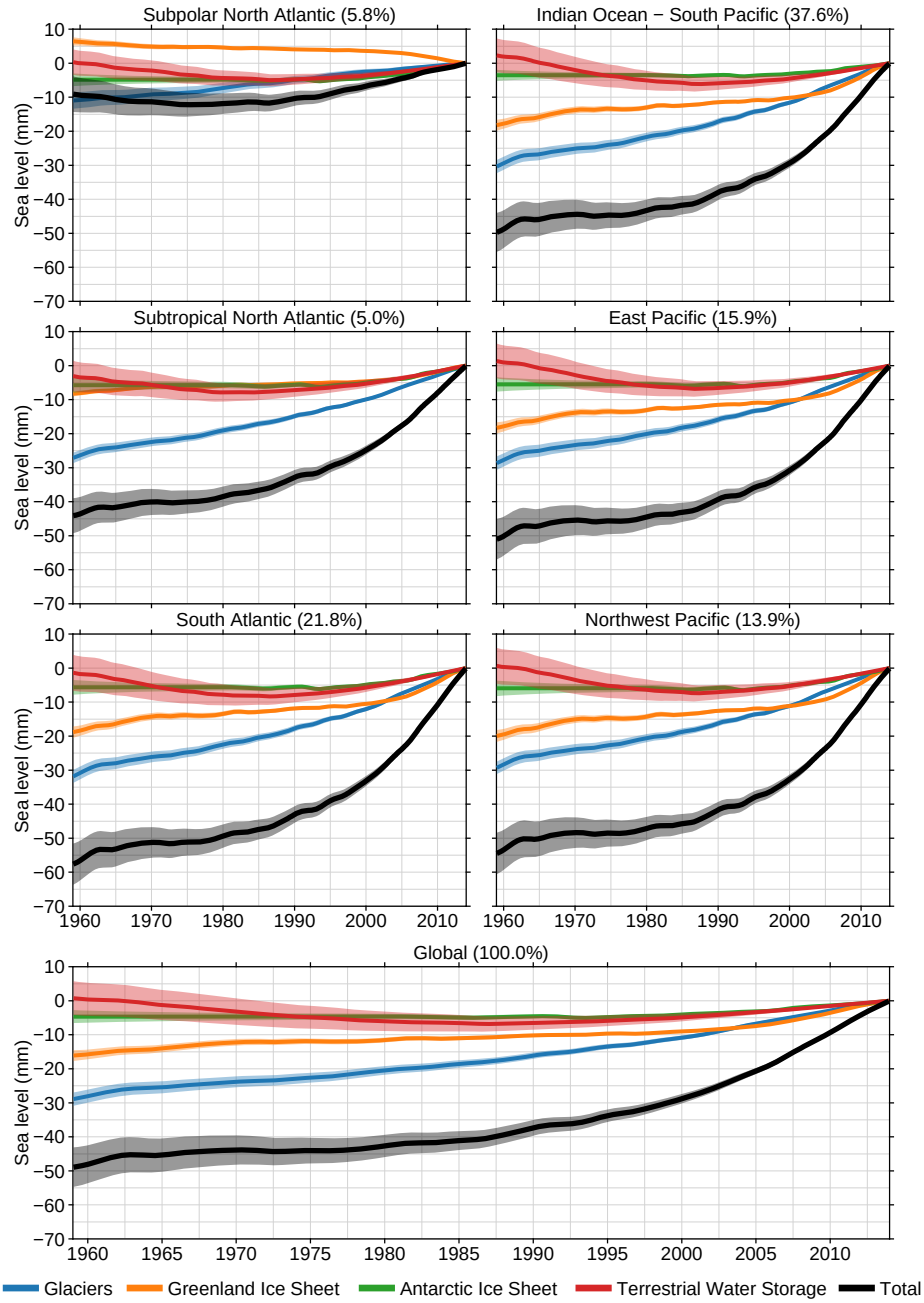

Figure 4.4: Basin-mean and global-mean modelled sea-level changes due to the individual present-day mass redistribution processes and their sum. The shading denotes an estimate of the confidence interval on the 1σ level. The fraction in the plot titles denotes the size of the basin relative to the size of the sum of basins.

altimetry before the gridded altimetry estimates are averaged.

Next to changes in the ocean mass and the ongoing response to GIA, changes in steric height are a major contributor to global sea-level changes. We use gridded estimates of in-situ observations of temperature and salinity to compute the resulting steric height changes. These estimates are obtained from the EN4 version 4.1.1 gridded temperature and salinity dataset (Good et al., 2013). From the gridded estimates of temperature and salinity, density anomalies are computed, which are converted into steric height anomalies, using the seawater properties described in Roquet et al. (2015). The density and steric height anomalies have been computed using the TEOS-10 software (McDougall and Barker, 2011). To obtain an estimate of the accompanying uncertainty, we have computed steric heights from other data sets, and use the spread between the different estimates as a measure of the uncertainty. We have used gridded temperature and salinity datasets from Ishii and Kimoto (2009, IK09), and the temperature-only dataset from Cheng and Zhu (2016, CZ16), as well as the pentadal steric height estimates from Levitus et al. (2012, IK09). We use the upper 2000m of the ocean in all datasets, except for Ishii and Kimoto (2009), which only covers the upper 1500m. The gridded fields are averaged over the individual basins to obtain estimates of basin-mean and global steric changes. The resulting estimates of the steric height anomalies are depicted in Figure 4.5.

The time series of the sea-level effect of GIA, present-day mass redistribution, and the steric contribution, together with an estimate of their uncertainties are depicted in figure 4.6. In general, the steric signal varies substantially from basin to basin, and dominates the variability signal, while the present-day mass redistribution terms are mostly showing changes over longer time scales. In the Subtropical and Subpolar North Atlantic ocean, GIA causes an upward trend, which is nearly absent in other basins and in the global mean. Furthermore, these regions have a smaller contribution from present-day mass redistribution, due to their proximity to the Greenland Ice Sheet and many glacier-covered regions. The below-average contribution of mass-related processes to sea-level changes in the North Atlantic has as a consequence that the accelerating contributions from the Greenland Ice Sheet and many glacier-covered regions to sea level are less observable in this basin. Many of the world's longest tide-gauge records are located in this basin, which could be a major factor in the difficulty to detect an acceleration in global-mean sea level from tide-gauge records. Furthermore, it can be noticed that the spread in estimates of steric changes is substantially larger in the Atlantic basins, compared to all other basins, despite the relatively high coverage of hydrographic profiles in the North Atlantic ocean (e.g. Cheng and Zhu, 2016). A possible cause for this large spread is the important role of deep-ocean variability in the Atlantic Ocean (Williams et al., 2014; Robson et al., 2014), which is less densely sampled than the upper ocean. Another possible cause of the spread is salinity, which shows substantial variability in the North Atlantic Ocean (Mauritzen et al., 2012; Durack et al., 2014), which could expain why the thermosteric anomalies from Cheng and Zhu (2016) deviate substantially from the other estimates in the Subpolar North Atlantic basin, as shown in Figure 4.5.

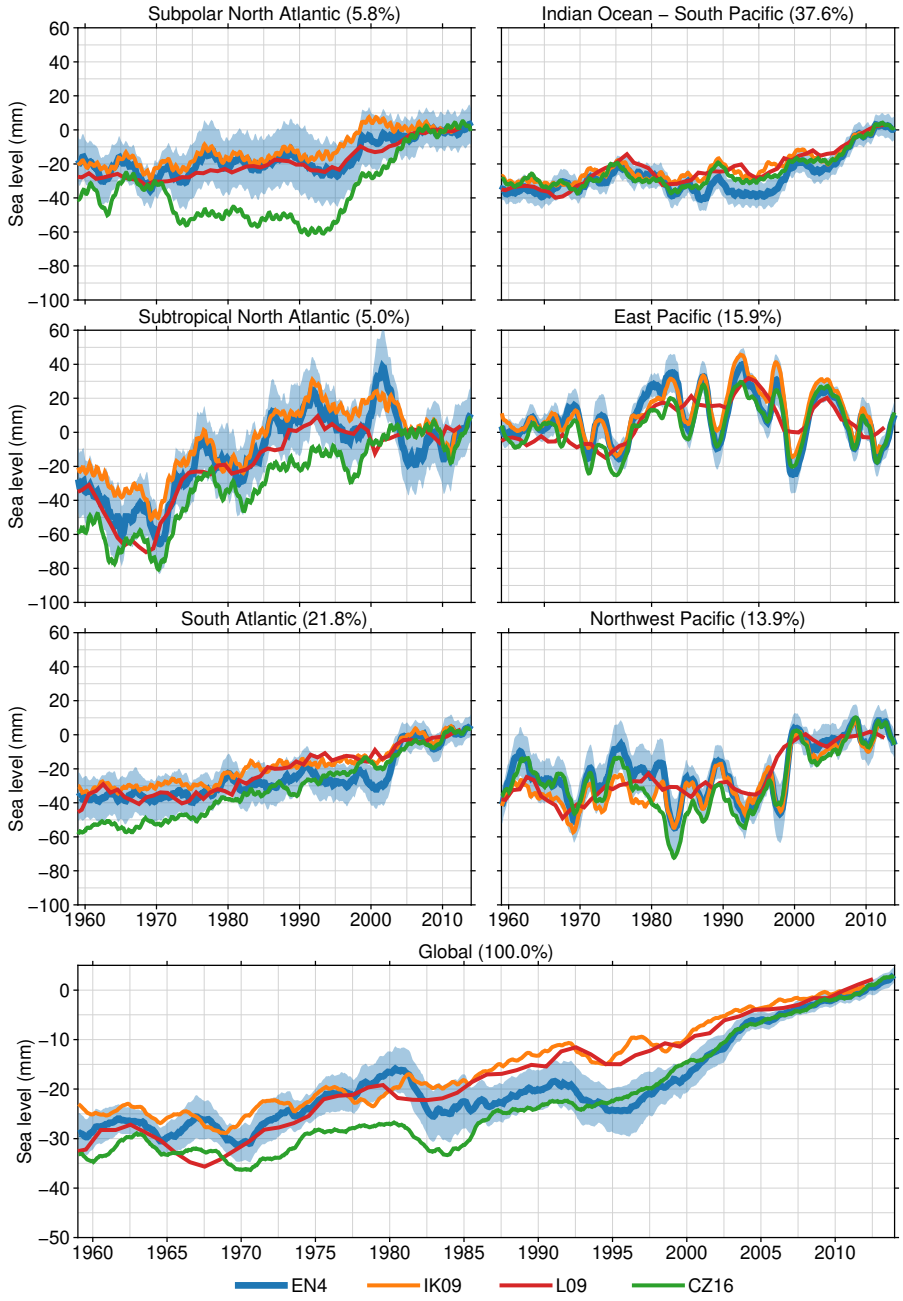

Figure 4.5: Time series of the steric height anomalies computed from different models for each basin. The shaded area is the standard deviation from the models centered around the EN4 estimates. All time series have been low-pass filtered using a 25-month running mean.

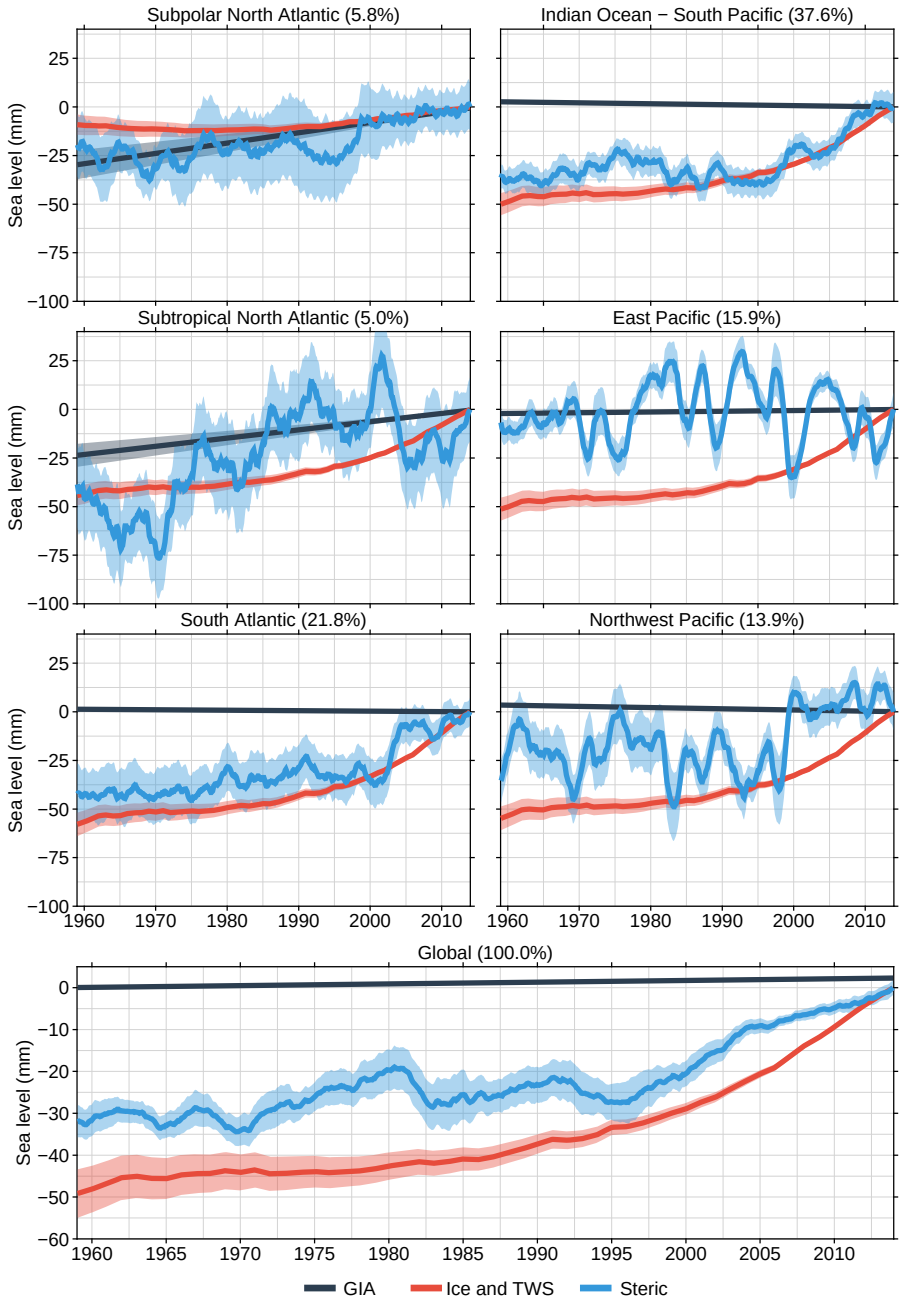

Figure 4.6: Contributors to basin-mean and global sea-level changes. The Mass contributions consists of the sum of the glacier, Greenland Ice Sheet, Antarctic Ice Sheet and Terrestrial Water Storage contribution. The shading denotes an estimate of the confidence interval on the 1σ level. All time series have been low-pass filtered using a 25-month running mean.

4.5 A local sea-level budget

The sea-level change fields that result from combining GIA, present-day mass redistribution and steric height can be sampled at each tide-gauge location. However, since many tide-gauge locations are located on shallow shelves, the steric signal will vanish when the signal is sampled at the coast, and local sea-level variability at most tide-gauge locations is associated with ocean-bottom pressure changes (Landerer et al., 2007a). Furthermore, due to the presence of fine-scale coastal and boundary dynamics, sampling the steric height field in the open ocean close to the tide-gauge location will not provide information about local ocean dynamics, since the observations are averaged over large spatial distances (Bingham and Hughes, 2012; Good et al., 2013). These issues imply that sampling the steric field at or close to the tide-gauge location will not provide a reliable estimate of the impact of ocean dynamics on local sea level. Hence, we use the basin-mean steric estimate as proxy for the local effect of steric changes on tide gauges. This approximation implies that local ocean dynamic effects on sea level are excluded. These local effects often lead to distinct trends, such as the strong acceleration along the Northwestern Atlantic coast (Sallenger et al., 2012). Therefore, local ocean dynamics are a likely candidate to explain the difference between observed sea level and our sum of contributors.

Local relative sea-level changes from GIA and present-day mass exchange are partially caused by solid-earth deformation, as shown in Equation 4.1, which will be recorded as a VLM signal. The contribution of present-day mass exchange is not linear over the study period, and because the VLM trends are not necessarily derived over the same period as the tide-gauge trends, the observed VLM trend may not be representative for the VLM trend over the full tide-gauge record (Riva et al., 2017). To avoid this bias, we use the method of Frederikse et al. (2016) to separate the observed VLM in a part explained by GIA and present-day mass effects and an unexplained part:

$$\frac{d\bar{z}_r}{dt} = \frac{d\bar{z}}{dt} - \frac{d\bar{R}_{\mathrm{GIA}}}{dt} - \frac{d\bar{R}_{\mathrm{PD}}}{dt}. \tag{4.2}$$

$\frac{d\bar{z}_r}{dt}$ is the unexplained part of the VLM trend, $\frac{d\bar{z}}{dt}$ is the observed linear VLM trend, $\frac{d\bar{R}_{\mathrm{GIA}}}{dt}$ is the modelled linear VLM trend resulting from GIA, and $\frac{d\bar{R}_{\mathrm{PD}}}{dt}$ is the linear trend in solid earth deformation resulting from present-day mass redistribution over the period covered by the VLM observation at each station. Since this linear trend is only computed over the time span of the VLM observations, its value differs from the trend over the tide-gauge observation epoch. We assume the unexplained VLM signal $\frac{d\bar{z}_r}{dt}$ to be constant over the whole time span of the tide-gauge observations. With this approach, we account for the non-linear VLM associated with solid-earth deformation resulting from present-day mass redistribution.

The average rate of VLM is −0.08 mm/yr with a standard deviation of 1.49 mm/yr. After removing the known terms, the average residual VLM becomes −0.11 mm/yr with a standard deviation of 1.05 mm/yr. Hence, on average, the tide gauges are not subject to large VLM signals before and after correcting for known processes that cause VLM. Since a substantial part of the tide-gauge stations are located in ar-

eas subject to GIA-related uplift, the distribution of the VLM trends may be skewed: if we compare the median trends, we do find a reduction from −0.28 mm/yr for the median VLM trend to −0.13 mm/yr for the median residual VLM trend. However, the standard deviation of uncorrected and residual VLM is still substantial. Histograms of the uncorrected and residual rates of VLM per basin are shown in Figure 4.7.

We use the estimate of VLM that is unrelated to both GIA and present-day mass transport only to correct for unknown local VLM. Hence, we can use the relative sea-level changes $\eta(\theta, \phi, t)$ resulting from GIA and present-day mass transport to compute the local sum of contributors. We define the local sum of contributors as follows:

$$\eta_{\text{Sum}}(t) = \eta_{\text{GIA}}(t) + \eta_{\text{PD}}(t) + \eta_{\text{Steric}}(t) - \overline{z}_r(t). \tag{4.3}$$

$\eta_{\text{Sum}}(t)$ is the sum of contributors; $\eta_{\text{GIA}}(t)$ and $\eta_{\text{PD}}(t)$ are the contributions of GIA and present-day mass redistribution; $\eta_{\text{Steric}}(t)$ is the steric height contribution, averaged over the basin to which the tide gauge is tied. The resulting sum of contributors per station is depicted in figure 4.8a. The sum of contributors shows considerable spatial variability with some distinct regional features: High rates are found around Australia, the Northwest Atlantic, while low rates can be found along the East Coast of the Pacific and Fennoscandia. The residual tide-gauge signal (η_{Residual}) can now be expressed as the difference between observed sea level (η_{Obs}) and the sum of contributors:

$$\eta_{\text{Residual}}(t) = \eta_{\text{Obs}}(t) - \eta_{\text{Sum}}(t). \tag{4.4}$$

The linear trend in the residual tide gauge signal for all individual stations is shown in Figure 4.8b. We see that many stations only show a small residual tide-gauge trend. However, in some regions, especially around Western Australia, the tide-gauge observations show a higher trend than explained by the sum of contributors. Around Western Australia, the alongshore propagation of multi-decadal wind-driven variability (Feng et al., 2004) may be one of the causes for this deviation.

The mean of the observed sea-level trends at the individual stations is 1.88 mm/yr, with a standard deviation of 1.74 mm/yr. This mean trend is larger than the mean trend of the sum of contributors sampled at the tide-gauge locations, which is 1.52 mm/yr with a standard deviation of 1.68 mm/yr. Also for each individual basin, the observed trends are on average higher than the sum of contributors. This global and basin-mean difference is also found when instead of the mean, the median observed trend and sum of contributors is used. Figure 4.9 shows global and basin-mean histograms of the observed trends and sum of processes. This difference may show that the sum of contributors underestimates the trend in global-mean sea-level rise. However, the spatial sampling of the tide gauges is uneven, which could result in some over-sampled regions, leading to biases when the observations are simply averaged without weighting. In the next section, we will discuss a reconstruction of basin-scale and global-scale sea-level changes where we show that this difference between observed sea-level and the sum of contributors is affected by the uneven spatial sampling and becomes smaller in the reconstructed basin-mean and global fields.

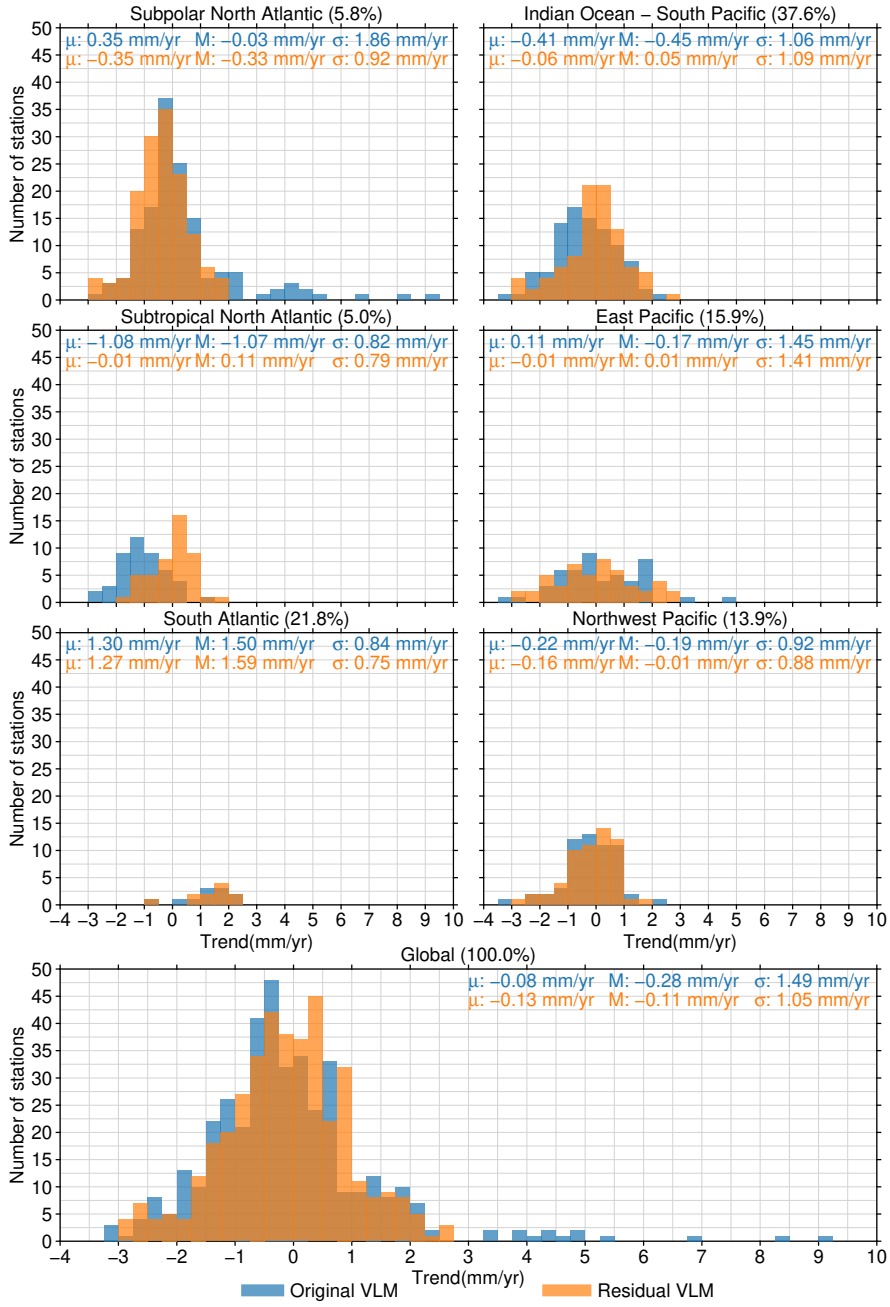

Figure 4.7: Histograms of the observed VLM at each tide gauge station, and the residual VLM after removing the solid earth response to GIA and present-day mass transport. μ denotes the mean of the distribution, M the median, and σ the standard deviation.

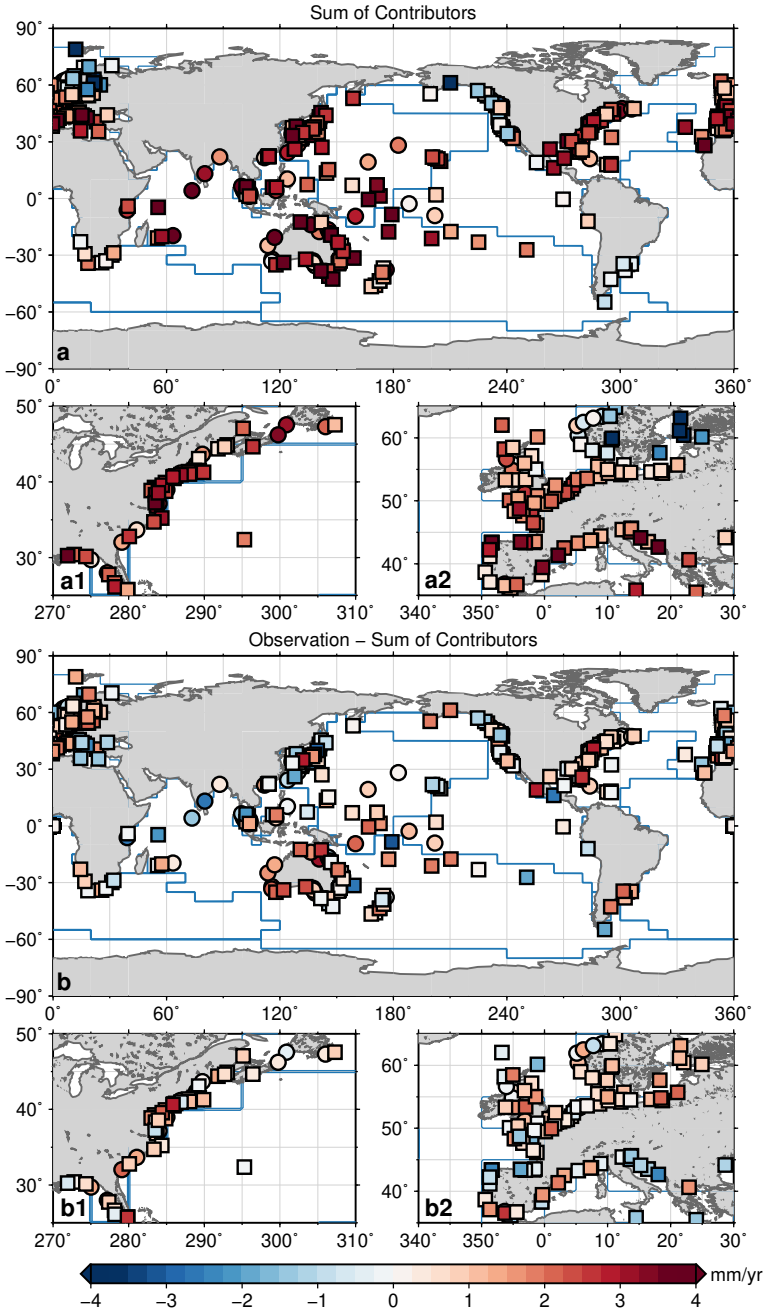

Figure 4.8: Modelled trends for the individual stations. a: Sum of contributors per station, computed as in equation 4.3. b: Observed trends in tide-gauge records (not corrected for VLM or residual VLM) minus the sum of contributors. The smaller panels on the right (a1,a2 and b1,b2) are zoom-ins of panels a and b along the densely-sampled European and American Atlantic coasts. The blue lines depict the boundaries of the individual basins.

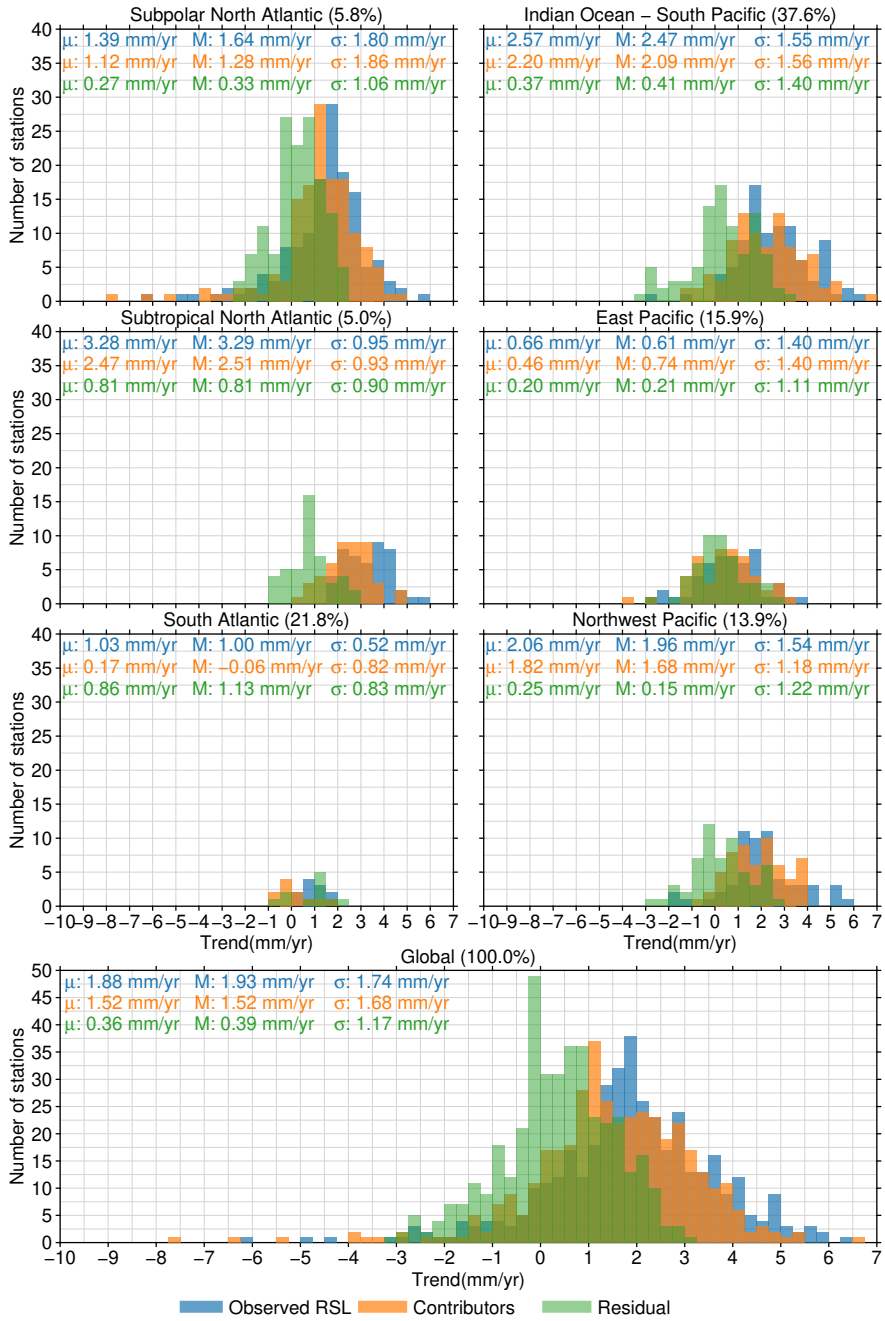

Figure 4.9: Histograms of observed sea-level trend at each tide gauge location, the trend of the sum of contributors, and the trend of the observations minus the sum of contributors ('residual'). μ denotes the mean of the distribution, M the median, and σ the standard deviation.

4.6 A basin-mean and global sea-level reconstruction

Since tide-gauge observations are not evenly sampled over each basin, and because the tide gauges are not linked to a common datum (Ray and Douglas, 2011; Woodworth et al., 2017), we cannot simply average the tide-gauge records over their overlapping period. To overcome this spatial and temporal sampling problem, we reconstruct sea-level changes in each basin from individual tide-gauge records using the virtual station technique (Jevrejeva et al., 2006, 2014). The virtual station technique recursively combines the two nearest stations to form a new virtual station halfway both stations. This procedure is repeated until only one station is left, which is used as the final estimate of sea-level changes over the basin. To overcome the problem of the unknown common datum, one could either obtain an empirical common datum or use first differences to remove the datum problem. Dangendorf et al. (2017) show that estimating a common datum when averaging two stations can be done by requiring both stations to share a minimum common observation time span. The average sea level of both stations over the common period is removed before both time series are averaged. They show using synthetic sea-level data that this procedure results in a more reliable estimate than using first differences. We also use this empirical common datum, and we require the stations to have an overlap length of at least 240 months.

To reduce the bias which occurs when the spatially and temporally varying sea-level field is sampled at tide-gauge locations, we correct for the spatial effects due to GIA, present-day mass redistribution, and residual VLM. We first compute the difference between the local and basin-mean relative sea-level change due to GIA and present-day mass redistribution, and remove this difference. We also remove the residual VLM at this stage. With these corrections, we make a best-guess of basin-mean sea level from an individual tide-gauge record, since the known local deviations from basin-mean sea level are removed. The corrected tide-gauge observation time series of each station then reads:

$$\eta_{\text{basin}} = \eta_{\text{tg}} + \overline{z_r} + \left[\eta_{\text{GIA,basin}} - \eta_{\text{GIA,tg}}\right] + \left[\eta_{\text{PD,basin}} - \eta_{\text{PD,tg}}\right]. \tag{4.5}$$

η_{basin} is the estimate of the basin-mean sea level, based on a single tide-gauge time series. $\overline{z_r}$ is the residual VLM term defined in Equation 4.2. $\left[\eta_{\text{GIA,basin}} - \eta_{\text{GIA,tg}}\right]$ is the negative local deviation from the basin-mean GIA signal, which is added to the basin-mean estimate, to minimize the sampling bias. $\left[\eta_{\text{PD,basin}} - \eta_{\text{PD,tg}}\right]$ is the same deviation, but for the present-day mass transport terms.

We compute η_{basin} for each station in a basin, and subsequently compute the basin-mean estimate by applying the aforementioned virtual station method, using the corrected η_{basin} term as time series for each station. Applying Equation 4.5 to all tide-gauge records reduces the standard deviation of the observed tide-gauge trends from 1.74 mm/yr to 1.47 mm/yr.

To obtain estimates of the uncertainties of our reconstructed basin estimates, we compute a Monte-Carlo estimate, by generating surrogate time series for each station. To do so, we assume that the autocorrelated noise properties of the tide-gauge

time series can be approximated by a power-law noise process. First, the properties of the powerlaw noise are estimated using a maximum-likelihood approach (Bos et al., 2013). Then, surrogate noise time series with the same length, gaps, and noise properties as the original time series are generated using the method from Kasdin (1995). The noise property estimation and the generation of surrogate time series are performed using the Hector software (Bos et al., 2013). Each surrogate noise time series is augmented with a linear trend, whose slope is generated from a normal distribution based on the standard error of the VLM term. The virtual station method is repeated 1000 times with the surrogate data, from which estimates of the confidence interval for the linear trend, acceleration, and time series are computed. Note that the spatial correlation between tide gauges is not taken into account when estimating the surrogate noise series. Hence, the obtained uncertainties may underestimate the real uncertainty in regions where the tide-gauge observations are spatially correlated.

The global reconstruction is based on the average of all basins, weighted by the area of each basin. The associated uncertainties are also computed from the basin-mean surrogate time series. The resulting reconstructions are shown in figure 4.10, together with the sum of contributors. The first observation that can be made is that for all regions, the reconstructed sea-level trends and accelerations are in agreement with the sum of contributors within 1σ intervals. The exception is the South Atlantic basin, where the observed sea-level trend is larger than the sum of contributors.

In the Pacific and Indian Ocean, the reconstructed sea-level variability shows good agreement with the sum of contributors and altimetry, while in all Atlantic basins, the observed decadal variability is not reproduced by the contributors. In the South Atlantic basin, where the difference is the most substantial, this discrepancy could be caused by the low number of observations in this region, which may result in the propagation of local variability at a limited number of locations into the basin-mean reconstruction. In the other Atlantic basins, the data coverage, both from tide gauges, as well as for hydrographic observations is generally high. A possible explanation of the discrepancy in these basins may be the decoupling between open-ocean and boundary sea-level variability, which is omnipresent in the Atlantic ocean (Hughes and Meredith, 2006), as well as the sea-level signal that emerges from changes in the AMOC strength and Gulf Stream variability, which generate very localized sea-level fingerprints (Ezer, 2015). In the Pacific and Indian Oceans, many tide gauges are located at open-ocean islands, which are generally more representative for open-ocean sea-level changes (Williams and Hughes, 2013). Another possible explanation for the differences in the Subtropical North Atlantic is non-linear subsidence due to sediment compaction and groundwater depletion along the northern coast of the Gulf of Mexico, which is not fully quantified in the VLM records (Kolker et al., 2011).

The global-mean reconstruction, which is the average of the basin-mean signals, weighted by their areas, also shows some decadal variability that is absent in the sum of contributors. A part of this variability signal is likely caused by the unexplained variability in the South Atlantic ocean, since the phase of the unexplained variability signal coincides. Over the altimetry era, the reconstructed sea level, altimetry, and the sum of contributors show a consistent upward trend.

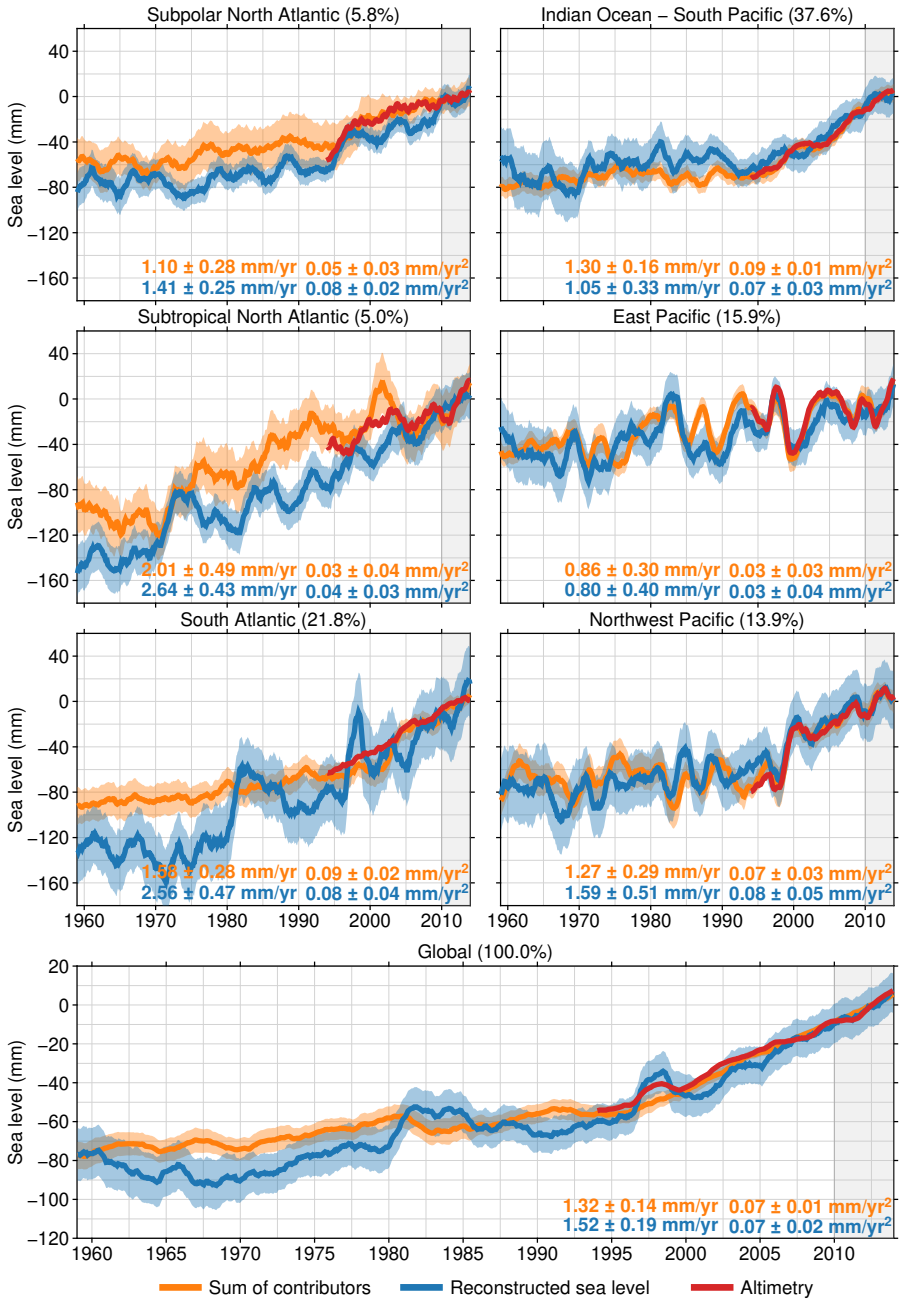

Figure 4.10: Reconstructed basin-mean and global sea level, together with the sum of contributors. All time series have been low-pass filtered using a 25-month moving average filter. The colored shadings denote the estimated confidence intervals. The confidence intervals for the trends, accelerations, and time series are on the 1σ level. The grey shading denotes the epoch (2010-2014) over which the mean of each time series has been removed.

Table 4.1: Global-mean trends and accelerations over 1958-2014 for the individual contributors, their sum, and reconstructed sea level. The confidence interval is at the 1 σ level.

	Trend (mm/yr)	Acceleration (mm/yr^2)
Glaciers	0.49 ± 0.03	0.011 ± 0.001
Greenland ice sheet	0.21 ± 0.02	0.007 ± 0.001
Antarctic ice sheet	0.06 ± 0.03	0.007 ± 0.001
Terrestrial water storage	-0.02 ± 0.09	0.019 ± 0.003
Present-day mass	0.74 ± 0.10	0.044 ± 0.004
Steric	0.54 ± 0.10	0.026 ± 0.011
GIA	0.04 ± 0.01	
Sum of contributors	1.32 ± 0.14	0.070 ± 0.011
Reconstructed GMSL	1.52 ± 0.19	0.067 ± 0.018

The trends and accelerations of the individual contributors to sea-level rise and their sum are shown in table 4.1. The estimated trend in sum of contributors is 1.3 ± 0.1 mm/yr, which explains the reconstructed global-mean sea level trend of 1.5 ± 0.2 mm/yr within the 1 σ confidence interval. Also, the acceleration in the sum of contributors (0.07 ± 0.01 mm/yr^2) explains the reconstructed sea-level acceleration of 0.07 ± 0.02 mm/yr^2. Note that the numbers in the table are not exactly equal to the equivalent barystatic mass changes, since some parts of the Arctic and Antarctic oceans are not part of the ocean basins over which the modelled sea-level change is averaged, as depicted in figure 4.1a. The acceleration in the sum of all present-day mass-redistribution processes is substantially larger than the acceleration in steric sea level. A positive acceleration is present in all individual basins, although in the East Pacific, the acceleration is not significant.

4.7 Discussion

To assess the impact of our new approach for reconstructing global-mean sea level on the resulting trend and variability, we computed the reconstruction, but with different corrections applied to the tide-gauge data before applying the virtual station method. In the 'no corrections' run, the virtual station method is applied to the time series without any prior correction. In the 'GIA only' run, we only remove the local relative sea-level deviation from the basin mean from each individual tide-gauge record due to GIA before averaging. The 'present-day only' run only applies the correction for present-day mass redistribution, the 'no VLM' run applies the GIA and present-day mass correction terms, but no VLM corrections. In the 'VLM only' run, we remove the uncorrected linear VLM trend from each station. The results are depicted in Figure 4.11. The choice of corrections applied to the tide-gauge data before merging them using the virtual station technique affects the resulting global-mean sea-level trend. The effects of GIA, local VLM, and present-day mass redistribution each have a different impact on sea-level reconstructions. The decadal variability does not show large differences between the reconstructions, which is not surprising, as the corrections applied to the tide-gauge stations are either linear (GIA, VLM, residual VLM) or only slowly-varying (present-day mass transport) in nature. Compared to the use of uncorrected tide-gauge data, our corrections result in a small in-

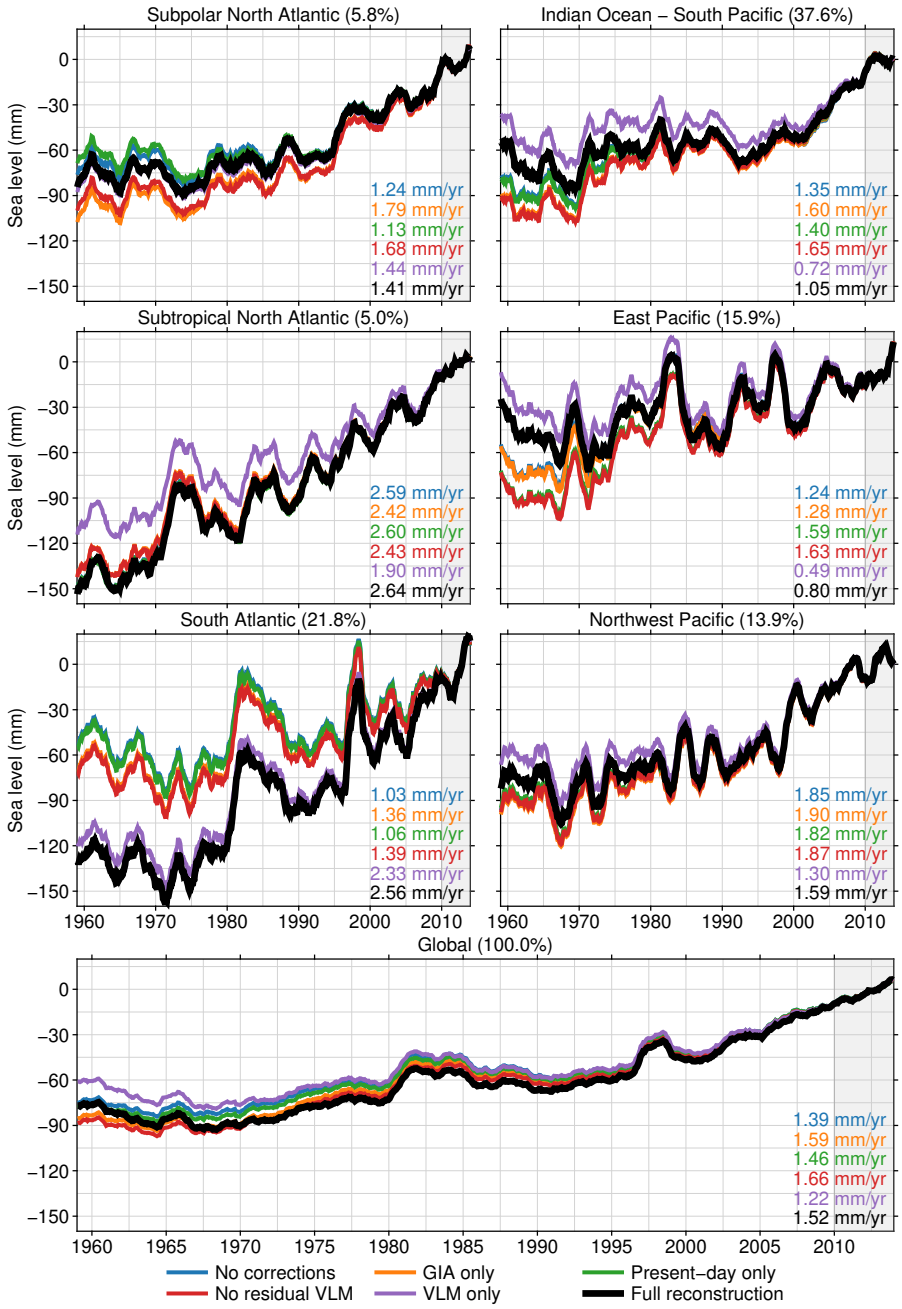

Figure 4.11: Reconstruction of basin-mean and global-mean sea level, with different corrections applied to the tide gauge records before applying the virtual station method. The mean value over the epoch marked by the grey bar (2010-2014) has been removed from each reconstruction. The applied corrections are explained in Table 4.2.

Table 4.2: Comparisons of corrections applied to tide gauge data before reconstructing basin-mean sea level reconstructions before applying the virtual station method, as used in Figure 4.11

No corrections	$\eta_{\text{basin}} = \eta_{\text{tg}}$
Present-day only	$\eta_{\text{basin}} = \eta_{\text{tg}} + \left[\eta_{\text{PD,basin}} - \eta_{\text{PD,tg}}\right]$
GIA only	$\eta_{\text{basin}} = \eta_{\text{tg}} + \left[\eta_{\text{GIA,basin}} - \eta_{\text{GIA,tg}}\right]$
No residual VLM	$\eta_{\text{basin}} = \eta_{\text{tg}} + \left[\eta_{\text{GIA,basin}} - \eta_{\text{GIA,tg}}\right] + \left[\eta_{\text{PD,basin}} - \eta_{\text{PD,tg}}\right]$
VLM only	$\eta_{\text{basin}} = \eta_{\text{tg}} + \overline{z}$
Full reconstruction	$\eta_{\text{basin}} = \eta_{\text{tg}} + \overline{z_r} + \left[\eta_{\text{GIA,basin}} - \eta_{\text{GIA,tg}}\right] + \left[\eta_{\text{PD,basin}} - \eta_{\text{PD,tg}}\right]$

crease in estimated global mean sea-level rise. The corrections for present-day mass redistribution and GIA both result in an increase of the reconstructed trend, compared to the uncorrected run. This increase is consistent with the results reported in Thompson et al. (2016), who also find that sampling spatial fingerprints of recent ice-mass loss at tide-gauge locations results in an underestimation of the barystatic sea-level rise.

When the original VLM signal is removed from the tide-gauge records, the resulting trend decreases substantially. One of the reasons that may cause this large difference, is that removing VLM from the tide-gauge records puts the reconstruction in a geocentric or absolute reference frame instead of a relative reference frame (Wöppelmann et al., 2009). Therefore, ocean-bottom deformation is removed from the sea-level rise estimate. Hence, if the ocean bottom subsides, sea level relative to the ocean bottom will stay constant, but geocentric sea level will drop. It is well-known that GIA results in such an ocean-bottom motion signal, which leads to a reduction of 0.15-0.45 mm/yr in global-mean geocentric sea-level rise, while the present-day barystatic contribution of GIA is zero (Tamisiea, 2011). Hence, the GIA contribution in Table 4.1 stays close to zero, and is not comparable to the GIA correction term applied to altimetry estimates. Furthermore, present-day mass transport results in a higher pressure on the ocean bottom, and the latter will subside further as a response (Ray et al., 2013). Hence, some caution must be taken when correcting tide gauges for VLM, when one is interested in global mean sea-level changes. The full reconstruction adds the residual VLM term to the corrections of GIA and present-day mass redistribution. The addition of residual VLM results in a lower GMSL estimate, despite the fact that the simple average residual VLM term is almost zero.

Forward GIA models, including the ICE6G_VM5a model applied here, rely on estimates of the glaciation-deglaciation history and the viscosity structure of the earth, which are both difficult to constrain. Hence, specific choices made in the GIA model may affect the global and regional sum of contributors. To determine whether changing the underlying GIA model affects the sum of contributors, we have also run the analysis using the ICE6G_ANU model (Purcell et al., 2016) and the ICE5G_VM2 model (Peltier, 2004). On a global scale, the differences are in the range of 0.04 mm/yr. In the Subpolar and Subtropical North Atlantic basins, differences in the order of 0.2 mm/yr occur, while outside these basins, the differences are smaller. Figure 4.12 shows the effects of changing the GIA model on the estimate of the sum of contributors.

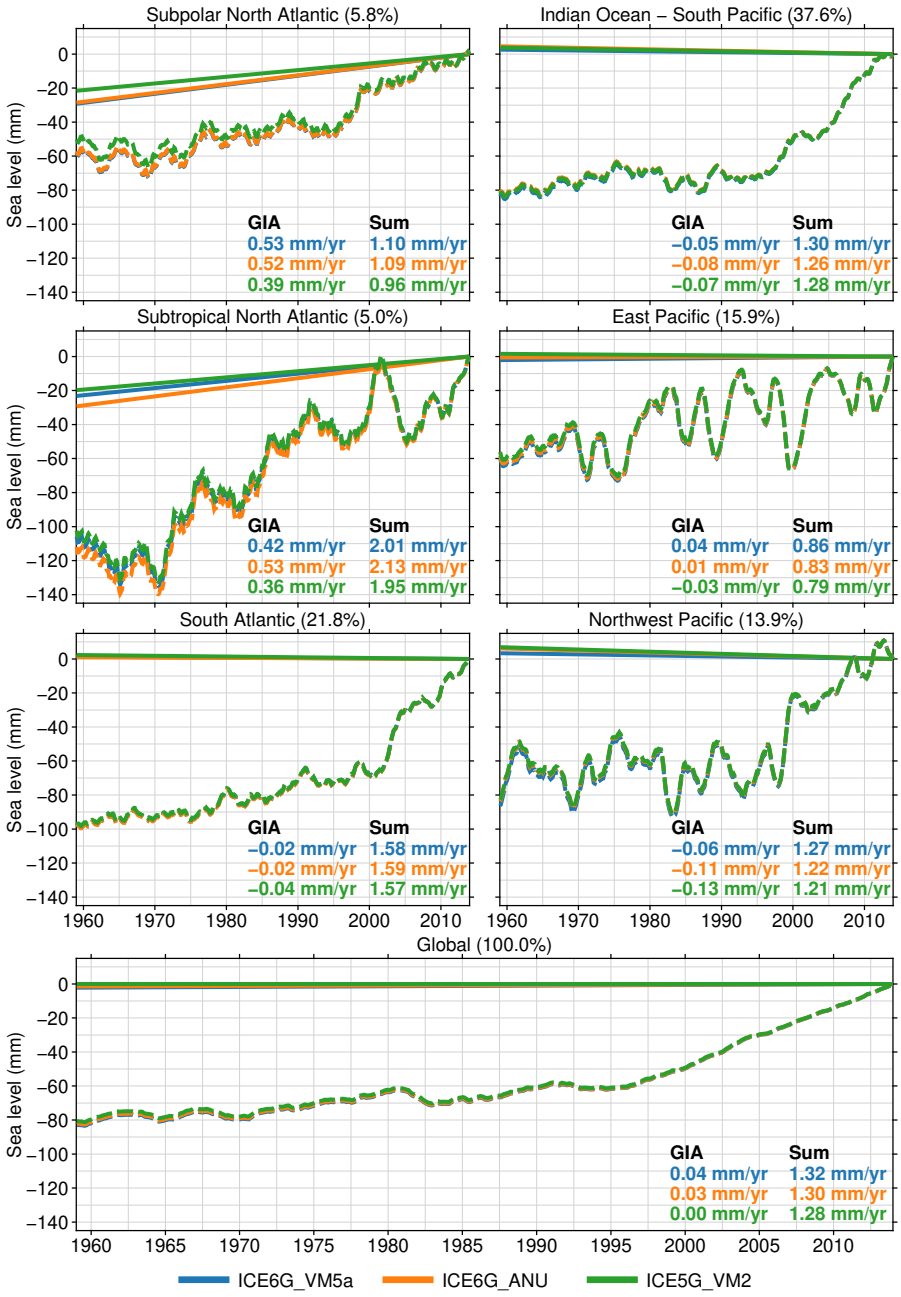

Figure 4.12: Comparison of three GIA models. The solid line shows the GIA component of the sum of contributors for each GIA model. The dashed line shows the total sum of contributors for each GIA model. The trends depicted in the lower right corner show the trend in the GIA component in each basin ('GIA'), as well as the trend of the total sum of contributors ('Sum') for each GIA model.

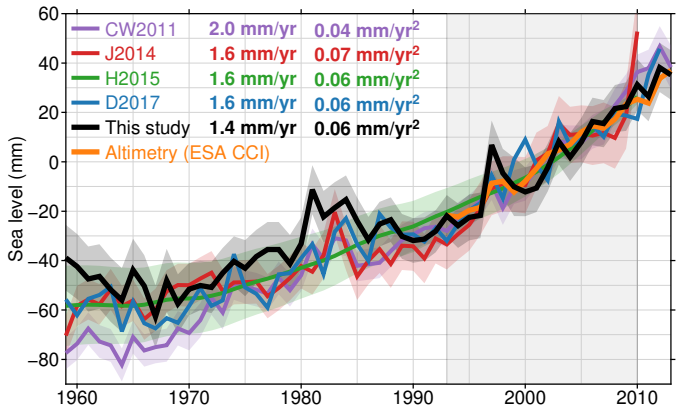

Figure 4.13: A comparison of global mean sea-level reconstructions based on tide-gauge observations from Church and White (2011, CW2011), Jevrejeva et al. (2014, J2014), Hay et al. (2015, H2015), Dangendorf et al. (2017, D2017), and this study. The shading denotes the estimated confidence interval on the 1σ level. All reconstructions are re-sampled to annual-mean values. Central estimates of the trends and accelerations for all reconstructions are computed over 1958-2010. The mean value over the epoch marked by the grey bar (1993-2010) has been removed from each reconstruction.

To assess how our reconstruction approach compares to other reconstructions, we have plotted our reconstruction together with the global reconstructions of Church and White (2011), Jevrejeva et al. (2014), Hay et al. (2015), and Dangendorf et al. (2017). Note that our reconstruction method is similar but not fully equal to the reconstruction method presented by Dangendorf et al. (2017): we use a different tide-gauge selection, a different GPS solution, and an alternative parametrisation of the local deviations from the basin-mean sea level, as described in Equation 4.5. The comparison between all reconstructions is depicted in figure 4.13. Our reconstruction shows a slightly smaller increase in sea level than most reconstructions over the common period. To assess the significance of this difference, we computed the central estimates of the reconstructed trends in the above reconstructions over the common overlap period (1958-2010). All central estimates are well within the 2σ range of our reconstruction, except for the reconstruction of Church and White (2011), which has a central value of 2.0 mm/yr. The central estimates of the accelerations of all reconstructions fall well within the 2σ range of our reconstruction. Over the altimetry era, all reconstructions show a consistent rise in sea level. Note that the reconstructed global sea-level acceleration over the period of this study (1958-2014) is higher than the acceleration found over the whole 20th century (Hay et al., 2015; Dangendorf et al., 2017). This difference can be attributed to the different time spans, since we do not include the pre-1958 sea-level changes, during which a sea-level deceleration can be noted (Dangendorf et al., 2017).

4.8 Conclusions

We have computed estimates of sea-level rise on a local, regional, and global scale over the last decades (1958-2014), and made an estimate of the sum of contributors to sea-level changes. We have developed an updated approach to reconstruct global and basin-mean sea level by explicitly taking into account local VLM and the non-linear effects of present-day mass redistribution on both tide-gauge and VLM observations in a consistent framework. Together with the use of a common mean to merge individual tide-gauge records, as described by Dangendorf et al. (2017), the resulting basin-mean trends and accelerations are in agreement with the sum of contributors in all basins, except for the sparsely-observed South Atlantic. In the Indian and Pacific Oceans, the sum of contributors show good agreement with the observed decadal variability, while for the Atlantic region, the reconstructed variability is not explained by the contributors. The spread between steric sea-level reconstructions is large in the Atlantic ocean, which also applies to the well-observed North Atlantic Ocean. Therefore, to obtain a more thorough understanding of the global sea-level budget, an assessment of the various observations in the Atlantic region is worthwhile.

When the basin-mean records are merged into a global reconstruction, we also find good agreement between the reconstructed trend and acceleration and the sum of contributors. Hence, the sea-level budget between 1958 and 2014 can be reasonably closed without requiring a large contribution from the Antarctic Ice Sheet before the nineties or a contribution from thermal expansion in the deep ocean below 2000m. However, the reconstructed decadal variability cannot be reproduced, which is partially caused by the spread in the sparsely-observed South Atlantic ocean.

Next to attempts to rescue more tide-gauge records (e.g. Hogarth, 2014), another approach to the issue of sparse observations may be the use of high resolution ocean models and reanalyses. These models may help separating local variability from basin-mean changes, which could reduce the large spread between observed sea-level changes at tide gauges and the local sum of contributors, for which the local effects of ocean dynamics are still unknown.

Chapter 5

Ocean-bottom deformation due to present-day mass transport and its impact on sea-level observations

> "Speaking as a soldier, we never have 100 percent certainty. If you wait until you have 100 percent certainty, something bad is going to happen on the battlefield."
>
> Gordon R. Sullivan

5.1 Summary

Present-day mass redistribution increases the total ocean mass and, on average, causes the ocean bottom to subside elastically. Therefore, barystatic sea level rise is larger than the resulting global-mean geocentric sea-level rise, observed by satellite altimetry and GPS-corrected tide gauges. We use realistic mass transport estimates to quantify the resulting ocean-bottom deformation and its effect on global and regional ocean-volume change estimates. Over 1993-2014, the resulting globally-averaged geocentric sea-level change is 8 percent smaller than the barystatic contribution. Over the altimetry domain, the difference is about 5 percent. Due to this effect, barystatic sea-level rise will be underestimated by more than 0.1 mm/yr over 1993-2014. At regional scales, the differences are often larger, up to 1 mm/yr over the Arctic Ocean and 0.4 mm/yr in the South Pacific. The contribution of ocean bottom deformation should be considered when regional sea-level changes are observed in a geocentric reference frame.

Parts of this chapter have been published as: Frederikse, T., Riva, R. E. M., and King, M. A.: Ocean-bottom deformation due to present-day mass transport and its impact on sea-level observations, Geophysical Research Letters, doi:10.1002/2017GL075419, 2017.

5.2 Introduction

Next to steric and dynamic changes, redistribution of mass between land and ocean is one of the major components driving global and regional sea-level change (Chambers et al., 2016; Stammer et al., 2013). The redistribution causes distinct regional sea-level change patterns, known as sea-level fingerprints, which are caused by gravitational effects, changes in the earth-rotation parameters, and by deformation of the solid earth (Clark and Lingle, 1977; Milne and Mitrovica, 1998). A substantial part of the regional pattern is caused by vertical deformation of the solid earth, that affects both land and the ocean bottom (King et al., 2012; Riva et al., 2017). Due to changes in the land ice-mass balance and land hydrology, the oceans have gained mass over the past decades (Chambers et al., 2016), which results in an increase of the total load on the ocean bottom. Under this increasing load, the ocean floor will subside due to elastic deformation. Assuming a constant geocentric ocean surface, the ocean volume will increase when the ocean bottom subsides. This elastic deformation is additional to the visco-elastic response to past ice-mass changes, known as Glacial Isostatic Adjustment (GIA), for which sea-level reconstructions are routinely corrected (Tamisiea, 2011). In this chapter, we examine how elastic deformation due to present-day ice mass loss and land water storage (LWS) changes has affected the shape of the ocean bottom over the last two decades, and whether this deformation does affect sea-level reconstructions from tide gauges corrected for vertical land motion (VLM) and altimetry.

Sea-level changes are generally expressed in two distinct reference frames: either relative to the local ocean floor (relative sea-level change), or relative to the earth's center of mass (geocentric, or absolute sea-level change). Global mean sea-level (GMSL) changes due to mass redistribution are called barystatic changes. These barystatic changes are defined as the total volume change of the ocean, divided by the ocean surface area. With this definition, barystatic changes are equal to relative sea-level changes, integrated over the whole ocean. However, because of the deformation of the ocean bottom due to the changing load, global-mean geocentric sea-level changes resulting from mass changes are not equal to the barystatic changes. Since the solid-earth deformation is not uniform over the oceans, the regional or basin-mean difference between relative and geocentric sea-level change may deviate from the global-mean difference.

The emergence of satellite altimetry has given a near-global overview of sea-level changes (Nerem et al., 2010). However, because satellite altimetry observes sea level in a geocentric reference frame, global mean sea-level estimates derived from altimetry will not observe the increase in ocean volume due to ocean subsidence, and hence, they may underestimate GMSL rise. A correction associated with the elastic response to present-day mass redistribution is almost never applied (see Kuo et al. (2008), Fenoglio-Marc et al. (2012), and Rietbroek et al. (2016) for exceptions), and altimetry-derived global-mean sea-level changes resulting from mass transport may thus differ from associated global ocean-volume changes.

The launch of the Gravity Recovery And Climate Experiment (GRACE) satellite mission has allowed more detailed global and regional estimates of ocean mass

changes and comparison with sea-level changes (Leuliette and Willis, 2011; Chen et al., 2017; Kleinherenbrink et al., 2016). GRACE observations show ocean mass changes, and hence show relative rather than geocentric sea-level changes (Kuo et al., 2008; Ray et al., 2013), and the direct comparison between altimetry and GRACE will thus also introduce a bias when the effect of ocean-bottom deformation is not corrected for.

On centennial time scales, sea-level change estimates are mainly based on tide gauge data. As land-based instruments, they observe relative sea level, and tide-gauge based reconstructions would ideally observe global ocean volume changes if the VLM component is not removed. Traditionally, only the GIA component of VLM was estimated and corrected for. More recently, GPS, altimetry, and DORIS observations have been used to correct tide-gauge records for VLM (Ray et al., 2010; Wöppelmann and Marcos, 2016). This correction brings tide gauges into a geocentric reference frame, and hence, the resulting sea-level rise estimates may be biased due to ocean-bottom deformation in the same way satellite-based estimates are.

In this chapter, we study the difference in relative and geocentric sea-level rise due to elastic deformation, given realistic estimates of present-day water-mass redistribution to see to what extent the different observational techniques are affected. Based on recent estimates of mass changes related to ice, land-water storage, and dam retention, we compute the resulting global-mean and regional ocean-bottom deformation. The impact on tide-gauge based sea-level reconstructions is estimated by computing a synthetic 'virtual station' sea-level solution (Jevrejeva et al., 2006).

5.3 Methods and data

The spatially-varying response of the geoid, the solid earth, and relative sea level to present-day mass exchange is computed by solving the sea-level equation (Clark and Lingle, 1977), which includes the earth-rotational feedback (Milne and Mitrovica, 1998). We assume that the earth is elastic and incompressible. We solve the sea-level equation using a pseudo-spectral method (Tamisiea et al., 2010) up to spherical harmonic degree 360 in the Center-of-mass of the whole earth system (CM) frame. The load Love numbers used to determine the geoid and solid-earth response are computed from the Preliminary Referenced Earth Model (PREM, Dziewonski and Anderson, 1981). The resulting relative sea-level change $\eta(\theta, \phi, t)$ at longitude θ, latitude ϕ, and time t can then be expressed as

$$\eta(\theta, \phi, t) = G(\theta, \phi, t) - R(\theta, \phi, t) + \mathscr{L}(t). \tag{5.1}$$

$G(\theta, \phi, t)$ is the deformation of the geoid, $R(\theta, \phi, t)$ is the change of the solid-earth height, and $\mathscr{L}(t)$ is a global-mean term, which is required to ensure mass conservation. Hence, regional variations in relative sea level are both caused by changes in the local geoid and solid-earth deformation. $R(\theta, \phi, t)$ and $G(\theta, \phi, t)$ evaluate to zero when integrated over the whole earth. However, they do not necessarily evaluate to zero when integrated over the global ocean or over the altimetry domain (±66°S). Therefore, $\mathscr{L}(t)$ is generally not equal to the total barystatic change.

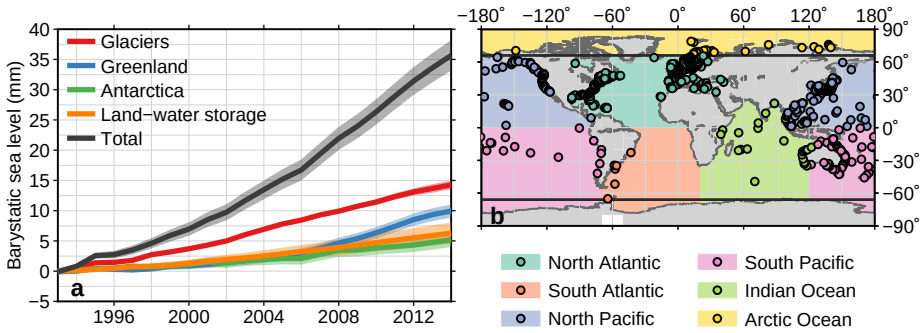

Figure 5.1: Modelled barystatic contributions and definition of the individual ocean basins. a. Time series of the modelled barystatic sea-level changes from each individual process and their sum. The shaded areas show the 1σ confidence interval. b. Definition of each ocean basin. The dots show the tide-gauge locations, and the color the basin to which each tide gauge is linked. The black lines show the upper and lower bound of the altimetry domain.

Local geocentric sea-level change $\zeta(\theta,\phi,t)$ only differs from local relative sea-level change by the local solid-earth height change. Therefore, geocentric sea-level change can be expressed as:

$$\zeta(\theta,\phi,t) = \eta(\theta,\phi,t) + R(\theta,\phi,t) = \mathscr{L}(t) + G(\theta,\phi,t). \tag{5.2}$$

Since geoid variations have more power at longer wavelengths than solid-earth deformations, the spatial patterns of relative sea-level changes (eq. 5.1) can substantially differ from those of geocentric changes (eq. 5.2).

We compute the sea-level response to mass redistribution related to glaciers, the Greenland and Antarctic ice sheets, and LWS over the period 1993-2014. We use the mass redistribution data from Frederikse et al. (2017), which provides estimates of the temporal and spatial distribution of the mass changes from the aforementioned processes, which we review here shortly. Glacier mass loss is based on a surface mass balance model (Marzeion et al., 2015). The Greenland and Antarctic Ice sheet contributions are based on an an input-output approach, where the surface mass balance contribution is based on RACMO2.3 (van Wessem et al., 2016; van den Broeke et al., 2016). The ice discharge is modelled as a constant acceleration of 6.6 Gt/yr^2 for the Greenland Ice Sheet and 2.0 Gt/yr^2 for the Antarctic Ice Sheet. The total mass change is partitioned over each ice sheet by normalized GRACE mascon solutions (Watkins et al., 2015). For LWS, we include groundwater depletion, based on modelled estimates from Wada et al. (2012), and dam retention, based on the GRaND dam database (Lehner et al., 2011), with reservoir filling and seepage rates from Chao et al. (2008). For a more complete description of the data and the associated uncertainties, we refer to Frederikse et al. (2016, 2017).

The barystatic contribution associated with each process is depicted in Figure 5.1a. To assess the impact on regional estimates, we have separated the ocean into six regions, as depicted in Figure 5.1b, which also shows the domain covered by the TOPEX/Poseidon and Jason 1/2/3 altimeters, which is between ±66°S.

To estimate the impact of corrections for VLM on tide-gauge based reconstructions, we apply the virtual-station method (Jevrejeva et al., 2006) on our synthetic sea-level change field. First, we sample our synthetic sea-level change field at the tide-gauge locations from the revised local reference (RLR) database from the Permanent Service for Mean Sea Level (PSMSL, Holgate et al., 2013). To avoid the inclusion of tide-gauge locations that have been abandoned, we only use station locations for which more than 15 valid annual sea-level observations between 1993-2014 are available, which results in 627 station locations. Each station location is assigned to an ocean basin, as depicted in Figure 5.1b. Secondly, the sampled sea-level time series are merged into a basin-mean reconstruction using the virtual-station method, in which the two closest stations in each basin are combined into a new virtual station located halfway between both stations, until only one station is left per basin. This last station is used as a proxy for the full basin. A global-mean is computed by averaging the basin-reconstructions, weighted by the individual basin sizes. Since our synthetic data field does not contain data gaps or have issues related to unknown reference levels, we compute a simple arithmetic mean between the time series of the two merged stations to compute a new virtual station.

5.4 The spatial pattern of the relative and geocentric sea-level response

The rates of elastic ocean-bottom deformation (expressed in the center-of-mass (CM) frame), relative sea-level, and geocentric sea-level changes due to the aforementioned mass transport processes are shown in Figure 5.2, together with the ocean-mean rates. Due to the increase of the total ocean load, the ocean bottom on average elastically deforms by -0.13 mm/yr over 1993-2014 (Figure 5.2a). This subsidence adds to the routinely considered effects of GIA, which cause a global-mean ocean-bottom deformation of about -0.15 to -0.4 mm/yr (Tamisiea, 2011), as well as regional deformation patterns. Due to differences in the underlying physical processes, the elastic pattern considered here differs substantially from the GIA-related pattern (Mitrovica and Milne, 2002). As a result of the fact that the rate of global-mean ocean bottom deformation is negative, the ocean bottom on average subsides, and the global-mean rate of geocentric sea-level change is smaller than the global-mean relative sea-level change (i.e. global ocean-volume change).

The rate of elastic subsidence shows distinct spatial features: an uplift signal is present close to the major melt sources around the Arctic Ocean, Alaska, and the West Antarctic Ice Sheet. A north-south gradient is visible in Figure 5.2a, with large parts of the Northern Hemisphere oceans showing uplift, while most of the Southern Hemisphere is affected by a subsidence rate above the global mean. This ocean-bottom deformation signal determines a large part of the regional variability of the resulting relative sea-level changes depicted in Figure 5.2b, especially close to the major ice-melt sources, while the variations in geocentric sea-level changes, for which the regional variability is only determined by geoid changes, show smaller spatial gradients (Figure 5.2c). Therefore, the largest differences between relative and geocentric

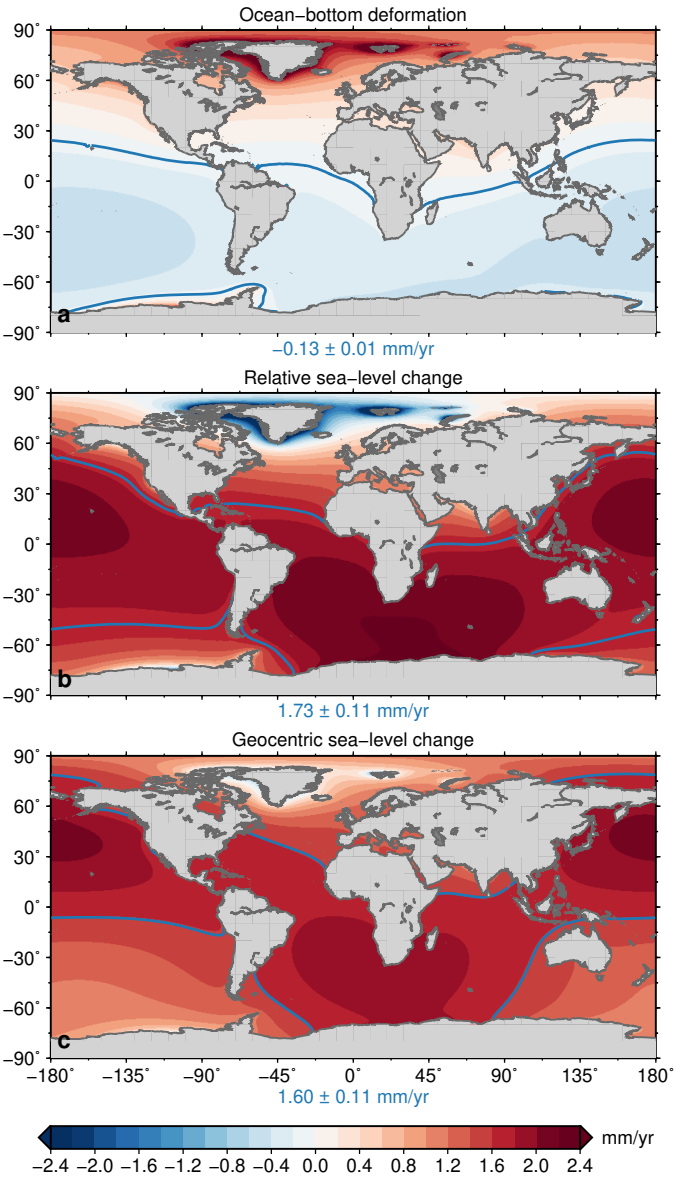

Figure 5.2: Linear trends resulting from ice-mass and LWS changes over 1993-2014 in a. solid-earth deformation over the oceans b. relative sea level, and c. geocentric sea level. Note that geocentric sea-level change is equivalent to the sum of relative sea-level and ocean-bottom deformation change. The blue line depicts the line where local sea-level change is equal to the ocean-mean sea-level trend, whose value, including its accompanying 1σ confidence interval, is written in blue under each map.

sea level can be found in high-latitude areas close to the major ice-melt sources.

The observed north-south pattern in Figure 5.2a suggests that motion of the geocenter plays a role in the observed deformation. A substantial part of the surface mass redistribution is caused by mass loss from Greenland and the glaciated regions surrounding the Arctic Ocean. This surface mass is redistributed over the oceans, resulting in a net southward shift of the earth center-of-mass in the center-of-figure (CF) frame. As a result, in the center-of-mass (CM) frame, the solid earth shifts northward, which causes uplift in the north and subsidence in the south. We explore this shift by examining the resulting deformation from the three degree-1 spherical harmonics of the solid-earth deformation field, which is depicted in Figure 5.3a. The figure shows that the solid-earth deformation related to geocenter motion explains a substantial part of the spatial signal at low frequencies. Due to this large signal, the near-field uplift resulting from mass loss at the West Antarctic Ice Sheet is barely visible in Figure 5.2a. The removal of the geocenter-related signal (Figure 5.3b), reveals that the influence of Antarctic uplift reaches over large parts of the Southern Oceans. The signal related to geocenter motion also affects the relative sea-level fingerprint, depicted in Figure 5.3c. Compared to Figure 5.2c, the impact of mass loss in West-Antarctica becomes more visible. A substantial part of the uncertainties in reference frame realizations, which affect multiple geodetic observations, including satellite altimetry and GPS, is related to geocenter motion (Santamaría-Gómez et al., 2017; Riddell et al., 2017). Since geocenter-motion related effects form a substantial contribution to the spatial patterns of sea-level changes and bottom deformation, the observed spatial patterns from satellite altimetry and VLM-corrected tide gauges will be affected by this uncertainty.

Because ocean-bottom deformation has a distinct regional pattern, its effect will vary between individual ocean basins. The resulting time series per basin, together with the linear trends, are shown in Figure 5.4. For most regions, the relative sea-level trend exceeds the geocentric trend. The difference in the trend varies between 0.04 mm/yr in the North Pacific and 0.41 mm/yr in the South Pacific. However, for the North Atlantic and Arctic oceans, both close to major sources of ice-mass loss, geocentric sea level exceeds relative sea level. In the Arctic ocean, the large regional uplift results in a negative rate of relative sea-level rise, while geocentric sea-level rise is still positive.

5.5 The effect on tide-gauge reconstructions

Tide gauges sample relative sea level at coastal locations. Recent developments in space geodesy allows for estimates of VLM at tide gauge locations (Wöppelmann and Marcos, 2016). Local ocean bottom deformation is observed as VLM, and thus removed from the tide-gauge observations when corrected for VLM. This removal leads to a possible bias in reconstructed global and regional relative sea-level changes from VLM-corrected tide-gauge records. However, since tide-gauge observations only sample the ocean at a limited number of locations, the magnitude of the bias in the tide-gauge reconstruction may differ from the bias in satellite altimetry. In this section, we estimate the size of this bias due present-day mass redistribution in VLM-corrected

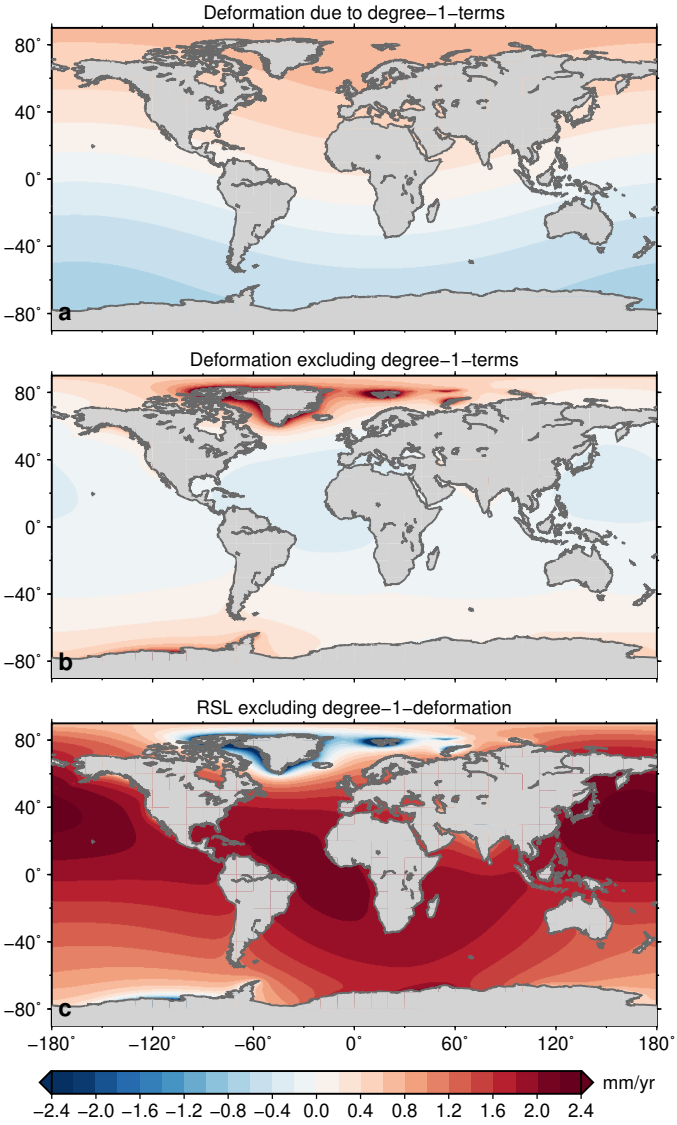

Figure 5.3: Ocean-bottom deformation in the CM-frame related to geocenter motion. a: Ocean-bottom deformation caused by the degree-1-terms. b: Ocean-bottom deformation from all other spherical harmonic terms. The sum of a and b equals the ocean-bottom deformation as shown in Figure 5.2a. c: Relative sea-level change excluding the degree-1-term in solid-earth deformation.

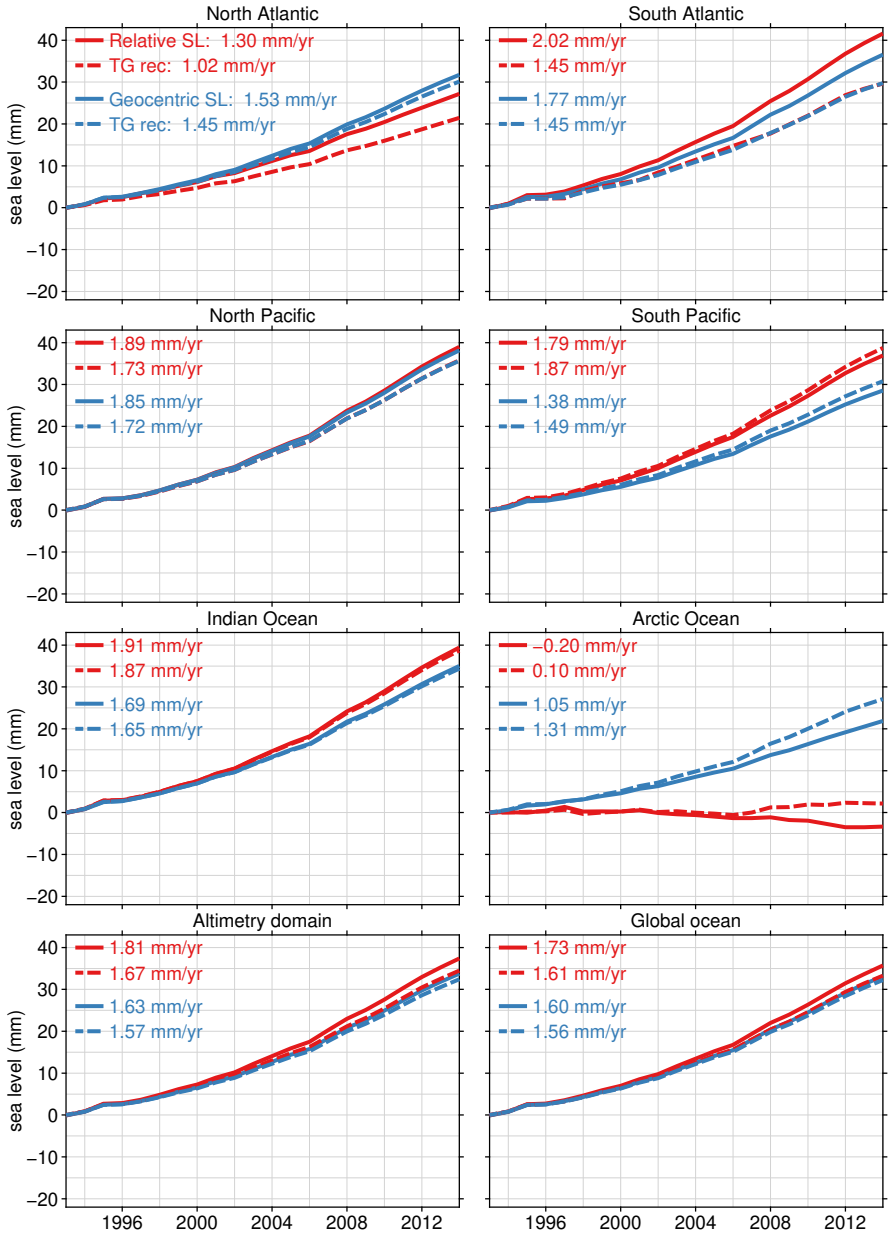

Figure 5.4: Basin-averaged and global-mean effects of present-day mass transport on observed relative and geocentric sea-level change. The solid line represents the average spatial signal over each region. The dashed line ('TG rec') represents tide-gauge reconstructions based on the virtual-station method using the locations of the 627 PSMSL tide gauges. The altimetry domain consists of the global oceans, bounded by ±66° latitude. For the virtual-station estimate of the altimetry domain, all regions, except the Arctic Ocean region are used.

tide-gauge reconstructions. We reconstruct basin-mean and global sea-level changes due to present-day mass loss using the virtual-station method. The synthetic relative and geocentric sea-level fields, as depicted in Figure 5.2, are sampled at 627 tide-gauge locations, as described in section 5.3. We assume that the solid-earth deformation is observed at the same grid cell as the tide-gauge location. In practice, the distance between the tide-gauge and VLM observations amount to tens of kilometres and cause an additional bias, especially in areas where a large spatial gradient in the deformation field is present.

Results from the basin-mean and global reconstruction are depicted as the dashed lines in Figure 5.4. At regional scales, reconstructions of basin-mean relative and geocentric sea level show distinct differences, which are generally similar in sign and magnitude to the differences computed from averaging the deformation field over the whole basin, as discussed in the previous section, although the uneven sampling of the tide-gauge records over the basins results in differences with the basin-mean values, especially in the South Atlantic, where the relative and geocentric sea-level reconstructions both deviate substantially from the original values.

Averaged over the global ocean, the difference between the synthetic geocentric and relative sea-level reconstructions is only 0.05 mm/yr, which is smaller than the difference in the underlying basin-mean trends, which is 0.13 mm/yr. This small difference suggests the effect of present-day surface mass redistribution is small on global reconstructions based on tide-gauge records that have been corrected for observed VLM. The reconstructed difference becomes larger when the high-latitude tide gauges are omitted ('Altimetry domain'), but is still smaller than the difference in the underlying fields. It should be noted that both the global relative and geocentric sea-level changes are underestimated by the tide-gauge reconstructions, as also found by Thompson et al. (2016), who note a 0.1 mm/yr underestimation when sea level is sampled at 15 tide gauges with long records, instead of the 627 tide-gauge locations used in this study.

5.6 Discussion and conclusions

We have quantified the effect of present-day mass loss on elastic ocean-bottom deformation, which results in differences between global and basin-mean relative and geocentric sea-level changes. These differences affect a multitude of sea-level observations. Over 1993-2014, global-mean geocentric sea level has risen about 8 percent less than the barystatic equivalent. Hence, if globally-covering satellite altimeters would observe sea level, due to present-day mass redistribution, the total volume increase would be underestimated by about 0.13 mm/yr. However, due to choices in the satellite orbits, the area covered by altimetry observations is generally limited, and the highest latitudes are often not observed. When GMSL is estimated from the range covered by the TOPEX/Poseidon and Jason altimeters, as depicted in Figure 5.1, the underestimation of the total volume change becomes about 0.10 mm/yr, or 6 percent of the barystatic contribution. Note that next to barystatic sea-level rise, steric changes are present, and total GMSL rise is substantially larger than barystatic

sea-level rise. Because the elastic response of the earth is reasonably well defined (Mitrovica et al., 2011), the uncertainty of the correction is largely due to uncertainties in changes of the ocean mass and the reference frame realization.

The global-mean ocean-bottom deformation due to elastic deformation caused by present-day mass redistribution is still smaller than the ocean-bottom deformation that results from the visco-elastic response to ice-mass changes in the past (GIA), which is on the order of -0.15 to -0.4 mm/yr (Tamisiea, 2011). Furthermore, the bias is still within the uncertainty range of altimetry-derived GMSL trends, which are on the order of 0.4 mm/yr (Chen et al., 2017). In a future warming climate, the sea-level rise induced by ice sheets will increase (e.g. Kopp et al., 2014), and therefore, the magnitude of the bias due to ocean-bottom deformation will grow. When we assume no changes in the altimetry trend uncertainty, the bias becomes significant when barystatic sea-level rise reaches 6.5 mm/yr. Under high-end sea-level rise scenarios, such barystatic contributions could be reached during the 21st century (DeConto and Pollard, 2016; Jevrejeva et al., 2016a).

Ocean-bottom deformation varies spatially, and on regional and basin-mean scales, the resulting difference between geocentric and relative sea level can deviate substantially. The largest differences can be found in the Arctic Ocean: due to the location close to many melt sources, the relative sea level in the Arctic drops, while geocentric sea-level rises, resulting in a 1.3 mm/yr difference between both metrics. Outside the Arctic ocean, basin-mean differences up to 0.4 mm/yr, or 23 percent of the regional relative sea-level changes occur. Although the spatial patterns show substantially less variability compared to the patterns related to ocean dynamic changes, the differences between geocentric and relative sea level are in the same range as uncertainties in basin-mean sea-level estimates from altimetry, which on the sub-millimetre level in many basins (Kleinherenbrink et al., 2016; Purkey et al., 2014).

In reconstructions in which no direct VLM observations or satellite-altimetry are used (e.g. Jevrejeva et al., 2006; Hay et al., 2015), the effects of ocean bottom deformation will not affect the reconstructions, although the sampling of the spatially-varying sea-level field by the limited number of tide gauges may result in a bias (Thompson et al., 2016). Recently, VLM-corrected tide-gauge observations have been used to reconstruct regional and global-mean sea-level changes (Wöppelmann et al., 2014; Dangendorf et al., 2017). Tide gauge reconstructions observe geocentric sea-level changes when the records are corrected for VLM. Therefore, bottom deformation could affect these reconstructions as well. Using the virtual-station technique using all locations of the PSMSL RLR database with 70% data availability over the altimetry area, we only find a small difference between reconstructed global-mean geocentric and relative sea level. We do find that the reconstruction of global-mean relative sea level underestimates the underlying real value, which was also noticed by Thompson et al. (2016). Leaving the Arctic Ocean out of the tide-gauge reconstructions results in a larger difference between geocentric and relative sea-level changes, although the aforementioned bias with the 'real' sea-level changes is still present. On regional scales, we find similar differences between relative and geocentric sea-level changes for the synthetic tide-gauge reconstruction as for the averaged fields, although in some basins, especially in the South Atlantic Ocean, the sparse sampling

results in differences with the underlying fields. The differences between relative and geocentric sea level in global and regional tide-gauge reconstructions are not independent from the station selection and reconstruction method, and the aforementioned values cannot be blindly used to quantify the effect of bottom deformation in a specific reconstruction. For example, the global reconstruction from Church and White (2011) uses spatial sea-level change patterns estimated from altimetry, which are also affected by ocean-bottom deformation, although in a different way than mentioned here.

Since the differences between relative and geocentric sea-level change are caused by deformation of the solid earth, they should be observable in VLM estimates at coastal locations. However, the uncertainties of individual VLM observations and 20-year linear trends in tide-gauge observations are still generally larger than the rates considered here (Wöppelmann and Marcos, 2016; Hughes and Williams, 2010; Dangendorf et al., 2014a). On regional scales, when multiple independent observations can be combined, analyses do suggest that ocean-bottom deformation resulting from present-day mass loss can be observed in GPS and tide-gauge records (Galassi and Spada, 2017; Pfeffer et al., 2017).

Since barystatic sea-level rise shows an acceleration over the last two decades (Chen et al., 2017), altimetry and VLM-corrected tide gauge observations also underestimate the global-mean sea-level acceleration. The mass contribution to sea-level rise is expected to increase further in a warming climate, and hence, this bias will also increase towards levels that possibly exceed the margins of uncertainty at individual tide-gauge locations.

To increase the accuracy of sea-level estimates, the effect of ocean-bottom deformation should be taken into account, either based on modelled estimates of ocean mass change, as was done in this study, or using more direct observations. For example, the GRACE mission allows direct estimates of global mass transport, from which ocean-bottom deformation can be computed (Ray et al., 2013), although with uncertainty associated with models of glacial isostatic adjustment (King et al., 2012). The large regional differences require caution when tide-gauge and altimetry observations are compared on a regional scale, or when regional volume changes are estimated from observations in a geocentric reference frame.

Chapter 6

Estimating decadal variability in sea level from tide gauge records: An application to the North Sea

De zee valt, de zee daalt
en brandend rijst de zon omhoog.
De bange waterdrager haalt meer water
want de zee valt droog.

De zee rijst, de zee stijgt
en langzaam daalt de zon omlaag.
De waterdrager zwoegt en hijgt,
misschien dat hij 't redt vandaag.

Want de zee moet gered van de zon.

Boudewijn de Groot

Summary

One of the primary observational datasets of sea level is represented by the tide gauge record. We propose a new method to estimate variability on decadal time scales from tide gauge data by using a state-space formulation, which couples the direct observations to a predefined state-space model by using a Kalman filter. The model consists of a time-varying trend and seasonal cycle, and variability induced by several physical processes, such as wind, atmospheric pressure changes and teleconnection patterns. This model has two advantages over the classical least-squares method that uses regression to explain variations due to known processes: a seasonal cycle with time-varying phase and amplitude can be estimated, and the trend is allowed to vary over time. This time-varying trend consists of a secular trend and low-frequency variability that is not explained by any other term in the model. As a test case, we

Parts of this chapter have been published as: Frederikse, T., Riva, R.E.M., Slobbe, D.C., Broerse, D.B.T., & Verlaan, M.: Estimating decadal variability in sea level from tide gauge records: An application to the North Sea. Journal of Geophysical Research: Oceans, doi:10.1002/2015JC011174, 2016

have used tide gauge data from stations around the North Sea over the period 1980-2013. We compare a model that only estimates a trend with two models that also remove intra-annual variability: one by means of time series of wind stress and sea level pressure, and one by using a two-dimensional hydrodynamic model. The last two models explain a large part of the variability, which significantly improves the accuracy of the estimated time-varying trend. The best results are obtained with the hydrodynamic model. We find a consistent low-frequency sea level signal in the North Sea, which can be linked to a steric signal over the northeastern part of the Atlantic.

6.1 Introduction

The tide gauge record represents the main source of information about sea-level change during the last two centuries (Gornitz et al., 1982; Douglas, 1991). Available observations are generally accurate and characterised by a dense (sub-daily) temporal sampling. However, their local nature in combination with a sparse and uneven spatial distribution largely limits the accuracy of global and regional sea-level change estimates (Woodworth et al., 2009).

In an effort to increase the achievable accuracy, many studies have focussed on estimating linear trends of sea-level change at secular scales (Douglas, 1991; Holgate, 2007; Church and White, 2011; Calafat and Chambers, 2013; Wenzel and Schröter, 2014). Nonetheless, the presence of (multi-)decadal variability can influence estimates of long-term effects (Dangendorf et al., 2014b, 2015), especially if the record is of limited extent: Jordà (2014) argued that, with the known properties of temporally correlated noise in sea level, at least 60 years of data is needed to detect a superposed long-term trend of 2 mm/year. Moreover, the implicit assumption that the long-term behaviour of sea level can be parametrized as a linear or quadratic trend might not be justified on time scales at which significant unexplained variability is present.

We propose a new parametrization of sea-level change for individual tide gauge stations, based on a state-space formulation. This formulation partitions the signal between a set of processes defined by a prescribed state-space model. The processes in our state-space model include a time-varying trend, cyclic terms, regressors, and a residual.

The time-varying trend is not bound to a shape that is prescribed a priori, such as a linear or quadratic function: it rather represents the combined effect of secular changes and of variability at scales not captured by other terms in the model. The smoothness of the time-varying trend can be controlled by letting the residual term absorb high-frequency signals. Cyclic terms allow variations in phase and amplitude over time. These variations are mainly driven by variability in the heating and cooling of the ocean, meteorological forcing, and to a smaller extent by ice and land hydrology processes. Regressors describe the impact of meteorological effects, such as wind and pressure, and of global teleconnection patterns, such as the North Atlantic Oscillation and the Multivariate ENSO index.

State-space formulations are widely used in econometrics (Harvey, 1990), and have been introduced recently in the geoscience community by Davis et al. (2012), Laine et al. (2014), and Didova et al. (2016).

Because the time-varying trend captures both the long-term trend as well as variability on decadal scales, the method provides insight in patterns of decadal variability of mean sea level in tide gauge records after the linear effects associated with wind, pressure, and global teleconnection patterns have been modelled. The time-varying trend will therefore contain the effects of remote atmospheric forcing and large-scale steric and ocean mass effects, which typically show variability on decadal and multidecadal time scales, as well as long-term trends related to changes in the climate system (Slangen et al., 2016; Meyssignac et al., 2017).

To study the performance of the state-space model, time series from tide-gauge stations around the North Sea have been analysed. The North Sea is a shallow sea, with an average depth of approximately 90 meters, located at the European continental shelf. It has been chosen because it shows variability over a wide range of scales, high quality tide gauge data are available, and it has already been the object of an extensive study (Wahl et al., 2013). The barotropic sea-level response to wind and pressure changes in the North Sea is significant, and accounts for a large part of the variability (Dangendorf et al., 2013, 2014a), although it does not explain variability at decadal scales (Dangendorf et al., 2014b). Calafat et al. (2012) have linked the decadal variability along the European coast to the cumulative response of the ocean to longshore winds, integrated from the equator to the European coast. This signal has also been observed further North along the Norwegian coast (Calafat et al., 2013). Dangendorf et al. (2014a) have shown that the Newlyn tide gauge record, for which the decadal variability is to a large extent linked to the integrated longshore wind, can be used as a proxy for this signal in the North Sea.

Three state space models are compared: the first model consists of a time-varying trend and a residual, the second model also includes cyclic terms and makes use of regressors to reduce the unexplained signal variability, while the third model reduces variability by means of a storm surge model. The storm surge model explicitly solves the depth-integrated equations of motion over the North Sea basin, and provides a more accurate estimate of the influence of the barotropic response of sea level to meteorological processes, compared to a model that uses simple linear regression between wind stress, pressure and sea level.

In section 6.2, we briefly discuss the theory behind the state-space formulation, which is to a great extent based on Durbin and Koopman (2012). In section 6.3, the three state-space models are defined. Results for the North Sea are presented in section 6.4. Discussion and conclusions can be found in section 6.5.

6.2 The state-space formulation

The state-space model uses time series of observations to estimate trends, next to other components such as cyclic (seasonal harmonic) signals or correlations with external time series (regression). In contrast to deterministic least squares estima-

tors, it allows trends and other components to vary in time. For the observations $\mathbf{y} = y_1, .., y_n$ (e.g. the sea level observed at a specific tide gauge station) we set up the general structure of our model following Harvey (1990) and Durbin and Koopman (2012) as:

$$y_i = \mu_i + \sum_{j=1}^{J} c_{i,j} + \sum_{k=1}^{K} h_{i,k} + \zeta_i + \epsilon_i \quad \text{for } i = 1...n. \tag{6.1}$$

This state-space model consists of a trend μ_i, J cycle terms $c_{i,j}$ with periods T_{cycle_j}, K regressors $h_{i,k}$, and a residual, which comprises two components: a component ζ_i that follows an autoregressive model and an irregular component ϵ_i, which is assumed to be Gaussian distributed. The subscript i denotes the scalar value at time t_i. In most state-space literature, equations are provided for time series with equally spaced time steps. Here, we use the so-called continuous time approach, which allows for arbitrarily spaced time steps. This approach has the advantage that the sampling rate does not have to be constant, and missing observations do not have to be treated separately. In state-space models each component is defined recursively, such that the trend μ_{i+1} (where μ_i is the level of the trend at time t_i) is an update of μ_i plus a slope times the normalized time step $dt_i = \frac{t_i - t_{i-1}}{\text{mean}(t_i - t_{i-1})}$, with $\text{mean}(t_i - t_{i-1})$ the mean time step size:

$$\mu_{i+1} = \mu_i + \nu_i dt_i. \tag{6.2}$$

Time variability is introduced by the update of the slope ν_i by an added random walk term ξ_i:

$$\nu_{i+1} = \nu_i + \xi_i \sqrt{dt_i} \quad \xi_i \sim N(0, \sigma_\xi^2). \tag{6.3}$$

This results in a trend model which is known in literature as the local trend model or integrated random walk. When we set the variance of the random walk term ξ_i to zero we arrive again at the common deterministic trend model that can be solved using least squares. The cycle term c_i reads in deterministic form as:

$$c_i = \tau \cos(\lambda t_i + \phi) = c \cos(\lambda t_i) + c^* \sin(\lambda t_i). \tag{6.4}$$

τ is the amplitude, ϕ the phase offset, and $\lambda = \frac{2\pi}{T_{cycle}}$. The cycle term can be written in a recursive form using the cosine and sine addition theorems as (Harvey, 1990):

$$\begin{aligned} c_{i+1} &= c_i \cos(\lambda \cdot dt_i) + c_i^* \sin(\lambda \cdot dt_i) + \omega_i \sqrt{dt_i} \quad \omega_i \sim N(0, \sigma_\omega^2), \\ c_{i+1}^* &= -c_i \sin(\lambda \cdot dt_i) + c_i^* \cos(\lambda \cdot dt_i) + \omega_i^* \sqrt{dt_i} \quad \omega_i^* \sim N(0, \sigma_{\omega^*}^2). \end{aligned} \tag{6.5}$$

The random walk term ω_i adds time variability to the cyclic terms. Phase offset ϕ_i and amplitude τ_i can be calculated from c_i and c_i^* as:

$$\tau_i = \sqrt{c_i^2 + c_i^{*2}}. \tag{6.6}$$

$$\phi_i = -\tan^{-1} \frac{c_i^*}{c_i} - t_i \lambda \mod(2\pi). \tag{6.7}$$

The contribution h_k of a regressor x_k (the time series of an explanatory variable) with constant regression coefficient β is defined as (Durbin and Koopman, 2012):

$$h_k = \beta x_k. \tag{6.8}$$

The autoregressive part of the residual is modelled following Harvey (1990):

$$\zeta_i = \phi^{dt_i}\zeta_{i-1} + \psi_i dt_i \quad \psi_i \sim N(0, \sigma^2_\psi). \tag{6.9}$$

The generalized state-space formulation can be written as:

$$y_i = Z_i\alpha_i + \epsilon_i. \tag{6.10}$$

where Z_i is the design matrix, state vector α_i contains the unknowns and again ϵ_i is the residual or irregular component. The updates of the state α_{i+1} are written as:

$$\alpha_{i+1} = T\alpha_i + \eta_i, \tag{6.11}$$

with transition matrix T and a combined disturbance vector η_i that contains all random walk terms of the trend, cyclic, and regressor components. In case we define a model including a trend, an annual cycle ($\lambda = 2\pi$), and one regressor, the state-space model has a design matrix Z_i and state vector α_i:

$$Z_i = \begin{bmatrix} 1 & 0 & 1 & 0 & x_i & 1 \end{bmatrix}. \tag{6.12}$$

$$\alpha_i = [\mu_i \ \nu_i \ c_i \ c_i^* \ \beta_i \ \zeta_i]'. \tag{6.13}$$

For this specific model, the transition matrix reads:

$$T_i = \begin{bmatrix} 1 & dt_i & 0 & 0 & 0 & 0 \\ 0 & 1 & 0 & 0 & 0 & 0 \\ 0 & 0 & \cos(\lambda dt_i) & \sin(\lambda dt_i) & 0 & 0 \\ 0 & 0 & -\sin(\lambda dt_i) & \cos(\lambda dt_i) & 0 & 0 \\ 0 & 0 & 0 & 0 & 1 & 0 \\ 0 & 0 & 0 & 0 & 0 & \phi^{dt_i} \end{bmatrix}, \tag{6.14}$$

and the disturbance vector reads:

$$\eta_i = [0 \ \xi_i \ \omega_i \ \omega_i^* \ 0 \ \psi_i]'. \tag{6.15}$$

6.2.1 Kalman filter and smoother

The estimation $\hat{\alpha}$ of the final smoothed state vector α is done in two steps. In the first step, the Kalman filter is used to estimate the state vector $\mathbf{a}_i$ using all observations up to time step i: $\mathbf{y_i} = y_1, .., y_i$. In the second step, the final smoothed state vector $\hat{\alpha}$ is estimated from all available observations using the Kalman smoother.

First, we use the Kalman filter to recursively estimate the state vector $\mathbf{a_{i+1}}$ $[1 \cdot m]$

at each time step, using the observations $\mathbf{y_i} = y_1, .., y_i$:

$$\mathbf{a}_{i+1} = \mathrm{E}(\alpha_{i+1}|\mathbf{y_i}). \tag{6.16}$$

We also estimate the error covariance matrix P_{i+1} $[m \cdot m]$:

$$P_{i+1} = \mathrm{var}(\alpha_{i+1}|\mathbf{y_i}). \tag{6.17}$$

For each time step, the Kalman filter first estimates the prediction error v_i with variance F_i and the Kalman gain K_i:

$$v_i = y_i - Z_i\mathbf{a}_i, \tag{6.18}$$
$$F_i = Z_iP_iZ_i' + H_i, \tag{6.19}$$
$$K_i = T_iP_iZ_i'F_i^{-1}. \tag{6.20}$$

For the first time step, we initialize $\mathbf{a_1}$ with 0 and P_1 with a large number (in our case $P_1 = 10^3$). Here H_i $[1 \cdot 1]$ contains the variance of the irregular component:

$$H_i = \sigma_\epsilon^2 dt_i. \tag{6.21}$$

Q [m x m] contains the disturbance variances:

$$Q_i = I\sigma_{\eta_i}^2 dt_i. \tag{6.22}$$

Using the estimated prediction error, variance, and the Kalman gain, the filtered state $\mathbf{a}_{i+1}$ and covariance matrix P_{i+1} for the next time step are predicted:

$$\mathbf{a}_{i+1} = T_i\mathbf{a}_i + K_iv_i, \tag{6.23}$$
$$P_{i+1} = T_iP_i(T_i - K_iZ_i)' + R_iQ_iR_i'. \tag{6.24}$$

R_i is an identity matrix (e.g. Durbin and Koopman, 2012).

The estimate $\mathbf{a}_i$ of the state vector α_i improves progressively using information up to $\mathbf{y}_{i-1} = y_1, ..., y_{i-1}$. Since the state vector estimate $\mathbf{a}_i$ is now only based on the information from time steps $\mathbf{y_{i-1}}$, we can improve the state estimate by using the information from all time steps. We use a state smoother that provides a smoothed estimate $\hat{\alpha}$ of the state α and error covariance V_t, based on all available observations $\mathbf{y} = y_1, .., y_n$:

$$\hat{\alpha_i} = \mathrm{E}(\alpha_i|\mathbf{y}), \tag{6.25}$$

and its error covariance matrix:

$$V_i = \mathrm{var}(\alpha_i|\mathbf{y}). \tag{6.26}$$

The state smoother computes smoothed estimates using the following steps (De Jong,

1989; Durbin and Koopman, 2012):

$$\begin{aligned} L_i &= T_i - K_i Z_i, && (6.27)\\ \mathbf{r}_{i-1} &= Z_i' F_i^{-1} v_i + L_i' \mathbf{r}_i, && (6.28)\\ N_{i-1} &= Z_i F_i^{-1} Z_i + L_i' N_i L_i, && (6.29)\\ \hat{\alpha_i} &= \mathbf{a}_i + P_i \mathbf{r}_{i-1}, && (6.30)\\ V_i &= P_i - P_i N_{i-1} P_i. && (6.31) \end{aligned}$$

with $\mathbf{r}_n$ and N_n equal to 0.

The disturbances ϵ_i and $\eta_\mathbf{i}$ can also be estimated using all available observations:

$$\begin{aligned} \hat{\epsilon_i} &= \mathrm{E}(\epsilon_i|\mathbf{y}), && (6.32)\\ \hat{\eta_i} &= \mathrm{E}(\eta_i|\mathbf{y}). && (6.33) \end{aligned}$$

Following the method of Koopman (1993) and chapter 4.5 of Durbin and Koopman (2012), this estimation is performed using the a backward recursion for $i = n, ..1$:

$$\begin{aligned} u_i &= F_i^{-1} v_i - K_i' \mathbf{r}_i, && (6.34)\\ D_i &= F_i^{-1} + K_i' N_i K_i, && (6.35)\\ N_{i-1} &= Z_i' D_i Z_i + T_i' N_i - Z_i' K_i' N_i T_i - T_i' N_i K_i Z_i, && (6.36)\\ r_{i-1} &= Z_i' u_i + T_i' \mathbf{r}_i, && (6.37)\\ \hat{\epsilon}_i &= H_i u_i, && (6.38)\\ \hat{\eta}_i &= Q_i R_i' \mathbf{r}_i. && (6.39) \end{aligned}$$

6.2.2 Estimation of state variance, process variance, and the autoregressive coefficient

Because the variance of the residual σ_ϵ^2 and the variance of the disturbances of each component σ_η^2, as well as the AR parameter ϕ, are unknowns we have to estimate them a priori. We statistically optimize these variances by maximizing the likelihood $\mathscr{L}(\mathbf{y})$ of the data, given the variances of the process noise and disturbance noise, defined as:

$$\mathscr{L}(\mathbf{y}) = \mathrm{p}(y_1, ..., y_n|\sigma_\epsilon^2, \sigma_\eta^2, \phi). \tag{6.40}$$

More specific, the $\log \mathscr{L}$ is maximized, which equals (Schweppe (1965), chapter 7.2 of Durbin and Koopman (2012)):

$$\log \mathscr{L}(\mathbf{y}) = -\frac{n}{2}\log(2\pi) - \frac{1}{2}\sum_{t=1}^{n}\left(\log|F_t| + v_t' F_t v_t\right). \tag{6.41}$$

For the variance parameters we maximize the log likelihood using the Estimation-Maximization (EM) algorithm (Shumway and Stoffer, 1982; Watson and Engle, 1983; Koopman, 1993), which iteratively updates the variances by maximizing the log like-

lihood of the data until convergence has been reached:

$$\sigma^2_{\epsilon,\text{new}} = \sigma^2_{\epsilon,\text{old}} + \sigma^2_{\epsilon,\text{old}} \frac{1}{n} \sum_{t=1}^{n} \left(u_t^2 - D_t\right) \sigma^2_{\epsilon,\text{old}}, \tag{6.42}$$

$$\sigma_{\eta,\text{new}} = \sigma^2_{\eta,\text{old}} + \sigma^2_{\eta,\text{old}} \frac{1}{n-1} \sum_{t=1}^{n} \left(\mathbf{r}_{i-1}\mathbf{r}'_{i-1} - N_{i-1}\right) \sigma^2_{\eta,\text{old}}. \tag{6.43}$$

This iterative procedure will result in a local maximum of the log likelihood for the process and noise variances, which requires a good initial guess, because more local maxima may be present. The iterations include runs of the Kalman filter and the disturbance filter that provides values for D_i and N_i.

The autoregressive coefficient ϕ is estimated by detecting the maximum of the log-likelihood for ϕ in the domain $(0,\ 1)$.

6.2.3 Mean trend and confidence intervals

When the integrated random walk term of the trend σ^2_ξ is non-zero (equation 6.3), the estimated trend will not have a constant slope. If we nevertheless want to estimate an average trend from the time-varying trend, we can integrate the slope ν over the complete time interval Δt. Following equation 6.2, we obtain

$$\overline{\nu} = \frac{1}{\Delta t} \left(\mu_n - \mu_1\right). \tag{6.44}$$

The standard deviations of the averaged slope can be derived using standard propagation of uncertainty using the standard deviation of the time variable mean σ_{μ_i} from the smoothed state covariance matrix V and the auto-covariance of the smoothed slope $\sigma_{\mu_{i,j}}$.

$$\sigma_{\overline{\nu}} = \frac{1}{\Delta t} \sqrt{\sigma^2_{\mu_1} + \sigma^2_{\mu_n} - 2\sigma_{\mu_1,\mu_n}}. \tag{6.45}$$

The auto-covariance matrix of the smoothed state $(\sigma_{\mu_{i,j}})$ is defined as (De Jong (1989) or section 4.7 of Durbin and Koopman (2012)):

$$\text{cov}(\hat{\alpha}_i, \hat{\alpha}_j) = P_i L'_i L'_{i+1} \cdots L'_{j-1} (I - N_{j-1} P_j) \quad j \geq i. \tag{6.46}$$

6.3 Three state-space models to parameterise regional sea-level changes

The available sea-level observations at a specific tide gauge location are coupled to the various processes that cause variability by a state-space model. The state-space model defines the regressors and cycles that are included in the analysis. We use three different state-space models: model A estimates a time-varying trend and

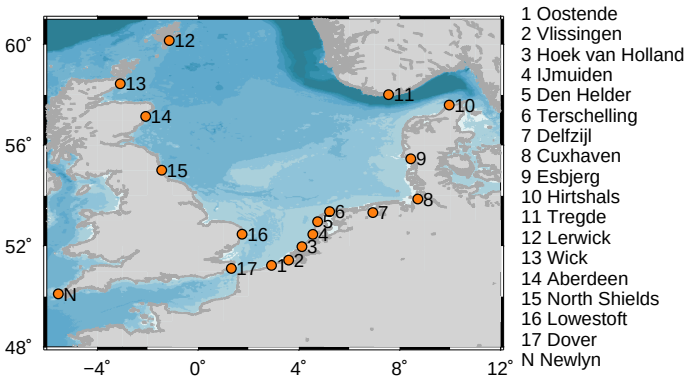

Figure 6.1: Location of the 17 tide gauge stations around the North Sea

noise. Model B also includes cycle and regressor terms. Model C is similar to model B, except that it uses the results from a storm surge model that calculates the barotropic sea-level response to wind, atmospheric pressure and tides as a regressor.

6.3.1 Model A: time-varying trend only

Model A parametrizes the sea level as a time-varying trend plus a residual:

$$y_i = \mu_i + \zeta_i + \epsilon_i. \tag{6.47}$$

In this equation, y_i are the observations of the sea level at time steps t_i. μ_i is the time-varying trend. This time-varying trend contains the time-mean of the series, the long-term trend, and multi-annual variability. Note that μ_i is expressed in mm and not in mm/yr. The residual term consists of an autoregressive part ζ_i and an irregular part ϵ_i, and contains variability that is not explained by the time-varying trend μ_i.

6.3.2 Model B: trend, cycles and regressors

In model B we extend model A by adding cyclic terms and regressors. The regressors account for variability in the sea level caused by various known processes. We estimate sea level as a linear combination of the individual contributions.

Two cyclic terms are used in this model: an annual and a semi-annual cycle. The annual cycle found in tide gauge records is caused by a sum of effects, including a seasonal cycle in sea water temperature, atmospheric forcing (Plag and Tsimplis, 1999), freshwater fluxes from land hydrology, and the tidal constituent SA (Solar Annual) (Pugh and Woodworth, 2014). Since these processes, except for the tidal component, are only approximately represented by a sinusoid, the phase offset and the amplitude of this cycle are treated as stochastic. Therefore, the phase offset and amplitude are allowed to vary over time. The semi-annual cycle is caused by the tidal constituent SSA (Solar semi-annual), and by a part of the seasonal signal.

The amplitude and the phase offset of the semi-annual cycle are also regarded as stochastic. Next to the annual and semi-annual tidal cycle, the nodal cycle with a period of 18.6 years is present in the astronomical equilibrium tide, and some authors suggest a significant influence on sea-level variability (Baart et al., 2011). To incorporate the effect of the nodal cycle on sea level, it has been added to the list of regressors with a fixed phase offset following the equilibrium law, as suggested by Proudman (1960) and (Woodworth, 2012):

$$C_{\text{nodal}} = \cos\left(\frac{2\pi\,(t_i - t_0)}{18.61}\right), \tag{6.48}$$

where C_{nodal} is the regressor, t_i the time at each time step in years, and t_0 is 1922.7 years. This cycle should produce a positive regression coefficient on latitudes smaller than 35°, and a negative regression coefficient on higher latitudes, according to the equilibrium law.

Next to the nodal tide, regressors account for variability caused by wind stress, atmospheric pressure, and variability associated with global teleconnection patterns. For the regressors that account for wind stress and atmospheric pressure, monthly mean time series have been obtained from ERA-interim, a global reanalysis product (Dee et al., 2011). By selecting grid points that are within one degree of the station and at sea and taking their average, a monthly time series is constructed. Note that, although the response to wind is not purely local, taking a larger averaging area, for example 4 degrees, does not lead to a significantly different fraction of variability explained. The regressor of pressure represents the inverse barometer effect, so the spatial-mean pressure over the ocean is calculated for each month, and subtracted from the local pressure, as described by Wunsch and Stammer (1997).

Following Calafat and Chambers (2013), we add monthly mean series of 3 global teleconnection patterns to the list of regressors: the North Atlantic Oscillation (NAO), the Pacific Decadal Oscillation (PDO) and the Multivariate El Niño-Southern Oscillation index (MEI). The NAO measures the differences in the anomalies of the sea-level pressure between subtropical and Arctic regions in the Atlantic Ocean (Hurrell et al., 2003). The PDO is defined by anomalies of ocean water temperatures in the Pacific Ocean (Mantua et al., 1997). The MEI represents the variability caused by El Niño events (Wolter and Timlin, 1993).

For each station, the significance of the correlation between each regressor and the observed sea level is calculated. Only regressors with a significant correlation are used in the state-space model for a specific station, which is enforced by only accepting regressors that are statistically significant at the 99% level.

We also require that each regressor solves a specific part of the variability that is independent from other regressors. This requirement is tested by adding the regressors stepwise into a least-squares model with an intercept, linear trend, and cycles without varying phase offset and amplitude, starting with the regressor that has the highest correlation with sea level. Each regressor is only allowed when the regression coefficient is significant at the 95% level, which is determined using t-statistics

under the assumption of white noise. If all regressors are included, the model reads:

$$\begin{aligned} y_i &= \mu_i + a_{1,i}\cos(2\pi f_1 t_i + \phi_{1,i}) + a_{2,i}\cos(2\pi f_2 t_i + \phi_{2,i}) \\ &\quad + b_1 \cdot u_{\text{wind}} + b_2 \cdot v_{\text{wind}} + b_3 \cdot (p - p_0) \\ &\quad + c_1 \cdot \text{NAO} + c_2 \cdot \text{MEI} + c_3 \cdot \text{PDO} \\ &\quad + d \cdot C_{\text{nodal}} + \zeta_i + \epsilon_i \end{aligned} \tag{6.49}$$

The annual cycle term is represented by $a_{1,i}\cos(2\pi f_1 t_i + \phi_{1,i})$, with $a_{1,i}$ the time-varying amplitude, fixed frequency $f_1 = 1y^{-1}$ and time-varying phase offset $\phi_{1,i}$. The term $a_{2,i}\cos(2\pi f_2 t_i + \phi_{2,i})$ represents the semi-annual cycle, also with a stochastic amplitude and phase offset. The cycle terms are implemented as in equation 6.5. The terms u_{wind}, v_{wind} are time series of the local zonal and meridional wind stress. p is the local pressure and p_0 is the monthly mean pressure over all oceans. The terms NAO, MEI, and PDO represent time series of the teleconnection patterns mentioned before. The term C_{nodal} represents the nodal cycle. The time-varying unknowns that are estimated by the state-space formulation are μ, a_1, ϕ_1, a_2 and ϕ_2. The unknowns b_1, b_2, b_3, c_1, c_2, c_3, and d are also estimated by the state-space formulation, but they are not allowed to vary over time.

6.3.3 Model C: corrections from a storm surge model

In model C, the barotropic response of sea level to wind stress, pressure changes, and tidal forces is modelled using the Dutch Continental Shelf Model (DCSM) version 6. The modelled sea-level height time series at the grid point closest to the tide gauge is subsequently added as a regressor. When adding the modelled water height as a regressor, rather than subtracting it from the observed water level, the uncertainty of the fitting parameter is taken into account in the error analysis of the state-space model. DCSM v6 (Zijl et al., 2013) is a two-dimensional hydrodynamic model that solves the depth-integrated shallow water equations over the North Sea continental shelf, ranging from 15°W to 13°E and from 43°N to 64°N with a horizontal grid spacing of about 1/40° in the east-west direction and 1/60° in the north-south-direction, which leads to a grid cell length of about 1 nautical mile. The model has been developed to forecast storm surge heights along the North Sea coast. The vertical boundaries are forced with wind stress at the top, and surface friction at the bottom. The horizontal boundaries are closed using a no-normal-flow condition at coastal boundaries. At the open boundaries, the sea surface height is prescribed, which is calculated from astronomical tides, mean sea level, and barotropic sea-level anomalies. Next to the diurnal and semi-diurnal tides, the long-period tidal constituents SSA (period of 182.6 days), MM (27.6 days), MSF (14.8 days), MF (13.7 days) and MTM (9.2 days) are prescribed. Before 1993, the barotropic sea-level anomalies are approximated by the inverse barometer correction, and computed from the ERA-Interim sea-level pressure fields. After 1993, the barotropic sea-level anomalies are taken from the barotropic model MOG2D (Carrère and Lyard, 2003). The surface drag coefficient has also been obtained from ERA-interim.

The use of a hydrodynamic model has the advantage over the method with re-

gressors for wind and pressure, that non-linear effects are taken into account, and that the interaction between tides and surges is explicitly solved.

Because the model is barotropic, height variations due to sea water temperature and salinity changes are still present in the signal after removing the modelled sea level, including the part of the seasonal cycle that is caused by steric effects. Furthermore, the long-term constituent SA and the nodal cycle are not forced at the boundaries. Hence, a stochastic annual and semi-annual cycle are added to the state-space model, together with the nodal cycle term.

The teleconnection patterns NAO, PDO and MEI are also added as a regressor. Each regressor is tested for significance using stepwise addition. If all terms are significant, model C reads:

$$\begin{aligned} y_i &= \mu_i + a_{1,i}\cos(2\pi f_1 t_i + \phi_{1,i}) + a_{2,i}\cos(2\pi f_2 t_i + \phi_{2,i}) \\ &\quad + b \cdot y_{\mathrm{DCSM}} \\ &\quad + c_1 \cdot \mathrm{NAO} + c_2 \cdot \mathrm{MEI} + c_3 \cdot \mathrm{PDO} \\ &\quad + d \cdot C_{\mathrm{nodal}} + \zeta_i + \epsilon_i \end{aligned} \tag{6.50}$$

where y_{DCSM} is the modelled water height at the specific tide gauge station.

6.3.4 Linear least squares models

In order to better evaluate the behaviour of the state-space models, we have also analyzed three models that can be solved by linear least squares. In models AL, BL, and CL, the time-varying trend μ_i is replaced by a linear trend and a bias, and the cyclic terms (in BL and CL) are not stochastic. The regressors are the same as in the corresponding state-space models.

6.4 Results and discussion for the North Sea

The three state-space models have been applied to tide gauges surrounding the North Sea. 17 tide gauge stations have been selected that meet the criterion for data availability of more than 75 percent during the interval 1980-2013. The stations, with their identification number, are depicted in Figure 6.1. The time span has been chosen to match the period for which ERA-interim reanalysis data are available, which is used as source for the regressor time series of wind and pressure and serves as input for DCSM. Furthermore, the series are long enough to capture at least one full nodal cycle. Monthly mean sea-level data has been obtained from the Permanent Service for Mean Sea Level (Holgate et al., 2013). All heights are relative to the PSMSL Revised Local Reference datum. For the Cuxhaven tide gauge, time series that are corrected for the conversion between mean sea level and mean tide level are used, following the method of Wahl et al. (2011).

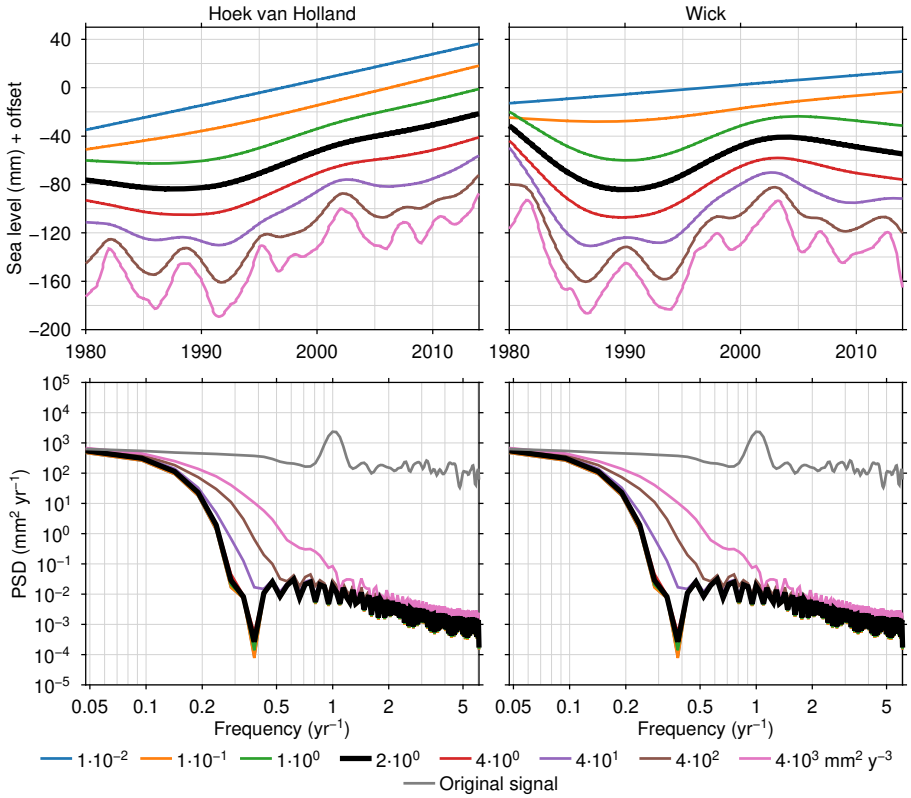

Figure 6.2: Top: Time-varying trend for different values for the slope disturbance variance parameter for the stations Terschelling and Wick using model C. Bottom: Power Spectral Density (PSD) of the time-varying trend and the original time series. Welch's method has been used to estimate the PSD.

6.4.1 Choice of the variance parameters

The choice of the disturbance variance parameters σ_ϵ^2 and σ_η^2 in the state-space formulation has an influence on the final result. The disturbance variance parameters of the cycle terms and the irregular component are determined using the EM-algorithm, as described in section 6.2.2. The initial values for the disturbance variance terms σ_η^2 are low, which ensures that when a local maximum of the log-likelihood is found, the variance in the parameters will not be overestimated. An overestimation could lead to the absorption of non-seasonal signals into the cycle terms. To make sure that the time-varying trend consists of long-term variations and variability on scales longer than a few years, the slope disturbance variance parameter is fixed, and a constant value is used for all stations. The slope disturbance variance parameter has been chosen in such a way that variability on decadal and longer scales is represented by the time-varying trend, while variability on shorter time scales that is not explained by the cycle and regressor terms will be captured by the residual term. The time-varying trends calculated using various values of the slope disturbance variance parameter

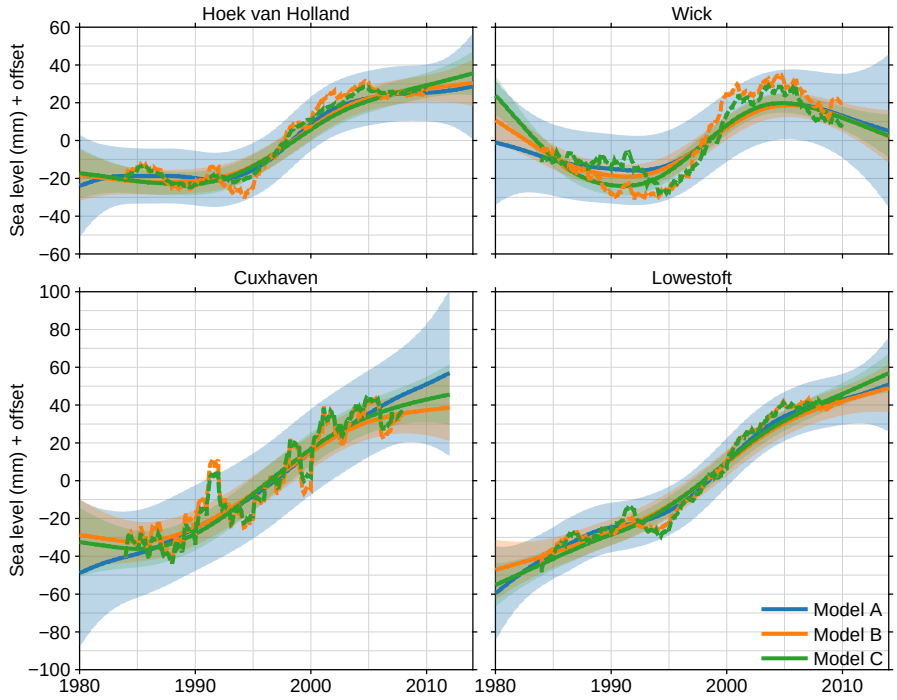

Figure 6.3: Trends and 68 %-level confidence intervals for state-space models A, B, and C. The dashed line denotes the 8-year moving average of the trend and residual of models BL and CL.

for stations Wick and Hoek van Holland are shown in Figure 6.2, together with the Power Spectral Densities (PSD's) of the time-varying trends. The figure shows that for a higher slope disturbance variance parameter, details at shorter time scales are revealed. Since for this study, we are interested in variability on decadal and longer scales, and higher disturbance variance parameters cause larger confidence intervals, we choose a slope variance parameter of 2 mm^2/y^3 for model C. With this value the time-varying trend shows almost no subdecadal variability, but still captures the decadal variability. The PSD's (lower panel of the same figure) quantitatively show that the signals on time scales of 10 years and longer are preserved, while short-term variability on time scales of 7 years and lower is removed for the chosen slope variance parameter. For model B, we use the same value for the slope disturbance variance parameter, because the same range of signals are captured in the time-varying trend. For model A, a parameter of 20 mm^2/y^3 is used, for which μ contains signals in the same frequency range as in model B and C.

To check whether the choice of the slope disturbance variance parameter influences the estimates of the regression coefficients and the phase and amplitude of the cycle terms, we have calculated the relative standard deviation of these numbers over the range of parameters in Figure 6.2. All relative standard deviations are smaller than one percent, which shows that the influence of the slope disturbance variance parameter on the estimation of the regression coefficients and cycle terms is low.

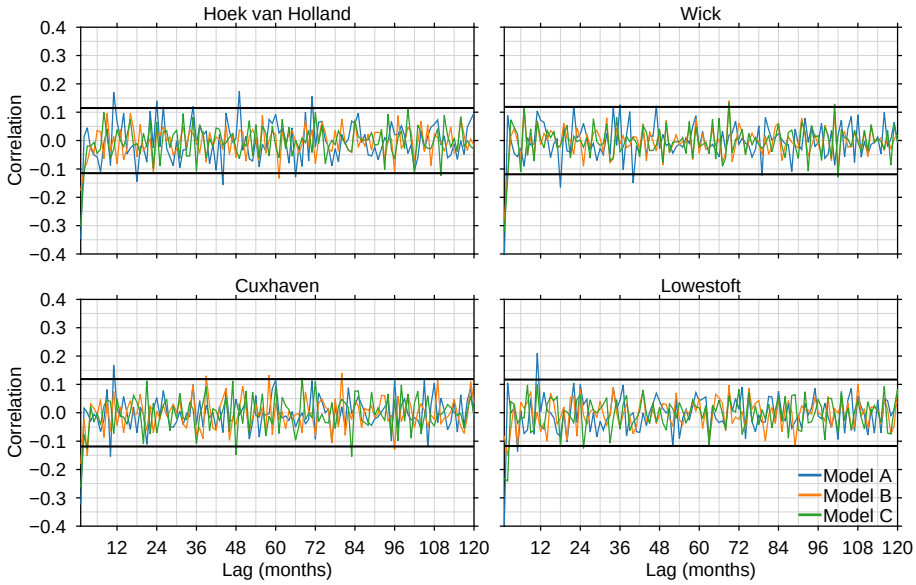

Figure 6.4: Lag autocorrelation of the irregular component for model A,B, and C. The black line represents the threshold for a significant correlation on the 95-%-level

6.4.2 Model comparison

The time-varying trends $\mu(t)$, with the 68% confidence interval from model A, B, and C for the stations Hoek van Holland, Cuxhaven, Wick and Lowestoft are shown in Figure 6.3. The picture also shows the 8-year moving average of the trend plus residual for models BL and CL. Moving average filters are commonly used to analyse inter-annual and decadal variability in sea level. The filter width of 8 years is chosen to match the frequency response of the state-space filter, that has a cut-off frequency at about 8 years.

For all stations, the confidence interval of the time-varying trend for the three state-space models overlap. Oscillating patterns on decadal time scales are visible in all three models, and the found patterns are very similar between the three models. The oscillatory pattern of model C does not differ significantly from the pattern of model B and A, except for the first and last few months of the series, where the confidence intervals are large. Models B and C have a much smaller confidence interval for all 4 stations compared to A, and therefore, we will focus on models B and C in the next sections.

The moving averages from models BL and CL show a similar pattern of variability, although some high-frequency signals remain visible. There are however differences visible between the patterns of BL and CL, especially for Cuxhaven and Wick. Models B and C show a similar pattern at these stations. Moreover, models B and C do not require data interpolation, and the confidence intervals, computed using the full variance-covariance structure, provide insight into the significance of the oscillations.

To ensure the correct functioning of the state-space method, two additional re-

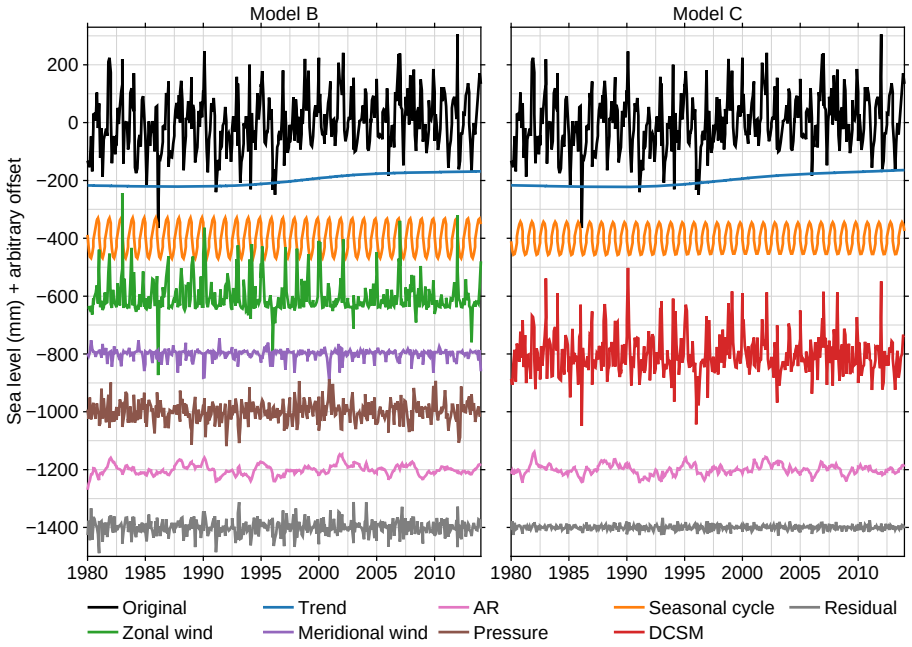

Figure 6.5: Individual components of the state-space model B (left) and C (right) for Hoek van Holland

quirements have to be fulfilled: the irregular part of the residuals has to follow a Gaussian distribution, and should not exhibit serial correlation. The first requirement is tested using a Kolmogorov-Smirnov test. On the 95%-level, none of the stations fail the test for model B, three for model C, but eight for model A. Therefore, the estimates of the formal errors for model A might be inaccurate. The second requirement is tested by calculating the lag-n-autocorrelation, with $n = 1..120$, which covers the variability at time scales that are not captured by the time-varying trend. The resulting autocorrelation functions for the four mentioned stations are shown in Figure 6.4. From the plot it can be seen that the irregular component does not show a statistically significant autocorrelation over the tested period.

The individual terms contributing to the signal of models B and C for Hoek van Holland are depicted in Figure 6.5. The residual of model C is clearly smaller than the residual of model B, which is due to the fact that DCSM is able to simulate the barotropic response to wind more accurately than the regressor model. Also note that at Hoek van Holland, the phase and amplitude of the seasonal cycle do not show large variations with time.

6.4.3 Patterns of decadal variability in the North Sea

With the state-space method we can show decadal sea-level variability at each tide gauge station. Hence, analyzing the time-varying trend obtained from the state-space models allows to look for common patterns of decadal variability. The time-varying

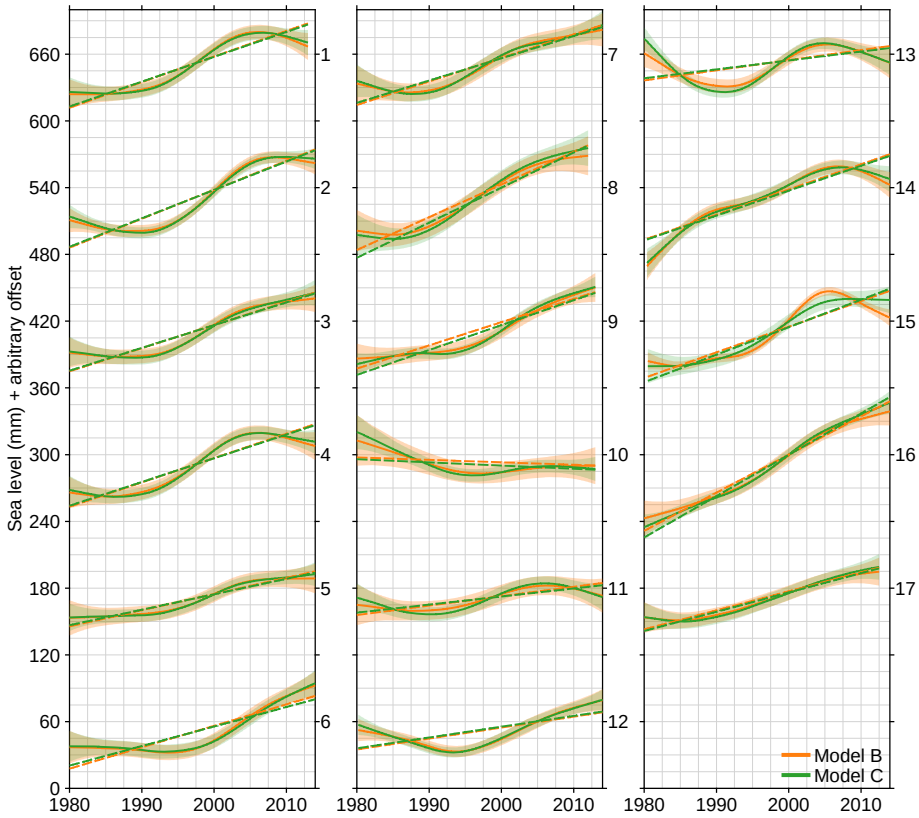

Figure 6.6: The time-varying trend calculated for model B (Orange) and C (Green) for all stations. The shaded area is the confidence interval for the time-varying trend at the 68 % level. The dashed lines depict the linear trend from models BL and CL. The station numbers are according to Figure 6.1.

trends from model B and C for all stations are shown in Figure 6.6. Almost all stations show similar behaviour: the highest rates of sea-level rise are found between 1995 and 2005, while after 2005 rates are much lower and for some stations even negative.

The inflection point around 2005 corresponds to a peak in the nodal cycle (Woodworth, 2012; Pugh and Woodworth, 2014). In both state-space models, the nodal cycle is present as possible regressor, which allows us to test whether the nodal cycle is responsible for the 2005 inflection point. We find for all stations a slightly negative correlation between the sea-level height and the nodal cycle. The negative correlation is expected, since all stations lie outside the 35°-zone, for which the astronomical amplitude of the nodal cycle given in equation 6.48 should be negative. However, on average the correlation coefficient between sea level and the regressor of the nodal tide is very low (-0.07). For all stations, except Aberdeen, for which a cycle with an amplitude of 25 mm was found, the correlation is not significant, according to p-statistics on a 95 percent level. This means that the deceleration after 2005 cannot be linked to the nodal cycle. Furthermore, according to the tidal equilibrium law, the

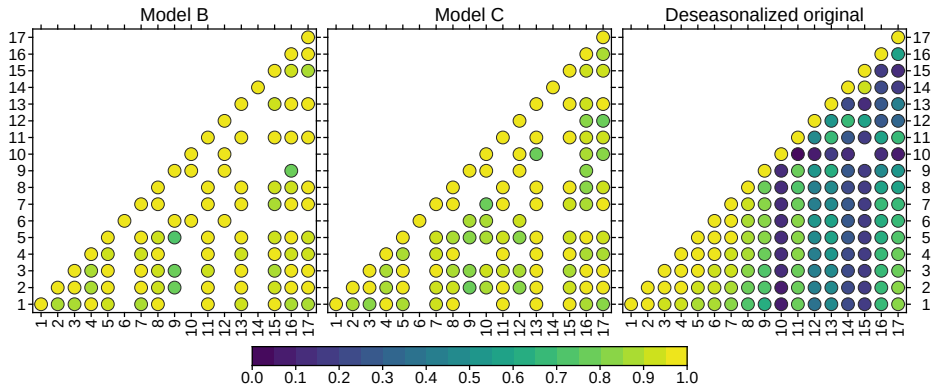

Figure 6.7: Correlation coefficient between de-trended time-varying trends from different stations for model B (left), model C (middle) and deseasonalized original data (right). Correlations that are lower than 0 or insignificant on the 95 % level are blank. The stations are numbered according to Figure 6.1.

nodal cycle in the North Sea has an amplitude of about 6 mm, considerably lower than the typical amplitude of the found variability, which is on the order of 20 mm. It is unlikely that the phase and amplitude of the nodal cycle would depart significantly from the equilibrium tide (Woodworth, 2012). The significant cycle in Aberdeen has an amplitude four times as large as the equilibrium value. Hence, the correlation is likely not caused by the nodal tide, but to a process with variability at a comparable temporal scale. Therefore, the nodal cycle is not used as a regressor.

The correlation of monthly and yearly tide gauge data between different North Sea stations is well-known (Wahl et al., 2013). In order to explicitly show similarities in the decadal variability over the whole North Sea, the correlation coefficient between the time-varying trends of all stations is calculated and shown in Figure 6.7. To prevent correlations due to long-term sea-level rise, the correlation coefficient has been calculated after removing the integrated trend. To determine the threshold for significance, the number of degrees of freedom is reduced to 5, which is based on an 8-year low-pass filter. This number of degrees of freedom leads to a threshold for significance of 0.76 at the 95 % level. We also show the correlation coefficients of the original sea-level data, after removing a linear trend and seasonal cycle in Figure 6.7. Most stations show a significant positive correlation of the time-varying trend with all other stations. The stations in the southern North Sea show a high mutual correlation, both on the Dutch and Belgian coast (stations 1-5) as well as the stations on the south part of the English coast (stations 15, 16, 17). The stations at the Wadden Sea (6,7) and in the German Bight (7,8,9) are not as strongly correlated with the southern stations.

Some stations show no significant correlation with any other station: station 14 (Aberdeen) does not show any significant correlation with other, even adjacent, stations. Also station 6 (Terschelling) has generally low correlations with almost all other stations. The German Bight consist of many shallow seas that are subject to rapid changes in bathymetry and current patterns, which could explain the regional

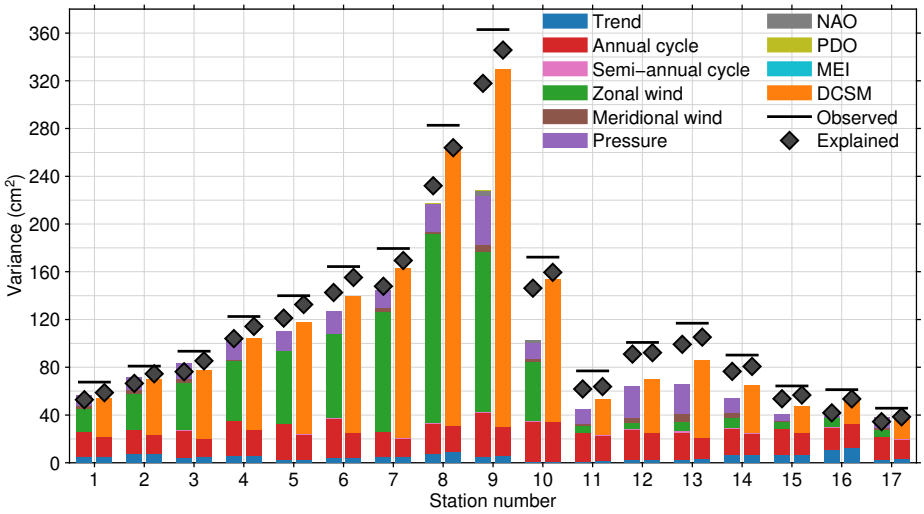

Figure 6.8: Total and explained variance per individual component: the black bar shows the variance of the observed sea level for each station, and the bar shows the variance of the individual components. The grey diamond shows the total explained variance. For each station, the left bar represents model B, and the right bar model C. The explained variance per component is defined as described in Dangendorf et al. (2013).

differences and the relatively low mutual correlation of decadal sea-level variability.

When we compare between the correlations of the time-varying trend and the original data, a different pattern can be seen. For example, the correlation between original data from stations along the Dutch coast show low correlation with stations in northern Great Britain (stations 12-15), while for the time-varying trend this correlation is higher. This difference shows the presence of a basin-wide signal of variability on decadal scales, which cannot be found without removing variability from known processes.

6.4.4 Sources of variability

Model B and C explain a large part of the variability in tide gauge observations, which leads to an improved estimate of the sea-level variability on decadal time scales that is unexplained by the regressors. The portion of the variability that is solved for each regressor is not equal for all stations. Figure 6.8 shows the variance explained by the individual terms for both models at each tide gauge station. Note that the total explained variance and the variance of the residual do not add up to the total observed variance, because the regressors and cycle terms are not mutually uncorrelated. For model B, a clear division can be seen between the stations along the south-eastern coast (1-9) and the stations at the British Isles (12-17): the stations along the south-eastern coast show a high total variability, with a peak at the stations in the German Bight (stations 7,8,9). The barotropic response to wind is one of the main contributors to this high variability, and model B and C explain a major part of

this variability. Along the British Isles, the total variability is lower, and the influence of wind is small. For all stations, the regressors for the teleconnection patterns only explain a small fraction of the variability, because the influence of the teleconnection patterns on sea level is driven to a great extent by wind and pressure (Dangendorf et al., 2013).

For all stations, the root mean square error (RMSE) of the residual from model C is smaller than the residual from model B. On average, the RMSE is 45% smaller for model C, compared to model B. Due to the larger fraction of the variability that can be explained, the confidence interval for the time-varying trend is smaller for model C than for model B. Although the typical time scale of the explained variability, which is largely atmosphere-forced, lies below 10 years (Dangendorf et al., 2014a), models B and C show a smaller confidence interval for the time-varying trend than model A.

Calafat et al. (2012, 2013) showed the existence of a consistent pattern of decadal variability along the European and Norwegian coast and linked the pattern to the integrated longshore wind. Dangendorf et al. (2014a) argue that the longshore wind signal propagates into the North Sea. They use Newlyn as a proxy for this effect and show that the combination of the Newlyn tide gauge record and remote steric forcing can explain a large part of the decadal variability in the North Sea. However, the coherent time-varying trend signal found here shows variability at longer time scales than the aforementioned studies, so the source of this variability may be different. Since the North Sea is located on a shallow continental shelf, no large local steric effect is expected. Nonetheless, remote steric changes over the much deeper North Atlantic will induce a flow of water over the shelf, affecting local sea level (Landerer et al., 2007b). To determine whether the found pattern in the time-varying trend can be linked to remote steric forcing, the correlation between the time-varying trend of the sea level at the tide gauge stations and steric height over the North Atlantic is calculated. We use the yearly mean steric height from the Ishii & Kimoto dataset (Ishii and Kimoto, 2009) to calculate a time-varying trend in the steric signal using state-space model A. Figure 6.9 shows that a large region covering the northeast Atlantic has a clear and positive correlation with the time varying trend at the North Sea stations. This finding supports the hypothesis that the observed low-frequency sea-level variability in the North Sea can be linked to a large-scale steric signal in the North Atlantic.

6.4.5 Average trends

By using equation 6.44 we can calculate average trends from the state-space model, and compare them with the results from the traditional least squares approach. The average time-varying trend contains the long-term secular trend as well as decadal variability, and does not rely on the assumption that the trend follows a linear path. Table 6.1 shows the mean trends calculated by the three state-space models, as well as the accompanying least squares solutions for all stations. The confidence intervals for the state-space models are calculated according to equation 6.45. For the least-squares fit, the confidence interval has been corrected for serial correlation by reducing the number of degrees of freedom, according to the procedure described in

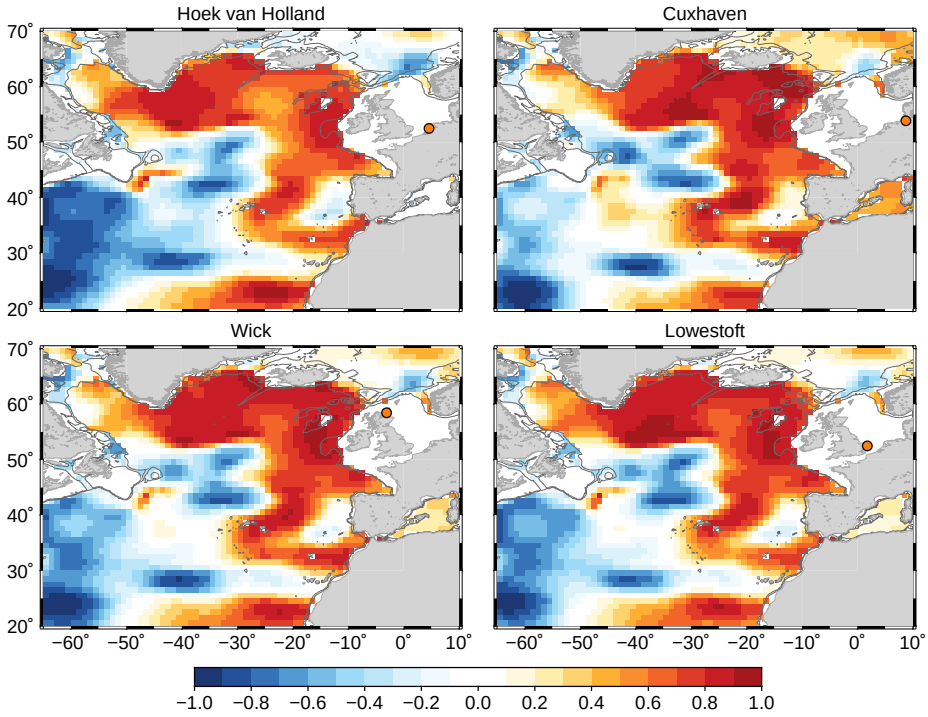

Figure 6.9: Correlation between time-varying trend in steric sea level and the time-varying sea-level trend from model C for four North Sea stations. The 250 and 1000 meter isobaths are shown in grey. No correlation is shown for grid points at a depth smaller than 250 meter. The averaged time-varying trend for each station and each grid point has been removed using equation 6.44.

Table 6.1: Mean trends and confidence intervals in mm/yr (at 68 % level) estimated for all North Sea stations for all least squares models (AL, BL, CL) and state-space models (A,B,C). Bold values denote trends for which the confidence interval of the state-space model and the accompanying linear model do not overlap.

Station	AL	BL	CL	Model A	Model B	Model C
Oostende	2.3 ± 0.4	2.4 ± 0.2	2.2 ± 0.2	1.4 ± 1.1	$\mathbf{1.3} \pm 0.5$	$\mathbf{1.3} \pm 0.5$
Vlissingen	2.4 ± 0.5	2.7 ± 0.2	2.5 ± 0.1	1.5 ± 1.0	$\mathbf{1.7} \pm 0.4$	$\mathbf{1.5} \pm 0.4$
Hoek van Holland	1.9 ± 0.5	2.3 ± 0.2	2.0 ± 0.1	1.5 ± 1.1	1.7 ± 0.5	1.6 ± 0.5
IJmuiden	1.9 ± 0.6	2.3 ± 0.2	2.1 ± 0.1	1.2 ± 1.3	$\mathbf{1.3} \pm 0.5$	$\mathbf{1.3} \pm 0.5$
Den Helder	1.1 ± 0.6	1.6 ± 0.2	1.4 ± 0.1	1.3 ± 1.4	1.2 ± 0.5	1.2 ± 0.5
Terschelling	1.5 ± 0.7	2.0 ± 0.2	1.7 ± 0.1	2.2 ± 1.5	1.8 ± 0.5	1.7 ± 0.5
Delfzijl	1.6 ± 0.7	2.2 ± 0.3	2.0 ± 0.2	1.5 ± 1.4	1.5 ± 0.6	1.5 ± 0.6
Cuxhaven	3.0 ± 1.0	3.1 ± 0.4	3.1 ± 0.2	3.2 ± 1.8	2.1 ± 0.8	2.4 ± 0.8
Esbjerg	1.9 ± 1.1	1.9 ± 0.4	2.2 ± 0.2	2.8 ± 1.9	1.8 ± 0.6	2.0 ± 0.4
Hirtshals	-0.1 ± 0.8	-0.2 ± 0.3	-0.3 ± 0.2	0.7 ± 1.6	-0.7 ± 0.8	-1.0 ± 0.5
Tregde	0.8 ± 0.5	0.8 ± 0.2	0.7 ± 0.2	0.7 ± 1.3	0.3 ± 0.7	0.1 ± 0.5
Lerwick	1.3 ± 0.6	1.0 ± 0.2	1.0 ± 0.2	2.0 ± 1.4	0.9 ± 0.4	0.7 ± 0.4
Wick	1.0 ± 0.6	0.8 ± 0.2	0.8 ± 0.2	0.1 ± 1.5	$\mathbf{-0.3} \pm 0.6$	$\mathbf{-0.7} \pm 0.4$
Aberdeen	2.1 ± 0.5	2.2 ± 0.2	2.3 ± 0.2	2.1 ± 1.3	2.2 ± 0.7	2.3 ± 0.5
North Shields	2.2 ± 0.4	2.3 ± 0.2	2.5 ± 0.2	1.7 ± 1.2	$\mathbf{1.1} \pm 0.3$	1.9 ± 0.6
Lowestoft	3.4 ± 0.4	3.5 ± 0.2	3.7 ± 0.2	3.3 ± 1.0	3.0 ± 0.4	3.3 ± 0.4
Dover	1.5 ± 0.4	1.7 ± 0.2	1.5 ± 0.1	0.6 ± 1.0	1.2 ± 0.6	1.1 ± 0.6

Nerem and Mitchum (2002). All the confidence intervals are calculated at the 68% confidence level.

At a number of stations, the average time-varying trend is statistically different (at the 68 % level) from the least squares trend. Variability on decadal scales is responsible for this difference, by leaking into the estimate of a long-term linear trend. In Figure 6.3 it can be seen that the variability has a low phase roughly between 1985 and 1995, and a high phase between 1995 and 2010, which causes a positive bias on the estimate of a linear trend. Therefore, linear trends estimated from 30 to 40 years of tide gauge data do not only represent a long-term trend, but also a bias due to decadal variability.

The averaged trends for the three state-space models show that the trends found by model B and C lie within the confidence interval of the trend from model A for all stations. The average trends of model B and C are also very similar: there are no stations for which the confidence intervals do not overlap. Of the three state-space models, model C shows the smallest confidence interval, averaged over all stations. The explanation of variability caused by the various meteorological components of models B and C, leads to a significant improvement of the accuracy of the estimated trend, compared to the estimation without explaining the various variability terms (model A).

6.5 Conclusions

We have introduced a new parametrization for time series of observed sea level that takes the presence of unexplained variability on decadal and multidecadal scales into account, which does not rely on the assumption that the underlying long-term trend is linear or quadratic. The time-varying trend captures long-term trends in sea level, as well as variability on decadal and multidecadal scales. Three state-space models have been compared using tide gauge data from stations around the North Sea over the period 1980-2013. It is shown that the removal of variability caused by known processes, including the barotropic response to wind and atmospheric pressure changes, contributes to the disclosure of unexplained variability: the state-space models that explain parts of the variability perform significantly better than a model that only estimates a long-term trend and a residual. Explaining variability does not only reduce the confidence interval for the estimated time-varying trend, but also reveals an oscillating pattern in sea level on decadal scales. Two models have been compared that remove the variability: one uses regressors from global reanalysis databases, and one uses DCSM, a two-dimensional shallow-water model that calculates sea-level changes due to wind, atmospheric pressure and tides. The model that uses DCSM is able to explain a larger part of the variability and estimates a time-varying trend with a smaller confidence interval, compared to the model that uses regressors. The advantage of the model that uses regressors from global reanalysis products, is that it can be used globally, opposed to the DCSM model, which only provides data for the North Sea.

The time-varying trends in sea level for the stations around the North Sea show

oscillations, that are consistent over the full basin, although the variability patterns caused by wind and pressure differ between stations. The sea level shows a steep rise between 1995 and 2005, followed by a slowdown between 2005 and 2013. The removal of atmospheric effects either by a simple linear regression or by a barotropic storm surge model reduces the uncertainty in the time-varying trend to an extent that the amplitude of the resulting decadal pattern is larger than the confidence interval of the time-varying trend. It is found that the pattern is not caused by the nodal cycle, but can be linked to a large-scale steric signal that covers the North-eastern part of the Atlantic ocean.

A drawback of the proposed method is that the extracted decadal signal depends on the chosen slope disturbance variance parameter, as shown in Figure 6.2. Alternatively, this parameter could be estimated using the EM algorithm, but the estimated slope disturbance variance parameter varies substantially between nearby stations. Therefore, the resulting estimate of the time-varying trend shows variability on different temporal scales, and hence, represents different physical processes. Therefore, we decided to keep this parameter fixed at a prescribed value for all stations. For other regions, a different slope disturbance variance parameter may be required to capture the relevant decadal signals. Other parameter estimation techniques, such as Markov-chain Monte Carlo (Laine et al., 2014), or a global optimization (Didova et al., 2016), may result in more consistent estimates of the slope disturbance variance parameter.

The presence of low-frequency variability influences the estimation of linear trends over short intervals, even after removing the barotropic response to wind and pressure. Variability on decadal (and multidecadal) scales that can not be linked to individual processes leaks into the estimate of a long term linear trend when the length of the analyzed sea-level record has a length of the same order as the typical time scale of unexplained variability. Furthermore, there is no reason to expect that on (multi-)decadal time scales, sea level is rising along a linear or quadratic path. In order to find the long-term behaviour of sea level, the processes that cause the variability and long-term trend have to be understood.

Chapter 7

Conclusions and recommendations

SOLLICITATIEPLICHT

je kan altijd nog
ROOKMELDER worden
... 'Hee mense!!...
...ROOK!!...
ROOK!!... ROOK!!

Ted Wesselo

In Chapter 1 a set of five research objectives have been formulated. In this chapter, the extent to which these research objectives have been reached is discussed. Furthermore, a list of recommendations on how this work, and sea-level science as a whole can be improved and extended are discussed.

7.1 Conclusions

1. **Can the sea-level budget be closed on a regional scale?**

   This question is discussed in Chapters 2 and 3.

   Based on two case studies, one along the Northern European coast of the Atlantic Ocean (Chapter 2), and one on the Atlantic coasts of North America (Chapter 3), it is possible to close the sea-level budget on a regional scale well within the margins of uncertainty: in both cases, the observed trends and decadal variability have been explained by the sum of contributors. However, the methods that have been developed to estimate the contributions from ocean dynamics do require prior knowledge about the dynamic processes that affect the trends and decadal variability of regional sea level. For the European coast, longshore wind-driven coastally-trapped waves travel northward along the continental shelf edge, and dominate sea-level variability on decadal scales. Westward-radiating Rossby-waves result in open-ocean adjustment to these coastally-trapped waves. Hence, information on the open-ocean density can be used as a proxy for this wind-driven signal.

For the West Atlantic coast, a similar adjustment takes place, although along the western ocean boundary, the waves travel southward. These waves are driven by variability at high latitudes, and the steric signal in the Subpolar gyre can serve as a proxy for this signal. Hence, for both regions, instead of the steric signal in the nearby open ocean, coastal sea-level variability has a remote driver that must be known or identified beforehand to estimate the impact of ocean dynamics on the regional sea-level budget. Its contribution forms a substantial part of the total linear trend, and in both cases, dominates the variability on decadal scales.

The contributions of mass loss in Antarctica before the nineties and density changes in the deep oceans are very uncertain due to a lack of observations and we assume no contribution from these sources and still found closure of the sea-level budget for both locations. Hence, the contributions of pre-nineties Antarctica and deep-ocean steric expansion to sea-level changes are probably limited.

Another opportunity that arises from determining the sea-level budget on regional scales is to assess the extent in which specific processes affect sea level. For the North Sea, the role of the 18.6-year nodal cycle in mean sea level had not been fully quantified yet. An analysis using the residual sea level after subtracting all mass and dynamic terms shows that the 18.6-year nodal cycle is present and detectable in the North Sea and along the Norwegian coast. The phase and amplitude of the observed nodal cycle do not deviate substantially from tidal equilibrium, which confirms the expectations from Proudman (1960) and Woodworth (2012), at least for the North Sea and along the Norwegian coast. Therefore, it is not needed to use a least squares estimator to determine the phase and amplitude of the nodal cycle, which is not a reliable method, since variability signals with similar frequencies, but different origins may be attributed to the nodal cycle.

2. **How can local sea-level and vertical land-motion observations be combined into reconstructions of regional sea level in a self-consistent manner?**

This question is discussed in Chapters 2, 3, and 4.

Since elastic and visco-elastic deformation of the solid earth affects both vertical land motion and relative sea level, both quantities are not independent. The epochs of sea-level and land-level observations often do not coincide, which could cause a bias if tide-gauge observations are corrected for vertical land motion without taking non-linear deformation into account. To prevent this bias, we have developed a framework that combines land-level and sea-level observations in a consistent way: the framework separates vertical land motion into a fraction that is explained by GIA and present-day mass transport, and an unexplained fraction. The fraction explained by present-day mass loss is non-linear on multi-decadal time scales, and hence, its decadal trend over the VLM observation record is not representative for the longer-term trend. The tide gauge observations are therefore only corrected for the unexplained part

of the observed vertical land motion. With this correction, the resulting corrected tide-gauge record still observes the effects of GIA and present-day mass redistribution in a relative sea level frame.

Although considerable uncertainty still exists in this method, we have reduced the uncertainty due to the non-linearity of solid-earth deformation driven by present-day mass transport. This term can be of considerable size, when the region of interest is close to locations of large land ice mass changes, such as Northwestern Europe.

3. **Can we improve estimates of global and basin-mean sea-level changes by using prior information of regional variations?**

   This question is discussed in Chapter 4.

   Since tide gauges sample the spatially and temporary-varying sea-level field, it is very challenging to estimate global sea level from a limited number of observations that are unevenly distributed along the ocean boundaries. Using a novel method, which combines the aforementioned separation of vertical land motion in an explained and unexplained part together with estimates of how local sea-level changes deviate from basin-mean sea-level changes, we reconstructed basin-mean and global-mean sea-level changes over 1958-2014. We found a smaller global sea-level rise over this period, compared to some of the most-cited global sea-level reconstructions. Our 1.5 ± 0.2 mm/yr trend is consistent with the 1.3 ± 0.1 mm/yr trend in the sum of contributors, which implies that the sea-level budget over this period can be closed. The observed sea-level acceleration of 0.06 ± 0.01 mm/yr^2 agrees with the sum of contributors, which shows an acceleration of 0.07 ± 0.01 mm/yr^2 over 1958-2014.

   We find that the resulting sea-level curve becomes different after the corrections have been applied: correcting for the regional deviations for GIA and present-day mass transport causes a higher estimate of GMSL, compared to the uncorrected estimate. The correction for vertical land motion result in a decrease of the estimated GMSL trend.

4. **How does deformation of the solid earth affect sea-level observations by tide gauges, GPS, and altimetry?**

   This question is discussed in Chapter 5.

   Based on estimates of mass transport resulting from ice mass loss, dam retention, and groundwater depletion, global and basin-mean ocean bottom deformation can be computed from the elastic sea-level equation. We find that in a geocentric reference frame, the ocean bottom subsides under the increasing load. Due to this present-day mass transport, the ocean bottom globally subsides by about 0.13 mm/yr. This subsidence results in a difference between geocentric and relative sea level equal to the rate of bottom deformation. Therefore, global-mean absolute sea level underestimates the total change in ocean volume caused by present-day mass transport. The underestimation of 0.13 mm/yr equals 8 percent of the total barystatic contribution. Since satellite

altimetry observes geocentric sea level, its global-mean sea-level change estimate due to mass transport is biased low. The error is reduced by the fact that altimeters do not observe sea level at high latitudes, where the difference between geocentric and relative sea level is the largest. Another source of uncertainty is geocenter motion, caused by present-day mass transport. Due to this geocenter motion, the ocean bottom deformation signal depends on whether the reference frame of the observations is relative to the centre-of-mass, which is often only approximately the case (Riddell et al., 2017). On regional scales, the difference between geocentric and relative sea-level trends increases to values up to 0.4 mm/yr. Hence, care must be taken if ocean volume is estimated from altimetry. The same issue affects VLM-corrected tide gauge records, although the spatial distribution of tide gauges result in a smaller effect, compared to global altimetry. The sampling bias in high-quality tide gauges, reported by Thompson et al. (2016), is also found using more than 600 PSMSL tide gauge locations, and global-mean sea level estimated from tide gauges, either corrected or uncorrected for vertical land motion, is biased low.

5. **How can a state-space model be used to avoid the assumption of a prescribed shape of the long-term trend in tide gauge records?**

   This question is discussed in Chapter 6.

   We have used a state-space approach to model sea-level variations at individual tide gauge locations. The advantage of such a model is that the effects of individual regressors, such as local wind stress or large-scale atmospheric teleconnections, can be co-estimated, with a long-term trend that does not have a prescribed functional model. The method provides robust error estimates. We have shown that the method allows for detection of basin-mean features on decadal and multi-decadal scales in the North Sea that can be linked to large-scale patterns in the ocean.

7.2 Recommendations

- The regional sea-level budget studies that have been performed show that for the European Shelf and the Northwestern Atlantic coast, contemporary regional sea-level changes are reasonably understood. Since these studies depend on knowledge of regional drivers of dynamic variability, they cannot be performed as an automatic task. Increasing the number of case studies may provide insight in regional changes at more locations, as well as determine regions and ocean basins in which observed sea-level changes can not be explained by the contributors. A quick scan suggests that for many locations, including Hawaii, Bermuda, and, the American Pacific coast, the proposed sea-level budget approach leads to promising results. For many island tide gauges, the observed sea-level variability can be explained well by using just the observed steric changes around the islands as dynamic contributor. Along the American Pacific Coast, using the dynamic signal that propagates as an equatorial Kelvin wave before it travels counterclockwise along the ocean boundary, a reasonable fit may be obtained. Increasing the number of locations for which a regional sea-level budget estimate can be achieved may lead to insight into regional biases that may be attributable to deep-ocean warming or Antarctic ice mass loss, both processes for which no direct observations before the nineties are available.

- The spatio-temporal variability of ocean dynamics is one of the major sources of the difference between local, regional, and global sea-level changes. Hence, if we are able to separate the local dynamic variability from variability on longer spatial scales, we can remove a major source of uncertainty in tide gauge reconstructions. Unfortunately, the resolution of most ocean models and reanalyses is not large enough to explicitly solve the relevant physical processes, including internal dynamics and coastally-trapped waves, and generally, the skill of these models in explaining local variability at tide gauge locations is low. Luckily, the increase in the availability of computational power allows eddy-resolving models to be run over multiple decades. With these higher horizontal resolutions, more relevant coastal processes are explicitly resolved, which results in a higher model skill with respect to coastal sea-level changes. Incorporating this prior information into reconstructed sea levels at multiple scales could help to improve the reliability of these reconstructions.

- Lack of data still forms a substantial source of uncertainty in sea-level reconstructions. As already noted by many others, undigitized tide gauge information is stored in data archives and maritime institutes. Succesful attempts of data rescue (for example Hogarth, 2014) have been done in the past. Especially in sparsely sampled regions, mostly in the Southern Hemisphere, additional tide gauge records can have a very high added value for our understanding of global sea-level changes.

- More and more tide gauges are equipped with permanent GPS receivers, although the majority of tide gauges are still unequipped. Since at many lo-

cations local vertical land motion can not be explained by known processes, a group of geodesist and sea-level scientists recently urged authorities to increase the efforts to equip tide-gauge stations with co-located and co-referenced GPS receivers (Woodworth et al., 2017). An increase of the number of tide-gauge stations equipped with GPS receivers will reduce the uncertainties in both regional and global reconstructions, and will be of great help to improve the knowledge about causes of local sea-level changes.

One of the problems with these GPS stations is the presence of large jumps in their time series, which adversely affect the capability to determine accurate linear trends of vertical land motion (Gazeaux et al., 2013). A consistent way of avoiding or documenting jumps is therefore to be welcomed.

- In this work, it is assumed that the GPS and altimetry observations are relative to the centre-of-mass (CM) reference frame. Therefore, the modelled solid-earth and geoid response to present-day mass transport are modelled in a CM reference frame. Due to geocenter motion, the CM frame differs from the centre-of-figure (CF) frame, which translates into differences in the degree-1 spherical harmonics in the geoid and solid-earth deformation fields between both reference frames. The satellite orbits and GPS positions are provided in an ITRF reference frame (Ablain et al., 2015; Blewitt et al., 2016). For ITRF reference frames, geocenter motion is modelled as a linear trend (Altamimi et al., 2016), and hence, forms a possible extra source of uncertainty (Riddell et al., 2017; Santamaría-Gómez et al., 2017). Hence, to increase the consistency between the modelled and observed geoid changes and solid-earth deformation, a common reference frame for both could be of help for eliminating this potential source of uncertainty.

- For the North Sea, decadal wind-driven variability plays a major role in sea-level changes on the long run. However, since the resolution of most climate models is too coarse to explicitly resolve the underlying physical processes, it is unknown how a changing wind climate will affect sea-level variability caused by alongshore wind stress. To improve forecasts of mean sea-level changes in a future climate in the North Sea and along the Norwegian coast, changes in the alongshore wind stress could be coupled to sea-level changes. This coupling may result in changes in the regional projections.

- The largest potential for future global-mean sea-level rise is the Antarctic Ice Sheet. However, the mass balance of this ice sheet remains uncertain due to the sparse observations. The improved knowledge of the other contributors for sea-level changes, together with the fingerprints for Antarctic ice mass loss may be combined to estimate its temporal evolution, or at least, provide bounds on the magnitude of the mass changes.

- One of the underlying assumptions that is frequently made when VLM estimates are used to complement the tide gauge observations is that the information recorded over a relatively short time span is representative for longer

periods. The study of Featherstone et al. (2015) discusses non-linear vertical land motion at the Fremantle tide gauge, and shows that the linearity assumption may cause errors. It may be worthwhile to investigate the non-linear land movements at more locations, especially at tide gauge locations with long records that have a large weight in sea-level reconstructions.

- A disadvantage of the state-space approach presented in Chapter 6, is that the temporal scales of the variability represented by the resulting time-varying trends depend on the choice of the slope disturbance variance parameter, which was prescribed in our approach. To eliminate the need of manually prescribing this paramater, an automated recipe to estimate an appropriate slope disturbance variance parameter from the tide-gauge data is desirable. The EM algorithm did not succeed in obtaining a consistent parameter for tide-gauge records that show very similar signals. Research into alternative methods to estimate this parameter may be helpful to solve this issue.

Bibliography

A, G., Wahr, J., and Zhong, S.: Computations of the viscoelastic response of a 3-D compressible Earth to surface loading: an application to Glacial Isostatic Adjustment in Antarctica and Canada, Geophysical Journal International, 192, 557–572, doi:10.1093/gji/ggs030, 2013.

Ablain, M., Cazenave, A., Larnicol, G., Balmaseda, M., Cipollini, P., Faugére, Y., Fernandes, M. J., Henry, O., Johannessen, J. A., Knudsen, P., Andersen, O., Legeais, J., Meyssignac, B., Picot, N., Roca, M., Rudenko, S., Scharffenberg, M. G., Stammer, D., Timms, G., and Benveniste, J.: Improved sea level record over the satellite altimetry era (1993-2010) from the Climate Change Initiative project, Ocean Science, 11, 67–82, doi:10.5194/os-11-67-2015, 2015.

Ablain, M., Legeais, J. F., Prandi, P., Marcos, M., Fenoglio-Marc, L., Dieng, H. B., Benveniste, J., and Cazenave, A.: Satellite Altimetry-Based Sea Level at Global and Regional Scales, Surveys In Geophysics, 38, 7–31, doi:10.1007/s10712-016-9389-8, 2017.

Altamimi, Z., Rebischung, P., Métivier, L., and Collilieux, X.: ITRF2014: A new release of the International Terrestrial Reference Frame modeling nonlinear station motions, Journal of Geophysical Research: Solid Earth, 121, 6109–6131, doi:10.1002/2016JB013098, 2016.

Andersen, O. B. and Knudsen, P.: DNSC08 mean sea surface and mean dynamic topography models, Journal of Geophysical Research: Oceans, 114, C11 001, doi:10.1029/2008JC005179, 2009.

Andres, M., Gawarkiewicz, G. G., and Toole, J. M.: Interannual sea level variability in the western North Atlantic: Regional forcing and remote response, Geophysical Research Letters, 40, 5915–5919, doi:10.1002/2013GL058013, 2013.

Baart, F., Van Gelder, P. H., De Ronde, J., Van Koningsveld, M., and Wouters, B.: The effect of the 18.6-year lunar nodal cycle on regional sea-level rise estimates, Journal of Coastal Research, 28, 511–516, doi:10.2112/JCOASTRES-D-11-00169.1, 2011.

Bamber, J. and Riva, R. E. M.: The sea level fingerprint of recent ice mass fluxes, The Cryosphere, 4 (4), 2010, doi:10.5194/tc-4-621-2010, 2010.

Bentsen, M., Bethke, I., Debernard, J. B., Iversen, T., Kirkevåg, A., Seland, Ø., Drange, H., Roelandt, C., Seierstad, I. A., Hoose, C., and Kristjánsson, J. E.: The Norwegian Earth System Model, NorESM1-M - Part 1: Description and basic evaluation of the physical climate, Geoscientific Model Development, 6, 687–720, doi:10.5194/gmd-6-687-2013, 2013.

Bingham, R. J. and Hughes, C. W.: The relationship between sea-level and bottom pressure variability in an eddy permitting ocean model, Geophysical Research Letters, 35, doi:10.1029/2007GL032662, 2008.

Bingham, R. J. and Hughes, C. W.: Signature of the Atlantic meridional overturning circulation in sea level along the east coast of North America, Geophysical Research Letters, 36, L02 603, doi:10.1029/2008GL036215, 2009.

Bingham, R. J. and Hughes, C. W.: Local diagnostics to estimate density-induced sea level variations over topography and along coastlines, Journal of Geophysical Research: Oceans, 117, C01 013, doi:10.1029/2011JC007276, 2012.

Blewitt, G., Kreemer, C., Hammond, W. C., and Gazeaux, J.: MIDAS robust trend estimator for accurate GPS station velocities without step detection, Journal of Geophysical Research: Solid Earth, 121, 2054–2068, doi:10.1002/2015JB012552, 2016.

Boening, C., Willis, J. K., Landerer, F. W., Nerem, R. S., and Fasullo, J.: The 2011 La Niña: So strong, the oceans fell, Geophysical Research Letters, 39, doi:10.1029/2012GL053055, 2012.

Boon, J. D.: Evidence of sea level acceleration at US and Canadian tide stations, Atlantic Coast, North America, Journal of Coastal Research, 28, 1437–1445, doi:10.2112/JCOASTRES-D-12-00102.1, 2012.

Bos, M. S., Fernandes, R. M. S., Williams, S. D. P., and Bastos, L.: Fast error analysis of continuous GNSS observations with missing data, Journal of Geodesy, 87, 351–360, doi:10.1007/s00190-012-0605-0, 2013.

Bos, M. S., Williams, S. D. P., Araújo, I. B., and Bastos, L.: The effect of temporal correlated noise on the sea level rate and acceleration uncertainty, Geophysical Journal International, 196, 1423–1430, doi:10.1093/gji/ggt481, 2014.

Calafat, F. M. and Chambers, D. P.: Quantifying recent acceleration in sea level unrelated to internal climate variability, Geophysical Research Letters, 40, 3661–3666, doi:10.1002/grl.50731, 2013.

Calafat, F. M., Chambers, D. P., and Tsimplis, M. N.: Mechanisms of decadal sea level variability in the eastern North Atlantic and the Mediterranean Sea, Journal Of Geophysical Research: Oceans, 117, doi:10.1029/2012JC008285, 2012.

Calafat, F. M., Chambers, D. P., and Tsimplis, M. N.: Inter-annual to decadal sea-level variability in the coastal zones of the Norwegian and Siberian Seas: The role of atmospheric forcing, Journal of Geophysical Research: Oceans, 118, 1287–1301, doi:10.1002/jgrc.20106, 2013.

Calafat, F. M., Chambers, D. P., and Tsimplis, M. N.: On the ability of global sea level reconstructions to determine trends and variability, Journal Of Geophysical Research: Oceans, 119, 1572–1592, doi:10.1002/2013JC009298, 2014.

Carrère, L. and Lyard, F.: Modeling the barotropic response of the global ocean to atmospheric wind and pressure forcing - comparisons with observations, Geophysical Research Letters, 30, 1275–1, doi:10.1029/2002GL016473, 2003.

Chambers, D. P., Merrifield, M. A., and Nerem, R. S.: Is there a 60-year oscillation in global mean sea level?, Geophysical Research Letters, 39, doi:10.1029/2012GL052885, 2012.

Chambers, D. P., Cazenave, A., Champollion, N., Dieng, H., Llovel, W., Forsberg, R., von Schuckmann, K., and Wada, Y.: Evaluation of the Global Mean Sea Level Budget between 1993 and 2014, Surveys in Geophysics, pp. 1–19, doi:10.1007/s10712-016-9381-3, 2016.

Chao, B. F., Wu, Y. H., and Li, Y. S.: Impact of artificial reservoir water impoundment on global sea level., Science, 320, 212–4, doi:10.1126/science.1154580, 2008.

Chaussard, E., Amelung, F., Abidin, H., and Hong, S.-H.: Sinking cities in Indonesia: ALOS PALSAR detects rapid subsidence due to groundwater and gas extraction, Remote Sensing of Environment, 128, 150–161, doi:10.1016/j.rse.2012.10.015, 2013.

Chen, X., Zhang, X., Church, J. A., Watson, C. S., King, M. A., Monselesan, D., Legresy, B., and Harig, C.: The increasing rate of global mean sea-level rise during 1993–2014, Nature Climate Change, 7, 492–495, doi:10.1038/nclimate3325, 2017.

Cheng, L. and Zhu, J.: Benefits of CMIP5 Multimodel Ensemble in Reconstructing Historical Ocean Subsurface Temperature Variations, Journal of Climate, 29, 5393–5416, doi:10.1175/JCLI-D-15-0730.1, 2016.

Cheng, L., Trenberth, K. E., Palmer, M. D., Zhu, J., and Abraham, J. P.: Observed and simulated full-depth ocean heat-content changes for 1970–2005, Ocean Science, 12, 925–935, doi:10.5194/os-12-925-2016, 2016.

Cheng, M., Tapley, B. D., and Ries, J. C.: Deceleration in the Earth's oblateness, Journal of Geophysical Research: Solid Earth, 118, 740–747, doi:10.1002/jgrb.50058, 2013.

Chimot, J., Vlemmix, T., Veefkind, J. P., de Haan, J. F., and Levelt, P. F.: Impact of aerosols on the OMI tropospheric NO_2 retrievals over industrialized regions: how accurate is the aerosol correction of cloud-free scenes via a simple cloud model?, Atmospheric Measurement Techniques, 9, 359–382, doi:10.5194/amt-9-359-2016, 2016.

Chimot, J., Veefkind, J. P., Vlemmix, T., de Haan, J. F., Amiridis, V., Proestakis, E., Marinou, E., and Levelt, P. F.: An exploratory study on the aerosol height retrieval from OMI measurements of the 477nm O_2-O_2 spectral band using a neural network approach, Atmospheric Measurement Techniques, 10, 783–809, doi:10.5194/amt-10-783-2017, 2017.

Church, J. A. and White, N. J.: Sea-Level Rise from the Late 19th to the Early 21st Century, Surveys In Geophysics, 32, 585–602, doi:10.1007/s10712-011-9119-1, 2011.

Church, J. A., White, N. J., Konikow, L. F., Domingues, C. M., Cogley, J. G., Rignot, E., Gregory, J. M., van den Broeke, M. R., Monaghan, A. J., and Velicogna, I.: Revisiting the Earth's sea-level and energy budgets from 1961 to 2008, Geophysical Research Letters, 38, doi:10.1029/2011GL048794, 2011.

Church, J. A., Clark, P. U., Cazenave, A., Gregory, J. M., Jevrejeva, S., Levermann, A., Merrifield, M. A., Milne, G. A., Nerem, R. S., Nunn, P. D., Payne, A. J., Pfeffer, W. T., Stammer, D., and Unnikrishnan, A. S.: Sea Level Change: The Physical Science Basis. Contribution of Working Group I to the Fifth Assessment Report of the Intergovernmental Panel on Climate Change, chap. 13, pp. 1137–1216, Cambridge University Press, Cambridge, United Kingdom and New York, NY, USA, doi:10.1017/CBO9781107415324.026, 2013.

Clark, J. A. and Lingle, C.: Future sea-level changes due to West-Antarctic ice sheet fluctuations, Nature, 269, 206–209, doi:10.1038/269206a0, 1977.

Compo, G. P., Whitaker, J. S., Sardeshmukh, P. D., Matsui, N., Allan, R. J., Yin, X., Gleason, B. E., Vose, R. S., Rutledge, G., Bessemoulin, P., et al.: The twentieth century reanalysis project, Quarterly Journal of the Royal Meteorological Society, 137, 1–28, doi:10.1002/qj.776, 2011.

Dangendorf, S., Mudersbach, C., Wahl, T., and Jensen, J.: Characteristics of intra-, inter-annual and decadal sea-level variability and the role of meteorological forcing: the long record of Cuxhaven, Ocean Dynamics, 63, 209–224, doi:10.1007/s10236-013-0598-0, 2013.

Dangendorf, S., Calafat, F. M., Arns, A., Wahl, T., Haigh, I. D., and Jensen, J.: Mean sea level variability in the North Sea: Processes and implications, Journal of Geophysical Research: Oceans, 119, doi:10.1002/2014JC009901, 2014a.

Dangendorf, S., Rybski, D., Mudersbach, C., Müller, A., Kaufmann, E., Zorita, E., and Jensen, J.: Evidence for long-term memory in sea level, Geophysical Research Letters, 41, 5530–5537, doi:10.1002/2014GL060538, 2014b.

Dangendorf, S., Marcos, M., Müller, A., Zorita, E., Riva, R., Berk, K., and Jensen, J.: Detecting anthropogenic footprints in sea level rise, Nature Communications, 6, 7849, doi:10.1038/ncomms8849, 2015.

Dangendorf, S., Marcos, M., Wöppelmann, G., Conrad, C. P., Frederikse, T., and Riva, R.: Reassessment of 20th century global mean sea level rise, Proceedings of the National Academy of Sciences, doi:10.1073/pnas.1616007114, 2017.

Davis, J. L. and Mitrovica, J. X.: Glacial isostatic adjustment and the anomalous tide gauge record of eastern North America, Nature, 379, 331–333, doi:10.1038/379331a0, 1996.

Davis, J. L., Wernicke, B. P., and Tamisiea, M. E.: On seasonal signals in geodetic time series, Journal of Geophysical Research: Solid Earth, 117, doi:10.1029/2011JB008690, 2012.

de Boer, B., van de Wal, R. S. W., Bintanja, R., Lourens, L. J., and Tuenter, E.: Cenozoic global ice-volume and temperature simulations with 1-D ice-sheet models forced by benthic δ18O records, Annals of Glaciology, 51, 23–33, doi:10.3189/172756410791392736, 2010.

De Jong, P.: Smoothing and interpolation with the state-space model, Journal of the American Statistical Association, 84, 1085–1088, doi:10.1080/01621459.1989.10478876, 1989.

DeConto, R. M. and Pollard, D.: Contribution of Antarctica to past and future sea-level rise, Nature, 531, 591–597, doi:10.1038/nature17145, 2016.

Dee, D. P., Uppala, S. M., Simmons, A. J., Berrisford, P., Poli, P., Kobayashi, S., Andrae, U., Balmaseda, M. A., Balsamo, G., Bauer, P., et al.: The ERA-Interim reanalysis: Configuration and performance of the data assimilation system, Quarterly Journal of the Royal Meteorological Society, 137, 553–597, doi:10.1002/qj.828, 2011.

Didova, O., Gunter, B., Riva, R., Klees, R., and Roese-Koerner, L.: An approach for estimating time-variable rates from geodetic time series, Journal Of Geodesy, 90, 1207–1221, doi:10.1007/s00190-016-0918-5, 2016.

Dieng, H. B., Champollion, N., Cazenave, A., Wada, Y., Schrama, E., and Meyssignac, B.: Total land water storage change over 2003–2013 estimated from a global mass budget approach, Environmental Research Letters, 10, 124 010, doi:10.1088/1748-9326/10/12/124010, 2015.

Dobslaw, H., Flechtner, F., Bergmann-Wolf, I., Dahle, C., Dill, R., Esselborn, S., Sasgen, I., and Thomas, M.: Simulating high-frequency atmosphere-ocean mass variability for dealiasing of satellite gravity observations: AOD1B RL05, Journal of Geophysical Research: Oceans, 118, 3704–3711, doi:10.1002/jgrc.20271, 2013.

Douglas, B. C.: Global sea level rise, Journal of Geophysical Research: Oceans, 96, 6981–6992, doi:10.1029/91JC00064, 1991.

Durack, P. J., Wijffels, S. E., and Gleckler, P. J.: Long-term sea-level change revisited: the role of salinity, Environmental Research Letters, 9, 114 017, doi:088/1748-9326/9/11/114017, 2014.

Durbin, J. and Koopman, S. J.: Time series analysis by state space methods, vol. 38, OUP Oxford, 2012.

Dziewonski, A. M. and Anderson, D. L.: Preliminary reference Earth model, Physics of the Earth and Planetary Interiors, 25, 297–356, doi:10.1016/0031-9201(81)90046-7, 1981.

Elderfield, H., Ferretti, P., Greaves, M., Crowhurst, S., McCave, I. N., Hodell, D., and Piotrowski, A. M.: Evolution of ocean temperature and ice volume through the mid-Pleistocene climate transition., Science, 337, 704–9, doi:10.1126/science.1221294, 2012.

Engelhart, S. E., Horton, B. P., Douglas, B. C., Peltier, W. R., and Törnqvist, T. E.: Spatial variability of late Holocene and 20th century sea-level rise along the Atlantic coast of the United States, Geology, 37, 1115–1118, doi:10.1130/G30360A.1, 2009.

Ezer, T.: Sea level rise, spatially uneven and temporally unsteady: Why the U.S. East Coast, the global tide gauge record, and the global altimeter data show different trends, Geophysical Research Letters, 40, 5439–5444, doi:10.1002/2013GL057952, 2013.

Ezer, T.: Detecting changes in the transport of the Gulf Stream and the Atlantic overturning circulation from coastal sea level data: The extreme decline in 2009-2010 and estimated variations for 1935-2012, Global and Planetary Change, 129, 23–36, doi:10.1016/j.gloplacha.2015.03.002, 2015.

Ezer, T. and Corlett, W. B.: Is sea level rise accelerating in the Chesapeake Bay? A demonstration of a novel new approach for analyzing sea level data, Geophysical Research Letters, 39, L19 605, doi:10.1029/2012GL053435, 2012.

Farrell, W. E. and Clark, J. A.: On postglacial sea level, Geophysical Journal International, 46, 647–667, doi:10.1111/j.1365-246X.1976.tb01252.x, 1976.

Featherstone, W. E., Penna, N. T., Filmer, M. S., and Williams, S. D. P.: Nonlinear subsidence at Fremantle, a long-recording tide gauge in the Southern Hemisphere, Journal of Geophysical Research: Oceans, 120, 7004–7014, doi:10.1002/2015JC011295, 2015.

Feng, M., Li, Y., and Meyers, G.: Multidecadal variations of Fremantle sea level: Footprint of climate variability in the tropical Pacific, Geophysical Research Letters, 31, doi:10.1029/2004GL019947, 2004.

Fenoglio-Marc, L., Rietbroek, R., Grayek, S., Becker, M., Kusche, J., and Stanev, E.: Water mass variation in the Mediterranean and Black Seas, Journal of Geodynamics, 59, 168–182, doi:10.1016/j.jog.2012.04.001, 2012.

Fischer, J., Schott, F. A., and Dengler, M.: Boundary circulation at the exit of the Labrador Sea, Journal of Physical Oceanography, 34, 1548–1570, doi:10.1175/1520-0485(2004)034<1548:BCATEO>2.0.CO;2, 2004.

Forget, G. and Ponte, R. M.: The partition of regional sea level variability, Progress in Oceanography, 137, 173–195, doi:10.1016/j.pocean.2015.06.002, 2015.

Förste, C., Bruinsma, S., Abrikosov, O., Flechtner, F., Marty, J.-C., Lemoine, J.-M., Dahle, C., Neumayer, H., Barthelmes, F., König, R., et al.: EIGEN-6C4-The latest combined global gravity field model including GOCE data up to degree and order 1949 of GFZ Potsdam and GRGS Toulouse, in: EGU General Assembly Conference Abstracts, vol. 16, p. 3707, doi:10.5880/icgem.2015.1, 2014.

Frederikse, T., Riva, R., Kleinherenbrink, M., Wada, Y., van den Broeke, M., and Marzeion, B.: Closing the sea level budget on a regional scale: Trends and variability on the Northwestern European continental shelf., Geophysical Research Letters, 43, 10 864–10 872, doi:10.1002/2016GL070750, 2016.

Frederikse, T., Simon, K., Katsman, C. A., and Riva, R.: The sea-level budget along the Northwest Atlantic coast: GIA, mass changes and large-scale ocean dynamics, Journal of Geophysical Research: Oceans, doi:10.1002/2017JC012699, 2017.

Freeman, E., Woodruff, S. D., Worley, S. J., Lubker, S. J., Kent, E. C., Angel, W. E., Berry, D. I., Brohan, P., Eastman, R., Gates, L., et al.: ICOADS Release 3.0: a major update to the historical marine climate record, International Journal of Climatology, doi:10.1002/joc.4775, 2016.

Galassi, G. and Spada, G.: Tide gauge observations in Antarctica (1958–2014) and recent ice loss, Antarctic Science, 29, 369–381, doi:10.1017/S0954102016000729, 2017.

Gazeaux, J., Williams, S., King, M., Bos, M., Dach, R., Deo, M., Moore, A. W., Ostini, L., Petrie, E., Roggero, M., Teferle, F. N., Olivares, G., and Webb, F. H.: Detecting offsets in GPS time series: First results from the detection of offsets in GPS experiment, Journal of Geophysical Research: Solid Earth, 118, 2397–2407, doi:10.1002/jgrb.50152, 2013.

Good, S. A., Martin, M. J., and Rayner, N. A.: EN4: Quality controlled ocean temperature and salinity profiles and monthly objective analyses with uncertainty estimates, Journal of Geophysical Research:

Oceans, 118, 6704–6716, doi:10.1002/2013JC009067, 2013.

Gornitz, V., Lebedeff, S., and Hansen, J.: Global Sea Level Trend in the Past Century, Science, 215, 1611–1614, doi:10.1126/science.215.4540.1611, 1982.

Gouretski, V. and Reseghetti, F.: On depth and temperature biases in bathythermograph data: Development of a new correction scheme based on analysis of a global ocean database, Deep Sea Research Part I: Oceanographic Research Papers, 57, 812–833, doi:10.1016/j.dsr.2010.03.011, 2010.

Gregory, J. M., White, N. J., Church, J. A., Bierkens, M. F. P., Box, J. E., Van den Broeke, M. R., Cogley, J. G., Fettweis, X., Hanna, E., Huybrechts, P., et al.: Twentieth-century global-mean sea level rise: is the whole greater than the sum of the parts?, Journal of Climate, 26, 4476–4499, doi:10.1175/JCLI-D-12-00319.1, 2013.

Haigh, I. D., Wahl, T., Rohling, E. J., Price, R. M., Pattiaratchi, C. B., Calafat, F. M., and Dangendorf, S.: Timescales for detecting a significant acceleration in sea level rise, Nature Communications, 5, 3635, doi:10.1038/ncomms4635, 2014.

Häkkinen, S.: Variability in sea surface height: A qualitative measure for the meridional overturning in the North Atlantic, Journal of Geophysical Research: Oceans, 106, 13 837–13 848, doi:10.1029/1999JC000155, 2001.

Hamlington, B. D. and Thompson, P. R.: Considerations for estimating the 20th century trend in global mean sea level, Geophysical Research Letters, 42, 4102–4109, doi:10.1002/2015GL064177, 2015.

Hamlington, B. D., Thompson, P., Hammond, W. C., Blewitt, G., and Ray, R. D.: Assessing the impact of vertical land motion on 20th century global mean sea level estimates, Journal of Geophysical Research: Oceans, doi:10.1002/2016JC011747, 2016.

Hamlington, B. D., Reager, J. T., Lo, M.-H., Karnauskas, K. B., and Leben, R. R.: Separating decadal global water cycle variability from sea level rise., Scientific Reports, 7, 995, doi:10.1038/s41598-017-00875-5, 2017.

Han, G., Ohashi, K., Chen, N., Myers, P. G., Nunes, N., and Fischer, J.: Decline and partial rebound of the Labrador Current 1993-2004: Monitoring ocean currents from altimetric and conductivity-temperature-depth data, Journal of Geophysical Research: Oceans, 115, C12 012, doi:10.1029/2009JC006091, 2010.

Han, G., Ma, Z., Bao, H., and Slangen, A.: Regional differences of relative sea level changes in the Northwest Atlantic: Historical trends and future projections, Journal of Geophysical Research: Oceans, 119, 156–164, doi:10.1002/2013JC009454, 2014.

Hartmann, D. L., Klein Tank, A. M. G., Rusticucci, M., Alexander, L. V., Brönnimann, S., Charabi, Y., Dentener, F. J., Dlugokencky, E. J., Easterling, D. R., Kaplan, A., Soden, B. J., Thorne, P. W., Wild, M., and Zhai, P. M.: Observations: Atmosphere and Surface, chap. 2, pp. 159–254, Cambridge University Press, Cambridge, United Kingdom and New York, NY, USA, doi:10.1017/CBO9781107415324.008, 2013.

Harvey, A. C.: Forecasting, structural time series models and the Kalman filter, Cambridge university press, 1990.

Hay, C. C., Morrow, E., Kopp, R. E., and Mitrovica, J. X.: Probabilistic reanalysis of twentieth-century sea-level rise, Nature, 517, 481–484, doi:10.1038/nature14093, 2015.

Hay, C. C., Morrow, E. D., Kopp, R. E., and Mitrovica, J. X.: On the Robustness of Bayesian Fingerprinting Estimates of Global Sea Level Change, Journal of Climate, 30, 3025–3038, doi:10.1175/JCLI-D-16-0271.1, 2017.

Hill, E. M., Davis, J. L., Tamisiea, M. E., and Lidberg, M.: Combination of geodetic observations and models for glacial isostatic adjustment fields in Fennoscandia, Journal of Geophysical Research: Solid Earth, 115, doi:10.1029/2009JB006967, 2010.

Hinkel, J., Lincke, D., Vafeidis, A. T., Perrette, M., Nicholls, R. J., Tol, R. S. J., Marzeion, B., Fettweis, X., Ionescu, C., and Levermann, A.: Coastal flood damage and adaptation costs under 21st century sea-level rise, Proceedings of the National Academy of Sciences, 111, 3292–3297, doi:10.1073/pnas.1222469111, 2014.

Hodson, D. L. R. and Sutton, R. T.: The impact of resolution on the adjustment and decadal variability of the Atlantic meridional overturning circulation in a coupled climate model, Climate Dynamics, 39, 3057–3073, doi:10.1007/s00382-012-1309-0, 2012.

Hogarth, P.: Preliminary analysis of acceleration of sea level rise through the twentieth century using

extended tide gauge data sets (August 2014), Journal of Geophysical Research: Oceans, 119, 7645–7659, doi:10.1002/2014JC009976, 2014.

Holgate, S. J.: On the decadal rates of sea level change during the twentieth century, Geophysical Research Letters, 34, L01 602, doi:10.1029/2006GL028492, 2007.

Holgate, S. J., Matthews, A., Woodworth, P. L., Rickards, L. J., Tamisiea, M. E., Bradshaw, E., Foden, P. R., Gordon, K. M., Jevrejeva, S., and Pugh, J.: New Data Systems and Products at the Permanent Service for Mean Sea Level, Journal Of Coastal Research, 29, 493–504, doi:10.2112/JCOASTRES-D-12-00175.1, 2013.

Houston, J. R. and Dean, R. G.: Accounting for the nodal tide to improve estimates of sea level acceleration, Journal of Coastal Research, 27, 801–807, doi:10.2112/JCOASTRES-D-11-00045.1, 2011.

Hsieh, W. W. and Bryan, K.: Redistribution of sea level rise associated with enhanced greenhouse warming: a simple model study, Climate Dynamics, 12, 535–544, doi:10.1007/BF00207937, 1996.

Hughes, C. W. and Meredith, M. P.: Coherent sea-level fluctuations along the global continental slope, Royal Society of London Transactions Series A, 364, 885–901, doi:10.1098/rsta.2006.1744, 2006.

Hughes, C. W. and Williams, S. D. P.: The color of sea level: Importance of spatial variations in spectral shape for assessing the significance of trends, Journal Of Geophysical Research: Oceans, 115, doi:10.1029/2010JC006102, 2010.

Hurrell, J. W., Kushnir, Y., Ottersen, G., and Visbeck, M.: An overview of the North Atlantic Oscillation, vol. 134, Wiley Online Library, doi:10.1029/134GM01, 2003.

Huthnance, J. M.: On Coastal Trapped Waves: Analysis and Numerical Calculation by Inverse Iteration, Journal of Physical Oceanography, 8, 74–92, doi:10.1175/1520-0485(1978)008<0074:OCTWAA>2.0.CO;2, 1978.

Ishii, M. and Kimoto, M.: Reevaluation of historical ocean heat content variations with time-varying XBT and MBT depth bias corrections, Journal Of Oceanography, 65, 287–299, doi:10.1007/s10872-009-0027-7, 2009.

Jevrejeva, S., Grinsted, A., Moore, J. C., and Holgate, S.: Nonlinear trends and multiyear cycles in sea level records, Journal Of Geophysical Research: Oceans, 111, doi:10.1029/2005JC003229, 2006.

Jevrejeva, S., Moore, J. C., Grinsted, A., Matthews, A. P., and Spada, G.: Trends and acceleration in global and regional sea levels since 1807, Global And Planetary Change, 113, 11–22, doi:10.1016/j.gloplacha.2013.12.004, 2014.

Jevrejeva, S., Jackson, L. P., Riva, R. E. M., Grinsted, A., and Moore, J. C.: Coastal sea level rise with warming above 2 °C, Proceedings of the National Academy of Sciences, 113, 13 342–13 347, doi:10.1073/pnas.1605312113, 2016a.

Jevrejeva, S., Matthews, A., and Slangen, A.: The Twentieth-Century Sea Level Budget: Recent Progress and Challenges, Surveys in Geophysics, pp. 1–13, doi:10.1007/s10712-016-9405-z, 2016b.

Johnson, H. L. and Marshall, D. P.: A Theory for the Surface Atlantic Response to Thermohaline Variability, Journal of Physical Oceanography, 32, 1121–1132, doi:10.1175/1520-0485(2002)032<1121:ATFTSA>2.0.CO;2, 2002.

Jordà, G.: Detection time for global and regional sea level trends and accelerations, Journal of Geophysical Research: Oceans, 119, 7164–7174, doi:10.1002/2014JC010005, 2014.

Karegar, M. A., Dixon, T. H., and Engelhart, S. E.: Subsidence along the Atlantic Coast of North America: Insights from GPS and late Holocene relative sea level data, Geophysical Research Letters, 43, 3126–3133, doi:10.1002/2016GL068015, 2016.

Kasdin, N. J.: Discrete simulation of colored noise and stochastic processes and $1/f^{\alpha}$ power law noise generation, Proceedings of the IEEE, 83, 802–827, doi:10.1109/5.381848, 1995.

Katsman, C. A., Sterl, A., Beersma, J. J., Van den Brink, H. W., Church, J. A., Hazeleger, W., Kopp, R. E., Kroon, D., Kwadijk, J., Lammersen, R., et al.: Exploring high-end scenarios for local sea level rise to develop flood protection strategies for a low-lying delta—the Netherlands as an example, Climatic change, 109, 617–645, doi:10.1007/s10584-011-0037-5, 2011.

Kieke, D. and Yashayaev, I.: Studies of Labrador Sea Water formation and variability in the subpolar North Atlantic in the light of international partnership and collaboration, Progress in Oceanography, 132, 220–232, doi:10.1016/j.pocean.2014.12.010, 2015.

Kierulf, H. P., Steffen, H., Simpson, M. J. R., Lidberg, M., Wu, P., and Wang, H.: A GPS velocity field for Fennoscandia and a consistent comparison to glacial isostatic adjustment models, Journal Of Geophys-

ical Research: Solid Earth, 119, 6613–6629, doi:10.1002/2013JB010889, 2014.

King, M. A., Keshin, M., Whitehouse, P. L., Thomas, I. D., Milne, G., and Riva, R. E. M.: Regional biases in absolute sea-level estimates from tide gauge data due to residual unmodeled vertical land movement, Geophysical Research Letters, 39, L14 604, doi:10.1029/2012GL052348, 2012.

Kjeldsen, K. K., Korsgaard, N. J., Bjørk, A. A., Khan, S. A., Box, J. E., Funder, S., Larsen, N. K., Bamber, J. L., Colgan, W., van den Broeke, M., Siggaard-Andersen, M.-L., Nuth, C., Schomacker, A., Andresen, C. S., Willerslev, E., and Kjær, K. H.: Spatial and temporal distribution of mass loss from the Greenland Ice Sheet since AD 1900, Nature, 528, 396–400, doi:10.1038/nature16183, 2015.

Klees, R., Revtova, E. A., Gunter, B. C., Ditmar, P., Oudman, E., Winsemius, H. C., and Savenije, H. H. G.: The design of an optimal filter for monthly GRACE gravity models, Geophysical Journal International, 175, 417–432, doi:10.1111/j.1365-246X.2008.03922.x, 2008.

Kleinherenbrink, M., Riva, R., and Sun, Y.: Sub-basin-scale sea level budgets from satellite altimetry, Argo floats and satellite gravimetry: a case study in the North Atlantic Ocean, Ocean Science, 12, 1179–1203, doi:10.5194/os-12-1179-2016, 2016.

Klinger, B., Mayer-Gürr, T., Behzadpour, S., Ellmer, M., Kvas, A., and Zehentner, N.: The new ITSG-Grace2016 release, EGU General Assembly 2016, Vienna, Austria, doi:10.13140/RG.2.1.1856.7280, 2016.

Kobayashi, S., Yukinari, O. T. A., Harada, Y., Ebita, A., Moriya, M., Onoda, H., Onogi, K., Kamahori, H., Kobayashi, C., MIYAOKA, K., et al.: The JRA-55 reanalysis: General specifications and basic characteristics, Journal of the Meteorological Society of Japan. Ser. II, 93, 5–48, doi:10.2151/jmsj.2015-001, 2015.

Kolker, A. S., Allison, M. A., and Hameed, S.: An evaluation of subsidence rates and sea-level variability in the northern Gulf of Mexico, Geophysical Research Letters, 38, doi:10.1029/2011GL049458, 2011.

Konikow, L. F.: Contribution of global groundwater depletion since 1900 to sea-level rise, Geophysical Research Letters, 38, doi:10.1029/2011GL048604, 2011.

Koopman, S. J.: Disturbance smoother for state space models, Biometrika, pp. 117–126, doi:10.2307/2336762, 1993.

Kopp, R. E.: Does the mid-Atlantic United States sea level acceleration hot spot reflect ocean dynamic variability?, Geophysical Research Letters, 40, 3981–3985, doi:10.1002/grl.50781, 2013.

Kopp, R. E., Horton, R. M., Little, C. M., Mitrovica, J. X., Oppenheimer, M., Rasmussen, D. J., Strauss, B. H., and Tebaldi, C.: Probabilistic 21st and 22nd century sea-level projections at a global network of tide-gauge sites, Earth's Future, 2, 383–406, doi:10.1002/2014EF000239, 2014.

Kopp, R. E., Kemp, A. C., Bittermann, K., Horton, B. P., Donnelly, J. P., Gehrels, W. R., Hay, C. C., Mitrovica, J. X., Morrow, E. D., and Rahmstorf, S.: Temperature-driven global sea-level variability in the Common Era, Proceedings of the National Academy of Sciences, 113, doi:10.1073/pnas.1517056113, 2016.

Kuo, C.-Y., Shum, C. K., Guo, J.-y., Yi, Y., Braun, A., Fukumori, I., Matsumoto, K., Sato, T., and Shibuya, K.: Southern Ocean mass variation studies using GRACE and satellite altimetry, Earth, Planets and Space, 60, 477–485, doi:10.1186/BF03352814, 2008.

Laine, M., Latva-Pukkila, N., and Kyrölä, E.: Analysing time-varying trends in stratospheric ozone time series using the state space approach, Atmospheric Chemistry and Physics, 14, 9707–9725, doi:10.5194/acp-14-9707-2014, 2014.

Landerer, F. W., Jungclaus, J. H., and Marotzke, J.: Ocean bottom pressure changes lead to a decreasing length-of-day in a warming climate, Geophysical Research Letters, 34, doi:10.1029/2006GL029106, 2007a.

Landerer, F. W., Jungclaus, J. H., and Marotzke, J.: Regional dynamic and steric sea level change in response to the IPCC-A1B scenario, Journal Of Physical Oceanography, 37, 296–312, doi:10.1175/JPO3013.1, 2007b.

Le Bars, D., Drijfhout, S., and de Vries, H.: A high-end sea level rise probabilistic projection including rapid Antarctic ice sheet mass loss, Environmental Research Letters, 12, 044 013, doi:10.1088/1748-9326/aa6512, 2017.

Lehner, B., Liermann, C. R., Revenga, C., Vörösmarty, C., Fekete, B., Crouzet, P., Döll, P., Endejan, M., Frenken, K., Magome, J., et al.: High-resolution mapping of the world's reservoirs and dams for sustainable river-flow management, Frontiers in Ecology and the Environment, 9, 494–502, doi:10.1890/100125, 2011.

Leuliette, E. W.: The balancing of the sea-level budget, Current Climate Change Reports, 1, 185–191, doi:10.1007/s40641-015-0012-8, 2015.

Leuliette, E. W. and Miller, L.: Closing the sea level rise budget with altimetry, Argo, and GRACE, Geophysical Research Letters, 36, doi:10.1029/2008GL036010, 2009.

Leuliette, E. W. and Willis, J. K.: Balancing the Sea Level Budget, Oceanography, 24, 122–129, doi:10.5670/oceanog.2011.32, 2011.

Leuliette, E. W., Nerem, R. S., and Mitchum, G. T.: Calibration of TOPEX/Poseidon and Jason altimeter data to construct a continuous record of mean sea level change, Marine Geodesy, 27, 79–94, doi:10.1080/01490410490465193, 2004.

Levitus, S., Antonov, J. I., Boyer, T. P., Baranova, O. K., Garcia, H. E., Locarnini, R. A., Mishonov, A. V., Reagan, J. R., Seidov, D., Yarosh, E. S., and Zweng, M. M.: World ocean heat content and thermosteric sea level change (0-2000 m), 1955-2010, Geophysical Research Letters, 39, L10 603, doi:10.1029/2012GL051106, 2012.

Li, Y., Ji, R., Fratantoni, P. S., Chen, C., Hare, J. A., Davis, C. S., and Beardsley, R. C.: Wind-induced interannual variability of sea level slope, along-shelf flow, and surface salinity on the Northwest Atlantic shelf, Journal of Geophysical Research: Oceans, 119, 2462–2479, doi:10.1002/2013JC009385, 2014.

Little, C. M., Piecuch, C. G., and Ponte, R. M.: On the relationship between the meridional overturning circulation, alongshore wind stress, and United States East Coast sea level in the Community Earth System Model Large Ensemble, Journal of Geophysical Research: Oceans, doi:10.1002/2017JC012713, 2017.

Mantua, N. J., Hare, S. R., Zhang, Y., Wallace, J. M., and Francis, R. C.: A Pacific Interdecadal Climate Oscillation with Impacts on Salmon Production., Bulletin of the American Meteorological Society, 78, 1069–1079, doi:10.1175/1520-0477(1997)078<1069:APICOW>2.0.CO;2, 1997.

Marcos, M., Puyol, B., Calafat, F. M., and Woppelmann, G.: Sea level changes at Tenerife Island (NE Tropical Atlantic) since 1927, Journal Of Geophysical Research: Oceans, 118, 4899–4910, doi:10.1002/jgrc.20377, 2013.

Marcos, M., Marzeion, B., Dangendorf, S., Slangen, A. B. A., Palanisamy, H., and Fenoglio-Marc, L.: Internal Variability Versus Anthropogenic Forcing on Sea Level and Its Components, Surveys in Geophysics, 38, 329–348, doi:10.1007/s10712-016-9373-3, 2017.

Marzeion, B., Leclercq, P. W., Cogley, J. G., and Jarosch, A. H.: Brief Communication: Global reconstructions of glacier mass change during the 20th century are consistent, The Cryosphere, 9, 2399–2404, doi:10.5194/tc-9-2399-2015, 2015.

Marzeion, B., Champollion, N., Haeberli, W., Langley, K., Leclercq, P., and Paul, F.: Observation-Based Estimates of Global Glacier Mass Change and Its Contribution to Sea-Level Change, Surveys in Geophysics, 38, 105–130, doi:10.1007/s10712-016-9394-y, 2017.

Mauritzen, C., Melsom, A., and Sutton, R. T.: Importance of density-compensated temperature change for deep North Atlantic Ocean heat uptake, Nature Geoscience, 5, 905–910, doi:10.1038/NGEO1639, 2012.

McCarthy, G. D., Haigh, I. D., Hirschi, J. J.-M., Grist, J. P., and Smeed, D. A.: Ocean impact on decadal Atlantic climate variability revealed by sea-level observations, Nature, 521, 508–510, doi:10.1038/nature14491, 2015.

McDougall, T. J. and Barker, P. M.: Getting started with TEOS-10 and the Gibbs Seawater (GSW) oceanographic toolbox, SCOR/IAPSO WG, 127, 1–28, 2011.

McGranahan, G., Balk, D., and Anderson, B.: The rising tide: assessing the risks of climate change and human settlements in low elevation coastal zones, Environment And Urbanization, 19, 17–37, doi:10.1177/0956247807076960, 2007.

Meyssignac, B., Slangen, A. B. A., Melet, A., Church, J. A., Fettweis, X., Marzeion, B., Agosta, C., Ligtenberg, S. R. M., Spada, G., Richter, K., Palmer, M. D., Roberts, C. D., and Champollion, N.: Evaluating Model Simulations of Twentieth-Century Sea-Level Rise. Part II: Regional Sea-Level Changes, Journal of Climate, 30, 8565–8593, doi:10.1175/JCLI-D-17-0112.1, 2017.

Milne, G. A. and Mitrovica, J. X.: Postglacial sea-level change on a rotating Earth, Geophysical Journal International, 133, 1–19, doi:10.1046/j.1365-246X.1998.1331455.x, 1998.

Minderhoud, P. S. J., Erkens, G., Pham, V. H., Bui, V. T., Erban, L., Kooi, H., and Stouthamer, E.: Impacts of 25 years of groundwater extraction on subsidence in the Mekong delta, Vietnam, Environmental

Research Letters, 12, 064 006, doi:10.1088/1748-9326/aa7146, 2017.

Minobe, S., Terada, M., Qiu, B., and Schneider, N.: Western Boundary Sea-Level: A Theory, Rule of Thumb, and Application to Climate Models, Journal of Physical Oceanography, doi:10.1175/JPO-D-16-0144.1, 2017.

Mitrovica, J. X. and Milne, G. A.: On the origin of late Holocene sea-level highstands within equatorial ocean basins, Quaternary Science Reviews, 21, 2179–2190, doi:10.1016/S0277-3791(02)00080-X, 2002.

Mitrovica, J. X., Tamisiea, M. E., Davis, J. L., and Milne, G. A.: Recent mass balance of polar ice sheets inferred from patterns of global sea-level change, Nature, 409, 1026–1029, doi:10.1038/35059054, 2001.

Mitrovica, J. X., Gomez, N., Morrow, E., Hay, C., Latychev, K., and Tamisiea, M. E.: On the robustness of predictions of sea level fingerprints, Geophysical Journal International, 187, 729–742, doi:10.1111/j.1365-246X.2011.05090.x, 2011.

Mitrovica, J. X., Hay, C. C., Morrow, E., Kopp, R. E., Dumberry, M., and Stanley, S.: Reconciling past changes in Earths rotation with 20th century global sea-level rise: Resolving Munks enigma, Science Advances, 1, e1500 679–e1500 679, doi:10.1126/sciadv.1500679, 2015.

Moore, J. C., Jevrejeva, S., and Grinsted, A.: The historical global sea-level budget, Annals of Glaciology, 52, 8–14, doi:10.3189/172756411799096196, 2011.

Morice, C. P., Kennedy, J. J., Rayner, N. A., and Jones, P. D.: Quantifying uncertainties in global and regional temperature change using an ensemble of observational estimates: The HadCRUT4 data set, Journal of Geophysical Research: Atmospheres, 117, doi:10.1029/2011JD017187, 2012.

Munk, W.: Twentieth century sea level: An enigma, Proceedings of the National Academy of Science, 99, 6550–6555, doi:10.1073/pnas.092704599, 2002.

Nerem, R. S. and Mitchum, G. T.: Estimates of vertical crustal motion derived from differences of TOPEX/POSEIDON and tide gauge sea level measurements, Geophysical Research Letters, 29, doi:10.1029/2002GL015037, 2002.

Nerem, R. S., Chambers, D. P., Choe, C., and Mitchum, G. T.: Estimating Mean Sea Level Change from the TOPEX and Jason Altimeter Missions, Marine Geodesy, 33, 435–446, doi:10.1080/01490419.2010.491031, 2010.

Nicholls, R. J. and Cazenave, A.: Sea-Level Rise and Its Impact on Coastal Zones, Science, 328, 1517–1520, doi:10.1126/science.1185782, 2010.

Noël, B., van de Berg, W. J., van Meijgaard, E., Kuipers Munneke, P., van de Wal, R. S. W., and van den Broeke, M. R.: Evaluation of the updated regional climate model RACMO2.3: summer snowfall impact on the Greenland Ice Sheet, The Cryosphere, 9, 1831–1844, doi:10.5194/tc-9-1831-2015, 2015.

Pawlowicz, R., McDougall, T., Feistel, R., and Tailleux, R.: An historical perspective on the development of the Thermodynamic Equation of Seawater - 2010, Ocean Science, 8, 161–174, doi:10.5194/os-8-161-2012, 2012.

Peltier, W. R.: Global Glacial Isostasy and the Surface of the Ice-Age Earth: The ICE-5G (VM2) Model and GRACE, Annual Review of Earth and Planetary Sciences, 32, 111–149, doi:10.1146/annurev.earth.32.082503.144359, 2004.

Peltier, W. R., Argus, D. F., and Drummond, R.: Space geodesy constrains ice age terminal deglaciation: The global ICE-6G_C (VM5a) model, Journal of Geophysical Research: Solid Earth, 120, 450–487, doi:10.1002/2014JB011176, 2015.

Pfeffer, J., Spada, G., Mémin, A., Boy, J. P., and Allemand, P.: Decoding the origins of vertical land motions observed today at coasts, Geophysical Journal International, 210, 148, doi:10.1093/gji/ggx142, 2017.

Pfeffer, W. T., Arendt, A. A., Bliss, A., Bolch, T., Cogley, J. G., Gardner, A. S., Hagen, J.-O., Hock, R., Kaser, G., Kienholz, C., Miles, E. S., Moholdt, G., Mölg, N., Paul, F., Radic, V., Rastner, P., Raup, B. H., Rich, J., and Sharp, M. J.: The Randolph Glacier Inventory: a globally complete inventory of glaciers, Journal of Glaciology, 60, 537–552, doi:10.3189/2014JoG13J176, 2014.

Piecuch, C. G. and Ponte, R. M.: Mechanisms of interannual steric sea level variability, Geophysical Research Letters, 38, doi:10.1029/2011GL048440, 2011.

Piecuch, C. G. and Ponte, R. M.: Inverted barometer contributions to recent sea level changes along the northeast coast of North America, Geophysical Research Letters, 42, 5918–5925, doi:10.1002/2015GL064580, 2015.

Piecuch, C. G., Quinn, K. J., and Ponte, R. M.: Satellite-derived interannual ocean bottom pressure variability and its relation to sea level, Geophysical Research Letters, 40, 3106–3110, doi:10.1002/grl.50549, 2013.

Piecuch, C. G., Dangendorf, S., Ponte, R. M., and Marcos, M.: Annual Sea Level Changes on the North American Northeast Coast: Influence of Local Winds and Barotropic Motions, Journal of Climate, 29, 4801–4816, doi:10.1175/JCLI-D-16-0048.1, 2016.

Plag, H.-P. and Tsimplis, M. N.: Temporal variability of the seasonal sea-level cycle in the North Sea and Baltic Sea in relation to climate variability, Global and Planetary Change, 20, 173–203, doi:10.1016/S0921-8181(98)00069-1, 1999.

Proudman, J.: The condition that a long-period tide shall follow the equilibrium-law, Geophysical Journal International, 3, 244–249, doi:10.1111/j.1365-246X.1960.tb00392.x, 1960.

Pugh, D. and Woodworth, P.: Sea-level science: understanding tides, surges, tsunamis and mean sea-level changes, Cambridge University Press, 2014.

Purcell, A., Tregoning, P., and Dehecq, A.: An assessment of the ICE6G_C(VM5a) glacial isostatic adjustment model, Journal of Geophysical Research: Solid Earth, 121, 3939–3950, doi:10.1002/2015JB012742, 2016.

Purkey, S. G. and Johnson, G. C.: Warming of Global Abyssal and Deep Southern Ocean Waters between the 1990s and 2000s: Contributions to Global Heat and Sea Level Rise Budgets, Journal Of Climate, 23, 6336–6351, doi:10.1175/2010JCLI3682.1, 2010.

Purkey, S. G., Johnson, G. C., and Chambers, D. P.: Relative contributions of ocean mass and deep steric changes to sea level rise between 1993 and 2013, Journal of Geophysical Research: Oceans, 119, 7509–7522, doi:10.1002/2014JC010180, 2014.

Rahmstorf, S., Box, J. E., Feulner, G., Mann, M. E., Robinson, A., Rutherford, S., and Schaffernicht, E. J.: Exceptional twentieth-century slowdown in Atlantic Ocean overturning circulation, Nature Climate Change, 5, 475–480, doi:10.1038/NCLIMATE2554, 2015.

Rahmstorf, S., Foster, G., and Cahill, N.: Global temperature evolution: recent trends and some pitfalls, Environmental Research Letters, 12, 054 001, doi:10.1088/1748-9326/aa6825, 2017.

Ray, R. D. and Douglas, B. C.: Experiments in reconstructing twentieth-century sea levels, Progress In Oceanography, 91, 496–515, doi:10.1016/j.pocean.2011.07.021, 2011.

Ray, R. D., Beckley, B. D., and Lemoine, F. G.: Vertical crustal motion derived from satellite altimetry and tide gauges, and comparisons with DORIS measurements, Advances in Space Research, 45, 1510–1522, doi:10.1016/j.asr.2010.02.020, 2010.

Ray, R. D., Luthcke, S. B., and van Dam, T.: Monthly Crustal Loading Corrections for Satellite Altimetry, Journal of Atmospheric and Oceanic Technology, 30, 999–1005, doi:10.1175/JTECH-D-12-00152.1, 2013.

Reager, J. T., Gardner, A. S., Famiglietti, J. S., Wiese, D. N., Eicker, A., and Lo, M. H.: A decade of sea level rise slowed by climate-driven hydrology, Science, 351, 699–703, doi:10.1126/science.aad8386, 2016.

Rhein, M., Kieke, D., Hüttl-Kabus, S., Roessler, A., Mertens, C., Meissner, R., Klein, B., Böning, C. W., and Yashayaev, I.: Deep water formation, the subpolar gyre, and the meridional overturning circulation in the subpolar North Atlantic, Deep Sea Research Part II: Topical Studies in Oceanography, 58, 1819–1832, doi:10.1016/j.dsr2.2010.10.061, 2011.

Richter, K., Nilsen, J. E. Ø., and Drange, H.: Contributions to sea level variability along the Norwegian coast for 1960-2010, Journal of Geophysical Research: Oceans, 117, C05 038, doi:10.1029/2011JC007826, 2012.

Richter, K., Riva, R. E. M., and Drange, H.: Impact of self-attraction and loading effects induced by shelf mass loading on projected regional sea level rise, Geophysical Research Letters, 40, 1144–1148, doi:10.1002/grl.50265, 2013.

Riddell, A. R., King, M. A., Watson, C. S., Sun, Y., Riva, R. E., and Rietbroek, R.: Uncertainty in geocenter estimates in the context of ITRF2014, Journal of Geophysical Research: Solid Earth, doi:10.1002/2016JB013698, 2017.

Rietbroek, R., Brunnabend, S.-E., Kusche, J., Schröter, J., and Dahle, C.: Revisiting the contemporary sea-level budget on global and regional scales, Proceedings of the National Academy of Sciences, 113, 1504–1509, doi:10.1073/pnas.1519132113, 2016.

Rignot, E., Velicogna, I., van den Broeke, M. R., Monaghan, A., and Lenaerts, J. T. M.: Acceleration of the

contribution of the Greenland and Antarctic ice sheets to sea level rise, Geophysical Research Letters, 38, L05 503, doi:10.1029/2011GL046583, 2011.

Riva, R. E. M., Frederikse, T., King, M. A., Marzeion, B., and van den Broeke, M.: Brief Communication: The global signature of post-1900 land ice wastage on vertical land motion, The Cryosphere, 11, 1327–1332, doi:10.5194/tc-11-1327-2017, 2017.

Roberts, C. D., Garry, F. K., and Jackson, L. C.: A Multimodel Study of Sea Surface Temperature and Subsurface Density Fingerprints of the Atlantic Meridional Overturning Circulation, Journal of Climate, 26, 9155–9174, doi:10.1175/JCLI-D-12-00762.1, 2013.

Robson, J., Hodson, D., Hawkins, E., and Sutton, R.: Atlantic overturning in decline?, Nature Geoscience, 7, 2–3, doi:10.1038/ngeo2050, 2014.

Roemmich, D. and Gilson, J.: The 2004-2008 mean and annual cycle of temperature, salinity, and steric height in the global ocean from the Argo Program, Progress in Oceanography, 82, 81–100, doi:10.1016/j.pocean.2009.03.004, 2009.

Roemmich, D., Johnson, G. C., Riser, S. C., Davis, R. E., Gilson, J., Owens, W. B., Garzoli, S. L., Schmid, C., and Ignaszewski, M.: The Argo Program: Observing the global ocean with profiling floats, Oceanography, doi:10.5670/oceanog.2009.36, 2009.

Rohling, E. J., Foster, G. L., Grant, K. M., Marino, G., Roberts, A. P., Tamisiea, M. E., and Williams, F.: Sea-level and deep-sea-temperature variability over the past 5.3 million years, Nature, 508, 477–482, doi:10.1038/nature13230, 2014.

Roquet, F., Madec, G., McDougall, T. J., and Barker, P. M.: Accurate polynomial expressions for the density and specific volume of seawater using the TEOS-10 standard, Ocean Modelling, 90, 29–43, doi:10.1016/j.ocemod.2015.04.002, 2015.

Roussenov, V. M., Williams, R. G., Hughes, C. W., and Bingham, R. J.: Boundary wave communication of bottom pressure and overturning changes for the North Atlantic, Journal of Geophysical Research: Oceans, 113, C08 042, doi:10.1029/2007JC004501, 2008.

Roy, K. and Peltier, W. R.: Glacial isostatic adjustment, relative sea level history and mantle viscosity: reconciling relative sea level model predictions for the U.S. East coast with geological constraints, Geophysical Journal International, 201, 1156–1181, doi:10.1093/gji/ggv066, 2015.

Sabadini, R., Vermeersen, B., and Cambiotti, G.: Global Dynamics of the Earth: Applications of Viscoelastic Relaxation Theory to Solid-Earth and Planetary Geophysics, Springer, doi:10.1007/978-94-017-7552-6-2, 2016.

Sallenger, A. H., Doran, K. S., and Howd, P. A.: Hotspot of accelerated sea-level rise on the Atlantic coast of North America, Nature Climate Change, 2, 884–888, doi:10.1038/nclimate1597, 2012.

Sanderson, C. and Curtin, R.: Armadillo: a template-based C++ library for linear algebra, Journal of Open Source Software, 1, doi:10.21105/joss.00026, 2016.

Santamaría-Gómez, A. and Mémin, A.: Geodetic secular velocity errors due to interannual surface loading deformation, Geophysical Journal International, 202, 763–767, doi:10.1093/gji/ggv190, 2015.

Santamaría-Gómez, A., Gravelle, M., Collilieux, X., Guichard, M., Míguez, B. M., Tiphaneau, P., and Wöppelmann, G.: Mitigating the effects of vertical land motion in tide gauge records using a state-of-the-art GPS velocity field, Global and Planetary Change, 98, 6–17, doi:10.1016/j.gloplacha.2012.07.007, 2012.

Santamaría-Gómez, A., Gravelle, M., Dangendorf, S., Marcos, M., Spada, G., and Wöppelmann, G.: Uncertainty of the 20th century sea-level rise due to vertical land motion errors, Earth and Planetary Science Letters, 473, 24–32, doi:10.1016/j.epsl.2017.05.038, 2017.

Schaeffer, N.: Efficient spherical harmonic transforms aimed at pseudospectral numerical simulations, Geochemistry, Geophysics, Geosystems, 14, 751–758, doi:10.1002/ggge.20071, 2013.

Schweppe, F.: Evaluation of likelihood functions for Gaussian signals, IEEE transactions on Information Theory, 11, 61–70, doi:10.1109/TIT.1965.1053737, 1965.

Shepherd, A., Ivins, E. R., A, G., Barletta, V. R., Bentley, M. J., Bettadpur, S., Briggs, K. H., Bromwich, D. H., Forsberg, R., Galin, N., Horwath, M., Jacobs, S., Joughin, I., King, M. A., Lenaerts, J. T. M., Li, J., Ligtenberg, S. R. M., Luckman, A., Luthcke, S. B., McMillan, M., Meister, R., Milne, G., Mouginot, J., Muir, A., Nicolas, J. P., Paden, J., Payne, A. J., Pritchard, H., Rignot, E., Rott, H., Sørensen, L. S., Scambos, T. A., Scheuchl, B., Schrama, E. J. O., Smith, B., Sundal, A. V., van Angelen, J. H., van de Berg, W. J., van den Broeke, M. R., Vaughan, D. G., Velicogna, I., Wahr, J., Whitehouse, P. L., Wingham,

D. J., Yi, D., Young, D., and Zwally, H. J.: A reconciled estimate of ice-sheet mass balance., Science, 338, 1183–9, doi:10.1126/science.1228102, 2012.

Shumway, R. H. and Stoffer, D. S.: An approach to time series smoothing and forecasting using the EM algorithm, Journal of time series analysis, 3, 253–264, doi:10.1111/j.1467-9892.1982.tb00349.x, 1982.

Simon, K. and Riva, R.: A data-driven model of present-day glacial isostatic adjustment in North America, Geophysical Research Abstracts (online), 18, 1–1, doi:10.13140/RG.2.2.13343.76964, 2016.

Simon, K. M., Riva, R. E. M., Kleinherenbrink, M., and Tangdamrongsub, N.: A data-driven model for constraint of present-day glacial isostatic adjustment in North America, Earth and Planetary Science Letters, 474, 322–333, doi:10.1016/j.epsl.2017.06.046, 2017.

Slangen, A. B. A., Carson, M., Katsman, C. A., Van de Wal, R. S. W., Köhl, A., Vermeersen, L. L. A., and Stammer, D.: Projecting twenty-first century regional sea-level changes, Climatic Change, 124, 317–332, doi:10.1007/s10584-014-1080-9, 2014a.

Slangen, A. B. A., van de Wal, R. S. W., Wada, Y., and Vermeersen, L. L. A.: Comparing tide gauge observations to regional patterns of sea-level change (1961-2003), Earth System Dynamics, 5, 243–255, doi:10.1194/esd-5-243-2014, 2014b.

Slangen, A. B. A., Church, J. A., Agosta, C., Fettweis, X., Marzeion, B., and Richter, K.: Anthropogenic forcing dominates global mean sea-level rise since 1970, Nature Climate Change, 6, 701–705, doi:10.1038/nclimate2991, 2016.

Slangen, A. B. A., Meyssignac, B., Agosta, C., Champollion, N., Church, J. A., Fettweis, X., Ligtenberg, S. R. M., Marzeion, B., Melet, A., Palmer, M. D., Richter, K., Roberts, C. D., and Spada, G.: Evaluating model simulations of 20th century sea-level rise. Part 1: Global mean sea-level change., Journal of Climate, doi:10.1175/JCLI-D-17-0110.1, 2017a.

Slangen, A. B. A., van de Wal, R. S. W., Reerink, T. J., de Winter, R. C., Hunter, J. R., Woodworth, P. L., and Edwards, T.: The Impact of Uncertainties in Ice Sheet Dynamics on Sea-Level Allowances at Tide Gauge Locations, Journal of Marine Science and Engineering, 5, doi:10.3390/jmse5020021, 2017b.

Sosdian, S. and Rosenthal, Y.: Deep-sea temperature and ice volume changes across the Pliocene-Pleistocene climate transitions., Science, 325, 306–10, doi:10.1126/science.1169938, 2009.

Stammer, D., Cazenave, A., Ponte, R. M., and Tamisiea, M. E.: Causes for contemporary regional sea level changes., Annual Review of Marine Science, 5, 21–46, doi:10.1146/annurev-marine-121211-172406, 2013.

Stouffer, R. J., Yin, J., Gregory, J. M., Dixon, K. W., Spelman, M. J., Hurlin, W., Weaver, A. J., Eby, M., Flato, G. M., Hasumi, H., et al.: Investigating the causes of the response of the thermohaline circulation to past and future climate changes, Journal of Climate, 19, 1365–1387, doi:10.1175/JCLI3689.1, 2006.

Sturges, W. and Douglas, B. C.: Wind effects on estimates of sea level rise, Journal Of Geophysical Research: Oceans, 116, doi:10.1029/2010JC006492, 2011.

Swenson, S., Chambers, D., and Wahr, J.: Estimating geocenter variations from a combination of GRACE and ocean model output, Journal Of Geophysical Research: Solid Earth, 113, doi:10.1029/2007JB005338, 2008.

Talpe, M. J., Nerem, R. S., Forootan, E., Schmidt, M., Lemoine, F. G., Enderlin, E. M., and Landerer, F. W.: Ice mass change in Greenland and Antarctica between 1993 and 2013 from satellite gravity measurements, Journal of Geodesy, pp. 1–16, doi:10.1007/s00190-017-1025-y, 2017.

Tamisiea, M. E.: Ongoing glacial isostatic contributions to observations of sea level change, Geophysical Journal International, 186, 1036–1044, doi:10.1111/j.1365-246X.2011.05116.x, 2011.

Tamisiea, M. E. and Mitrovica, J. X.: The Moving Boundaries of Sea Level Change Understanding the Origins of Geographic Variability, Oceanography, 24, 24–39, doi:10.5670/oceanog.2011.25, 2011.

Tamisiea, M. E., Hill, E. M., Ponte, R. M., Davis, J. L., Velicogna, I., and Vinogradova, N. T.: Impact of self-attraction and loading on the annual cycle in sea level, Journal of Geophysical Research: Oceans, 115, C07 004, doi:10.1029/2009JC005687, 2010.

Tapley, B. D., Bettadpur, S., Ries, J. C., Thompson, P. F., and Watkins, M. M.: GRACE measurements of mass variability in the Earth system, Science, 305, 503–505, doi:10.1126/science.1099192, 2004.

Thompson, K. R.: North Atlantic sea-level and circulation, Geophysical Journal International, 87, 15–32, doi:10.1111/j.1365-246X.1986.tb04543.x, 1986.

Thompson, P. R. and Merrifield, M. A.: A unique asymmetry in the pattern of recent sea level change, Geophysical Research Letters, 41, 7675–7683, doi:10.1002/2014GL061263, 2014.

Thompson, P. R. and Mitchum, G. T.: Coherent sea level variability on the North Atlantic western boundary, Journal of Geophysical Research: Oceans, 119, 5676–5689, doi:10.1002/2014JC009999, 2014.

Thompson, P. R., Hamlington, B. D., Landerer, F. W., and Adhikari, S.: Are long tide gauge records in the wrong place to measure global mean sea level rise?, Geophysical Research Letters, 43, 10 403–10 411, doi:10.1002/2016GL070552, 2016.

van den Broeke, M. R., Enderlin, E. M., Howat, I. M., Kuipers Munneke, P., Noël, B. P. Y., van de Berg, W. J., van Meijgaard, E., and Wouters, B.: On the recent contribution of the Greenland ice sheet to sea level change, The Cryosphere, 10, 1933–1946, doi:10.5194/tc-10-1933-2016, 2016.

van Wessem, J. M., Reijmer, C. H., Morlighem, M., Mouginot, J., Rignot, E., Medley, B., Joughin, I., Wouters, B., Depoorter, M. A., Bamber, J. L., Lenaerts, J. T. M., van de Berg, W. J., van den Broeke, M. R., and van Meijgaard, E.: Improved representation of East Antarctic surface mass balance in a regional atmospheric climate model, Journal of Glaciology, 60, 761–770, doi:10.3189/2014JoG14J051, 2014.

van Wessem, J. M., Ligtenberg, S. R. M., Reijmer, C. H., van de Berg, W. J., van den Broeke, M. R., Barrand, N. E., Thomas, E. R., Turner, J., Wuite, J., Scambos, T. A., and van Meijgaard, E.: The modelled surface mass balance of the Antarctic Peninsula at 5.5 km horizontal resolution, The Cryosphere, 10, 271–285, doi:10.5194/tc-10-271-2016, 2016.

Veit, E. and Conrad, C. P.: The impact of groundwater depletion on spatial variations in sea level change during the past century, Geophysical Research Letters, 43, 3351–3359, doi:10.1002/2016GL068118, 2016.

Vermeer, M. and Rahmstorf, S.: From the Cover: Global sea level linked to global temperature, Proceedings of the National Academy of Sciences, 106, 21 527–21 532, doi:10.1073/pnas.0907765106, 2009.

Vinogradova, N. T. and Ponte, R. M.: In search for fingerprints of the recent intensification of the ocean water cycle, Journal of Climate, 0, doi:10.1175/JCLI-D-16-0626.1, 2017.

Wada, Y., van Beek, L. P. H., van Kempen, C. M., Reckman, J. W. T. M., Vasak, S., and Bierkens, M. F. P.: Global depletion of groundwater resources, Geophysical Research Letters, 37, doi:10.1029/2010GL044571, 2010.

Wada, Y., van Beek, L. P. H., and Bierkens, M. F. P.: Modelling global water stress of the recent past: on the relative importance of trends in water demand and climate variability, Hydrology and Earth System Sciences, 15, 3785–3808, doi:10.5194/hess-15-3785-2011, 2011.

Wada, Y., van Beek, L. P. H., Sperna Weiland, F. C., Chao, B. F., Wu, Y.-H., and Bierkens, M. F. P.: Past and future contribution of global groundwater depletion to sea-level rise, Geophysical Research Letters, 39, L09 402, doi:10.1029/2012GL051230, 2012.

Wada, Y., Wisser, D., and Bierkens, M. F. P.: Global modeling of withdrawal, allocation and consumptive use of surface water and groundwater resources, Earth System Dynamics, 5, 15–40, doi:10.5194/esd-5-15-2014, 2014.

Wada, Y., Lo, M.-H., Yeh, P. J.-F., Reager, J. T., Famiglietti, J. S., Wu, R.-J., and Tseng, Y.-H.: Fate of water pumped from underground and contributions to sea-level rise, Nature Climate Change, 6, 777–780, doi:10.1038/nclimate3001, 2016.

Wahl, T., Jensen, J., Frank, T., and Haigh, I. D.: Improved estimates of mean sea level changes in the German Bight over the last 166 years, Ocean Dynamics, 61, 701–715, doi:10.1007/s10236-011-0383-x, 2011.

Wahl, T., Haigh, I. D., Woodworth, P. L., Albrecht, F., Dillingh, D., Jensen, J., Nicholls, R. J., Weisse, R., and Wöppelmann, G.: Observed mean sea level changes around the North Sea coastline from 1800 to present, Earth-Science Reviews, 124, 51–67, doi:10.1016/j.earscirev.2013.05.003, 2013.

Wahl, T., Haigh, I. D., Nicholls, R. J., Arns, A., Dangendorf, S., Hinkel, J., and Slangen, A. B. A.: Understanding extreme sea levels for broad-scale coastal impact and adaptation analysis, Nature Communications, 8, doi:10.1038/ncomms16075, 2017.

Watkins, M. M., Wiese, D. N., Yuan, D.-N., Boening, C., and Landerer, F. W.: Improved methods for observing Earth's time variable mass distribution with GRACE using spherical cap mascons, Journal of Geophysical Research: Solid Earth, 120, 2648–2671, doi:10.1002/2014JB011547, 2015.

Watson, M. W. and Engle, R. F.: Alternative algorithms for the estimation of dynamic factor, mimic and varying coefficient regression models, Journal of Econometrics, 23, 385–400, doi:10.1016/0304-4076(83)90066-0, 1983.

Wenzel, M. and Schröter, J.: Global and regional sea level change during the 20th century, Journal of

Geophysical Research: Oceans, 119, 7493–7508, doi:10.1002/2014JC009900, 2014.

Wessel, P., Smith, W. H. F., Scharroo, R., Luis, J., and Wobbe, F.: Generic Mapping Tools: Improved Version Released, Eos, Transactions American Geophysical Union, 94, 409–410, doi:10.1002/2013EO450001, 2013.

Whitehouse, P. L., Bentley, M. J., Milne, G. A., King, M. A., and Thomas, I. D.: A new glacial isostatic adjustment model for Antarctica: calibrated and tested using observations of relative sea-level change and present-day uplift rates, Geophysical Journal International, 190, 1464–1482, doi:10.1111/j.1365-246X.2012.05557.x, 2012.

Williams, J. and Hughes, C. W.: The coherence of small island sea level with the wider ocean: a model study, Ocean Science, 9, 111–119, doi:10.1194/os-9-111-2013, 2013.

Williams, R. G., Roussenov, V., Smith, D., and Lozier, M. S.: Decadal Evolution of Ocean Thermal Anomalies in the North Atlantic: The Effects of Ekman, Overturning, and Horizontal Transport, Journal Of Climate, 27, 698–719, doi:175/JCLI-D-12-00234.1, 2014.

Wolter, K. and Timlin, M. S.: Monitoring ENSO in COADS with a seasonally adjusted principal component index, in: Proc. of the 17th Climate Diagnostics Workshop, vol. 5257, 1993.

Woodworth, P. L.: A Note on the Nodal Tide in Sea Level Records, Journal Of Coastal Research, 28, 316–323, doi:10.1112/JCOASTRES-D-11A-00023.1, 2012.

Woodworth, P. L., White, N. J., Jevrejeva, S., Holgate, S. J., Church, J. A., and Gehrels, W. R.: Evidence for the accelerations of sea level on multi-decade and century timescales, International Journal of Climatology, 29, 777–789, doi:10.1002/joc.1771, 2009.

Woodworth, P. L., Maqueda, M. Á. M., Roussenov, V. M., Williams, R. G., and Hughes, C. W.: Mean sea-level variability along the northeast American Atlantic coast and the roles of the wind and the overturning circulation, Journal of Geophysical Research: Oceans, 119, 8916–8935, doi:10.1002/2014JC010520, 2014.

Woodworth, P. L., Wöppelmann, G., Marcos, M., Gravelle, M., and Bingley, R. M.: Why we must tie satellite positioning to tide gauge data, Eos, doi:10.1029/2017EO064037, 2017.

Wöppelmann, G. and Marcos, M.: Vertical land motion as a key to understanding sea level change and variability, Reviews of Geophysics, 54, 64–92, doi:10.1002/2015RG000502, 2016.

Wöppelmann, G., Letetrel, C., Santamaria, A., Bouin, M.-N., Collilieux, X., Altamimi, Z., Williams, S. D. P., and Miguez, B. M.: Rates of sea-level change over the past century in a geocentric reference frame, Geophysical Research Letters, 36, L12 607, doi:10.1029/2009GL038720, 2009.

Wöppelmann, G., Marcos, M., Santamaría-Gómez, A., Martín-Míguez, B., Bouin, M.-N., and Gravelle, M.: Evidence for a differential sea level rise between hemispheres over the twentieth century, Geophysical Research Letters, 41, 1639–1643, doi:10.1002/2013GL059039, 2014.

Wunsch, C. and Stammer, D.: Atmospheric loading and the oceanic "inverted barometer" effect, Reviews of Geophysics, 35, 79–107, doi:10.1029/96RG03037, 1997.

Yin, J., Schlesinger, M. E., and Stouffer, R. J.: Model projections of rapid sea-level rise on the northeast coast of the United States, Nature Geoscience, 2, 262–266, doi:10.1038/ngeo462, 2009.

Yin, J., Griffies, S. M., and Stouffer, R. J.: Spatial Variability of Sea Level Rise in Twenty-First Century Projections, Journal Of Climate, 23, 4585–4607, doi:10.1175/2010JCLI3533.1, 2010.

Zeebe, R. E., Ridgwell, A., and Zachos, J. C.: Anthropogenic carbon release rate unprecedented during the past 66 million years, Nature Geoscience, 9, 325–329, doi:10.1038/ngeo2681, 2016.

Zhang, R.: Coherent surface-subsurface fingerprint of the Atlantic meridional overturning circulation, Geophysical Research Letters, 35, doi:10.1029/2008GL035463, 2008.

Zijl, F., Verlaan, M., and Gerritsen, H.: Improved water-level forecasting for the Northwest European Shelf and North Sea through direct modelling of tide, surge and non-linear interaction, Ocean Dynamics, 63, 823–847, doi:10.1007/s10236-013-0624-2, 2013.

Acknowledgements

This section contains all sources of the data thas has been used in this thesis, except for data that either has been provided by co-authors of the published articles on which this thesis is based, or can be found in the main body or supporting information of the articles to which is referred in the text.

Tide-gauge data

All tide-gauge data, as well as the global sea-level reconstructions from Jevrejeva et al. (2014) and Ray and Douglas (2011) have been obtained from the Permanent Service for Mean Sea Level (PSMSL, Holgate et al. (2013), `www.psmsl.org`), except for the Cuxhaven tide-gauge record in Chapters 2 and 6, which have been obtained from Sönke Dangendorf. The tide-gauge reconstruction from Church and White (2011) has been obtained from `www.cmar.csiro.au/sealevel/`.

Vertical Land Motion

The GPS data and derived trends have been obtained from the Nevada Geodetic Laboratory (`http://geodesy.unr.edu/`), except for the Norwegian GPS records in Chapter 2, which have been obtained from Kierulf et al. (2014).

Glacial Isostatic Adjustment

The present-day sea-level, geoid and solid-earth deformation fields based on the ICE5G-VM2 model and the ICE6G-VM5a model have been obtained from `www.atmosp.physics.utoronto.ca/~peltier/data.php`.

Subsurface Temperature and Salinity

The EN4.1.1 gridded T/S profiles have been downloaded from the Met Office Hadley Center (`www.metoffice.gov.uk/hadobs/en4`). The Ishii and Kimoto (2009) dataset has been obtained from `https://rda.ucar.edu/datasets/ds285.3/`. The Cheng et al. (2016) dataset has been obtained from `http://159.226.119.60/cheng/`. The Levitus et al. (2012) data comes from `www.nodc.noaa.gov/OC5/3M_HEAT_CONTENT/`. T/S profiles from fixed hydrographic stations along the Norwegian coast have been obtained from `www.imr.no/forskning/forskningsdata/stasjoner`. Ocean Weather Station Mike data has been obtained from `www.eurosites.info/stationm.php`. For computing steric anomalies from the T/S profiles, the

TEOS-10 GSW matlab and C++ routines (Roquet et al., 2015) have been used (www.teos-10.org/software.htm).

Mass Redistribution Models

Data from the IMBIE intercomparison project has been obtained from www.imbie.org. Kurt H. Kjær and Kristian K. Kjeldsen are acknowledged for providing the Greenland mass balance data described in Kjeldsen et al. (2015).

Earth System Models

NorESM2-M (Bentsen et al., 2013) model results have been obtained from the ESGF Node at DKRZ (https://esgf-data.dkrz.de/projects/esgf-dkrz/).

Teleconnections and Atmospheric Reanalysis

The pressure and wind fields from the 20th Century Reanalysis Project V2c have been obtained from NOAA Earth System Research Laboratory (www.esrl.noaa.gov/psd/data/gridded). JRA55 reanalysis data has been obtained from the Japan Meteorological Agency (http://jra.kishou.go.jp/JRA-55/index_en.html). ICOADS 3.0 data has been downloaded from the UCAR/NCAR Research Data Archive (https://rda.ucar.edu/datasets/ds548.0/).
ERA-interim reanalysis data have been obtained from ECMWF (http://apps.ecmwf.int/datasets/data/interim-full-daily/). The indices for the NAO and the PDO have been obtained from NOAA climate prediction center (www.cpc.ncep.noaa.gov/products/precip/CWlink/daily_ao_index/teleconnections.shtml). The MEI has been obtained from NOAA's Earth System Research Laboratory (www.esrl.noaa.gov/psd/enso/mei).

Altimetry

Gridded altimetry observations from the ESA CCI project have been downloaded from http://cci.esa.int/data. AVISO gridded altimetry observations have been obtained from https://aviso.altimetry.fr.

GRACE

The ITSG spherical harmonics solutions have been downloaded from www.tugraz.at/institute/ifg/downloads/gravity-field-models/. The JPL mascon solution has been obtained from https://grace.jpl.nasa.gov/data/get-data/.

Sea-level equation

The sea-level equation solver uses the SHTNS C++ toolbox (Schaeffer, 2013) for computing the spherical harmonics syntheses and analyses, which has been obtained

from https://users.isterre.fr/nschaeff/SHTns/pages.html. For matrix and vector computations, the Armadillo C++ routines (Sanderson and Curtin, 2016) have been used.

Trend analysis

The Hector software (Bos et al., 2013), obtained from http://segal.ubi.pt/hector, has been used to estimate trends in time series with autocorrelated residuals and to generate surrogate noise series for Monte Carlo simulations.

Figures

All figures in this thesis, except for Figure 1.6, have been generated using the Generic Mapping Tools (Wessel et al., 2013). Some color schemes are based on the ColorBrewer2 schemes by Cynthia Brewer (www.colorbrewer2.org). The bathymetry shown in some figures has been obtained from the GEBCO database (www.gebco.net/).

List of Publications

Frederikse, T., Riva, R. E. M., Slobbe, D. C., Broerse, D. B. T., and Verlaan, M.: Estimating decadal variability in sea level from tide gauge records: An application to the North Sea, Journal of Geophysical Research: Oceans, doi:10.1002/2015JC011174, 2016.

Frederikse, T., Riva, R. E. M., Kleinherenbrink, M., Wada, Y., van den Broeke, M. R., and Marzeion, B.: Closing the sea level budget on a regional scale: Trends and variability on the Northwestern European continental shelf., Geophysical Research Letters, doi:10.1002/2016GL070750, 2016.

Riva, R. E. M., Frederikse, T., King, M. A., Marzeion, B., and van den Broeke, M. R.: Brief Communication: The global signature of post-1900 land ice wastage on vertical land motion, The Cryosphere, doi:10.5194/tc-2016-274, 2016.

Frederikse, T., Simon, K. M., Katsman, C. A., and Riva, R. E. M..: The sea-level budget along the Northwest Atlantic coast: GIA, mass changes and large-scale ocean dynamics, Journal of Geophysical Research: Oceans, doi:10.1002/2017JC012699, 2017.

Dangendorf, S., Marcos, M., Wöppelmann, G., Conrad, C. P., Frederikse, T., and Riva, R. E. M.: Reassessment of 20th century global mean sea level rise, Proceedings of the National Academy of Sciences, doi:10.1073/pnas.1616007114, 2017.

Kleinherenbrink, M., Riva, R. E. M., Frederikse, T., Merrifield, M., and Wada, Y.: Trends and interannual variability of mass and steric sea level in the Tropical Asian Seas, Journal of Geophysical Research: Oceans,doi:10.1002/2017JC012792, 2017.

Slobbe, D. C., Sumihar, J., Frederikse, T., Verlaan, M., Klees, R., Zijl, F., Farahani, H. H., and Broekman, R.: A Kalman filter approach to realize the lowest astronomical tide surface, Marine Geodesy, doi:10.1080/01490419.2017.1391900, 2017.

Frederikse, T., Jevrejeva, S., Riva, R. E. M., and Dangendorf, S.: A consistent sea-level reconstruction and its budget on basin and global scales over 1958-2014, Journal of Climate, doi:10.1175/JCLI-D-17-0502.1, 2017.

Frederikse, T., Riva, R. E. M., and King, M. A.: Ocean-bottom deformation due to present-day mass transport and its impact on sea-level observations, Geophysical Research Letters, doi:10.1002/2017GL075419, 2017.

Kleinherenbrink, M., Riva, R. E. M., Frederikse, T.: A comparison of data weighting methods to derive vertical land motion trends from GNSS and altimetry at tide-gauge stations. Accepted for publication in Ocean Sciences, doi:10.5194/os-2017-92.

Simon, K. M., Riva, R. E. M., Kleinherenbrink, M., Frederikse, T.: The long-term GIA signal at present-day in Scandinavia, northern Europe and the British Isles estimated from GPS and GRACE data. Submitted to Solid Earth, doi:10.5194/se-2018-8.

Frederikse, T., De Roode, S. R., Jonker, H. J. J., and Siebesma, A. P.: Precipitation control on mesoscale cloud cellular organization. Submitted to Journal of the Atmospheric Sciences.

Dangendorf, S., Niehüser, S., Schmidt, J., Frederikse, T., Gehrels, R., Gräwe, U., Steffen, H., Jänicke, L., Arns, A., Jensen, J.: Progress in understanding sea level changes in the southeastern North Sea, In preparation.

De Roode, S. R., Frederikse, T., Siebesma, A. P., Hill, A., Field, P., Lac, C., Tomassini, L., Fricke, J., Noda, A., Honnert, R., Krueger, S., Lasage, A. T.: The Cold Air Outbreak intercomparison project. In preparation.

Curriculum Vitae

De stoftor begreep dat hij iets moest doen
voor het zo mis zou gaan met hem dat
het nooit meer goed zou komen.

Toon Tellegen

December 26, 1988	Born in Amsterdam, The Netherlands
2001-2007	Stedelijk Gymnasium Haarlem
2007-2011	Bachelor of Science in Applied Physics, Delft University of Technology
2011-2013	Master of Science in Applied Physics, Delft University of Technology Master thesis "Simulations and explanations of large-scale structures during a Cold Air Outbreak" Internship at Max Planck institute for Meteorology: "Soil moisture - precipitation feedback: Simulations in a LES framework"
2013 - present	PhD candidate at Geoscience and Remote Sensing
2017 - present	Postdoc at the Institute of Marine and Atmospheric Research, Utrecht University